



**HAL**  
open science

# Numerical assessment of heat stress in dwellings and immediate surroundings : Development of a microclimate zonal model coupled to building models

Flavia Barone Mourand

## ► To cite this version:

Flavia Barone Mourand. Numerical assessment of heat stress in dwellings and immediate surroundings : Development of a microclimate zonal model coupled to building models. Architecture, space management. INSA de Lyon, 2024. English. NNT : 2024ISAL0020 . tel-04769709

**HAL Id: tel-04769709**

**<https://theses.hal.science/tel-04769709v1>**

Submitted on 6 Nov 2024

**HAL** is a multi-disciplinary open access archive for the deposit and dissemination of scientific research documents, whether they are published or not. The documents may come from teaching and research institutions in France or abroad, or from public or private research centers.

L'archive ouverte pluridisciplinaire **HAL**, est destinée au dépôt et à la diffusion de documents scientifiques de niveau recherche, publiés ou non, émanant des établissements d'enseignement et de recherche français ou étrangers, des laboratoires publics ou privés.



NNT : 2024ISAL0020

**THESE de DOCTORAT DE L'UNIVERSITE DE LYON**

Opérée au sein de :

**L'Institut National des Sciences Appliquées de Lyon**

**Ecole Doctorale N°162**

**MECANIQUE, ENERGETIQUE, GENIE CIVIL, ACOUSTIQUE**

**Spécialité/discipline de doctorat :**

Thermique Energétique

Soutenue publiquement le 15 février 2024, par :

**Flavia BARONE**

---

**Numerical assessment of heat stress in dwellings and immediate surroundings: development of a Microclimate Zonal Model coupled to Building Models**

---

Devant le jury composé de :

BOZONNET Emmanuel	Maitre de conférence- HDR, Université La Rochelle	Rapporteur
MATZARAKIS Andreas	Professeur des universités, German Meteorological Service (Research Centre Human Biometeorology )	Rapporteur
ROUX Jean-Jaques	Professeur émérite, INSA Lyon	Examineur
WOLOSZYN Monica	Professeure des universités, Université Savoie Mont Blanc (LOCIE)	Examinatrice
KUZNIK Frédéric	Professeur des universités, INSA Lyon (CETHIL)	Directeur de thèse
MERLIER Lucie	Maitresse de conférence, Université Lyon 1 (CETHIL)	Co-directrice

Référence : TH1062\_BARONE Flavia

L'INSA Lyon a mis en place une procédure de contrôle systématique via un outil de détection de similitudes (logiciel Compilatio). Après le dépôt du manuscrit de thèse, celui-ci est analysé par l'outil. Pour tout taux de similarité supérieur à 10%, le manuscrit est vérifié par l'équipe de FEDORA. Il s'agit notamment d'exclure les auto-citations, à condition qu'elles soient correctement référencées avec citation expresse dans le manuscrit.

Par ce document, il est attesté que ce manuscrit, dans la forme communiquée par la personne doctorante à l'INSA Lyon, satisfait aux exigences de l'Établissement concernant le taux maximal de similitude admissible.

## Département FEDORA – INSA Lyon - Ecoles Doctorales

SIGLE	ECOLE DOCTORALE	NOM ET COORDONNEES DU RESPONSABLE
ED 206 CHIMIE	<b>CHIMIE DE LYON</b> <a href="https://www.edchimie-lyon.fr">https://www.edchimie-lyon.fr</a> Sec. : Renée EL MELHEM Bât. Blaise PASCAL, 3e étage <a href="mailto:secretariat@edchimie-lyon.fr">secretariat@edchimie-lyon.fr</a>	<b>M. Stéphane DANIELE</b> C2P2-CPE LYON-UMR 5265 Bâtiment F308, BP 2077 43 Boulevard du 11 novembre 1918 69616 Villeurbanne <a href="mailto:directeur@edchimie-lyon.fr">directeur@edchimie-lyon.fr</a>
ED 341 E2M2	<b>ÉVOLUTION, ÉCOSYSTÈME, MICROBIOLOGIE, MODÉLISATION</b> <a href="http://e2m2.universite-lyon.fr">http://e2m2.universite-lyon.fr</a> Sec. : Bénédicte LANZA Bât. Atrium, UCB Lyon 1 Tél : 04.72.44.83.62 <a href="mailto:secretariat.e2m2@univ-lyon1.fr">secretariat.e2m2@univ-lyon1.fr</a>	<b>Mme Sandrine CHARLES</b> Université Claude Bernard Lyon 1 UFR Biosciences Bâtiment Mendel 43, boulevard du 11 Novembre 1918 69622 Villeurbanne CEDEX <a href="mailto:e2m2.codir@listes.univ-lyon1.fr">e2m2.codir@listes.univ-lyon1.fr</a>
ED 205 EDISS	<b>INTERDISCIPLINAIRE SCIENCES-SANTÉ</b> <a href="http://ediss.universite-lyon.fr">http://ediss.universite-lyon.fr</a> Sec. : Bénédicte LANZA Bât. Atrium, UCB Lyon 1 Tél : 04.72.44.83.62 <a href="mailto:secretariat.ediss@univ-lyon1.fr">secretariat.ediss@univ-lyon1.fr</a>	<b>Mme Sylvie RICARD-BLUM</b> Laboratoire ICBMS - UMR 5246 CNRS - Université Lyon 1 Bâtiment Raulin - 2ème étage Nord 43 Boulevard du 11 novembre 1918 69622 Villeurbanne Cedex Tél : +33(0)4 72 44 82 32 <a href="mailto:sylvie.ricard-blum@univ-lyon1.fr">sylvie.ricard-blum@univ-lyon1.fr</a>
ED 34 EDML	<b>MATÉRIAUX DE LYON</b> <a href="http://ed34.universite-lyon.fr">http://ed34.universite-lyon.fr</a> Sec. : Yann DE ORDENANA Tél : 04.72.18.62.44 <a href="mailto:yann.de-ordenana@ec-lyon.fr">yann.de-ordenana@ec-lyon.fr</a>	<b>M. Stéphane BENAYOUN</b> Ecole Centrale de Lyon Laboratoire LTDS 36 avenue Guy de Collongue 69134 Ecully CEDEX Tél : 04.72.18.64.37 <a href="mailto:stephane.benayoun@ec-lyon.fr">stephane.benayoun@ec-lyon.fr</a>
ED 160 EEA	<b>ÉLECTRONIQUE, ÉLECTROTECHNIQUE, AUTOMATIQUE</b> <a href="https://edeea.universite-lyon.fr">https://edeea.universite-lyon.fr</a> Sec. : Philomène TRE COURT Bâtiment Direction INSA Lyon Tél : 04.72.43.71.70 <a href="mailto:secretariat.edeea@insa-lyon.fr">secretariat.edeea@insa-lyon.fr</a>	<b>M. Philippe DELACHARTRE</b> INSA LYON Laboratoire CREATIS Bâtiment Blaise Pascal, 7 avenue Jean Capelle 69621 Villeurbanne CEDEX Tél : 04.72.43.88.63 <a href="mailto:philippe.delachartre@insa-lyon.fr">philippe.delachartre@insa-lyon.fr</a>
ED 512 INFOMATHS	<b>INFORMATIQUE ET MATHÉMATIQUES</b> <a href="http://edinfomaths.universite-lyon.fr">http://edinfomaths.universite-lyon.fr</a> Sec. : Renée EL MELHEM Bât. Blaise PASCAL, 3e étage Tél : 04.72.43.80.46 <a href="mailto:infomaths@univ-lyon1.fr">infomaths@univ-lyon1.fr</a>	<b>M. Hamamache KHEDDOUCI</b> Université Claude Bernard Lyon 1 Bât. Nautilus 43, Boulevard du 11 novembre 1918 69 622 Villeurbanne Cedex France Tél : 04.72.44.83.69 <a href="mailto:direction.infomaths@listes.univ-lyon1.fr">direction.infomaths@listes.univ-lyon1.fr</a>
ED 162 MEGA	<b>MÉCANIQUE, ÉNERGÉTIQUE, GÉNIE CIVIL, ACOUSTIQUE</b> <a href="http://edmega.universite-lyon.fr">http://edmega.universite-lyon.fr</a> Sec. : Philomène TRE COURT Tél : 04.72.43.71.70 Bâtiment Direction INSA Lyon <a href="mailto:mega@insa-lyon.fr">mega@insa-lyon.fr</a>	<b>M. Etienne PARIZET</b> INSA Lyon Laboratoire LVA Bâtiment St. Exupéry 25 bis av. Jean Capelle 69621 Villeurbanne CEDEX <a href="mailto:etienne.parizet@insa-lyon.fr">etienne.parizet@insa-lyon.fr</a>
ED 483 ScSo	<b>ScSo<sup>1</sup></b> <a href="https://edsciencesociales.universite-lyon.fr">https://edsciencesociales.universite-lyon.fr</a> Sec. : Mélina FAVETON Tél : 04.78.69.77.79 <a href="mailto:melina.faveton@univ-lyon2.fr">melina.faveton@univ-lyon2.fr</a>	<b>M. Bruno MILLY</b> (INSA : J.Y. TOUSSAINT) Univ. Lyon 2 Campus Berges du Rhône 18, quai Claude Bernard 69365 LYON CEDEX 07 Bureau BEL 319 <a href="mailto:bruno.milly@univ-lyon2.fr">bruno.milly@univ-lyon2.fr</a>











# Remerciements

Je tiens à remercier avant tout ma famille et mes amis. Mon mari Thomas, pour m'avoir encouragé et supporté dans les moments plus difficiles. Merci à mes enfants pour m'avoir aidé à prendre du recul, mais aussi pour m'avoir donné une raison de plus de m'accrocher et j'espère avec cette expérience de leur avoir transmis la valeur du travail et le goût de l'effort. Merci à ma belle-famille : mamie Lili toujours prête à monter avec son vélo dans le premier TER depuis Besançon pour venir à notre secours, Jean-Louis et Pascale qui entre la Corse et Lyon nous ont également bien aidé avec les enfants. Merci à mes parents, pour leur confiance et à mes frères. Merci à mes amis, Julie, Barbara, Marie Laure, Béatrice, Véro, Sego, Jeanne, Carola, Claire, Anna. . .

Merci à Valérie Sartre qui a été d'un grand soutien moral, avec qui j'ai partagé des très bon moments et appris l'endurance par nos sorties de course à pied.

Je tiens évidemment à remercier mon encadrement : Frédéric Kuznic pour m'avoir ouvert la porte et donné la possibilité d'accéder à l'environnement de la recherche alors que je venais d'un autre milieu professionnel et qui a ensuite encadré mes travaux de thèse. Merci à Lucie Merlier qui a été d'un grand apport sur la méthode scientifique. Un grand merci à Mathias Bouquerel, qui m'a apporté énormément du point de vue de la modélisation numérique, mais aussi qui a été d'un grand soutien pratique et moral. Merci également à Gilles Rosaouën et Jean Jaques Roux qui ont été de bon conseils en tout début de mes travaux de thèse. Aussi merci aux membres de mon comité de suivi de thèse Lionel Soulhac et Frédéric André qui a été également de très bon conseils et d'un grand soutien moral.

Un grand merci à Abdelkrim Trabelsi pour ses excellents cours en modélisation thermo-hygro -aéraulique, ainsi qu'à Etienne Vergnault et Kevin Joahannes, qui ont également contribué à bien m'armer via le master BHEE pour affronter la thermique des bâtiments. Merci au groupe ville : Célia, Julie, Aurore, Teddy, Adrien et Felix et Damien qui n'a pas manqué de me challenger. Et enfin merci aux doctorants et post doctorants du labo qui m'ont tenu compagnie avec leur groupe whatsapp et aux reste du labo qui a rendu mon quotidien plus agréable.



# Abstract

Consistent high temperatures during hot spells can significantly escalate the risk to health by increasing heat exposure.

The purpose of this thesis is therefore to develop a methodology to assess heat stress over daily and seasonal periods in dwellings and their nearby. Two exposure approaches are suggested: an Eulerian approach in regards of a fixed place, and a Lagrangian approach in regards of an individual's displacement. A numerical assessment method is chosen.

This thesis aims to establish a methodology that assesses heat stress over both daily and seasonal periods in residential areas. Two approaches to exposure are proposed; the Eulerian approach focuses on a fixed location, while the Lagrangian approach examines the movement of individuals. The thesis chooses a numerical assessment method and introduces the concepts of heat stress and heat strain. It defines daily and seasonal indices, pinpoints the climatic variables influencing them, and determines their spatial and temporal scales. An analysis of the factors contributing to urban heat exposure underscores the necessity for numerical modelling in heat stress assessment. This analysis, however, reveals a gap in the existing modelling approach.

Hence, this study involves the development and coupling of a microclimate zonal model (McZM) with a building energy model (BEM). The McZM is based on interpolating mass flow rates obtained from pre-computed Computational Fluid Dynamics (CFD) simulations using steady RANS realisable  $k - \epsilon$ . CFD simulations also predict spatial wind speeds, external heat transfer coefficients, and pressure coefficients.

The McZM integrates a soil model and outdoor radiation models that account for solar and long-wave radiations as well as the mean radiant temperature. The study introduces an indoor airflow pressure model coupled with both the McZM and BEM. The accuracy of model components is verified using experimental data or model comparison.

The Ydeal Square block in Confluence served as the application site for the developed model to validate the benefits of using a spatial approach in assessing heat stress. It also allowed for the evaluation of the effectiveness of various cooling measures on heat stress.

In conclusion, the thesis proposes broader views on the advancement of microclimate and building modelling based on residents' summer cooling practices according to a social

survey. Future work highlights improving the existing McZM and its validation process.

**Keywords:**

Urban overheating, heat stress, microclimate model, buiding energy model, zonal model.

# Résumé

La persistance des épisodes de surchauffe urbaine affecte directement l'exposition à la chaleur, augmentant ainsi les risques pour la santé tout particulièrement en milieu urbain.

Le but de cette thèse est donc de développer une méthodologie pour évaluer le stress thermique sur une base quotidienne et saisonnière dans le logement et son environnement proche. Deux approches d'exposition sont suggérées : une approche eulérienne par rapport à un lieu fixe, et une approche lagrangienne par rapport au déplacement de l'individu. Une méthode d'évaluation numérique est choisie.

Ainsi, la thèse introduit les concepts de stress thermique et de contrainte thermique, définit les indices journaliers et saisonniers et identifie les variables climatiques influentes ainsi que leurs échelles spatiales et temporelles. Un aperçu des facteurs influençant l'exposition à la chaleur urbaine met en évidence les besoins en modélisation numérique pour l'évaluation du stress thermique, tandis que l'analyse des modèles existants de microclimat et de simulation thermique dynamique (STD) du bâtiment met en évidence l'absence d'une approche de modélisation appropriée.

Par conséquent, le travail de thèse consiste à développer et à coupler un modèle zonal de microclimat (McZM) avec un modèle de STD du bâtiment. Le McZM repose sur une interpolation linéaire des débits massiques obtenus avec un précalcul CFD (Computational Fluid Dynamics) k-epsilon realizable RANS stationnaire. Les simulations CFD sont également utilisées pour prédire les vitesses du vent spatialisées, les coefficients de transfert convectifs extérieurs et les coefficients de pression.

Le McZM inclut un modèle de sol et des modèles radiatifs pour les calculs du rayonnement solaires et de grandes longueurs d'ondes, ainsi que pour le calcul de la température radiante moyenne. Pour les écoulements dans le bâtiment, un modèle de pression couplé au McZM et au modèle de STD du bâtiment est développé. Les composants des modèles sont soumis à une validation à l'aide de données expérimentales ou de comparaisons de modèles.

Une application du modèle couplé au cas d'étude de l'îlot Ydeal Square à Confluence, confirme les avantages de l'utilisation d'une approche spatialisée dans l'évaluation du stress thermique. Ce cas permet également d'évaluer les avantages relatifs de la mise en œuvre de différentes mesures de rafraîchissement sur le stress thermique.

Enfin, cette thèse suggère des perspectives élargies sur l'évolution de la modélisation du microclimat et des bâtiments, basées en partie sur une enquête sociale sur les pratiques de rafraîchissement des résidents pendant l'été. D'autres perspectives se concentrent sur l'amélioration du McZM actuel et de son processus de validation.

**mots clés:**

Surchauffe urbaine, stress thermique, Modélisation de microclimat, Modélisation énergétique du bâtiment, Modèle zonal.







# Long Résumé

## Introduction

Le réchauffement climatique dû à l'activité humaine entraîne des événements extrêmes de vagues de chaleur de plus en plus fréquents et intenses (Perkins-Kirkpatrick and Lewis, 2020). En ville, la densité élevée des bâtiments, l'imperméabilisation des sols et l'activité humaine créent des conditions favorables au développement de l'effet d'îlot de chaleur urbain (ICU), caractérisé par des températures plus élevées par rapport aux zones rurales et une limitation significative de la baisse des températures la nuit. Ce dernier contribue à un autre phénomène plus vaste de surchauffe urbaine (Su et al., 2021) pouvant se produire de jour et de nuit, de manière répétée tout au long de la saison et à toutes les échelles, allant de la ville à l'individu. Pendant ces périodes de surchauffe, les températures particulièrement élevées ont un impact direct sur l'exposition des personnes à la chaleur et, par conséquent, sur le stress thermique subi par les individus. La santé humaine en est affectée, non seulement par l'intensité de la chaleur, mais aussi par la fréquence de l'exposition à la chaleur extrême (Matthies, 2008). La question de l'adaptation et de l'atténuation de la surchauffe urbaine devient donc une priorité de santé publique.

C'est dans ce cadre que les politiques locales s'engagent de manière croissante dans l'intégration de la question climatique dans les outils de planification territoriale. Cela se reflète dans diverses politiques publiques locales (urbanisme, logement, transport, santé, développement économique et social, etc.), donnant lieu à des actions ciblées adaptées aux contextes urbain, social, économique et environnemental. Plus spécifiquement, dans le contexte urbain, bien que des leviers d'adaptation et de lutte contre la surchauffe aient été identifiés (végétalisation des villes, efficacité énergétique et rénovation thermique des bâtiments existants, approche bioclimatique de la construction, perméabilisation des sols, adoption d'actions de refroidissement passif, gestion de l'eau, etc.), des questions subsistent quant à la manière de les déployer, voire d'innover.

Pour guider ces choix, les outils d'aide à la décision, basés sur des approches de modélisation spatialisée du climat sont de plus en plus adoptés par la communauté des urbanistes en lien avec la communauté scientifique (Zhou, An, and Yao, 2022; ADEME, 2017). Ces approches de modélisation et les outils qui en résultent varient en fonction de l'échelle géographique étudiée : la ville, les quartiers, les espaces publics, les îlots et les bâtiments. Parmi

ces outils, nous nous intéressons plus particulièrement dans cette thèse à ceux qui permettent de modéliser numériquement les phénomènes physiques influant les ambiances thermiques. Par rapport à une approche expérimentale de terrain, l'adoption d'une approche numérique présente en effet l'avantage de pouvoir tester et comparer diverses hypothèses de conception du bâtiment ou d'aménagement urbain. Cependant, le défi réside dans la disponibilité de modèles robustes capables de simuler des configurations urbaines réalistes (Musy, 2012). La modélisation numérique nécessite notamment de comprendre les interactions entre le climat, l'environnement urbain, et en particulier les bâtiments. Le choix des phénomènes physiques à représenter et leur niveau de détail dépend de l'objectif de la modélisation et de l'échelle de l'étude.

Lorsqu'il s'agit d'examiner l'influence de l'aménagement urbain et du bâtiment sur le stress thermique subi par les individus, il est pertinent de considérer les échelles représentatives des environnements d'exposition individuels, allant de la ville au bâtiment. En ce qui concerne l'action individuelle, c'est à l'échelle du logement et de son environnement proche que les habitants, en collaboration avec les parties prenantes locales (maîtres d'ouvrage, autorités publiques, syndicats), ont le plus de marge de manoeuvre sur l'évolution de leur environnement d'exposition. Par ailleurs, compte tenu du fait qu'en France les personnes passent environ 80% de leur temps à l'intérieur des bâtiments (Ministère de la transition Ecologique, 2013), il est important de pouvoir modéliser les ambiances thermiques à l'intérieur des bâtiments, lors de l'évaluation du stress thermique. Cependant, tout particulièrement dans les villes, ces dernières sont influencées par l'environnement extérieur proche (Peuportier, 2016, Oke et al., 2017). La modélisation des espaces urbains extérieurs est donc également importante, d'autant plus qu'ils constituent un cadre de vie pour les individus. Enfin, dans une perspective d'évaluation des effets de la surchauffe sur la santé, il est crucial de considérer les effets de l'exposition à la chaleur non seulement sur la période de vague de chaleur, mais tout au long de la saison estivale. Dans ce cadre, cette thèse vise spécifiquement à répondre à la question suivante :

*Comment évaluer le stress thermique journalier et saisonnier subi dans le logement et son environnement proche en intégrant leurs interactions mutuelles ?*

## **Objectif de la thèse**

Dans ce cadre, l'objectif de la thèse est de développer une méthodologie de modélisation numérique pour évaluer le stress thermique sur une période journalière et saisonnière dans le logement et son environnement proche, en prenant en compte les interactions entre intérieur et extérieur, à l'échelle d'un îlot.

La période saisonnière permet de quantifier le stress thermique cumulé. La période journalière permet d'étudier plus spécifiquement des épisodes particuliers de stress thermique intense. La nécessité de prendre en compte l'hétérogénéité de l'environnement thermique d'exposition justifie l'adoption d'une approche de modélisation spatialisée. L'évaluation du

stress thermique est analysée selon deux approches d'exposition :

- Une approche Eulérienne, où le stress thermique est évalué par rapport à un endroit fixe.
- Une approche Lagrangienne, où le stress thermique est évalué en fonction des déplacements d'un individu d'un environnement d'exposition à un autre.

Pour répondre à cet objectif, le travail effectué dans la thèse est divisée en trois parties. Une première partie de travail préliminaire permet de définir le cadre d'évaluation du stress thermique, d'identifier les indices pertinents, les variables climatiques impactantes et les besoins de modélisation. Elle permet in fine d'aboutir à une problématique spécifique de modélisation numérique et à la définition d'une stratégie de modélisation.

Une deuxième partie détaille la mise en oeuvre de la stratégie de modélisation, comprenant une description des composants du modèle et proposant une approche de validation pour chacun de ses composants.

Une troisième partie consiste à illustrer les résultats obtenus grâce à la mise en oeuvre de l'approche de modélisation développée sur un cas d'étude.

## 1. Cadre d'évaluation du stress thermique

### 1.1 Définition du stress thermique et des facteurs l'influençant

L'évaluation du stress thermique à une échelle journalière et saisonnière dans l'optique d'une évaluation de l'impact de la chaleur sur la santé nécessite tout d'abord de définir ce que l'on entend par « stress thermique » (heat stress en anglais). Selon la définition de Yang Chan (2015), ce dernier fait référence à la charge thermique totale subie par le corps humain, résultante de facteurs environnementaux, physiques et individuels. Dans la mesure où elle fait intervenir des facteurs physiques et individuels, la notion de stress thermique est fortement corrélée à la notion de contrainte que ce stress thermique engendre sur le corps (« heat strain » en anglais). Cette dernière fait référence à la réponse physiologique et/ou psychologique de l'individu, générée par le stress thermique (Yang and Chan, 2015).

Pour comprendre la relation entre le stress thermique et la contrainte engendrée sur le corps, ainsi que les principaux paramètres affectant leur évaluation, il est nécessaire de comprendre l'interaction thermique entre le corps et son environnement d'exposition, ainsi que la manière dont la chaleur est échangée entre eux. Le processus de thermorégulation humaine, dont le but est de maintenir une température corporelle autour de 37°C est au coeur de cette interaction (Périard, Racinais, and Sawka, 2015). Ce processus fait intervenir deux systèmes. Le système passif intervenant dans les bilans thermiques qui ont lieu entre l'intérieur du corps, la surface de la peau et l'environnement. Le système actif, qui active

les mécanismes de thermorégulation, c'est-à-dire la vasodilatation, la vasoconstriction, la transpiration et la production de chaleur par frissonnement (Zhao et al., 2020).

Lorsqu'il s'agit de modéliser le stress thermique et la contrainte engendrée sur le corps, les facteurs couramment pris en compte sont les facteurs climatiques, les facteurs comportementaux et les facteurs physiologiques.

**Les facteurs climatiques** déterminent l'environnement thermique. Ils peuvent être exprimés par les variables climatiques suivants :

- La température de l'air  $T_a$  [°C] : intervenant dans les échanges de chaleur par convection avec la peau ou la vêtue.
- L'humidité dans l'air, exprimée par humidité relative (HR) [%] : influant sur la capacité du corps à libérer de la chaleur latente par transpiration ou respiration.
- La vitesse de l'air  $v_a$  [ $\text{m s}^{-1}$ ] : intervenant dans les échanges de chaleur par convection avec la surface du corps ou de la vêtue et dans la capacité du corps à transpirer.
- Le flux de chaleur radiatif, pouvant être exprimé par la température radiante moyenne  $T_{mrt}$  [°C], et intervenant dans le bilan énergétique à la surface du corps. La  $T_{mrt}$  est définie comme la *température de surface uniforme d'une enceinte noire imaginaire dans laquelle un occupant échangerait la même quantité de chaleur par rayonnement que dans l'enceinte non uniforme réelle* (Ramspeck et al., 2003a).

**Les facteurs comportementaux** comprennent le métabolisme  $M$  [met] ( $1\text{met} = 52.8 \text{ W m}^{-2}$ ), l'énergie du corps nécessaire à l'activité  $W$  [ $\text{W m}^{-2}$ ], la vêtue, la posture, des actions orientées vers le corps (hydratation, alimentation . . .), des actions orientées envers l'environnement d'exposition (fermeture de volets, ventilation . . .) ou encore des actions visant à se déplacer pour chercher un environnement d'exposition thermiquement plus favorable.

**Les facteurs physiologiques** interviennent dans la réponse du corps au stress thermique et peuvent se classer selon le type de contrainte qu'ils reflètent. Les paramètres reflétant une contrainte thermique sont par exemple la température centrale  $T_{core}$  [°C] ou la température de la peau  $T_{sk}$  [°C]. Les paramètres reflétant la contrainte hydrique sont par exemple le taux de sudation  $sw_R$  [ $\text{g s}^{-1}$ ] ou la mouillure de peau  $SkinWet$  [%]. Enfin un paramètre reflétant la contrainte cardiovasculaire est par exemple le débit cardiaque  $CO$  [ $\text{L h}^{-1}$ ]. Il est à noter que les facteurs physiologiques sont utilisés indirectement dans la détermination du stress thermique lorsque ce dernier est déterminé à partir de modèles de thermorégulation reposant sur l'interaction entre le système actif et le système passif.

## 1.2 Choix de l'indice de stress thermique et des indices dérivés

Parmi les indices permettant de caractériser le stress thermique, une distinction peut être faite entre les indices rationnels, les indices basés sur des modèles de régression empiriques et les indices basés sur le bilan thermique du corps humain. Ce sont ces derniers qui sont le plus appropriés pour notre analyse dans la mesure où ils considèrent à la fois les facteurs climatiques et certains facteurs comportementaux et physiologiques. Au sein de ce groupe d'indices, un choix est fait parmi : l'Index de stress thermique (ITS) (B., 1963), le PMV, le Pourcentage Prévu d'Insatisfaction (PPD) (Fanger, 1970) et la Température Perçue (PT)(VDI, 1998), la Température Effective Standard (SET) dérivée du modèle Gagge thermo-physiologique à deux noeuds en régime permanent (P., 1937), la température physiologique équivalente (PET) dérivée du modèle MEMI à deux noeuds en régime permanent (Höppe, 1993; Höppe, 1999b) et l'Indice Thermique Universel (UTCI) résultant du modèle de thermorégulation transitoire à plusieurs segments de Fiala (1998), ainsi qu'un modèle adaptatif de vêture.

L'indice retenu est la PET. Ce dernier est le plus approprié à notre besoin dans la mesure où il considère les quatre variables climatiques en jeu dans le stress thermique, il s'applique aussi bien à l'intérieur qu'à l'extérieur sur des plages correspondantes à celles observées en été en France. La PET fournit la température d'un environnement de référence qui provoquerait la même réponse physiologique en termes de  $T_{core}$  et  $T_{sk}$  que l'environnement étudié. L'environnement de référence correspond à un environnement intérieur avec  $v_a = 0.1 \text{ m s}^{-1}$ , HR = 50 % et  $T_a = T_{mrt}$ . Cependant, le modèle de thermorégulation à deux noeuds MEMI (Höppe, 1993; Höppe, 1999b) sur lequel est basé la PET est valide dans un environnement thermique stationnaire. Il est donc important d'étudier les conséquences d'une exposition à un environnement thermique évolutif. Cela est réalisé en comparant la  $T_{core}$  et la  $T_{sk}$  obtenues en régime permanent aux  $T_{core}$  et la  $T_{sk}$  obtenues en régime transitoire. Les  $T_{core}$  et  $T_{sk}$  en régime transitoire et permanent sont obtenues à partir du modèle de thermorégulation du corps humain JOS-3 (Takahashi et al., 2021), présentant un découpage du corps en 17 segments et présentant l'avantage de s'appliquer en régime transitoire. Les valeurs de  $T_{core}$  et  $T_{sk}$  ainsi obtenues sont utilisées dans le modèle de PET afin de calculer la température de l'environnement de référence de la PET.

Deux analyses sont réalisées. La première porte sur un environnement d'exposition fixe, correspondant à une approche d'exposition Eulérienne. Dans cet environnement d'exposition, les variables climatiques évoluent à un pas de temps horaire à des amplitudes correspondantes à celles observées à la station météo de Confluence à Lyon l'été 2020 (Table 1). Les amplitudes maximales sont de 2°C pour la  $T_a$ , de 16°C pour la  $T_{mrt}$ , de 6% pour la HR et sont fixées à zéro pour la vitesse du vent (à la fin de simplification de l'analyse). Il résulte de cette première analyse que les différences de  $T_{core}$  et  $T_{sk}$  entre le régime transitoire et le régime stationnaire sont très faibles (un écart maximal de 0.16 °C pour la  $T_{core}$ , comme illustré en Figure 1) et ont des répercussions négligeables sur la PET (inférieure à 0.1 °C).

Table 1: Scenario d'évolution des variables climatiques associées à un lieu fixe correspondantes au 8 août de 11AM à 3PM.

	11 AM	12 AM	1 PM	2 PM	3PM
$T_a$ [°C]	30	31	32	30	29
$T_{mrt}$ [°C]	51	56	60	56	57
$v_a$ [m/s]	0.1	0.1	0.1	0.1	0.1
$RH$ [%]	40	34	33	32	35

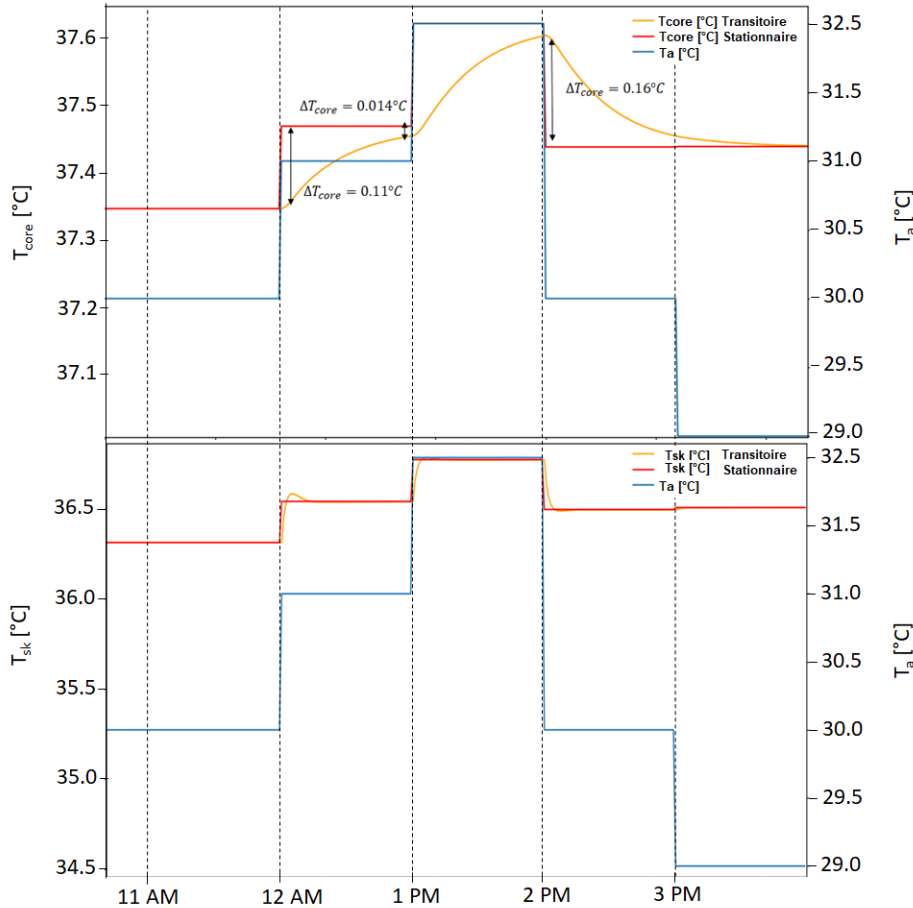


Figure 1: Evolution des  $T_{core}$  et  $T_{sk}$  en régime stationnaire et transitoire pour une évolution des variables climatiques correspondantes au 8 août de 11AM à 3PM.

Il est donc possible d'utiliser cet indice également dans un environnement thermique dont les évolutions horaires ont des amplitudes comparables à celles observées à la station météo. Il est à noter cependant que ces résultats sont conditionnés par le fait que les données climatiques varient à un pas de temps horaire. Les variations infra-horaires de rayonnement solaire incident une surface, pouvant avoir lieu dans un lieu fixe en raison de la présence de masques solaires, ne se reflètent pas lorsque les données sont au pas de temps horaire et en conséquences l'impact de ces variations infra-horaires sur l'évolution des la  $T_{core}$  et la  $T_{sk}$  n'est pas évalué.

La deuxième analyse porte sur un environnement d'exposition dynamique, représentatif

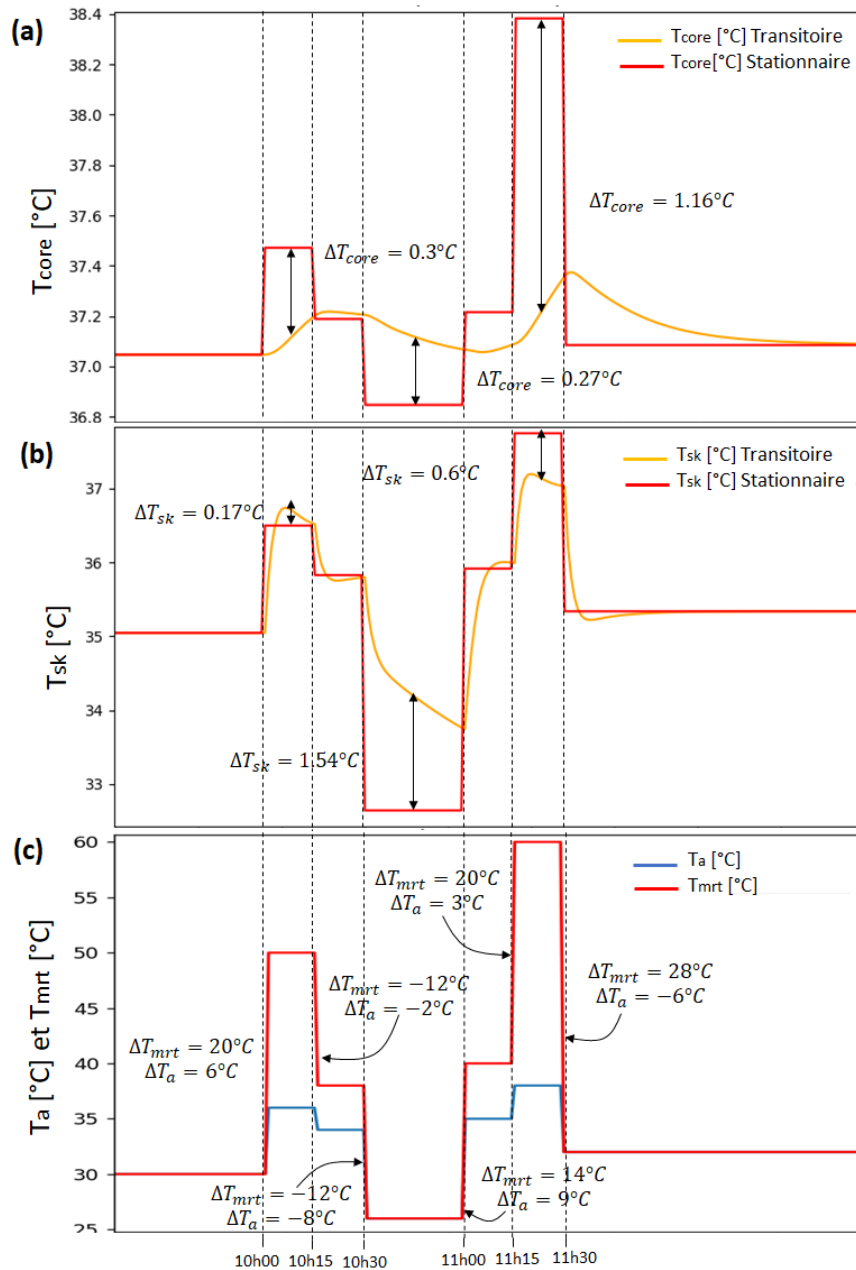


Figure 2: Evolution des (a)  $T_{core}$  et (b)  $T_{sk}$  correspondantes aux évolutions de (c)  $T_a$  et  $T_{mrt}$  pour HR=50% et  $v_a = 0.1 \text{ m s}^{-1}$ .

d'un individu en mouvement et correspondant donc à une approche d'exposition Lagrangienne. Le parcours étudié comporte des durées d'exposition de l'ordre du quart d'heure, avec des amplitudes maximales de  $T_a$  de  $9^{\circ}C$  et de  $T_{mrt}$  de  $28^{\circ}C$  correspondantes respectivement au passage d'un environnement climatisé à un environnement chaud (de 11h à 11h15 en Figure 2) et au passage du soleil à l'ombre (de 11h30 à 12h00 en Figure 2). Cette fois-ci les répercussions sur la PET conduisent à des écarts dépassant les  $2^{\circ}C$ . Cela s'explique à la fois par les amplitudes plus larges de  $T_a$  et de  $T_{mrt}$ , mais également par les plus courtes durées d'exposition qui font que la  $T_{core}$  en régime transitoire s'écarte plus de la  $T_{core}$  en régime stationnaire (Figure 2). Dans ces conditions, l'utilisation d'un indice basé sur un modèle de

thermorégulation stationnaire comporte des limites.

Enfin, une analyse de sensibilité de la PET aux variables climatiques sur différentes plages de valeurs de ces dernières, a montré une forte sensibilité de la PET à la  $T_a$  et en plus faible mesure à la  $T_{mrt}$ , cette dernière comporte cependant des variations plus importantes. Ceci justifie l'importance d'une bonne caractérisation de ces variables climatiques. La  $v_a$ , bien que moins impactante sur la PET (surtout pour des  $v_a > 1 \text{ m s}^{-1}$ ), joue un rôle déterminant dans les échanges de chaleur par advection et en conséquence sur la  $T_a$ . Il est dans ce cadre important de la prendre en compte. Enfin l'humidité relative joue un rôle important dans le calcul de la capacité du corps à évacuer de la chaleur latente et apparaît comme le troisième paramètre auquel la PET est le plus sensible après la  $T_a$  et la  $T_{mrt}$ .

Au-delà de la PET, des indices dérivés de surchauffe, définie ici lorsque la PET  $> 29^\circ\text{C}$ , ont été élaborés pour l'analyse saisonnière. Ces indices permettent de caractériser (1) la durée maximale de l'épisode de surchauffe  $OhD_{max}$  [h] parmi tous les épisodes enregistrés dans la saison, (2)  $OhI_{max}$  [ $^\circ\text{C}\cdot\text{h}$ ], correspondant à la valeur maximale des degrés heures de surchauffe sur tous les épisodes de surchauffe, (3) la surchauffe maximale  $Oh_{max}$  [ $^\circ\text{C}$ ], correspondante aux degrés maximaux de dépassement de la limite de surchauffe, (4) la surchauffe moyenne  $Oh_{mean}$  [ $^\circ\text{C}$ ], correspondante aux degrés moyens de dépassement de la limite de surchauffe. Un indice global de distribution de stress thermique par plages de PET a également été introduit.

### 1.3 indices pour l'évaluation de la contrainte engendrée sur le corps

Lorsqu'il s'agit d'évaluer la contrainte que le stress thermique engendre sur le corps, il est plus pertinent d'utiliser comme indices directement les variables physiologiques. Celles retenues dans notre étude sont la  $T_{core}$ , la  $T_{sk}$  le  $sw_R$  la  $SkinWet$  et le  $CO$ . Ces dernières sont modélisées à partir du modèle de thermorégulation JOS-3 (Takahashi et al., 2021). Cependant JOS-3, tout comme le reste des modèles de thermorégulation actuels, n'est valable que pour de courtes durées d'expositions à la chaleur et est donc utilisé uniquement dans l'analyse journalière selon l'approche d'exposition Lagrangienne, afin d'évaluer la contrainte thermique d'un individu se déplaçant dans différents environnements d'exposition.

Une étude de la réponse de JOS-3 aux variations du pas de temps des variables climatiques d'entrée a démontré que le pas de temps horaire par rapport à un pas de temps de 10 minutes a peu d'impact sur la variation de la  $T_{core}$  et de la  $T_{sk}$ . Dans ces conditions, le fait de calculer les variables climatiques d'intérêt au pas de temps horaire est acceptable.



## 2. Modélisation du microclimat et du bâtiment pour l'évaluation du stress thermique

La modélisation du stress thermique dans le logement et son environnement proche à une échelle journalière et saisonnière doit pouvoir reproduire l'effet des différentes interactions physiques entre le bâtiment, le contexte urbain proche et l'atmosphère. La chaleur engendrée par l'activité humaine, les propriétés radiatives, aérodynamiques et thermiques des surfaces, leur distribution dans le périmètre d'étude considéré et la forme urbaine sont autant de facteurs venant impacter le bilan énergétique de l'atmosphère. Des besoins de modélisation sont identifiés afin de prendre au mieux en compte ces facteurs à l'échelle d'étude ciblée.

### 2.1 Besoins en modélisation

Les variables climatiques à modéliser sont la  $T_a$ , la  $T_{mrt}$ , l' $HR$  et la  $v_a$ . Pour prédire ces variables, les phénomènes physiques à modéliser sont les flux de chaleur advectifs, radiatifs, convectifs, conductifs et latents. Les caractéristiques urbaines à modéliser, en interaction avec l'atmosphère, sont en priorité les bâtiments, le sol (imperméable et perméable), la végétation (haute, basse). Les variables de couplage impliquées dans les échanges de chaleur entre air-surface, air-air et air extérieur et air intérieur sont respectivement le coefficient d'échange convectif ( $h_c$  [ $\text{W m}^{-2} \text{K}^{-1}$ ]), le débit massique ( $mfr$  [ $\text{kg s}^{-1}$ ]) et le coefficient de pression ( $cp$ ). Une estimation fiable de ces variables de couplage est cruciale pour une prise en compte concrète de ces interactions. Pour prendre en compte l'interaction entre les occupants et le bâtiment, le modèle de bâtiment doit être capable de simuler des stratégies de refroidissement courantes (ventilation naturelle et occultation des baies), des systèmes de ventilation et des sources de chaleur internes. En ce qui concerne la discrétisation spatiale, l'échelle est celle d'une résidence (environ 300m x 300m), comprenant les bâtiments avec une résolution horizontale représentative des lieux de vie dans le bâtiment (les pièces) et dans l'espace urbain et une résolution verticale représentant le niveau du piéton et les étages du bâtiment.

### 2.2 Problématique de modélisation et enjeux de modélisation

Une recherche bibliographique a permis de faire une sélection de modèles de microclimat urbain (SOLENE Microclimat (Vinet, 2000; Bouyer et al., 2009), ENVI-met (Bruse and Fleer, 1998), EnviBatE (Bozonnet, 2005; Gros, 2014)), de modèles de canopée urbaine (TEB (Masson et al., 2000; Masson, 2000)), de modèles de modélisation thermique dynamique de bâtiments (EnergyPlus (Crawley et al., 2000), CitySim Pro (Robinson et al., 2009), MyBEM (Bouquerel et al., 2019) et de modèles de rayonnement (RayMan (Matzarakis and Mayer, 1996) et LadyBug (Sadeghipour Roudsari, Pak, and Viola, 2013)). L'analyse de ces modèles met en évidence un manque par rapport aux besoins de modélisation préalablement définis.

Ce manque réside dans l'impossibilité d'un seul modèle à modéliser aussi bien l'extérieur que l'intérieur en incluant la modélisation de stratégies de rafraîchissement tels que la ventilation naturelle et permettant d'obtenir systématiquement les quatre variables climatiques nécessaires au calcul du stress thermique (notamment la  $T_{mrt}$  et la  $v_a$ ) à l'intérieur et extérieur.

Le constat d'un besoin d'une approche de modélisation adaptée donne naissance à la problématique spécifique de la thèse consistant à développer et à coupler un modèle zonal de microclimat (McZM) avec un modèle de bâtiment (STD) afin de fournir une représentation spatiale du stress thermique sur des périodes saisonnières et journalières.

Trois enjeux de modélisation ont été identifiés. Le premier porte sur le développement d'un modèle zonal extérieur capable de prendre en compte les impacts de la forme urbaine, de la variation de la vitesse et de l'orientation du vent en entrée du domaine dans la modélisation de l'écoulement. Cette dernière doit garantir une cohérence physique de l'écoulement et respecter le principe de conservation de la masse. Le deuxième porte sur la définition d'une structure de zonage pertinente pour l'évaluation du stress thermique. Le troisième porte sur la réalisation d'un couplage intérieur-extérieur.

### 3. Présentation du modèle McZM couplé au BEM et validation

#### 3.1 Architecture et composants

La stratégie de modélisation proposée vise à répondre aux enjeux et besoins de modélisation identifiés en proposant des durées de modélisation abordables sur la période saisonnière. L'architecture globale du modèle est présentée en Figure 3, elle comporte quatre principales étapes.

La première étape constitue la mise en données où sont définies la géométrie 3D cubique, les conditions aux limites du domaine de calcul (fichier météo, sol) les propriétés thermiques du bâtiment du sol ainsi que les propriétés de rugosité des surfaces.

La deuxième étape constitue le pré-calcul radiatif et aéraulique. Le pré-calcul radiatif solaire, ou rayonnement de courtes longueurs d'ondes (CLO) utilise le modèle de lancer de rayon de l'outil HelioBIM (Bouquerel et al., 2019) pour obtenir l'irradiance courte longueur d'onde (1) et les facteurs de forme (2) pour chaque surface du bâtiment, du sol ainsi que du modèle d'individu à l'extérieur du logement. Les facteurs de forme sont ensuite utilisés pour le calcul extérieur des grandes longueurs d'ondes (GLO) avec la méthode des radiosités dans la phase de simulation dynamique. Un modèle simplifié de calcul des GLO, prenant en compte uniquement les échanges avec le ciel et le sol est également développé afin de réduire les temps de calcul. Le pré-calcul aéraulique (3) se fait par simulation stationnaire CFD RANS  $k - \varepsilon$  réalisable ( $rk - \varepsilon$ ) et l'utilisation d'un modèle de fonction de parois standard. Ces simulations visent à obtenir les débits massiques ( $mfr$ ), les  $h_c$  externes et les  $cp$  pour différentes orientations et vitesses de vent définies dans un plan d'expérience

construit en accord avec le fichier météo (3.1) et (3.2). Ces données sont ensuite interpolées dans l'étape de simulation dynamique (3.5) afin d'avoir une valeur à chaque pas de temps du fichier météo. C'est également dans l'étape de précalcul qu'est créé le zonage (3.3) et est réalisé un premier équilibrage des bilans de masse (3.4) selon une méthode basée sur le rééquilibrage des faces en aval de la zone d'air par rapport aux débits des faces en amont. La notion d'amont et aval se réfère au repère orthonormé  $(x,y,z)$  sur lequel est construit le zonage. Le zonage est de forme parallélépipède, calé sur le découpage des zones thermiques du bâtiment. Ce découpage est prolongé à l'extérieur. L'étape de précalcul s'achève par la génération automatique d'un modèle Dymola couplant un modèle de STD de la bibliothèque BuildSysPro (5) avec le modèle zonal de microclimat (McZM) constitué de volumes d'air et de trois modèles de sol (4) : sol imperméable, sol perméable sans végétation, sol avec végétation basse. Un modèle en pression des écoulements dans le bâtiment (6), développé

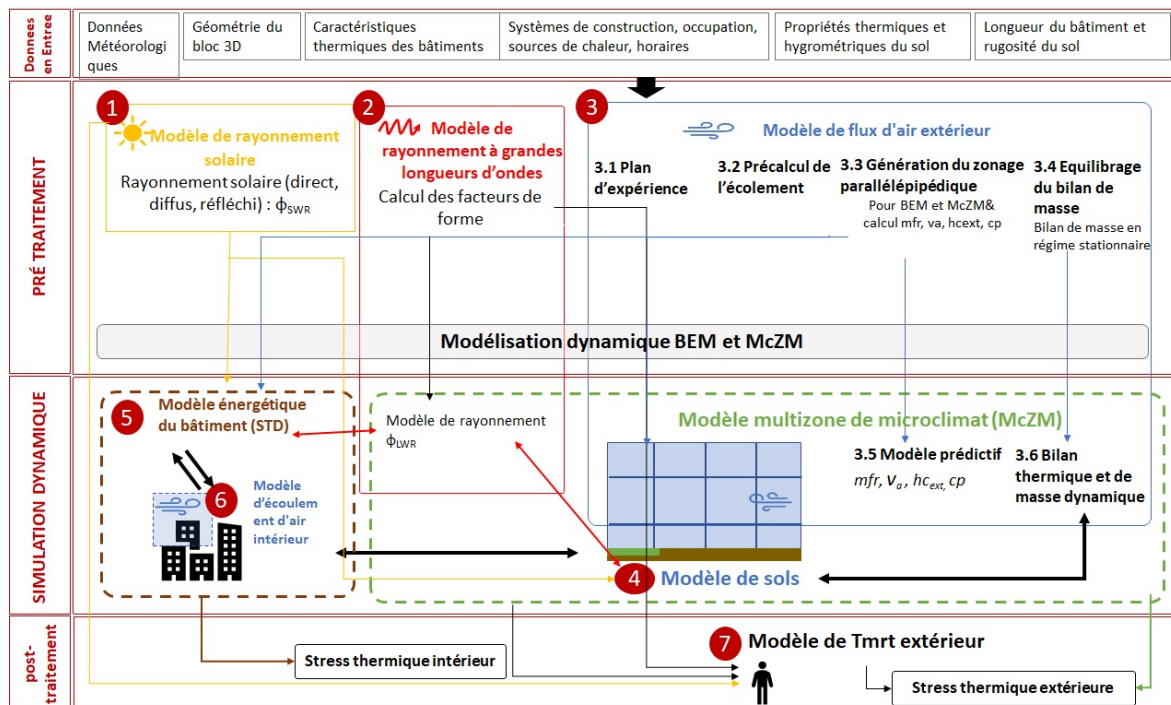


Figure 3: Architecture de la chaîne de modèles de McZM couplés à un BEM permettant de modéliser le stress thermique.

à partir de la bibliothèque IBPSA de Modelica, est également couplé aux autres modèles lorsque l'option de ventilation naturelle est activée.

La troisième étape de simulation thermo-aéraulique dynamique sous Dymola résout simultanément les équations de bilan énergétique à l'extérieur et dans le bâtiment et assure l'équilibrage des bilans de masse dans chaque zone d'air (3.6). La résolution des équations se fait par une méthode de discrétisation temporelle implicite, et pour la conduction, une discrétisation spatiale 1D et la méthode des volumes finis.

La quatrième étape constitue le post-traitement des données de simulation et comporte un modèle de calcul de la  $T_{mrt}$  à l'extérieur (7), utilisé pour le calcul final du stress thermique.

Le calcul de la  $T_{mrt}$  repose sur un modèle d'homme sous forme de pavé droit et prend en compte les rayonnements CLO, GLO et des facteurs de forme. L'ensemble de l'architecture s'appuie sur la chaîne de modélisation MyBEM (Bouquerel, Ruben Deutz, et al. 2021) comportant les sous-modèles 1, 2, et 5 présentés en Figure 3, à laquelle a été intégré un couplage avec le McZM (modèles 3, 4, 6 et 7 en Figure 3).

### 3.2 Validation modulaire

La validation des modèles de microclimat basés sur des mesures réelles est complexe à mettre en oeuvre principalement en raison du manque de données expérimentales adaptés et en raison de la complexité des interactions entre les phénomènes physiques et le grand nombre de paramètres régissant le microclimat urbain. Dans ce cadre, il a été choisi dans cette thèse d'évaluer la validité de la chaîne de modèles de Figure 3 par une approche comparative modulaire (composant par composant) avec des modèles de référence ou des données expérimentales.

La validité du modèle de précalcul aérodynamique extérieur réalisée sur Fluent en utilisant le modèle de turbulence RANS  $rk - \varepsilon$  a été vérifiée en comparant les résultats d'une simulation CFD en stationnaire avec des données expérimentales obtenues par l'expérience en soufflerie d'un écoulement sur un pavé droit isolé (Meng and Hibi, 1998). Les profils de vitesse de vent obtenus par simulation sont cohérents avec ceux mesurés, avec une surestimation par le modèle RANS de la recirculation en aval du cube.

Le calcul des  $h_c$  extérieurs a été vérifié en comparant les résultats d'une simulation CFD RANS utilisant un modèle de turbulence  $rk - \varepsilon$  et un modèle de fonction de parois standard avec les résultats de la simulation CFD RANS réalisée par Defraeye, Blocken et Carmeliet (2010) qui utilise également un modèle de turbulence  $rk - \varepsilon$  et un modèle de fonction de parois standard. Les deux simulations sont réalisées sur un cube de 10 m placé dans une couche limite atmosphérique. Les profils horizontaux et verticaux des  $h_c$  sur les faces du cube résultants de deux simulations sont très proches. Les résultats fournis par la simulation RANS  $rk - \varepsilon$  réalisée par Defraeye, Blocken et Carmeliet (2010) avec le modèle de fonction de parois, sont utilisés ici comme référence, ayant fait eux même l'objet d'une comparaison avec les résultats obtenus avec une simulation RANS  $rk - \varepsilon$  en appliquant un modèle bas Reynolds sur la même configuration d'étude. Selon les observations de Defraeye, Blocken et Carmeliet (2010), le modèle bas Reynolds fournit une bonne estimation du profil de  $h_c$  uniquement sur les surfaces face au vent (Defraeye, Blocken, and Carmeliet, 2010). La comparaison entre le modèle de fonction de parois et le modèle bas Reynolds montre une similitude dans la distribution des  $h_c$  mais avec des valeurs systématiquement plus élevées lorsque la fonction de paroi est utilisée (Defraeye, Blocken, and Carmeliet, 2010). Néanmoins, l'impossibilité d'utiliser un modèle de bas Reynolds dans les problèmes de physique du bâtiment, conduit généralement à utiliser en alternative les fonctions de parois pour l'estimation des  $h_c$ .

Les résultats d'une simulation utilisant le modèle en pression pour les écoulements intérieurs ont été comparés avec ceux du modèle CONTAM (Wetter, 2006) sur une même configuration d'ouvertures. Les deux modèles donnent des résultats proches avec des erreurs relatives de débits massiques inférieurs à 5%.

Les résultats de simulation des flux radiatifs CLO et GLO en appliquant les modèles de rayonnement CLO et de GLO utilisés dans le McZM ont été comparés avec ceux d'un modèle validé de lancer de rayon basé sur la méthode de Monte Carlo (Galtier et al., 2022) dans une rue canyonne. Les erreurs relatives sont inférieures à 6%. Le même cas d'étude a été utilisé pour comparer le modèle de parois du modèle de STD BuildSysPro avec un modèle de paroi basé sur la même méthode de résolution par volumes finis, mais n'ayant cependant pas encore fait l'objet de validation. Cette comparaison permet néanmoins de vérifier les tendances et les ordres de grandeurs des températures des surfaces extérieures. L'erreur relative moyenne ne dépasse pas 3% avec une erreur relative maximale de 11% sur les périodes de grande exposition solaire.

Le modèle de sol évaporatif sans végétation a été validé en comparant les résultats d'une simulation avec les résultats issus de l'expérience de Bittelli et al.(2008) réalisée sur un sol limoneux (argile et sable) à côté de Holtville en Californie. Le modèle fournit une bonne estimation de l'évolution de la température de surface avec un écart relatif moyen de 6.2%.

Une comparaison entre la  $T_{mrt}$  extérieure obtenue avec le McZM et celle obtenue avec le modèle RayMan, sur une même configuration d'étude correspondante à un individu situé dans un espace extérieur dépourvu d'obstacles, a permis de vérifier les bons ordres de grandeurs et la bonne tendance de la  $T_{mrt}$ .

## 4. Application du couplage McZM et BEM sur un cas d'étude

Un cas d'application de la chaîne de modélisation comprenant le couplage du McZM avec le modèle de STD est réalisé sur l'îlot Ydeal Square de Confluence à Lyon.

La Figure 4 illustre les étapes de passage de la géométrie réelle au modèle simulé par la CFD pour le précalcul aérodynamique. Les bâtiments au contour jaune sont ensuite exclus de la zone d'étude et du calcul des flux CLO incident sur les parois. L'étude à l'intérieur du bâtiment se focalise sur le dernier étage du bâtiment A (Figure 5) et entouré de rouge en Figure 4 et en particulier sur l'appartement situé au dernier étage du bâtiment A côté ouest. Les conditions aux limites du domaine sont données par les mesures de  $T_a$ ,  $HR$  et  $v_a$  de la station météo qui se situe sur le bâtiment F du domaine.

### 4.1 Configuration du cas d'étude et scenari de simulation

Les simulations réalisées pour l'évaluation du stress thermique portent sur des bâtiments isolés au niveau de la toiture et des fenêtres et faiblement isolés au niveau des parois.



La configuration est illustrée dans le Tableau 2, où  $R_{th}$  est la résistance thermique,  $h_{c_{in}}$  est le coefficient d'échange convectif intérieur,  $a_{ext}$  est l'albédo des surfaces extérieures,  $sf$  est le facteur solaire et  $\epsilon_{ext}$  est l'émissivité.

Deux options de configuration de systèmes et d'occupation dans le bâtiment sont proposées dans le Tableau 3: l'option avec ( $NV_{on}$ ) et sans ventilation naturelle ( $NV_{off}$ ).

Table 2: Propriétés thermiques et radiatives des bâtiments.

<b>LowRth</b>	$R_{Th} [m^2 K W^{-1}]$	$h_{c_{in}} [W m^{-2} K^{-1}]$	$a_{ext}$	$sf$ [%]	$\epsilon_{ext}$
Murs extérieurs <sup>(*)</sup>	0.66	7.69	0.4	-	0.9
Toiture <sup>(*)</sup>	8.99	10	0.3	-	0.9
Fenêtres	1.24	-	-	66	-
Plancher bas	0.212	5.8	-	-	0.9

(\*) Plus les ponts thermiques qui représentent 6% des pertes thermiques totales

Table 3: Options de configuration des systèmes et d'occupation.

<b>Systèmes et occupation</b>	$NV_{off}$	$NV_{on}$
Occultation des fenêtres	70% <sup>(*)</sup>	
Ventilation mécanique [ $Volh^{-1}$ ]	0.34 <sup>(**)</sup>	
Ventilation naturelle	-	
ouverture porte [ $m^2$ ]		0.55
ouverture fenêtre [ $m^2$ ]		0.25
Gains internes [ $W m^{-2}$ de surface au sol]	4	

(\*) Prends en compte la réduction du flux CLO transmis par les loggias

(\*\*) Débits réglementaires

Deux options de modèle de sol (sol minéral imperméable et sol en terre évaporatif) sont proposées dans le Tableau 4.

Table 4: Propriétés thermiques et radiatives du sol.

	$R_{Th} [m^2 K W^{-1}]$	$a$	$\epsilon$
<b>Sol minéral</b>	1.49	0.05	0.9
<b>Sol en terre</b>	1.34	0.3	0.9

Trois scénarios sont simulés correspondants à un cas de base  $S_{Base}$ , un cas avec l'activation de la ventilation naturelle dans l'appartement étudié aux contour jaunes en Figure 5 ( $S_{NV}$ ) et un cas avec le remplacement du sol extérieur imperméable par un sol perméable ( $S_{Veg}$ ) (Tableau 5). La simulation a portée sur la période de juin a septembre inclus. Chaque simulation a duré environ 10 heures avec un processeur Intel(R) Core(TM) i5-1145G7 à 1,50 GHz et une RAM utilisable de 15,7 Go. La phase de précalcul a nécessité des temps de simulation CFD d'environ 3 heures par expérience, pour un total de 19 expériences. Le précalcul de la radiation solaire et des facteurs de forme a duré moins d'une minute.

Table 5: Scenarii de simulation : cas de base  $S_{Base}$ , application de la ventilation naturelle  $S_{NV}$  et application d'un sol perméable  $S_{Veg}$ .

	$S_{Base}$	$S_{NV}$	$S_{Veg}$
Configuration thermique du bâtiment	LowRth	LowRth	LowRth
Configuration thermique du sol	Mineral soil	Mineral soil	Bare soil
Systèmes et occupation	$NV_{off}$	$NV_{on}$	$NV_{off}$

## 4.2 Impact d'hypothèses de modélisation simplificatrices des conditions aux limites du bâtiment

Des simulations préliminaires, menées sur un bâtiment isolé RT2012 avec la configuration des systèmes et d'occupation  $NV_{off}$  décrite au Tableau 3, visent à comparer les températures intérieures résultantes du modèle McZM avec celles résultantes d'hypothèses de conditions aux limites simplifiées. Ces dernières concernent le  $h_c$  extérieur (une valeur constante de  $h_c$  a été utilisée à la place du  $h_c$  obtenu par interpolation) et la  $T_a$  extérieure (la température mesurée à la station météo a été utilisée à la place des températures des zones du modèle McZM). Les résultats mettent en évidence l'impact non négligeable des hypothèses de conditions aux limites sur les températures de l'air intérieur avec des écarts de températures allant de 1.1 °C (comparaison avec le  $h_c$  constant) à 1.5 °C (comparaison avec la température d'air correspondante à celle du fichier météo).

## 4.3 Modélisation du stress thermique saisonnier et journalier : résultats

Le stress thermique est analysé en utilisant une approche d'exposition Eulérienne pour l'analyse journalière et saisonnière, et en utilisant une approche d'exposition Lagrangienne uniquement pour l'analyse journalière. La contrainte sur le corps est exclusivement analysée en utilisant une approche d'exposition Lagrangienne sur une base journalière.

### Analyse journalière selon l'approche Lagrangienne

La spatialisation des environnements thermiques se révèle nécessaire car elle permet de saisir le stress thermique subi par l'individu qui se déplace. Des variations importantes de PET sont observées en passant de l'intérieur à l'extérieur du logement ainsi que au sein d'une même zone en raison de variations importantes de la  $T_{mrt}$ . L'application des  $S_{NV}$  et  $S_{Veg}$  montre également une amélioration du stress thermique subi lors du déplacement (Figure 6), notamment pour le  $S_{Veg}$  où les écarts avec le  $S_{Base}$  à l'extérieur peuvent atteindre 4 °C. Cette analyse nécessite cependant la connaissance des déplacements individuels et de leur comportement (par exemple, activité, vêtements, niveau d'hydratation), qui ne sont pas toujours connus. Pour l'évaluation de la contrainte thermique, il est difficile de tirer des conclusions uniquement sur la base de l'observation des indices physiologiques calculés à partir du modèle JOS-3. Cependant, ces indices peuvent être utilisés à des fins comparatives



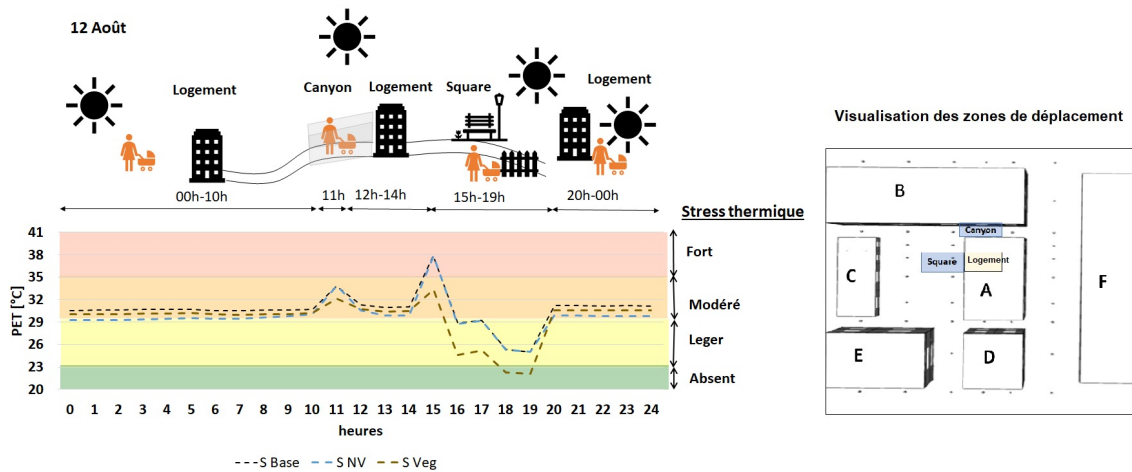


Figure 6: Evolution de la PET suivant le parcours dynamique et au niveau des 3 sites : Logement, Square et Canyon pour les 3 scénarios simulés :  $S_{Base}$ ,  $S_{NV}$  et  $S_{Veg}$ .

lors de l'évaluation des impacts des mesures de refroidissement.

### Analyse journalière selon l'approche d'exposition Eulérienne

Pour s'affranchir de l'effet des conditions limites, l'analyse exclut les zones aux bords du domaine. Cette analyse fournit l'évolution du stress thermique au fil de la journée lié à un lieu et permet d'identifier à chaque heure de la journée les zones avec le stress thermique le plus faible ou le plus élevé pour les trois scénarios simulés. L'analyse à l'intérieur du bâtiment est limitée ici à différentes pièces d'un même étage. Cette analyse révèle que les zones exposées à l'ouest sont constamment plus fraîches que celles exposées à l'est (Figure 7). Cela s'explique par le fait que les pièces exposées à l'est reçoivent le rayonnement solaire dès le matin et montent de ce fait en température. Leur température se maintient ensuite plus élevée que celle des autres pièces tout au long de la journée, en raison de la hausse progressive de la  $T_a$  extérieure entre le matin et le début d'après-midi.

La Figure 7 montre également comment le  $S_{NV}$  apporte un bénéfice ciblé dans les pièces où elle est activée avec une réduction de la PET plus importante le soir, lorsque la  $T_a$  extérieure est inférieure à la  $T_a$  dans le logement. Les réductions de PET associées au  $S_{NV}$  par rapport au  $S_{Base}$  reste cependant faible, de l'ordre de 1°C. Le bénéfice de cette mesure dépend en effet du débit de ventilation et de l'écart entre la  $T_a$  extérieure et intérieure. Quant au  $S_{Veg}$ , il apporte un bénéfice global à l'extérieur plus marqué (pouvant atteindre 4°C) qui se repercute très peu à l'intérieur avec des valeurs de PET légèrement plus faibles que dans le  $S_{Base}$ .

L'analyse en extérieur, au niveau piéton, montre la forte influence de l'exposition solaire des zones sur l'évaluation du stress thermique. L'impact de la vitesse et de la direction du vent sur le stress thermique est également visible. La Figure 8 illustre comment les températures sont plus élevées dans les zones d'air adjacentes aux bâtiments et où les vitesses

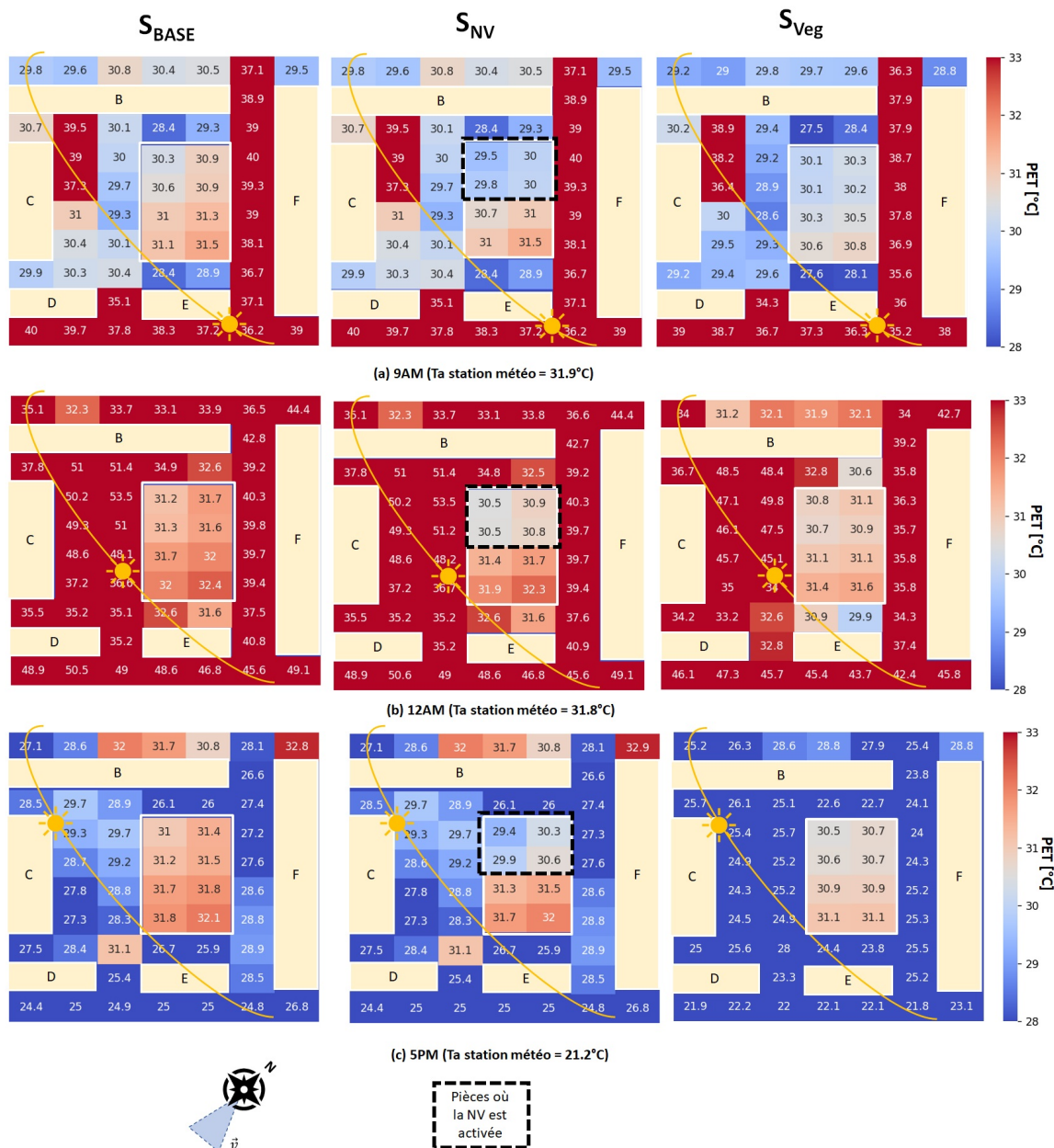


Figure 7: Spatialisation de la PET selon l'approche d'exposition Eulérienne journalière le 12 août à 9h, 12h et 17h pour les 3 scénarios :  $S_{Base}$ ,  $S_{NV}$  et  $S_{Veg}$ . La position du soleil est donnée à titre indicatif.

d'air sont plus faibles. Alors que les zones du côté sud du bâtiment A sont les plus exposées au soleil à 17h, leur  $T_a$  est plus faible que celle des trois zones d'air entre les bâtiments A, F et entre les bâtiments A, B. Cela s'explique par le fait que ces dernières sont en contact direct avec les murs, qui fournissent des sources de chaleur supplémentaires par convection. De plus, les faibles vitesses du vent limitent les échanges advectifs entre les zones d'air plus chaudes et plus fraîches. Quant à la PET, celle des zones au sud du bâtiment A est supérieure à celle des zones situées entre les bâtiments A, F et entre les bâtiments A, B. En effet, bien que la PET soit plus sensible aux variations de  $T_a$  que aux variations de  $T_{mrt}$ , les

amplitudes de la  $T_{mrt}$  étant plus importantes que celles de la  $T_a$ , son impact sur la PET est au global plus important.

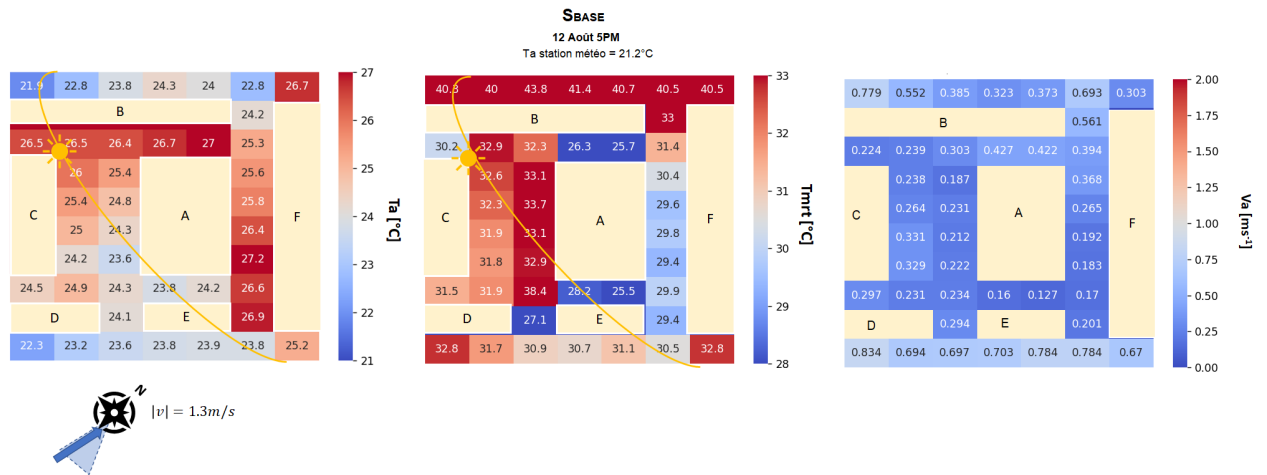


Figure 8: Spatialisation de la  $T_a$ , la  $T_{mrt}$  et la  $v_a$  selon l'approche d'exposition Eulérienne journalière le 12 août à 5PM pour le scénario  $S_{Base}$ .

### Analyse saisonnière selon l'approche d'exposition Eulérielle

Cette analyse spatialisée met en évidence les différents niveaux de surchauffe d'une zone à l'autre, à travers des indices informant sur la durée maximale de surchauffe, l'intensité, le pic et les valeurs moyennes de la surchauffe. On observe que les zones avec la plus longue durée moyenne de stress thermique sont également celles avec la plus grande intensité et avec les pics plus élevés. Les Figures 9 et 10 reportent deux des principaux indices étudiés: les heures maximales de surchauffe ( $OhD_{max}$ ) et la surchauffe moyenne sur la période estivale ( $Oh_{mean}$ ) à l'extérieur et à l'intérieur du logement.

A l'extérieur (Figure 9), l'influence de l'exposition solaire sur le stress thermique se ressent également dans l'analyse saisonnière. Les deux indices  $OhD_{max}$  et  $Oh_{mean}$  permettent d'identifier les zones les plus sujettes au stress thermique, à prioriser lors du déploiement de mesures de rafraîchissement. L'application générale du sol évaporatif a des répercussions plus visibles sur l'indice  $OhD_{max}$  que sur l'indice  $Oh_{mean}$ . La réduction des  $OhD_{max}$ , en relatif, est plus importante dans les zones déjà peu exposées au stress thermique.

A l'intérieur du logement (Figure 10) le  $S_{NV}$  permet une réduction globale des heures de surchauffe maximales dans tous l'étage. Plus particulièrement, dans le logement où la ventilation naturelle est appliquée, une réduction allant jusqu'à un facteur 3 des heures de surchauffe maximales peut être observée. La quantification de la surchauffe moyenne ( $Oh_{mean}$ ) montre peu de variations d'une zone à l'autre sur le même étage.

Les différents niveaux d'analyse mettent ainsi en évidence les avantages d'une approche spatialisée dans l'évaluation du stress thermique à la fois pour l'intérieur que pour l'extérieur

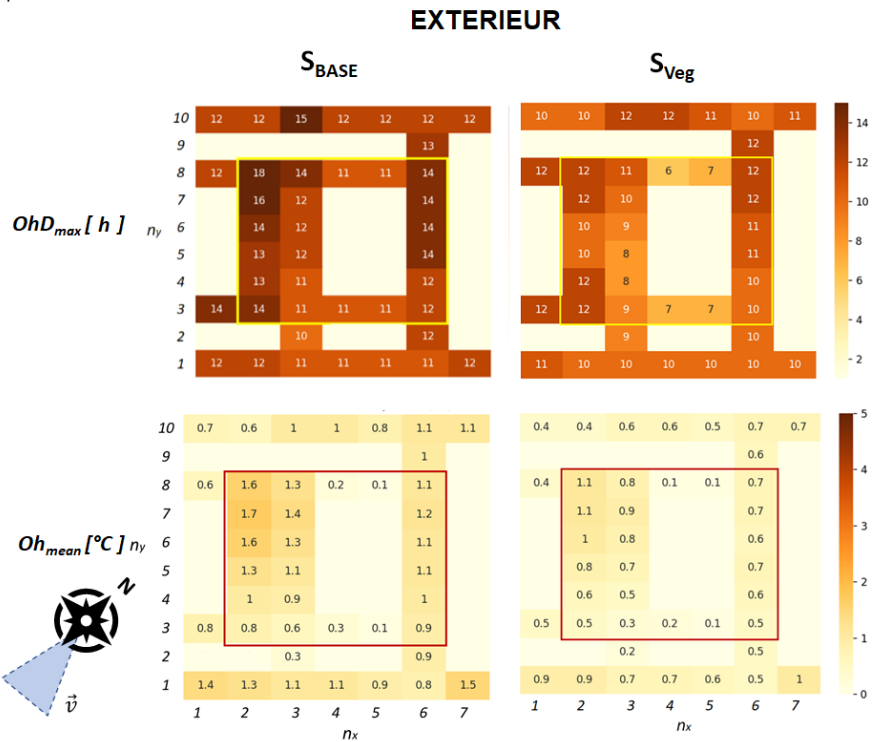


Figure 9: Spatialisation des indices de durée de surchauffe maximale ( $Oh_{D_{max}}$ ) et surchauffe moyenne ( $Oh_{mean}$ ) à l'extérieur étudiés dans l'analyse saisonnière selon une approche d'exposition Eulérienne pour les scénarios  $S_{Base}$  et  $S_{Veg}$ .

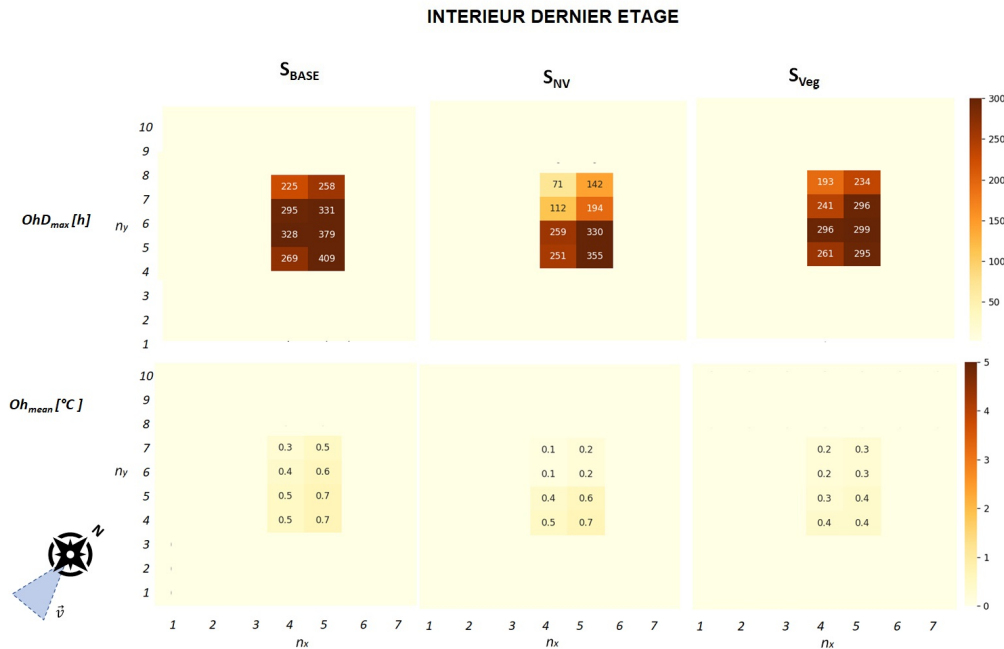


Figure 10: Spatialisation des indices de durée de surchauffe maximale ( $Oh_{D_{max}}$ ) et surchauffe moyenne ( $Oh_{mean}$ ) à l'intérieur, au dernier étage, étudiés dans l'analyse saisonnière selon une approche d'exposition Eulérienne pour les scénarios  $S_{Base}$ ,  $S_{NV}$  et  $S_{Veg}$ .

du logement ainsi que la complémentarité des approches d'évaluation du stress thermique selon une approche Eulérienne et Lagrangienne et sur une durée journalière et saisonnière.

## Conclusions et perspectives

En conclusion, ce travail de recherche a démontré la pertinence d'une approche de modélisation couplant un McZM avec un modèle STD de bâtiment dans l'évaluation du stress thermique saisonnier et journalier. Le modèle de McZM permet de répondre aux enjeux de modélisation relatifs à la mise en oeuvre d'un modèle zonal d'écoulement extérieur capable de prendre en compte l'impact de la géométrie urbaine, adapté à l'évolution de la vitesse et de la direction du vent, garantissant un équilibrage des bilans de masse sans altérer la nature de l'écoulement. Il propose une structure de zonage appropriée et répond à l'enjeu d'assurer le couplage thermique et aérodynamique entre l'intérieur et l'extérieur.

De plus, ce travail a montré la valeur ajoutée d'une approche de modélisation spatialisée dans l'évaluation du stress thermique journalier et saisonnier. Il a démontré la capacité du modèle couplé McZM et STD du bâtiment à modéliser les pratiques de rafraîchissement couramment adoptées dans le logement et certaines pratiques observées à l'extérieur (par exemple le sol évaporatif). Cependant, des améliorations restant à apporter ont été identifiées, conduisant aux perspectives de recherche suivantes.

La première implique l'évaluation du stress thermique des individus en tenant compte de leurs déplacements à une plus large échelle temporelle, voir spatiale, et en prenant en compte l'interaction avec l'environnement extérieur. Cela soulève des questions sur la modélisation d'une séquence d'environnements extérieurs et nécessite l'intégration de modèles basés sur des agents (capables de prendre en compte l'interaction entre l'agent et l'environnement) couplés à des modèles de bâtiment et de microclimat.

La deuxième consiste à évaluer le stress thermique en utilisant des indices dynamiques en employant des modèles de thermorégulation transitoires.

La troisième porte sur l'étude des effets cumulatifs, en terme de contrainte thermique, d'une exposition prolongée à des températures élevées sur une saison, cela dans le but de prendre en compte les effets d'acclimatation ou de fatigue du système de thermorégulation. Ce domaine de recherche dépasse le cadre des sciences de l'ingénierie et bénéficierait de la recherche multidisciplinaire avec le domaine de la santé.

La quatrième consiste à améliorer les modèles utilisés dans le McZM. Actuellement, seul un sol imperméable, un sol perméable et un sol avec végétation basse sont modélisés. Les effets de la végétation haute (arbres) sur les échanges thermiques radiatifs et sur les écoulements ainsi que d'autres stratégies de rafraîchissement mises en avant par les villes pour atténuer la surchauffe urbaine tel que les toitures végétalisées ou les stratégies fondées sur l'eau ne sont pas modélisés.

La cinquième implique la prise en compte de la flottabilité dans le McZM. En effet, le McZM actuel est applicable uniquement dans des conditions où les forces liées au vent dominant sur les forces dues à la flottabilité. Par exemple, cette approche n'est pas adaptée pour étudier les flux dans les cours intérieures fermées en cas de faible vent.

La sixième concerne le couplage entre le McZM et des modèles à plus grande échelle (par exemple, des modèles à méso-échelle, des modèles de couche limite urbaine ou des modèles de canopée urbaine) pour assurer la continuité entre les mesures prises dans les stations météorologiques situées loin du site d'étude.

La septième porte sur la validation de l'ensemble du McZM, à la fois grâce à des protocoles expérimentaux appropriés et en utilisant des approches de validation qui impliquent une comparaison avec d'autres modèles validés.







# Contents

<b>Contents</b>	<b>xxxvii</b>
<b>List of figures</b>	<b>xxxix</b>
<b>List of tables</b>	<b>xlix</b>
<b>Introduction</b>	<b>1</b>
<b>I Definition of heat stress assessment and modelling issues</b>	<b>5</b>
<b>1 Heat stress and heat strain assessment</b>	<b>7</b>
1.1 Assessment of overheating effects on the human body . . . . .	9
1.2 Relation between heat stress and heat strain and the main variables affecting their assessment . . . . .	12
1.3 Indices used to asses heat stress and (indirectly) heat strain . . . . .	17
1.4 Applicability of steady and transient modelling approaches under different climatic conditions . . . . .	29
1.5 Sensitivity of heat stress and heat strain indices to climatic variables evolution and time step . . . . .	36
1.6 Selected heat stress and heat strain indices . . . . .	43
1.7 Conclusions . . . . .	45
<b>2 Modelling of urban microclimate and buildings for heat stress assessment</b>	<b>47</b>
2.1 Physical phenomena to be modelled . . . . .	49
2.2 Cooling solutions to be modelled in urban spaces and buildings . . . . .	59

2.3	Modelling thermal environments for heat stress and heat strain assessment . . .	61
2.4	Specific problem formulation, expected outcomes and modelling issues . . . .	68
2.5	Modelling strategy . . . . .	70
2.6	Conclusions . . . . .	74
<b>II</b>	<b>Coupled Microclimate Zonal Model and Building Energy Model</b>	<b>77</b>
<b>3</b>	<b>Outdoor and indoor airflow models</b>	<b>79</b>
3.1	Outdoor airflow model . . . . .	80
3.2	Natural ventilation model . . . . .	105
3.3	Conclusions . . . . .	113
<b>4</b>	<b>Radiative, BEM, Soil and <math>T_{mrt}</math> models</b>	<b>115</b>
4.1	Solar radiation model . . . . .	116
4.2	Long Wave radiation model . . . . .	120
4.3	Outdoor soil model . . . . .	124
4.4	Building energy model (BEM) . . . . .	133
4.5	Indoor and Outdoor $T_{mrt}$ model . . . . .	139
4.6	Conclusions . . . . .	146
<b>III</b>	<b>Application of McZM coupled with BEM to a case study</b>	<b>149</b>
<b>5</b>	<b>Case study on Confluence Ydeal Square</b>	<b>151</b>
5.1	Case study configuration . . . . .	153
5.2	Analysis framework and simulated scenarios . . . . .	158
5.3	Results : Modelling approaches comparison . . . . .	164
5.4	Results: base scenario . . . . .	171
5.5	Results : cooling strategy comparison . . . . .	186
5.6	Conclusions . . . . .	195
	<b>General conclusion and enlarged perspectives</b>	<b>197</b>

---

<b>Bibliography</b>	<b>203</b>
<b>Appendices</b>	<b>216</b>
A Heat stress index and thermophysiological models . . . . .	A. 1
B Dynamic response of $T_{core}$ in JOS-3 model . . . . .	A. 7
C Richardson number in thermal convection problem . . . . .	A. 9
D Velocity profile at a specific point in the domain . . . . .	A. 11
E DOE segmentation . . . . .	A. 14
F Comparison of CFD results with the isolated building experiment . . . . .	A. 15
G Building model - Conduction model comparison . . . . .	A. 24
H Soil model - Penman-Monteith equation . . . . .	A. 25
I Individuals' cooling measures implementation in BEMs . . . . .	A. 28



# List of Figures

1.1	Heat stress and heat strain within the risk-hazard framework. . . . .	11
1.2	Interaction of exposure environment and thermoregulation. . . . .	13
1.3	$T_{core}$ evolution for different values of (a) $T_a$ when $HR = 80\%$ and $v_a = 0.1 \text{ m s}^{-1}$ (b) $HR T_a = 39^\circ\text{C}$ and $v_a = 0.1 \text{ m s}^{-1}$ (from Deng et al., 2018). . . . .	15
1.4	Heat stress and heat strain indices. . . . .	20
1.5	PET concentric two node ( $T_{core}$ and $T_{sk}$ ) model representation and main input variables (adapted from Walther and Goestchel, 2018). . . . .	21
1.6	JOS-3 Model concept (form Takahashi et al., 2021) and main input parameters. . . . .	22
1.7	Adaptive comfort model of ANSI/ASHRAE 55:2017. . . . .	25
1.8	Hourly variation of climatic variables $T_a, T_{mrt}, RH, v_a$ (Lyon Confluence Weather file). . . . .	30
1.9	Example of $T_a, T_{mrt}, RH, v_a$ a typical summer day (Lyon Confluence Weather file and computation of the $T_{mrt}$ based on 4.5.1 model). . . . .	31
1.10	Steady and transient $T_{core}$ and $T_{sk}$ evolution for climatic variables evolution corresponding to the 8th of August from 11 AM to 3 PM. . . . .	33
1.11	Displacement scenario though different exposure environments. . . . .	34
1.12	$T_{core}$ and $T_{sk}$ evolution under exposure environments of Figure 1.11. . . . .	35
1.13	$T_{mrt}$ triangular distribution for the four ranges of climatic variables R1, R2, R3 and R4. . . . .	37
1.14	$v_a$ triangular distribution for the four ranges of climatic variables R1, R2, R3 and R4. . . . .	38
1.15	ST, S1 and S2 indices for Sobol PET Sensitivity analysis for the range R1. . . . .	38
1.16	ST, S1 and S2 indices for Sobol PET Sensitivity analysis for the range R2. . . . .	39
1.17	ST, S1 and S2 indices for Sobol PET Sensitivity analysis for the range R3. . . . .	39

1.18	ST, S1 and S2 indices for Sobol PET Sensitivity analysis for the range R4. . . . .	40
1.19	Increase of PET with an increase of 1°C of $T_a$ and 1°C of $T_{mrt}$ . . . . .	41
1.20	Increase of PET with an increase of 0.1 m s <sup>-1</sup> in the case of $T_a = T_{mrt} = 31$ °C and $T_a = 31$ °C and $T_{mrt} = 45$ °C. . . . .	41
1.21	$T_{core}$ evolution for hourly and 10 min $T_a$ time step. . . . .	42
1.22	$T_{sk}$ evolution for hourly and 10 min $T_a$ time step. . . . .	43
2.1	The atmosphere structure layer and temperature evolution (Figure from UCAR/Randy Russell). . . . .	49
2.2	Schematic typical layering of the atmosphere over a city (a) by day and (b) by night (Figure from Oke et al., 2017). . . . .	51
2.3	Mean wind profile depending on the land use (based on (Merlier, 2015), (Blocken, Stathopoulos, and Carmeliet, 2007)). . . . .	51
2.4	Schematic illustration of urban features modifying the atmosphere and their characteristic parameters. . . . .	53
2.5	Classification of urban morphological units and their urban climate phenomena, based on horizontal length scale and climate scale. Units from canyon to city are based on a city with about 1M inhabitants (source: Oke et al., 2017). . . . .	54
2.6	Schematic of the fluxes in the surface energy balance of a building-soil-air volume. The volume that extends from the top of the RSL ( $z_{top}$ ) down to a depth where there is no net conduction over the period of interest ( $z_{bot}$ ). (Source: Oke et al., 2017). . . . .	55
2.7	(a) Section of Figure 2.6. (b) Fluxes involved in the heat transfers at block scale. The air volume at the block scale is subdivided into air-zones : $\Phi_A$ is the heat flux density exchanged by the air-zones by advection. $\Phi_c$ , $\Phi_{SW}$ , $\Phi_{LWR}$ , $\Phi_K$ , $\Phi_F$ and $\Phi_L$ are respectively the convective heat flux density, the solar heat flux density, the net long wave radiation heat flux density, the conductive heat flux density, the sources/sink heat flux density and the latent heat flux density. . . . .	57
2.8	Adaptative and mitigation measures and their direct and indirect impact on heat stress and heat strain. . . . .	60
2.9	Modelling process design: from the main question to the modelling requirements. . . . .	63
2.10	BEM and urban microclimate models comparison. . . . .	65
2.11	Global model architecture: model components vision. The double arrow indicates that the models are coupled and the one-way arrow indicates that the data is going from one model to another in the direction of the arrow. . . . .	72

2.12	Global model architecture : data workflow. . . . .	75
3.1	Confluence Ydeal Square: global view of the square and view of the target building and weather station. . . . .	80
3.2	Confluence wind direction distributions from June to September 2020. Yellow bars represent Southeast to Southeast wind direction. The blue bars represent Southwest to Northwest and Northeast to Southeast wind direction. The gray bars represents Northwest to Northeast wind direction. The $y$ axis represents the wind direction occurrences and the $x$ axis represents the wind direction ranges in degrees from North. . . . .	81
3.3	Segmentation of the DOE based on the Wind speed and orientation distribution for the Confluence urban weather station and Bron rural weather. . . . .	83
3.4	Confluence district plan and zoom on the Ydeal square block. Horizontal view. . . . .	84
3.5	CFD domain. . . . .	85
3.6	Geometry to and mesh for the CFD computation. Horizontal view. . . . .	86
3.7	Transition from the fine mesh to a coarser zoning. Horizontal view and 3D view showing the vertical sections. . . . .	89
3.8	Zoning implemented in the Ydeal Square case study (Confluence), horizontal view, vertical view and 3D view. . . . .	89
3.9	Schematic view of the balancing approach (independent of the wind flow direction). . . . .	90
3.10	Net mass flow rates crossing air zones at pedestrian level [0 m – 3 m] (a) before mass balance (b) after mass balance, and (c) % of correction on the pedestrian level [0 m-3 m], $v_{10} = 2 \text{ m s}^{-1}$ and wind blowing from South. . . . .	91
3.11	$mfr[\text{kg s}^{-1}]$ crossing the $x$ and $y$ up air surfaces and the $x,y,z$ down air surfaces for the pedestrian level [0m – 3m], $v_{10} = 2 \text{ m s}^{-1}$ and wind blowing from South (a) before balance and (b) after balance. . . . .	92
3.12	Schematic view of the mfr exchange in an air zone. . . . .	97
3.13	Schematic representation of the square prism experiment (Meng and Hibi, 1998). . . . .	99
3.14	Measuring points for the (a) vertical section and the two (b) horizontal sections at $z=0.125b$ and $z=1.25b$ (from Meng and Hibi, 1998). . . . .	99
3.15	CFD setting for the reproduction of the square prism experiment (Meng and Hibi, 1998). . . . .	100

3.16	Vertical section: Airflow simulated by CFD RANS $rk - \varepsilon$ in the reproduction of the square prism experiment (Meng and Hibi, 1998). . . . .	100
3.17	Wind profile for XZ vertical section (Part I : from $x=-0.75b$ to $0.5b$ ). Average RNMSE on $x = 0.89$ , on $y = 7.08$ on $z = 1.70$ . Average error relative to $U_0$ on $x = 9.6\%$ , on $y = 0.9\%$ on $z = 4.9\%$ . . . . .	101
3.18	Wind profile for XZ vertical section (Part II : from $x=0.75b$ to $3.25b$ ). Average RNMSE on $x = 0.89$ , on $y = 7.08$ on $z = 1.70$ . Average error relative to $U_0$ on $x = 9.6\%$ , on $y = 0.9\%$ on $z = 4.9\%$ . . . . .	102
3.19	Domain and size and simulation setting for the simulation of the single cube immersed in a turbulent boundary layer using RANS $rk - \varepsilon$ turbulence model (Defraeye, Blocken, and Carmeliet, 2010). . . . .	104
3.20	Comparison of the $h_c$ distribution on the surfaces of the cube resulting from a DCF RANS $rk - \varepsilon$ turbulence model and using a standard wall function for the Defraeye, Blocken and Carmeliet (2010) numerical simulation and the simulation reproduced in this thesis. . . . .	104
3.21	Vertical airflow velocity profiles for two-way buoyancy-driven flow in the absence of wind forces (adapted from Truong, 2012). . . . .	106
3.22	Schematics of pressure distribution of two rooms connected by a large vertical aperture of height $h$ . (Adapted from Wetter, 2006). . . . .	108
3.23	Schematic view of the assembled air flow components in a 4 rooms apartment.	110
3.24	Plan 2D and dimensions of the studied dwelling. . . . .	111
3.25	Mass flow rates computed with Modelica and CONTAM models for an isothermal configuration and a difference of temperature configuration. . . . .	112
4.1	Four components of solar irradiance calculated by HelioBIM (Bouquerel et al., 2021). . . . .	116
4.2	Simple canyon geometry configuration. . . . .	118
4.3	Illustration of the 3 vertical (1,2,3) and 3 horizontal (4,5,6) profiles for the 3 surfaces A, B and C. . . . .	118
4.4	Reproduction of the DIAMS canyon configuration in HelioBIM. . . . .	119
4.5	Average irradiance on the A, B, C surface at different periods of the day and corresponding RE at 6:30 AM, 12:30 AM and 5:30 PM on July the 18th. . . . .	119
4.6	Solar irradiance profile on the A, B, C surfaces at different periods of the day on July the 18th. . . . .	120



4.7	Average long wave irradiation for the Monte-Carlo method and the LWR model of the McZM and the RE July 18th at 12:30 PM. . . . .	123
4.8	Comparison of the long wave irradiation profiles and RE: Monte Carlo model and LWR model of the McZM. . . . .	124
4.9	Outdoor soils models. . . . .	126
4.10	Schematic view of the displacement height and roughness length for low vegetation model (C) ( $z_{0h}$ not at scale). . . . .	129
4.11	Two reservoirs water balance model. . . . .	130
4.12	Measured and modelled soil temperatures at a depth of 2 cm and measured air temperature from 2 - 17 October 2003 (Hotville, California). . . . .	132
4.13	Measured and modelled soil temperature differences at a depth of 2 cm from 2 - 17 October 2003 (Hotville, California). . . . .	133
4.14	Example of spatial discretization along the x-axis. . . . .	135
4.15	Canyon side view. . . . .	137
4.16	Surface temperatures on Wall A, Wall B, Roof A and Ground. . . . .	138
4.17	Differences of surface temperatures ( $T_s$ Traboule - $T_s$ HelioBIM) on Wall A, Wall B, Roof A and Ground. . . . .	138
4.18	Rectangular boxes for $T_{mrt_{out}}$ modelling. . . . .	141
4.19	Dayly solar radiation and $T_{mrt}$ evolution for (A) RayMan model, (B) McZM and (C) comparison between $T_{mrt}$ evolution for RayMan and McZM. . . . .	145
5.1	Confluence Ydeal Square: global view of the square and view of the target building and weather station. . . . .	153
5.2	3D illustration of the case study building geometry and dimensions in the McZM domain. $T_a$ and $RH$ and wind speed boundary conditions are provided by the data measured at the Confluence weather station. Wind speed direction varies within the ranges from $150^\circ N$ to $196^\circ N$ and direct and diffuse solar radiation are provided by the European Commission's Photovoltaic geographical information system database. . . . .	154
5.3	Three modelling options scenarios for the outdoor heat flux: $S_{McZM}$ corresponding to the original McZM, $S_{h_c \text{ cnst}}$ corresponding to constant $h_{c_{ext}}$ values and $S_{T_{vs}}$ corresponding to weather station $T_a$ and $RH$ . . . . .	159
5.4	Heat stress and heat strain analysis framework. . . . .	161
5.5	2D plan of the studied dwelling : indoor and outdoor air zones, exterior walls and roofs. . . . .	164

5.6	$S_{McZM}$ and $S_{h_c, const}$ the 12th of August :evolution of (a) $h_{c, ext}$ , (b) Air temperatures in the outdoor air zones adjacent to walls $T_{a, ext}$ , (c) outdoor walls surfaces temperature $T_{s, ext}$ (d) Convective heat flux between exterior walls surfaces and adjacent air zones $\Phi_{c, ext}$ . . . . .	165
5.7	$S_{McZM}$ and $S_{h_c, const}$ the 12th of August :evolution of (a) $h_{c, ext}$ , (b) outdoor air temperatures difference of air zones adjacent to walls $\Delta T_{a, ext}$ , (c) outdoor walls and roofs surface temperature difference $\Delta T_{s, ext}$ (d) indoor air temperature difference $\Delta T_{a, in}$ . . . . .	166
5.8	$S_{McZM}$ and $S_{h_c, const}$ the 12th of August : evolution of (a) Roof1 surface temperature $T_s$ , (b) air temperature of air zone adjacent to Roof1 ( $T_a$ Roof1) and air temperature at the weather station ( $T_a$ ws) (c) Convective heat flux between Roof1 and the adjacent air zone $\Phi_c$ (positive from the surface to the air). . . .	168
5.9	$S_{McZM}$ and $S_{T_{ws}}$ the 12th of August : (a) inlet wind speed (V speed) and wind direction (V dir) (b) outdoor air temperatures of air zones adjacent to walls ( $T_{a, ext}$ ), (c) outdoor walls surfaces temperature ( $T_{s, ext}$ ) (d) indoor air temperature difference ( $T_{a, in}$ ). . . . .	169
5.10	$S_{McZM}$ and $S_{T_{ws}}$ the 12th of August : (a) outdoor air temperatures difference of air zones adjacent to walls $\Delta T_{a, ext}$ , (b) outdoor walls and roofs surfaces temperature difference $\Delta T_{s, ext}$ (c) indoor air temperature difference $\Delta T_{a, in}$ . . . . .	170
5.11	3D view of the modelled scene and the target dwelling. . . . .	172
5.12	2D view of the (x,y) horizontal plan at the top level corresponding to $z \in [21 - 24m]$ and 2D plan of the studied dwelling. . . . .	172
5.13	Wind speed magnitude for an inlet velocity of $2 \text{ m s}^{-1}$ and a wind direction of (a) $180^\circ N$ and (b) $151^\circ N$ . . . . .	173
5.14	Pedestrian level spatial distribution of climatic variables on August the 12th at 9 AM and 5 PM. Note: Sun position is purely indicative. . . . .	175
5.15	Pedestrian level PET spatial distribution on August the 12th at 9 AM and 5 PM. Note: Sun position is purely indicative. . . . .	176
5.16	August the 12 <sup>th</sup> , studied dwelling: (a) Walls incident solar radiation (b) Air temperature of the air-zones adjacent to the walls (c) Indoor air temperature. . . . .	176
5.17	Pedestrian level and top floor PET spatial distribution on August 12th from 9 AM to 7 PM. Note: Sun position is purely indicative. . . . .	177
5.18	An example of the daily path of a person spending the day in his dwelling and its surroundings. . . . .	178
5.19	Illustration of the three displacement zones. . . . .	178

5.20	August the 12 <sup>th</sup> . PET evolution related to the dynamic path (PET Dynamic) and PET evolution in the dwelling, in the square and in the canyon air zone. . . . .	179
5.21	Heat strain response corresponding to the exposure path of Figure 5.20: (a) $T_{sk}$ , (b) $T_{core}$ , (c) $SkinWet$ (d) $sw_R$ , (e) $CO$ . . . . .	180
5.22	PET assessment scale (Matzarakis and Mayer, 1996). . . . .	181
5.23	Outdoor minimal and maximal HSD for the global season and for June, July, August and September. . . . .	181
5.24	Top floor minimal and maximal HSD for the global season and for June, July, August and September. . . . .	182
5.25	Studied dwelling minimal and maximal HSD for the global season and for June, July, August and September. . . . .	182
5.26	Outdoor and top floor Maximal overheating duration ( $OhD_{max}[h]$ ). . . . .	183
5.27	Outdoor and top floor Cumulative overheating intensity ( $OhI_{max}[^{\circ}C h]$ ). . . . .	183
5.28	Outdoor and top floor Maximal overheating ( $Oh_{max}[^{\circ}C]$ ). . . . .	184
5.29	Outdoor and top floor Average overheating ( $Oh_{mean}[^{\circ}C]$ ). . . . .	184
5.30	From June to September 2020: periods corresponding to the maximal overheating duration ( $OhD_{max}$ ) represented by the bubble size and color, the average degrees of exceedance ( $^{\circ}C$ ) during the $OhD_{max}$ episode represented by the black number, the maximum temperatures ( $^{\circ}C$ ) during the $OhD_{max}$ episode represented by the red number. . . . .	185
5.31	Pedestrian level and top floor PET spatial distribution for $S_{Base}$ and $S_{NV}$ and $S_{Veg}$ at 9AM, 12AP and 5PM the 12 <sup>th</sup> of August. Note: Sun position is purely indicative. . . . .	187
5.32	Weather station ( $T_{wf}$ ) air temperature and the air temperature in the R1 air-zone (Z_4_6_4) from the 12 <sup>th</sup> to the 15 <sup>th</sup> of August 12 AM. . . . .	188
5.33	August the 12 <sup>th</sup> . Comparison of the $S_{Base}$ , $S_{NV}$ and $S_{Veg}$ : PET evolution related to the dynamic path. . . . .	188
5.34	Comparison of heat strain response corresponding to the exposure path of Figure 5.20 for $S_{Base}$ and $S_{Veg}$ : (a) $T_{sk}$ , (b) $T_{core}$ , (c) $SkinWet$ (d) $sw_R$ , (e) $CO$ . . . . .	190
5.35	Outdoor $HSD_{min}$ and $HSD_{max}$ for the $S_{Base}$ and $S_{NV}$ and $S_{Veg}$ . . . . .	191
5.36	Studied dwelling $HSD_{min}$ and $HSD_{max}$ for the $S_{Base}$ , $S_{NV}$ and $S_{Veg}$ . . . . .	192
5.37	$OhD_{max}$ , $OhI_{max}$ , $Oh_{max}$ and $OhD_{mean}$ at pedestrian level for the $S_{Base}$ and $S_{Veg}$ . . . . .	193
5.38	$OhD_{max}$ , $OhI_{max}$ , $Oh_{max}$ and $OhD_{mean}$ at the top floor for the $S_{Base}$ , $S_{NV}$ and $S_{Veg}$ . . . . .	194

a.1	Graphical sketch of heat wave duration (HWD) and amplitude (HWA, grey shading) exceedances. $T_{th}$ and $dth$ denote the thermal stress and duration thresholds, respectively (Amengual et al., 2014). . . . .	A. 5
a.2	Evolution of the $T_{core}$ in the JOS-3 model under $T_a$ variation from 30°C to 33°C and from 33°C to 30°C. . . . .	A. 7
a.3	Evolution of the $T_{core}$ in the JOS-3 model under $T_a$ variation from 30°C to 33°C and from 33°C to 21°C. . . . .	A. 7
a.4	Plot box of the Richardson number calculated based on the hypothesis described above from June to September 2020. . . . .	A. 9
a.5	Location of (a) the $V_1$ wind profile and (b) average surface $mfr$ in the $(xy)$ plan for a wind coming from South to North. . . . .	A. 11
a.6	Evolution of the wind speed at different heights in $V_1$ as a function of the inlet wind speed $V_{10}$ for a constant inlet wind direction ( $\beta = 180^\circ$ N). . . . .	A. 12
a.7	Evolution of the average $mfr$ across different air zone surfaces. . . . .	A. 12
a.8	Evolution of the wind speed at different heights in $V_1$ as a function of the inlet wind direction $\beta$ for a constant inlet wind speed ( $V_{10}$ )=2 m s <sup>-1</sup> . . . . .	A. 13
a.9	DOE segmentation for different ranges of wind speed and direction. . . . .	A. 14
a.10	Measurement points - Vertical section (Meng and Hibi, 1998). . . . .	A. 15
a.11	Wind profile for XZ vertical section (Part I : from $x=-0.75b$ to $0.5b$ ). Average RNMSE on $x = 0.89$ , on $y = 7.08$ on $z = 1.70$ . Average error relative to $U_0$ on $x = 9.6\%$ , on $y = 0.9\%$ on $z = 4.9\%$ . . . . .	A. 16
a.12	Wind profile for XZ vertical section (Part II : from $x=0.75b$ to $3.25b$ ). Average RNMSE on $x = 0.89$ , on $y = 7.08$ on $z = 1.70$ . Average error relative to $U_0$ on $x = 9.6\%$ , on $y = 0.9\%$ on $z = 4.9\%$ . . . . .	A. 17
a.13	Measurements points - Horizontal section ( $z=0.125b$ ) (Meng and Hibi, 1998). . . . .	A. 18
a.14	Wind profile for $xy$ section, (Part I: from $x=-0.75b$ to $0.5b$ and $z=0.125b$ ). Average RNMSE on $x = 0.88$ , on $y = 1.49$ on $z = 2.9$ . Average error relative to $U_0$ on $x = 20.0\%$ , on $y = 4.6\%$ on $z = 3.6\%$ . . . . .	A. 19
a.15	Wind profile for $xy$ section, (part II, from $x=0.125b$ to $3.25b$ and $z=0.125b$ ). Average RNMSE on $x = 0.88$ , on $y = 1.49$ on $z = 2.9$ . Average error relative to $U_0$ on $x = 20.0\%$ , on $y = 4.6\%$ on $z = 3.6\%$ . . . . .	A. 20
a.16	Measurements points - Horizontal section ( $z=1.25b$ ) (Meng and Hibi, 1998). . . . .	A. 21
a.17	Wind profile for $xy$ section, (Part I: from $x=-0.75b$ to $0.5b$ and $z=1.25b$ ). Average RNMSE on $x = 0.78$ , on $y = 1.7$ on $z = 1.8$ . Average error relative to $U_0$ on $x = 10.6\%$ , on $y = 3.4\%$ on $z = 2.6\%$ . . . . .	A. 22

---

a.18	Wind profile for xy section, (Part II: from $x=0.75b$ to $3.25b$ and $z=0.125b$ ). Average RNMSE on $x = 0.78$ , on $y = 1.7$ on $z = 1.8$ . Average error relative to $U_0$ on $x = 10.6\%$ , on $y = 3.4\%$ on $z = 2.6\%$ . . . . .	A. 23
a.19	SWR on Wall A, Wall B, Roof A and Ground. . . . .	A. 24
a.20	LWR on Wall A, Wall B, Roof A and Ground. . . . .	A. 24
a.21	Identification of BEM needs corresponding to exposure-oriented cooling measures from the local survey. . . . .	A. 31
a.22	Identification of BEM needs corresponding to body oriented cooling measures from the local survey. . . . .	A. 32



# List of Tables

1.1	Thermal perception and grade of thermal stress for various biometeorological indices adaptation of Zare et al., 2018. . . . .	26
1.2	Heat strain variables threshold. . . . .	27
1.3	Climatic variables evolution scenario within a fixed exposure environment corresponding to the 8th of August from 11AM to 3PM. . . . .	31
1.4	Behavioural and physiological variables. . . . .	32
1.5	$T_{core}$ and $T_{sk}$ at steady state for different $T_a$ values. . . . .	32
1.6	Ranges of values and probability distribution of climatic variables. . . . .	37
1.7	Selected indices for seasonal analysis of heat stress and overheating. . . . .	44
3.1	Computational domain recommendation and adopted values. . . . .	85
3.2	Meshing recommendation and adopted values. . . . .	85
3.3	Adopted boundary conditions. . . . .	87
3.4	Mean surfaces relative error. . . . .	94
3.5	Airflow model parameters. . . . .	110
3.6	Airflow model parameters for the two comparison configurations. . . . .	112
4.1	SWR radiative surface properties and direct and diffuse solar flux for the SWR study configuration. . . . .	117
4.2	SWR radiative surfaces properties. . . . .	123
4.3	Soil properties used in model (B). . . . .	131
4.4	Conduction study configuration. . . . .	137
4.5	Body Box dimensions. . . . .	142
5.1	Studied dwelling dimensions. . . . .	155

## List of Tables

---

5.2	Building thermal properties for the insulated building. . . . .	155
5.3	Building thermal properties for the low-insulated building. . . . .	156
5.4	Building systems and occupancy. . . . .	157
5.5	Ground thermal properties. . . . .	158
5.6	Input parameters used for the PET and JOS-3 model. . . . .	158
5.7	Simulated modelling approaches. . . . .	160
5.8	Selected indices for seasonal analysis of heat stress and overheating. . . . .	162
5.9	Simulated cooling scenarios. . . . .	163



# Nomenclature

## Abbreviations

1D/2D/3D	One /Two / Three Dimensional
ABL	Atmospheric Boundary Layer
ACH	Air changes per hour
ASHRAE	American Society of Heating, Refrigerating and Air-Conditioning Engineers
BEM	Building Energy Model
BIM	Building Information Modelling
CFD	Computational Fluid Dynamics
DOE	Design Of Experiment
DOM	Discrete Ordinate Method
ext	Exterior
FA	Free atmosphere
HVAC	Heat Ventilation Air Conditioning
in	Interior
IPCC	Intergovernmental Panel on Climate Change
ISL	Inertial Sub-Layer
LES	Large Eddy Simulation
LRNM	Low Reynolds Number Modelling
ML	Mixed Layer
MRE	Mean Relative Error
McM	Microclimate Model
McZM	Microclimate Zonal Model
RANS	Reynolds Averaged Navier–Stokes
RE	Relative Error
$rk - \varepsilon$	Realizable $k - \varepsilon$ model
RNMSE	Root normalized mean square error
RSL	Roughness Sub-Layer
SL	Surface Layer
SRA	Simplified Radiosity Algorithm
HSS	Humanities and Social Sciences
UBL	Urban Boundary Layer
UCL	Urban Canopy Layer
UCM	Urban Canopy Model
UHI	Urban Heat Island

## Symbols related to urban or building energy exchanges

$a$	Albedo	$[-]$
$Adv$	Advection sensible heat	$[W]$
$C_a$	Specific heat of air	$[J\ kg^{-1}\ K^{-1}]$
$C_d$	Discharge coefficient	$[kg^{0.5}m^{-0.5}Pa^{-m}s^{-1}]$
$C_i$	Clearness index	$[-]$
$c_n$	Weighting coefficient	$[-]$
$C_p$	Specific heat of a material	$[J\ kg^{-1}\ K^{-1}]$
$cp$	Pressure coefficient	$[-]$
$E$	Incident long wave irradiation flux density	$[W\ m^{-2}]$
$E_v$	Soil evaporation	$[mm\ s^{-1}]$
$E_0$	Evaporation potential	$[mm\ s^{-1}]$
$F_{i,j}$	View of form factor	$[-]$
$FI$	Fluctuation index	$[-]$
$h_c$	Convective heat transfer coefficient	$[W\ m^{-2}\ K^{-1}]$
$h_r$	Radiative heat transfer coefficient	$[W\ m^{-2}\ K^{-1}]$
$I$	Solar irradiance	$[W\ m^{-2}]$
$I_n$	Normal solar irradiance	$[W\ m^{-2}]$
$I_{Dir}$	Direct solar irradiance	$[W\ m^{-2}]$
$J$	Radiosity	$[W\ m^{-2}]$
$K$	Turbulent kinetic energy	$[m^2\ s^{-2}]$
$k_s$	Equivalent roughness height	$[m]$
$L$	Specific latent heat of vaporization of water	$[J\ kg^{-1}]$
$L_{Adv}$	Advection latent heat	$[W]$
$LAD$	Leaf area density	$[m^2\ m^{-3}]$
$LAI$	Leaf area index	$[m^2\ m^{-2}]$
$M^0$	Radiant exitance	$[W\ m^{-2}]$
$m$	Power law exponent	$[-]$
$m_a$	Air mass	$[kg]$
$mfr$	Mass flow rate	$[kg\ s^{-1}]$
$P$	Pressure	$[Pa]$
$P_r$	Precipitation	$[mm\ s^{-1}]$
$P_l$	Latent power generated by systems	$[W]$
$P_s$	Sensible power generated by systems	$[W]$
$Q^*$	Net all wave radiative flux density	$[W\ m^{-2}]$
$\Delta Q_A$	Net advective flux density	$[W\ m^{-2}]$
$Q_E$	Turbulent latent heat flux density	$[W\ m^{-2}]$
$Q_F$	Anthropogenic heat flux density	$[W\ m^{-2}]$
$Q_H$	Turbulent sensible heat flux density	$[W\ m^{-2}]$
$Q_S$	Heat storage flux density	$[W\ m^{-2}]$
$Q_R$	Absorbed net solar and long wave radiation	$[W\ m^{-2}]$
$r$	Specific humidity	$[kg_{water}/kg_{dry\ air}]$
$r_a$	Aerodynamic resistance	$[s\ m^{-1}]$
$r_c$	Crop canopy resistance	$[s\ m^{-1}]$
$RH$	Relative humidity	$[\%]$
$R_{Th}$	Thermal resistance of the building envelope	$[m^2\ K\ W^{-1}]$
$S$	Surface	$[m^2]$
$sf$	Solar factor	$[-]$

$S_l$	Latent heat source	[W]
$S_s$	Sensible heat source	[W]
$T$	Temperature	[K] or [°C]
$u^*$	Friction velocity	[m s <sup>-1</sup> ]
$v$	Velocity	[m s <sup>-1</sup> ]
$V$	Volume	[m <sup>3</sup> ]
$u(z)$	Vertical wind profile	[m s <sup>-1</sup> ]
$v_p$	Vapour pressure	[Pa]
$v_{p^*}$	Vapour pressure at the saturation point	[Pa]
$z_0$	Aerodynamic roughness length	[m]
$z_d$	Zero displacement height	[m]

### Symbols related to the body's energy balance

$C$	Convective heat exchange between air and body surface	[W m <sup>-2</sup> ]
$E_d$	Skin diffuse evaporative heat loss per body surface	[W m <sup>-2</sup> ]
$E_{re}$	Latent heat loss from respiration per body surface	[W m <sup>-2</sup> ]
$E_{sw}$	Skin latent heat loss from regulatory sweating per body surface	[W m <sup>-2</sup> ]
$I_{clo}$	Thermal insulation of clothes	[clo]
$K_{sk}$	Conduction heat transfer through the skin per body surface	[W m <sup>-2</sup> ]
$M$	Metabolic rate	[met]
$R$	Radiative heat exchange between the air and the body surface	[W m <sup>-2</sup> ]
$S_{re}$	Sensible heat loss from respiration per body surface	[W m <sup>-2</sup> ]
$\Delta S$	Heat storage per body surface	[W m <sup>-2</sup> ]
$W$	Mechanical work per body surface	[W m <sup>-2</sup> ]
$\Delta w$	Dehydration or weight loss	[g]

**Indices related to heat stress and strain**

<i>AT</i>	Apparent temperature	[°C]
<i>CO</i>	Cardiac output	[L h <sup>-1</sup> ]
<i>HI</i>	Heat index	[°C]
<i>HR</i>	Heart rate	[bpm]
<i>Humidex</i>		[-]
<i>Oh<sub>max</sub></i>	Maximal overheating	[°C]
<i>Oh<sub>mean</sub></i>	Average overheating	[°C]
<i>OhD<sub>max</sub></i>	Maximal overheating duration	[h]
<i>OhI<sub>max</sub></i>	Maximal cumulative overheating	[°C h]
<i>Ohr</i>	Overheating hours	[h]
<i>dhr</i>	Degree hours	[°C h]
<i>HSD</i>	Heat stress distribution	[%]
<i>HWN</i>	Heatwave number	[-]
<i>HWF</i>	Heatwave frequency	[day]
<i>HWA</i>	Heatwave amplitude	[°C h]
<i>ISI</i>	Indoor Stress Index	[-]
<i>ITS</i>	Index of Thermal Stress	[-]
<i>NET</i>	Net Effective Temperature	[°C]
<i>PPD</i>	Predicted Percentage of Dissatisfaction	[%]
<i>PET</i>	Physiological Equivalent Temperature	[°C]
<i>PHS</i>	Predicted Heat Strain	[-]
<i>PMV</i>	Predicted Mean Vote	[-]
<i>PT</i>	Perceived Temperature	[°C]
<i>SET</i>	Standard Effective Temperature	[°C]
<i>SkinWet</i>	Skin Wettedness	[%]
<i>SkBF</i>	Flow of blood from core to skin	[mL min <sup>-1</sup> m <sup>-2</sup> ]
<i>sw<sub>R</sub></i>	Sweat rate	[g s <sup>-1</sup> ]
<i>UTCI</i>	Universal Thermal Climate Index	[°C]
<i>WBGT</i>	Wet-bulb globe temperature	[°C]

## Greek symbols

$\alpha$	Absorption coefficient	[—]
$\alpha_w$	Wind direction from $x$ in the orthonormal coordinate system	[°]
$\beta$	Evaporation potential weighting coefficient	[—]
$\beta_w$	Wind direction from North	[°]
$\Delta$	Slope of the saturation vapour pressure	[kPa K <sup>-1</sup> ]
$\epsilon$	Long wave radiation emissivity	[—]
$\varepsilon$	Turbulence dissipation rate	[m <sup>2</sup> s <sup>-3</sup> ]
$\Phi$	Heat flux density	[W m <sup>-2</sup> ]
$\lambda$	Thermal conductivity	[W m <sup>-1</sup> K <sup>-1</sup> ]
$\lambda_p$	Pressure loss coefficient	[m <sup>-1</sup> ]
$\mu$	Dynamic viscosity	[kg m <sup>-1</sup> s <sup>-1</sup> ]
$\tau_w$	Solar transmission coefficient	[—]
$\theta$	Volumetric water content	[m <sup>3</sup> m <sup>-3</sup> ]
$\rho$	Density	[kg m <sup>-3</sup> ]
$\rho_{rad}$	Diffuse reflection coefficient	[—]

### Subscripts

<i>a</i>	Air
<i>c</i>	Convective
<i>core</i>	Core
<i>D</i>	Direct
<i>d</i>	Diffuse
<i>dwn</i>	Down
<i>ext</i>	Exterior
<i>F</i>	Sources or sink
<i>g</i>	Black globe
<i>grd</i>	Ground
<i>in</i>	indoor
<i>k</i>	Conductive
<i>L</i>	Latent
<i>mix</i>	Mixing
<i>mrt</i>	Mean radiant temperature
<i>net</i>	Net
<i>out</i>	Outdoor
<i>LWR</i>	Long wave radiation
<i>o</i>	Operative
<i>pred</i>	Predicted
<i>r</i>	Reflected
<i>s</i>	Surface
<i>sk</i>	Skin
<i>sky</i>	Sky
<i>sur</i>	Surrounding
<i>SWR</i>	Short wave radiation
<i>t</i>	Transmitted
<i>up</i>	Up

### Dimensionless numbers

<i>Gr</i>	Grashof number	$\frac{g \beta \Delta T L_c^3 \rho^2}{\mu^2}$
<i>Re</i>	Reynolds number	$\frac{U \times L_c}{\nu}$
<i>Ri</i>	Richardson number	$\frac{g\beta(T - T_{ref})L}{U^2}$
<i>y*</i>	Dimensionless wall unit based on <i>K</i>	$\frac{\rho C_\mu^{1/4} k_p^{1/2} z_p}{\mu}$

**Constants**

$k$	Von Karman constant	0.42
$C_\mu$	RANS model constant	0.09
$C_s$	Roughness constant	
$\gamma$	Psychometric constant	0.063 kPa K <sup>-1</sup>
$\sigma$	Stefan-Boltzmann constant	$5.67 \times 10^{-8} \text{ W m}^{-2} \text{ K}^{-4}$
$g$	Gravitational acceleration	9.8 m s <sup>-2</sup>





# Introduction

## Context: Adapting to urban overheating is an urgent challenge for cities

Human activities contributing to global warming are causing extreme events, particularly heatwaves, to occur more frequently and with greater intensity. Since the 1950s, there has been a significant increase in the frequency, duration, and cumulative heat of heatwaves. Specifically, in the Mediterranean region, the frequency of heatwaves has grown by more than two days per decade (Perkins-Kirkpatrick and Lewis, 2020). These hazards not only increase human society's exposure to changing climate conditions but also escalate the vulnerability of individuals. This reminds us of the importance of climate justice and inter-generational justice, as it highlights how communities least responsible for current global warming are disproportionately affected. Studies have strongly linked increased outdoor temperatures with higher mortality and illness rates (Salagnac, 2007, Zuo et al., 2015). Therefore, exposure to extreme heat presents more than just a comfort problem; it poses a wider health risk.

In cities, the urban heat island (UHI) effect is prevalent due to high building density, increased soil sealing, and human activity. This phenomenon is characterized by higher temperatures than in rural areas and a limited decrease in temperature during nighttime. For example, there's an average annual nighttime temperature difference of approximately 2 to 3°C between Paris and its surrounding rural and wooded areas (Météo-France, 2013). The UHI effect significantly contributes to urban overheating (Su et al., 2021). This urban-specific phenomenon occurs both during the day and night, affecting all levels - from the city as a whole to individual scales. Urban overheating encompasses the urban heat island (UHI) effect and the thermal discomfort experienced by city residents. This term refers to periods of abnormally high temperatures that persist over several days, directly impacting heat exposure and leading to thermal stress for people both indoors and outdoors.

Human health is adversely affected by not just the intensity of this heat but also the frequency and duration of such heat exposure events (Matthies, 2008). These extremes can occur repeatedly throughout the summer season. Therefore, to assess the impact of overheating on health, it is crucial to consider the effects of heat exposure, not just during single heat wave events but throughout the whole summer. Ultimately, health risks from high-temperature exposure are mitigated by adaptive measures taken at individual, community,

and institutional levels (Stocker et al., 2013). Measures such as building cooling strategies or urban greening can directly influence the thermal environment

Despite an expanding climate action movement leading to a consistent reduction in greenhouse gas emissions in 18 countries, including France, global emissions persistently increase. The most recent report from the Intergovernmental Panel on Climate Change (2022), states that public policy frameworks regulate over half of the world's greenhouse gas emissions. There has been progress in formulating public policies for adaptive measures. The IPCC report specifically highlights energy efficiency and demand-side management actions, which are broadly endorsed by society. We also see eco-friendly initiatives at the city level. However, the current speed and scope of these actions and commitments are inadequate to limit the risks posed by climate change.

Recognizing the urgent need to act and prepare for unparalleled climate events, many regions are implementing adaptive and preventative measures. A key part of this adaptation is the system's capacity to stay resilient amid climate changes. In France, local authorities are integrating climate concerns into their territorial planning tools to formulate a long-term strategic vision. This is seen in various public policies like urban planning, housing, transport, health, and socio-economic development, leading to locally targeted actions that suit the urban, social, economic, and environmental context.

In an urban setting, several strategies have been identified to adapt to and counteract overheating. These include greening cities, improving energy efficiency, thermally renovating existing buildings, adopting a bioclimatic construction approach, reducing soil sealing, implementing passive cooling measures, managing water, and considering typomorphology. However, their feasibility in specific local contexts is uncertain. Additionally, it is unclear which of these measures might offer the most benefits in reducing heat exposure.

Planning support tools are increasingly popular among urban planners and building designers for guiding their decision-making process (Zhou, An, and Yao, 2022; ADEME, 2017). These tools use spatialized modelling, which incorporates climate, natural and urban spaces, and socio-economic factors. The models and corresponding tools vary based on the geographical scale under study – be it the city, districts, public spaces, city blocks, or individual buildings.

In this context, we use numerical modelling of physical phenomena to analyze how various urban configurations affect the thermal environment. This numerical method provides the unique benefit of allowing us to test and compare different urban planning or building design hypotheses, an allowance field experimentation may not always provide. However, the challenge here is to develop strong models that can realistically simulate urban configurations (Musy, 2012). For numerical modelling, it is crucial to understand the interactions between climate, the urban environment, and, specifically, buildings. The physical phenomena to include in the model and the level of detail to incorporate are determined by the model's goal and the scale of the study.

---

When assessing the impact of urban planning and building design on heat stress in individuals, it is crucial to consider varying scales of exposure, ranging from city-wide environments to specific buildings.

Individuals and local stakeholders— such as developers, project owners, and public authorities— can most effectively influence their exposure to environmental factors at the level of their homes and their immediate surroundings. Furthermore, considering that people in France spend approximately 80% of their time indoors, as per a 2013 study by the French Ministry of Energy Transition, understanding indoor thermal environments is crucial when evaluating heat stress. The thermal climates within buildings are impacted by outer conditions, especially in urban areas (Peuportier, 2016, Oke et al., 2017). Therefore, it is necessary to examine the interplay between indoor settings and nearby outdoor environments. Ultimately, because urban spaces serve as living environments, there is a need to prioritize thermal comfort.

## Thesis outline

The introduction highlights numerical modelling as a crucial tool for decision-making. It helps illuminate the climatic consequences of choices in urban planning and building design.

## Objectives

Within this framework, this thesis specifically aims to address the following question :

*How to assess daily and seasonal heat stress in the building and its immediate surroundings, considering their mutual interaction?*

The aim of this thesis is to create a numerical model to assess heat stress on a daily and seasonal basis. This model will consider the interplay between indoor and outdoor thermal environments in residences and their immediate surroundings at the block level.

The seasonal period helps study the accumulated heat stress over time. The daily period allows for a more detailed study of intense heat stress incidents. Given the need to account for the diverse outdoor thermal environment, it is justified to adopt a spatial modelling approach..

Two exposure approaches are suggested:

- An Eulerian approach, where heat stress is assessed in regards to a fixed place.
- A Lagrangian approach, where heat stress is assessed in regard to an individual's movements from one place to another. This approach considers the individual ex-

posure, implying a dynamic approach to the heat exposure environment and requires knowledge of the individual's movements.

This thesis is divided into three main sections, aiming to fulfil a specific objective.

The first part involves a preliminary work where are defined heat stress assessment, the modelling requirement, the model problem formulation and the modelling strategy.

The first section encompasses preliminary work, where the heat stress evaluation, model requirements, problem formulation, and strategy are defined. Chapter 1 introduces the concept of heat stress and strain, leading to the selection of a heat stress index and a thermoregulation model for assessing heat strain. Related thermal indices are proposed based on the chosen heat stress and strain indices. Additionally, this chapter also aids in identifying the significant climatic variables for modelling.

Chapter 2 aims to discern and expound upon modelling issues by first providing a comprehensive understanding of the primary principles of urban microclimate. It describes key influencers of urban microclimate and the common indoor and outdoor cooling strategies employed to lessen the effects of overheating. This forms the basis for determining the modelling requirements necessary for both indoor and outdoor heat stress assessment on a daily and seasonal basis. Upon analyzing Building Energy Models (BEMs) and Microclimate Models (McMs), it becomes apparent that there are no existing modelling approaches that adequately meet the identified needs. This realisation prompts an exploration of the modelling issues relevant to this thesis, the identification of accompanying challenges, and the proposal for a modelling strategy to be developed throughout the remaining segments of the thesis.

The second part entails executing the modelling strategy outlined in the first part. Chapters 3 and 4 detail the components of this model and the approach to its validation.

The third part illustrates the results of applying the developed modelling approach to a case study, as detailed in Chapter 5.

## **Part I**

# **Definition of heat stress assessment and modelling issues**



# Chapter 1

## Heat stress and heat strain assessment

This chapter pursues two primary aims. First, it seeks to select an index and thermoregulation model from which a set of indices can be derived to evaluate heat stress and strain. Second, it aims to aid in defining the comprehensive model strategy, to be further developed in subsequent chapters. Crucially, we will examine the sensitivity of the chosen index and thermoregulation model to fluctuations in climatic variables. Our objective is to determine the most impactful climatic variables and establish the most suitable time step for climate-related demands. To accomplish these aims, this chapter:

1. Introduces a comprehensive framework for assessing heat stress and strain, highlighting major environmental and individual factors impacting it.
2. Discusses prevalent heat stress and strain indices and thermoregulation models, including their limitations, to help guide our study's index choice.
3. Recognizes situations where steady and transient indices are advised.
4. Conducts a sensitivity analysis of the chosen index in response to climate variations.
5. Pinpoints relevant climate variables and their relevant time step on the basis of thermoregulation model response to climate variables input.
6. Proposes a range of heat stress and strain indices.

## Contents

---

<b>1.1</b>	<b>Assessment of overheating effects on the human body . . . . .</b>	<b>9</b>
1.1.1	Overheating effects on the human body and its factors . . . . .	9
1.1.2	Heat stress and heat strain assessment . . . . .	11
<b>1.2</b>	<b>Relation between heat stress and heat strain and the main variables affecting their assessment . . . . .</b>	<b>12</b>
1.2.1	Climatic variables . . . . .	14
1.2.2	Behavioural variables . . . . .	16
1.2.3	Physiological variables . . . . .	16
<b>1.3</b>	<b>Indices used to assess heat stress and (indirectly) heat strain . . . . .</b>	<b>17</b>
1.3.1	Indices classification by affecting variables and application scope . . . . .	17
1.3.2	Assessment scales and methods . . . . .	22
1.3.3	Conclusions and limits of heat stress and strain assessment . . . . .	26
<b>1.4</b>	<b>Applicability of steady and transient modelling approaches under different climatic conditions . . . . .</b>	<b>29</b>
1.4.1	Impact of climatic variables evolution within a fixed environment . . . . .	30
1.4.2	Impact of cumulative climatic variables time evolution and displacement dynamics . . . . .	33
1.4.3	Conclusions on the applicability of steady and unsteady models . . . . .	35
<b>1.5</b>	<b>Sensitivity of heat stress and heat strain indices to climatic variables evolution and time step . . . . .</b>	<b>36</b>
1.5.1	Sensitivity analysis of PET to climatic variation . . . . .	37
1.5.2	Impact of input climatic variable time step on physiological variables . . . . .	42
1.5.3	Conclusions on the sensitivity of heat stress and strain indices to climatic time evolution and time-step . . . . .	43
<b>1.6</b>	<b>Selected heat stress and heat strain indices . . . . .</b>	<b>43</b>
1.6.1	Seasonal analysis indices . . . . .	44
1.6.2	Daily analysis indices . . . . .	45
<b>1.7</b>	<b>Conclusions . . . . .</b>	<b>45</b>

---



## 1.1 Assessment of overheating effects on the human body

### 1.1.1 Overheating effects on the human body and its factors

Human health is widely known to be interconnected with climate change (Campbell-Lendrum et al., 2022). In particular, escalating intensities and frequencies of heatwaves pose direct threats to health. Continuous exposure to intense heat can push the human body's thermoregulation beyond its limits, affecting multiple bodily functions and leading to an array of physical ailments such as cutaneous, cardiovascular, respiratory, muscular and neurological diseases (Cheshire, 2016). Left untreated, heat exhaustion can escalate to heat stroke, a potentially deadly condition (Ebi et al., 2021; Cheshire, 2016). Research further strengthens the link between peak outdoor temperatures and the rates of morbidity and mortality during or after heatwave occurrences (Zuo et al., 2015; Salagnac, 2007).

Urbanization impacts the microclimate of residential and work areas by altering radiative, thermal, moisture, and aerodynamic processes. Furthermore, human-induced heat from activities such as transport and energy waste from buildings can increase urban temperatures, as noted by Ebi et al. (2021). This leads to a phenomenon known as the UHI effect, causing cities to be warmer on average than surrounding rural areas.

In relation to exposure to overheating, aside from thermal comfort, the issue of health is pivotal and should be a priority for urban and building designers. According to the World Health Organization (WHO), *a state of complete physical, mental and social well-being and not merely the absence of disease or infirmity* (Santé, 2016).

The effects of overheating on the human body are influenced by both environmental and individual factors. People's responses and perceptions of heat can differ greatly (Parsons, 2002). These two-factor groups are closely interconnected.

Environmental factors, tied to exogenous elements, consist of the exposure context, exposure dynamics, and a community of individuals and institutions engaging with the person in question. These elements can either facilitate or restrict the execution of adaptation responses. The exposure context is defined by local climatic variables and is influenced by the individual's surroundings, such as urban areas, buildings, streets, infrastructure, and vegetation.

Exposure dynamics represent changes in the exposure environment, including climate changes and individual movements. These changes affect how much heat accumulates during exposure and how the body reacts to it.

Individual factors include social, behavioural, psychological, personal attributes, physiological factors and thermal history relative to the individual. Individual factors influencing heat sensitivity include social, behavioural, psychological, personal attributes, physiological elements, and an individual's previous exposure to heat. Social factors encompass socio-economic status, self-care ability, access to heat mitigation facilities, and understand-

ing of heat impacts and prevention. These factors are highly influenced by individual habits and behaviour, which can either mitigate or escalate the risk associated with heat exposure. Examples include activity level, appropriateness of clothing, and substance use. Personal attributes like age, gender, and ethnicity also impact heat sensitivity, as studies reported by Dayi L. et al. (2020). Physiological factors include the thermoregulatory system, metabolism, and existing health conditions like cardiovascular and respiratory diseases, diabetes, heat-related illness, and mental health disorders (Ebi et al., 2021; Cramer and Jay, 2016). Lastly, an individual's thermal history or previous exposure to heat can positively or negatively influence the aforementioned factors. For example, a person's thermal history can impact the heat acclimation process.

The risk-hazard framework portrays both individual and environmental factors (Füssel, 2005). This framework, widely used in risk assessments, helps estimate potential damages from various hazards, including climatic ones. Here, we present the definitions of hazard, exposure, vulnerability, adaptation, and risk as reported by the IPCC (Dokken, 2015):

- Hazard is *the potential occurrence of a natural or human-induced physical event or trend or physical impact that may cause loss of life, injury, or other health impacts, [...]*.
- Exposure is *the presence of people, livelihoods, species or ecosystems, environmental functions, services, and resources, infrastructure, or economic, social, or cultural assets in places and settings that could be adversely affected.*
- Vulnerability is *the propensity or predisposition to be adversely affected [...] encompasses a variety of concepts and elements including sensitivity or susceptibility to harm and lack of capacity to cope and adapt.*
- Sensitivity is *the degree to which a system or species is affected, either adversely or beneficially, by climate variability or change.*
- Adaptation is *the process of adjustment to actual or expected climate and its effects. In human systems, adaptation seeks to moderate or avoid harm or exploit beneficial opportunities.*
- Risk is *often represented as the probability of occurrence of hazardous events or trends multiplied by the impacts if these events or trends occur. Risk results from the interaction of vulnerability, exposure, and hazard.*

Risks can be either reduced or increased by the type of adaptive responses at the exposure or vulnerability level (Campbell-Lendrum et al., 2022).

Considering health risks associated with urban overheating (Figure 1.1), a hazard corresponds to a heat wave occurrence, while the risk refers to health injuries and damage to well-being. Exposure denotes the context and the dynamics of environmental factors. The exposure context must also consider indoor environments, such as homes. Vulnerability, according to the World Health Organization (2015), refers to the predisposition to be affected by overheating. This takes into account personal, psychological, physiological, and social

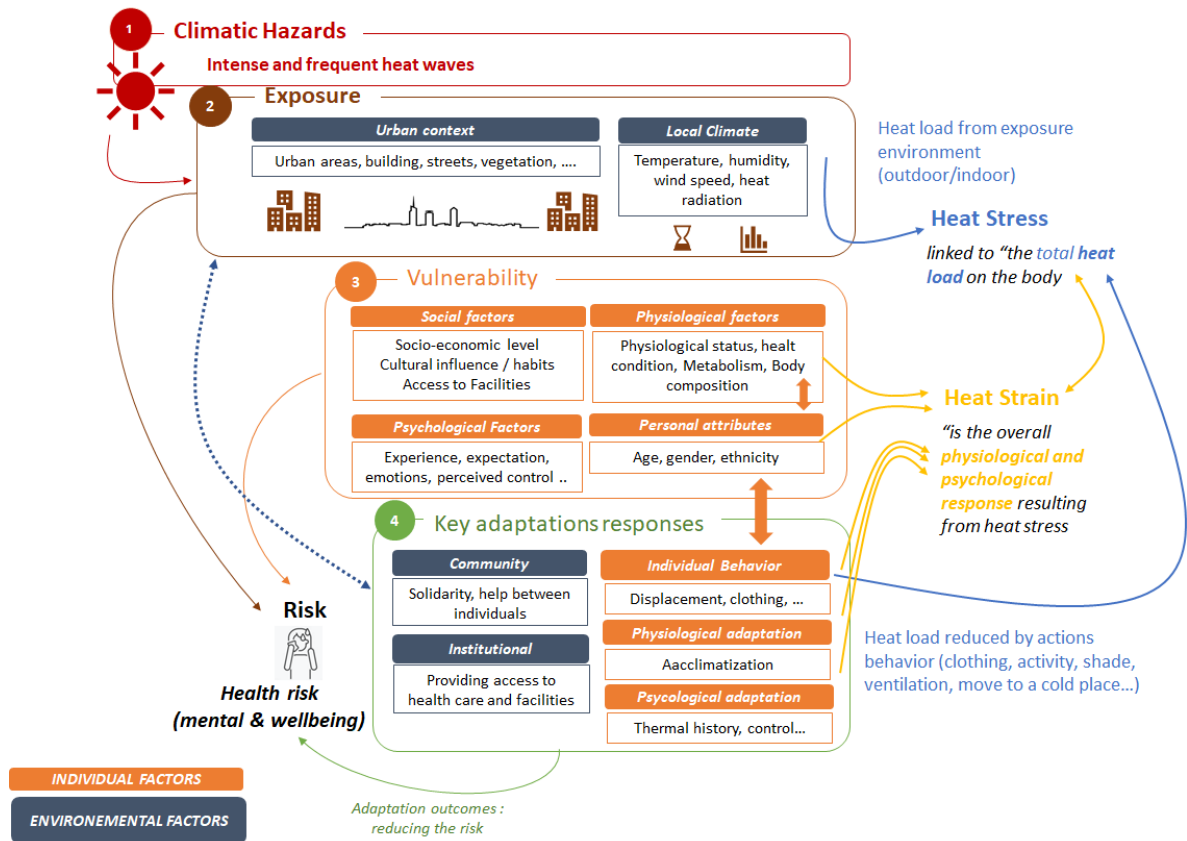


Figure 1.1: Heat stress and heat strain within the risk-hazard framework.

factors. Adaptation, in this instance, refers to the deliberate or incidental responses (like the physiological acclimatization process) that individuals, groups, institutions, and other stakeholders use to mitigate or prevent overheating. This concept involves a community of people and institutions affected by environmental factors, as well as individual behaviour, physiology, and psychology.

### 1.1.2 Heat stress and heat strain assessment

It is within this framework that two assessments of heat effects on the human body can be introduced: the heat stress, referring to "the total heat load on the body imposed by cumulative environmental, physical, and individual factors" (Yang and Chan, 2015) and the heat strain referring "to the physiological and/or psychological consequences of heat stress" (Yang and Chan, 2015).

This global framework outlines different assessments that evaluate the risk of overheating hazards. These assessments include risk, vulnerability, adaptability, heat stress, and heat strain assessment. Heat stress assessment takes into account both climatic conditions and individual factors, whereas heat strain assessment specifically seeks to understand a person's physiological and psychological responses to heat stress.

Heat stress assessment is also employed to evaluate thermal comfort, defined as *a state of satisfaction or neutral temperature sensation which usually occurs when man is primarily in thermal equilibrium and when man is not regulating his body temperature by sweating and by any vascular change* (Fanger, 1970; Gonzalez, Nishi, and Gagge, 1974). In essence, thermal comfort equates to a particular level of heat stress, subject to individual perception.

As outlined in the thesis objectives, this work specifically concentrates on the assessment of heat stress and strain.

## 1.2 Relation between heat stress and heat strain and the main variables affecting their assessment

To understand the relation between heat stress and heat strain, as well as the primary factors influencing their assessment, it is essential to grasp the thermal interactions between the body and its environment, as well as the heat exchange that occurs. The process of human thermoregulation is essential for heat balance. It is a phenomenon where organisms keep their core body temperature ( $T_{core}$ ) within a specified range. The average  $T_{core}$  for humans is approximately 37 °C, yet it can fluctuate between 35 °C and 41 °C (Périard, Racinais, and Sawka, 2015).

The process of thermoregulation encompasses two primary systems, the passive and active (Figure 1.2). The passive system pertains to the body's physical attributes, like insulation and the speed of heat loss to the environment. Body insulation relates to fat content, skin and hair thickness and density. Heat loss rate links to the sensible and latent heat exchange between a body and its surroundings, influenced by the exposed surface area. Temperature signals are delivered to the hypothalamus via peripheral and central thermoreceptors located on the skin. The hypothalamus administers the active system's activation thresholds, which are responsible for regulating various responses. These reactions include vasoconstriction, where blood vessels in the skin constrict, decreasing blood flow and preserving heat. Vasodilation is another response where blood vessels dilate, increasing blood flow and promoting heat loss. Shivering, an involuntary muscle contraction that produces heat, and sweating, a skin response involving sweat evaporation that cools the body, are also activated under these regulatory responses (Zhao et al., 2020).

The passive system typically models heat exchange between the body and the environment using the human heat balance equation, which is based on the following principles:

$$\textit{heat storage in the body} = \textit{heat production} - \textit{heat losses}$$

This equation can also be expressed by the following steady equation, where the terms are expressed in  $[W m^{-2}]$  (Fanger, 1970; Schwede, 2007; Havenith and Fiala, 2015) :

$$M - W - \Delta S - E_d - E_{sw} - E_{re} - S_{re} = K_{sk} = (R + C) \quad (1.1)$$

Where:  $M$ : is the metabolic rate expressed [met]. (Where: 1 met= 52.8 W m<sup>-2</sup>).  
 It represents the heat released from the body per unit skin area and depends on muscular activity (W), environment and physiological factors such as body size and age [W m<sup>-2</sup>]  
 $W$ : is the energy in the human body transformed into external mechanical work [W m<sup>-2</sup>]  
 $\Delta S$ : is the heat storage in the body, adjusted by the thermoregulatory system of the body and expressing the heat strain [W m<sup>-2</sup>]  
 $E_d$ : is the skin diffuse evaporative heat loss [W m<sup>-2</sup>]  
 $E_{sw}$ : is the skin latent heat loss from regulatory sweating [W m<sup>-2</sup>]  
 $E_{re}$ : is the latent heat loss from respiration [W m<sup>-2</sup>]  
 $S_{re}$ : is the sensible heat loss from respiration [W m<sup>-2</sup>]  
 $K_{sk}$ : is the conduction heat transfer from the skin to the outer surface of the clothed body [W m<sup>-2</sup>]  
 $C + R$ : are the convective and radiative heat exchanges between the environment and the body surface [W m<sup>-2</sup>]

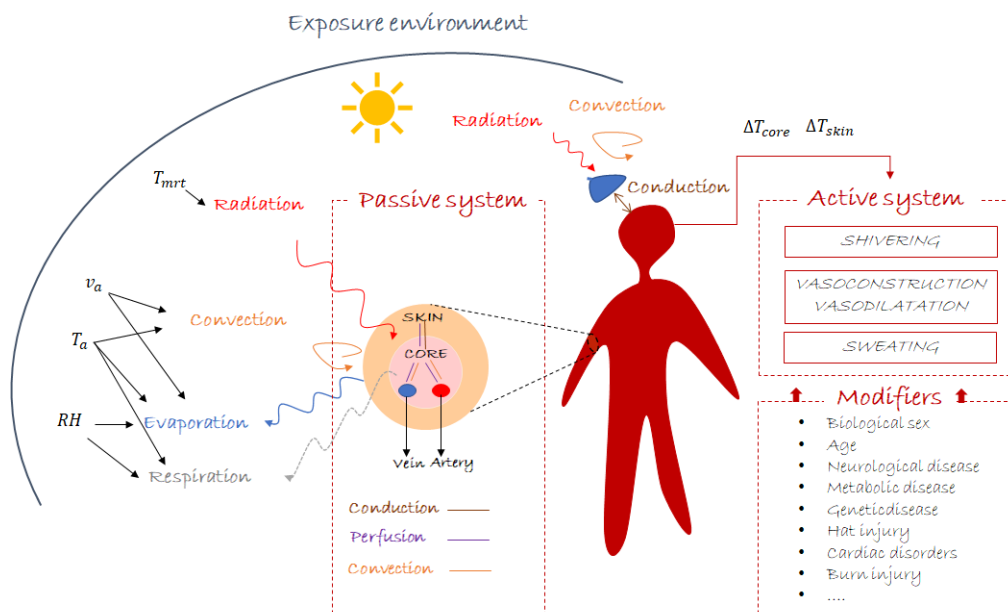


Figure 1.2: Interaction of exposure environment and thermoregulation.

From equation 1.1, it is possible to distinguish the variables involved in heat stress, which are responsible for the heat load on the body ( $K_{sk}$ ,  $R$ ,  $C$ , and  $(M-W)$ ), from those involved in heat strain, which affects the body's response in reducing the heat load ( $\Delta S$ ,  $E_d$ ,  $E_{sw}$ ,  $E_{re}$ ,  $S_{re}$ ).

These variables can be regrouped into climatic variables, being part of environmental determinants and behavioural variables and physiological variables, which are part of indi-

vidual variables.

### 1.2.1 Climatic variables

Within the environmental factors, climatic exposure variables influence the exchange of heat with the body. Climatic variables commonly used in body heat balance models include: air temperature, air humidity, air velocity and radiative flux.

#### 1.2.1.1 Air temperature

The air temperature in the exposure environment ( $T_a$  [°C]) is directly linked to the sensible heat exchanged with the body. This exchange happens through convection and the process of inspiring air. Air temperature is the primary variable influencing heat stress. Numerous studies have recognized  $T_a$  as the crucial parameter for outdoor thermal comfort, contributing approximately 65% to the overall outdoor human thermal sensation (Lai et al., 2020).

#### 1.2.1.2 Air humidity

Air humidity influences the ability of the body to release latent heat by sweating and breathing. It is expressed by the specific humidity (the ratio of the mass of water vapour to the total mass of the moist air parcel  $kg_{\text{water}}/kg_{\text{dry air}}$ ), the vapour pressure ( $v_p$  [Pa]) or the relative humidity ( $RH$  [%]), defined as the  $v_p/v_p^*$ , where  $v_p^*$  [Pa] is the vapour pressure at the saturation point. Humidity is important as it affects heat exchange between the body and the environment by evaporation. The higher the water vapour pressure, the lower the evaporative heat loss will be. High levels of  $RH$  (>80%) combined with high  $T_a$  (> 39 °C) occurring in tropical climates are very dangerous for the human body as the ability to sweat is reduced (Deng et al., 2018) and increases the risk of heat disease. Figure 1.3 illustrates the variation of  $T_{\text{core}}$  within a stationary indoor exposure resulting from the application of a dynamic thermoregulation model from Deng (2018). Figure 1.3 (a) displays the temperature evolution for different values of  $T_a$ , with  $RH = 80\%$  and air velocity  $v_a = 0.1 \text{ m s}^{-1}$  and Figure 1.3 (b) shows the temperature evolution for different values of  $HR$ , with  $T_a = 39^\circ\text{C}$  and  $v_a = 0.1 \text{ m s}^{-1}$ . High values of both  $RH$  and  $T_a$  can result in exceeding the critical core temperature threshold within 3 to 11 hours.

#### 1.2.1.3 Air velocity

Air velocity ( $v_a$  [ $\text{m s}^{-1}$ ]) affects the convective heat exchanges with the body and the body sweating. High air velocity levels lessen heat stress when the air temperature ( $T_a$ ) is below skin temperature ( $T_{sk}$ ). However, the opposite is true when  $T_a$  is greater than  $T_{sk}$ . With regard to thermal sensation, many studies reveal that the impact of wind speed outdoors is minor compared to radiation and  $T_a$ 's effects (Tseliou et al., 2016; Lai et al., 2020). Lai et

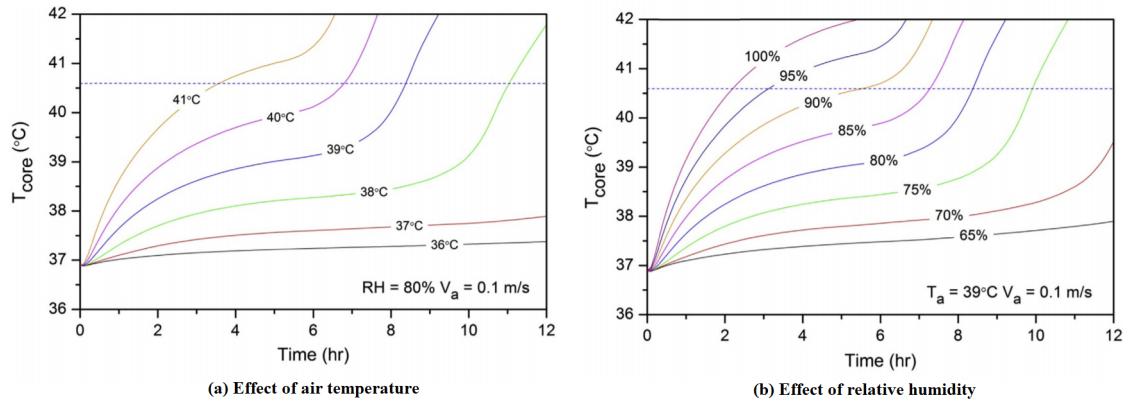


Figure 1.3:  $T_{core}$  evolution for different values of (a)  $T_a$  when  $HR = 80\%$  and  $v_a = 0.1 \text{ m s}^{-1}$  (b)  $HR$   $T_a = 39^\circ\text{C}$  and  $v_a = 0.1 \text{ m s}^{-1}$  (from Deng et al., 2018).

al. (2020) attribute the weak correlation between wind and thermal sensation to the rapid changes in outdoor wind and the challenges in quantifying the effects of its dynamic fluctuations. Lai et al (2017) developed a fluctuation index (FI) to reflect fluctuations in outdoor climatic variables. Their research showed the FI for relative humidity  $RH$  and  $T_a$  was less than 0.05. For global solar radiation, the index was approximately 0.2, and for wind speed, it was near 0.5. Despite this, the authors note that the consequences of wind fluctuations, and more broadly, the influence of varying thermal environments, remain insufficiently researched. Wind direction significantly influences thermal perception. Hadianpour et al.(2019) have observed varying thermal sensations depending on whether one is facing the wind or away from it. Due to the difficulty and expense associated with measuring wind speed and direction changes in varied environments, wind speed is typically gauged at a set height without obstructions. Wind profiles are then used to deduce the wind's velocity, while more intricate details about wind characteristics can be obtained using Computational Fluid Dynamic (CFD) simulation.

#### 1.2.1.4 Radiation flux

Radiative heat exchanges are critical to consider, particularly in fluctuating radiation conditions of different urban outdoor areas. Moreover, heat radiation that the body absorbs is the primary cause of heat stress during sunny summer days (Monteiro, 2005).

Heat radiation is occasionally depicted as the net absorbed solar and long-wave radiation ( $Q_R [\text{W}^2 \text{ m}^{-1}]$ ) or the normal solar radiation ( $I_n [\text{W}^2 \text{ m}^{-1}]$ )(Reynolds, 1982). However, it is commonly expressed through the mean radiant temperature ( $T_{mrt} [^\circ\text{C}]$ ). The  $T_{mrt}$ , as per Fanger (1970) represents the combined thermal effect of all short- and long-wave radiation fluxes reaching the body in one temperature unit. The American Society of Heating, Refrigerating and Air Conditioning Engineers (ASHRAE) defines  $T_{mrt}$  as the *uniform temperature of an imaginary enclosure in which the radiant heat transfer of the human body equals the radiant heat transfer of the actual non uniform enclosure* (Ramspeck et al., 2003a).

### 1.2.2 Behavioural variables

Behavioural variables are impacted by individual and external elements, such as social and environmental factors. The primary behavioural variables that influence heat stress and strain include (Brager and Dear, 1998):

- Body activity: influencing the body heat production corresponding to the metabolic rate ( $M$ ).
- Clothing insulation: influencing the heat transmitted by conduction between the skin and the environment. The thermal insulation effects of clothes ( $I_{clo}$ ) are measured in  $clo$  ( $1clo = 0.155 \text{ m}^2 \text{ K}^{-1} \text{ W}^{-1}$ ).
- Body posture (seated, standing...): influencing the metabolism, clothing resistance, and surface heat exchanges.
- The change of location: influencing the thermal environment really perceived by the body when moving from one environment to another.
- Eating and drinking habits: influencing hydration and metabolism levels.
- Heat reduction actions oriented on the exposure environment: influences the thermal environment by reducing the global perceived heat stress (e.g. using blinds, to open windows when outdoor temperature is lower than indoor one).

ASHRAE Fundamentals (Ramspeck et al., 2003b) provides information on posture, movement to different locations, beverage consumption, heating, metabolic rates for various activities, and  $I_{clo}$  values for different garments

### 1.2.3 Physiological variables

Physiological variables significantly influence heat strain assessment as they determine the responses of thermoregulatory systems to environmental and behavioural stimuli.

Specific clinical and physiological variables that affect these thermoregulatory responses and, therefore, influence the intensity of heat strain include biological sex, age, weight, existing health conditions (such as cardiac, metabolic, or neurological diseases), and the individual's level of acclimation to heat, whether short or long-term.

The physiological variables that reflect the intensity of heat strain can be categorized into three types of strain, as outlined by the World Health Organization (2018) and Cheshire (2016):

- Thermal strain variables: reflecting hyperthermia, heat stroke, etc. e.g.:  $T_{core}$ , skin temperature ( $T_{sk}$ ), heat storage.



- Hydration strain variables: reflecting dehydration, heat exhaustion, etc. e.g., sweat rate ( $sw_R$ ), skin wettedness (*SkinWet*), dehydration rate or weight loss ( $\Delta w$ ).
- Cardiovascular strain variables: reflecting cardiovascular or respiratory morbidity. e.g., Skin blood flow (*SkBF*), representing the flow of blood from core to skin is controlled by thermoregulation; heart rate (*HR*), equal to cardiac output (*CO*) (the blood flow rate in the heart) multiplied by the stroke volume (volume of blood pumped per heart beat); arterial pressure.

Other social and psychological aspects included in the individual determinants (see Figure 1.1) are not directly considered in the classical heat balance approach used to assess heat strain and heat stress but are in some cases considered in the assessment of the thermal perception.

The classic heat balance approach used to assess heat stress and strain does not directly consider other social and psychological variables listed as individual factors (see Figure 1.1). However, in some instances, these variables are taken into account when evaluating thermal perception.

## 1.3 Indices used to assess heat stress and (indirectly) heat strain

This section provides a summary of the primary indices commonly referenced in literature and their corresponding models used to assess heat stress. Since heat stress correlates with heat strain, some assessment models are predicated on heat strain theories. Their usage breadth, evaluation scales, and limitations are also discussed. Following this summary, one index will be chosen for heat stress evaluation and another thermoregulation model for heat strain analysis. The ultimate objective is to create specific heat stress and heat strain indices using this chosen index and model, applicable across seasonal and daily exposure periods.

### 1.3.1 Indices classification by affecting variables and application scope

This sub-section outlines the latest biometeorological indices used to assess heat stress, at times heat strain, and associated thermoregulation models. A comprehensive explanation of these indices can be found in Appendix A.

We can categorize indices into three types: First, those based solely on climatic exposure variables; second, those derived from empirical regression models considering climatic exposure variables, as well as some behavioural and physiological variables; and third, those grounded in human thermal balance, taking into account climatic exposure variables and some behavioural and physiological variables. These categories are further discussed in Section 1.4).

Rational indices take into account various climatic variables that impact human thermal

perception offering a more comprehensive and precise measure of thermal comfort than basic climatic variables, such as ambient temperature ( $T_a$ ). The operative temperature ( $T_o$ ), a significant component of these indices, is commonly used for indoor environments, as attested by Herrington, Winslow, and Gagge (1937), and mandated in ASRHAE Standards outlined by Ramspeck et al. (2003a). One significant drawback of this approach is that it does not take the effect of humidity into account. During a heatwave, other indices more suited to assessing indoor heat stress are used. These include the Overheating Hours (Ohr), which counts the hours when the perceived indoor temperature (e.g.  $T_o$ ) exceeds a certain limit, and the Degree Hour (dhr), which measures the intensity of overheating (Hooff et al., 2015). There are also various outdoor heatwave indices available, such as the Heat Wave Number (HWN), Frequency (HWF), Duration (HWD) and Amplitude (HWA) (Amengual et al., 2014).

Empirical indices are based on objective and subjective strain response data obtained from individuals and groups of individuals exposed to a combination of climatic, metabolic and clothing conditions. They typically consider climatic factors, such as  $T_a$ , humidity,  $v_a$ , and solar radiation, and they may also consider physiological factors, such as thermal strain variables, hydration variables, and heat loss. As based on regressions models, they are applicable only to specific climatic ranges corresponding to the experimental setting used to build up the model. These indices are currently used by meteorologists, working institutions or public administrations to assess risks related to heat stress. Within these indices, the most current for outdoor heat stress assessment are the Net Effective Temperature (NET) (Li and Chan, 2000), the Apparent temperature (AT) (Steadman, 1984), and its hot version, the Heat index (HI) and the wet-bulb globe temperature (WBGT) (Yaglou and Minard, 1957). For indoor heat stress assessment, it is possible to cite the Indoor stress index (ISI) (Deng et al., 2018). For both indoor and outdoor assessments, it is possible to cite the Humidex (Masterton and Richardson, 1979) and the Predicted Heat Strain (PHS) index (ISO7933, 2004). Indices based on energy balance models are widely utilised in building and urban design. These models range from steady single-segment and single-node body energy balance to complex transient multi-segment and multi-node thermoregulation models. Such models consider the interaction between passive and active thermoregulation systems. Within these indices, a distinction can be made between ones based on thermal load models and those based on equivalent temperatures. The former includes indices like the Index of Thermal Stress (ITS) (B., 1963), Predicted Mean Vote (PMV), Predicted Percentage of Dissatisfaction (PPD) (Fanger, 1970), and perceived temperature (PT) (VDI, 1998). These indices utilise a thermal load to set the index level.

On the other hand, the group, based on an equivalent temperature, provides an output that is easier to interpret. For example, the Standard effective temperature (SET\*) is derived from the two-node thermoregulation Gagge steady model (1937). Similarly, the Physiological Equivalent Temperature (PET) is derived from the two-node MEMI steady model (Höppe, 1993; Höppe, 1999b), and the Universal Thermal Index (UTCI) is a result of the multi-segment transient Fiala thermoregulation model (Fiala, 1998), along with an adaptive

clothing model.

The choice of the heat stress index that will be used in the rest of the work, the following criteria will be observed:

- The type of assessment: the main purpose of the index is to assess heat stress. Heat strain assessment will be secondary.
- The applicability domain: what is sought is an index that can be used both indoors and outdoors, and over a range of temperatures, humidity and wind speeds corresponding to the values observed indoor and outdoor during the summer season.
- The comprehensiveness of climatic and individual variables affecting heat stress.

For easier analysis, we have categorized the aforementioned indices in Figure 1.4 according to specific criteria. This analysis utilises a selection of the most frequently cited indices, as determined by various literature reviews (Monteiro, 2005; Lai et al., 2020; Katić, Li, and Zeiler, 2016; Santos Nouri et al., 2018; Feng et al., 2022; Ioannou et al., 2022). A detailed explanation of these indices can be found in Appendix A.

Few indices effectively cover both indoor and outdoor environments. These include the ITS, which only considers climatic variables, as well as the SET and PET, which also account for physiological variables. Among them, PET stands out with its broader application range and higher sensitivity to climatic variables, making it the best choice for further analysis. The outcome provided by PET is an equivalent temperature, which is useful in evaluating heat stress.

The thermoregulation model from which PET is derived can determine key heat stress parameters: core temperature ( $T_{core}$ ), skin temperature ( $T_{sk}$ ), and skin humidity. The idea is to identify the temperature of a reference environment that would cause the same physiological response in  $T_{core}$  and  $T_{sk}$  as the environment being studied. This reference environment is characterized by an indoor setting with wind speed  $v_a = 0.1 \text{ m s}^{-1}$ ,  $RH = 50\%$ , and air temperature ( $T_a$ ) equalling mean radiant temperature ( $T_{mrt}$ ). The metabolic rate is determined by activity (80 W) and metabolism, which is dependent on age, gender, and individual physical attributes. Clothing insulation ( $I_{clo}$ ) is set to 0.9 clo (Figure 1.5). Figure 1.5 also presents an electrical illustration of thermal exchanges in a two-node thermoregulation MEMI model from which PET is derived.



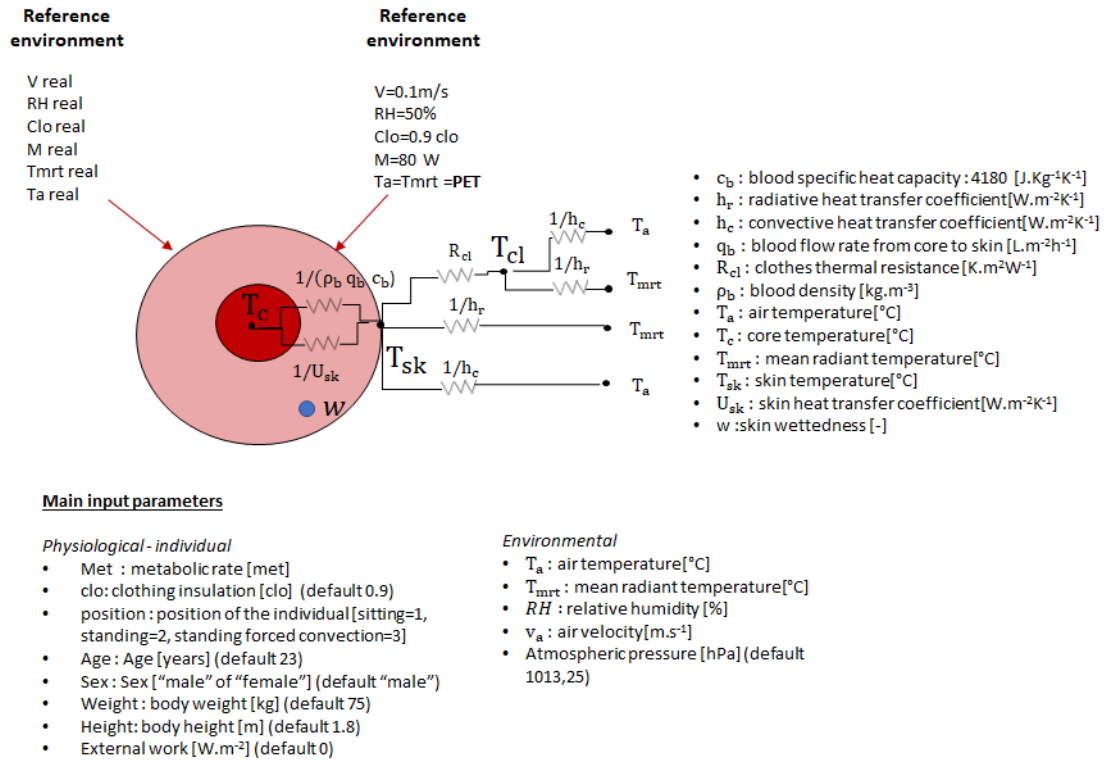


Figure 1.5: PET concentric two node ( $T_{core}$  and  $T_{sk}$ ) model representation and main input variables (adapted from Walther and Goestchel, 2018).

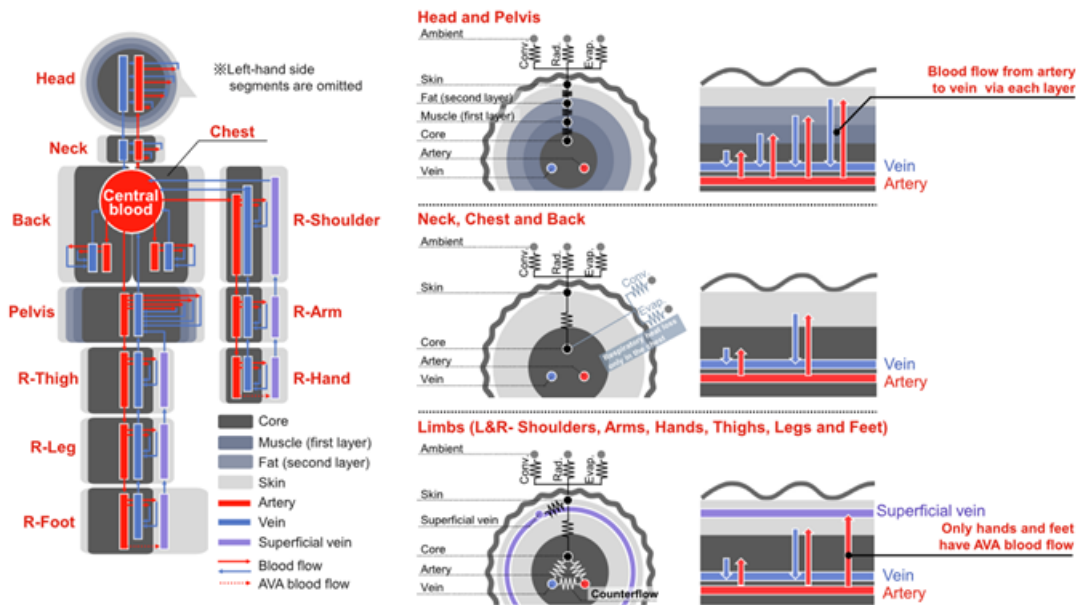
Please note that aside from the PHS, all indices discussed in this section, including the PET, are applicable under steady conditions. This signifies that they do not factor in dynamic physiological responses, instead focusing on steady-state values.

To account for the dynamic reactions of thermoregulatory systems, it is recommended to use transient human thermoregulation models rather than their steady counterparts. The Joint System Thermoregulation model (JOS-3) (Takahashi et al., 2021), is particularly suited for transient conditions. The model's validity was confirmed by comparing its predictions with actual human tests under constant and variable conditions. This model will be utilised to analyze transient body responses in this chapter.

JOS-3, like its predecessors JOS and JOS-2 (Kobayashi and Tanabe, 2013), is based on the Stolwijk model (1971). It employs 17 simplified segments to depict the entire body, including the head, neck, chest, pelvis, shoulders, arms, hands, thighs, legs, and feet. Each segment comprises distinct layers and blood pools. Notably, the limb segments feature a detailed vascular system (Figure 1.6). The vascular system comprises superficial veins and arteriovenous anastomoses (AVA). Figure 1.6 visually depicts the heat interaction between the body's core, skin, and external environment, labelled as "Ambient." The model incorporates thermoregulatory processes such as vasoconstriction, vasodilation, sweating, and shivering. JOS-3, incorporating a total of 83 nodes, leverages the backward difference method to estimate human physiological responses and body temperatures. It incorporates factors such as activity in brown adipose tissue, ageing effects, and heat from solar radiation to forecast in-

dividual reactions under varying thermal conditions. The model generates over 40 thermal and physiological variables indicative of thermal, hydric, and cardiac strain, for instance, core and skin temperature, water loss, and CO, among others. It improves upon JOS-2 by providing modifications for determining shivering thermogenesis, sweating distribution, and basal metabolic rate.

Coded in Python 3, JOS-3 is available through the pythermalcomfort library. Users can customise the model’s parameters, including height, weight, sex, age, body fat percentage, basal metabolic rate, and cardiac index.



**Main input parameters**

- Height : body height [m] (default 1.72)
- Weight : body weight [kg] (default 74.43)
- Fat : Fat percentage [%] (default 15)
- Age : Age [years] (default 20)
- Sex : Sex ["male" or "female"] (default "male")
- Ci : Cardiac index [L/min/m<sup>2</sup>] (default 2.6432)

Figure 1.6: JOS-3 Model concept (form Takahashi et al., 2021) and main input parameters.

As heat strain variables are not directly output by the PET index, the JOS-3 model will be used in further work to calculate heat strain outputs.

**1.3.2 Assessment scales and methods**

**1.3.2.1 General assessment principles**

As outlined in Section 1.1.1, individual responses to heat stress vary. The indices in Section 1.3.1 can guide evaluations on two fronts: thermal comfort perception and degree of physical stress. Thermal comfort perception encompasses both physiological and psychological

elements (Hoppe, 2002). Physiological variables can be objectively measured or modelled through thermoregulation models. However, evaluating psychological variables which pertain to subjective comfort levels presents a challenge.

Different approaches can be used indistinctly or combined to assess heat stress or heat strain. For heat stress assessment, perceived heat-based approaches or climate event-based approaches are generally used. Perceived heat-based approaches use human feedback on individuals' perception of discomfort. Correlations between perceived feelings and climatic data, and in some cases physiological data, are used to establish an assessment scale (e.g. PET, SET, PMV, PDD). Climate event-based approaches fix the level of heat stress by comparing evaluated weather conditions to historical climate data (e.g. NET, AT). For heat strain, medical and physiological data-based approaches are generally used and correlations are established between physiological variables' values and environmental climatic data.

In most of the cases, scales refer to both individual perception and physiological variables reflecting heat strain intensity. This is done through two methods:

- Deterministic: using physiological models to calculate the physiological variables (ex. PET, SET, UTCI, PMV...).
- Empiric: assessing heat stress from environmental data and assuming a relationship between heat strain and heat stress (ex. WBGT, Humidex...).

#### 1.3.2.2 Adjustments of the assessment scales to better consider individual specificity

Among individual factors affecting heat stress and corresponding heat strain, alliesthesia and adaptation have been in some cases considered by in defining comfort scales.

**Alliesthesia**, a term coined by Cabanac (1971; 2020), refers to the perception of an external stimulus as either pleasant or unpleasant, contingent on internal bodily signals. If these external factors decrease the departure from the individual's internal regulatory set point, the sensation is deemed pleasant. Dayi Lai (2020), Dear (2011) and Parkinson (2016) attribute these internal signals to anthropometric processes, specifically disparities between core and skin temperature or spatial-temporal variations in skin temperature. This theory is widely employed to interpret patterns noticed in indoor and outdoor thermal comfort studies. For instance, Beacker et al. (2003) observed that even minimal cooling during a span of heat stress exposure could evoke comfort feelings, an occurrence explicable via temporal alliesthesia (Lai et al., 2020). Schweiker et al. (2020), Lai et al. (Lai et al., 2014), and Yao et al. (2018) also reported seasonal alliesthesia. During cold months, a slightly warm thermal sensation was considered the most comfortable; conversely, in warm months, a slightly cool sensation was deemed the most pleasant.

**Adaptation** refers to three notions:

- Behavioural adaptation: is associated with an individual's behaviour aimed at improving their thermal condition, for example by acting on clothing, diet, physical activity, or transportation Lai et al., 2020.
- Physiological adaptation: linked to the body's adaptation to a given exposure environment. In this context, it is possible to distinguish short-term body acclimation, appearing over one (Peeters et al., 2009) to six weeks (WHO, 2015) of overheating exposure and disappearing after 8 to 12 days of non-exposure, from long-term body acclimation occurring over several years.
- Psychological adaptation: is linked to individual conditioning and influenced by factors such as the ability to control one's thermal environment, social norms, and previous thermal experiences (Lai et al., 2020).

Numerous studies have shown the positive effect of individual adaptation on thermal comfort perception (Carlucci et al., 2018). According to adaptive theories, individuals perceive optimal temperatures as higher in the summer and lower in the winter. This adaptive effect, if not accounted for in the index model, can be reflected in the assessment scale by adjusting the threshold values. This is seen in the WBGT assessment scale, as well as standards like ASHRAE or European EN, which use adaptive comfort models to predict optimal indoor temperature ranges for comfort. The development of adaptive comfort theories helps to consider this adaptive component for indoor thermal comfort. These theories suggest that the ideal indoor temperature for occupants who can interact with the building is linked to the outdoor climatic conditions. This correlation is usually represented by a linear equation:  $T_o = a.T_{outR} + b$ . In this equation,  $T_o$  is the indoor operative temperature, adjusted based on the reference outdoor temperature  $T_{outR}$  and  $a$  and  $b$  are model parameters statistically modified using data from on-site studies.

Different approaches exist to calculate  $T_{outR}$ . The adaptive model of Humphreys (Carlucci et al., 2018; Humphreys, 1978) suggests using the monthly average of  $T_a$ , while the Dear Berger model (Dear and Brager, n.d.) uses the equivalent temperature (ET) in the final report ASHRAE RP-884. However, in 2004, the SSPC55 committee of ASHRAE finally retained the approach consisting of monthly averaging of  $T_a$ . In 2013, ASHRAE evolved its adaptive model by taking as  $T_{outR}$  the prevailing mean outdoor temperature, based on no fewer than seven and no more than 30 sequential days prior to the day of interest. Two acceptability ranges of 80% and 90% are proposed for the neutral indoor temperature ( $T_n$ ) as shown in Figure 1.7.

This model is only suitable for external temperatures ranging from 10°C to 33.5°C. As per the standard, active air conditioning systems are presumed to be operational at higher temperatures, operating based on the comfort parameters outlined by the Fanger model. Other thermal comfort standards, such as the European standard EN 15251, the Dutch standard ISSO74, and the Chinese standard GB/T 50785 (since 2012), also incorporate this adaptive approach. However, they are not valid when external temperatures rise above 30°C for



EN15251 and GB/T50785 and 25°C for ISSO74.

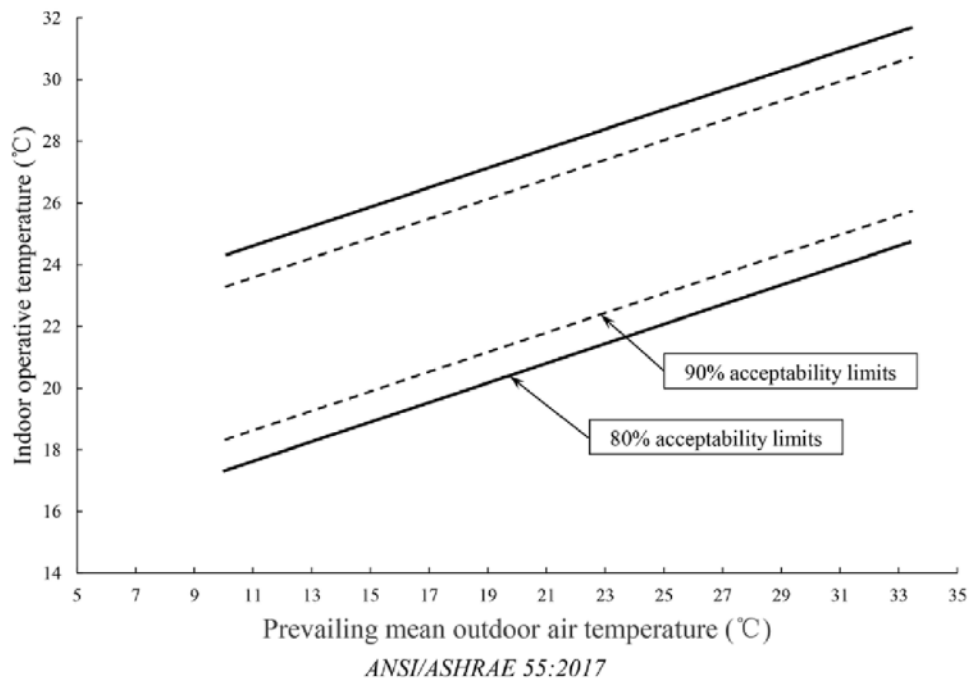


Figure 1.7: Adaptive comfort model of ANSI/ASHRAE 55:2017.

In conclusion, current adaptive models are inadequate for this project as their validity range does not include temperatures above 33.5°C, which can occur during hot summers. This restricts the evaluation of heat stress across multiple days of intense heat exposure.

### 1.3.2.3 Some heat stress assessment scales

The PET assessment scale used in this thesis is shown in Table 1.1. Adapted for a continental climate zone, it does not directly account for individual adaptation or the alliesthesia effect (Zare et al., 2018). A separate study assessing individual and local variables of the exposure area and observation period would be necessary to consider these three adaptive dimensions. Zare et al. (2018) found a strong correlation between the UTCI, PET, and other thermal indices (SET, PMV) in a study comparing the UTCI index with other thermal indices. This implies that despite the PET using a simpler thermoregulation model than the UTCI, predictions of thermal stress align closely with UTCI outcomes. Table 1.1 also includes a comparison of four index assessment scales. These indices cannot be used interchangeably due to differing ranges of applicability (Section 1.3.1); however, a comparison could be feasible within overlapping applicability ranges.

Table 1.1: Thermal perception and grade of thermal stress for various biometeorological indices adaptation of Zare et al., 2018.

PMV	SET	PET	UTCI	Thermal perception	Grade of thermal stress
-	[°C]	[°C]	[°C]		
		<4	<-40	Very cold	Extreme cold stress
			-40 to -27		Very strong cold stress
-2.5		4-8	-27 to -13	Cold	Strong cold stress
-1.5	<17	8-13	-13 to 0	Cool	Moderate cold stress/Moderate hazard
-0.5		13-18	0 to 9	Slightly cool	Slight cold stress
0	17-30	18-23	9 to 26	Comfortable	No thermal stress/ No danger
0.5		23-29		Slightly warm	Slight heat stress
1.5	30-34	29-35	26-32	Warm	Moderate heat stress/Caution
2.5	34-37	35-41	32-38	Hot	Strong heat stress/Extreme Caution
			38-46		Very Strong heat stress
3	>37	>41	>46	Very hot	Extreme heat stress/Extreme danger

#### 1.3.2.4 Some physiological thresholds to assess heat strain

This paragraph discusses thresholds from medical literature related to key parameters of heat strain used in thermoregulation models. It represents the three types of heat strain: thermal, hydration, and cardiovascular.

Table 1.2 outlines various assessment scales for physiological variables used in the JOS-3 thermoregulation model. These include  $T_{sk}$ ,  $T_{core}$ ,  $sw_R$  and  $SkinWet$ , which represent the percentage of the skin's wet surface area, a key factor in thermal behaviour during exercise and recovery (Vargas et al., 2018). Another major variable is the cardiac output ( $CO$ ) - the volume of blood the heart pumps per minute, which significantly impacts the body's total blood flow. These physiological variables serve as indicators for evaluating heat strain in this study.

Please note that authors and objectives determine limits, and only some thresholds are included here. Individual factors such as age, sex, activity, and acclimatization also influence tolerance thresholds. For instance, soccer players have been observed to reach a core temperature ( $T_{core}$ ) of 41.9°C during physical activity without any adverse health effects. However, heat injury or even death has occurred in individuals running less than 10km at  $T_{core}$  temperatures below 40°C (NIOSH, 2016).

### 1.3.3 Conclusions and limits of heat stress and strain assessment

The models and indices outlined in this section provide insight into heat stress and strain, factoring in climatic elements that affect thermal stress along with some behavioural and physiological aspects. However, it is noteworthy to mention certain limitations associated with these indices and models.

**The inability of steady indices to assess heat stress and strain in changing exposure environments:** Indices rooted in steady thermoregulation models are not suited for brief ex-

Table 1.2: Heat strain variables threshold.

Strain	Threshold	Assessment	Reference
Thermal:			
$T_{core}$	Mean increase 0.8°C Mean increase 1°C $T_{core} = 38°C$ $38.5°C > T_{core} < 39.5°C$  $T_{core} > 40.5°C$	Danger Alarm Fatigue Heat exhaustion  Heat stroke	Nag, Nag, and Ashtekar, 2007  Brake, 2002 Hanna and Tait, 2015 Gonzalez, Halford, and Keach, 2010 Cheshire, 2016
$T_{sk}$	$35°C > T_{sk} < 33.9°C$	Heat stress	(ACGIH <sup>(*)</sup> RELS <sup>(**)</sup> )
Hydration:			
$sw_R$	$\geq 12\%$ of the body weight average loss : 0.06L/h (1.5L/day)	Chock	Loutan and Chappuis, 2002 Loutan and Chappuis, 2002
<i>SkinWet</i>	[0.06-1]		Vargas et al., 2018
Cardiovascular:			
CO	$4 < CO < 8$ L/min $CO > 10$ L/min	Normal Heat stress	Sawka and Pandolf, 1990 Montain and Coyle, 1992 Ganio et al., 2011

(\*) American Conference of Governmental Industrial Hygienists

(\*\*) Recommend exposure Limits

posure duration, shorter than the time required for the core temperature ( $T_{core}$ ) and skin temperature ( $T_{skin}$ ) to achieve equilibrium. The time constants vary when the body transitions from a cold to a warm environment and vice versa. Höpfe (2002) evidenced that time constants take longer when shifting from a neutral to a cold environment compared to transitioning from a neutral to a hot environment. Consequently, assessing heat stress in dynamic exposure environments and overall heat strain necessitates a dynamic approach to tracking changes in physiological parameters.

**The limitations of transient models for gauging long-term exposure effects:** The health implications of prolonged heat exposure are largely unknown. The American National Institute for Occupational Safety and Health emphasizes the heightened sensitivity to chronic heat exposure of individuals, especially those undergoing treatment that could potentially conflict with the effects of heat exposure, particularly on blood pressure (NIOSH, 2016). The World Health Organization also spotlights the role of human acclimatization to heat in evaluating the health consequences of heat effects<sup>1</sup>. However, existing thermoregulation models fail to take into account the long-term impacts of climatic exposure to hot environments. As such, these transient thermoregulation models are not suitable for assessing long-term heat stress and strain.

**Thermoregulation models and indices do not account for individual differences:** They gauge heat stress and strain based on an average, young, healthy man. This standard neglects a broad range of the population, specifically individuals who are more vulnerable to heat, such as children and the elderly. A study by Clusiault (2022) found that 82% of the

<sup>1</sup><https://www.who.int/news-room/fact-sheets/detail/climate-change-heat-and-health>

subjects in heat stress studies using physiological parameters were male. Among them, 78% were aged between 21 and 29 years. Furthermore, these models disregard social-related factors. They may occasionally factor in psychological and behavioural variables using adaptive modelling, but these are largely based on statistical field data and correlations with outdoor temperature changes rather than explicit representations of psychological and behavioural aspects.

**Assessment scales do not account for individual differences:** Such scales derive from a baseline healthy population, excluding vulnerable individuals and rendering these scales non-generalizable to this group. Additionally, they are grounded in outdated studies that fail to mirror the current physiological state or the ongoing climate changes. More succinctly, assessment scales need to recognize the unique climate conditions of the regions where they are applied.

In summary, due to numerous factors and their intricate interactions, evaluating heat stress and strain cannot be simplified to a single index. While indices are helpful in identifying potential heat stress or strain, they cannot be used in isolation. This is especially the case when evaluating heat stress for a person rather than a place. Such assessments need to consider individual specificities for a more accurate analysis.

The aim of this study is to select the most suitable index that effectively captures the impact of climate and individual differences on indoor and outdoor heat stress and strain assessments for daily and seasonal exposure periods.

Biometeorological indices are ideal for heat stress assessment as they are designed to provide an accurate measure of heat stress level. The PET index stands out among the rest because it evaluates both indoor and outdoor heat stress. It takes into account all the essential climatic parameters and is suitable for a wide variety of climatic conditions. Furthermore, PET employs a thermoregulation model to consider the interaction between the body and its surroundings. However, it should be noted that these interactions are evaluated under steady-state conditions.

The next step involves determining the exposure conditions under which the use of the steady PET index is acceptable and when it is preferable to assess heat stress based on a transient thermoregulation model. This will be explored in the subsequent Section (1.4).

Physiological variables are crucial to assessing heat strain. Thermoregulation models are especially suitable for this as they generate relevant physiological outputs. Among these models, JOS-3 seems to be a favourable choice, employing a transient approach that more accurately mirrors the dynamic responses of physiological variables. This model is also conveniently accessible through the thermal comfort python library. However, like all current thermoregulation models, JOS-3 is only valid for short-term exposure, limiting its utility in this work to daily heat strain assessments. Consequently, heat strain analysis should be confined to a daily basis.

## 1.4 Applicability of steady and transient modelling approaches under different climatic conditions

The previous section highlights that no single index can fully account for the myriad factors involved in heat stress and strain. Even indices based on advanced thermoregulation models designed to replicate the body's heat stress response have their shortcomings. Specifically, steady indices only show the stabilized core and skin temperatures at specific climatic conditions, overlooking the time response of the thermoregulatory system. The slow-evolving  $T_{core}$  can be either overestimated or under-estimated based on whether the body's temperature transitions from cold to hot or vice versa. This can result in either an overestimation or underestimation of the health risks and heat strain linked to the  $T_{core}$ . A demonstration of  $T_{core}$  evolution trends using the JOS-3 thermoregulation model can be found in Appendix B. Consequently, indices rooted in steady models are generally recommended for uniform, stationary environments. Conversely, indices based on transient models are advised for dynamic exposure environments. However, in situations where the exposure environment changes slowly, steady indices may adequately represent an average of heat stress and strain.

This section aims to determine the circumstances under which a steady or transient approach should be used for heat stress assessment via PET. This will be evaluated by comparing the PET output from physiological variables ( $T_{core}$  and  $T_{sk}$ ) calculated under both steady and transient conditions.

The MEMI model utilised in the PET provides a constant output, making it unsuitable for calculating both stationary and fluctuating  $T_{core}$  and  $T_{sk}$  values. So, we switch to the JOS-3 model to obtain these values under both conditions. We then use the PET to assess the impacts of the varied  $T_{core}$  and  $T_{sk}$  values, as determined by the JOS-3 model, in evaluating heat stress. It is important to remember that the JOS-3 model yields different steady-state  $T_{core}$  and  $T_{sk}$  values compared to the MEMI model. Therefore, to ensure integrity in our data comparisons, we consistently use the JOS-3 model for both steady-state and transient calculations.

The dynamic of the exposure environment can be represented as the result of two dynamics:

- The time evolution of the climatic variables within a specific fixed environment.
- The displacement dynamic through the different fixed environments is experienced by the individual as he moves from one environment to another.

These two dynamics will be studied as follows: firstly, the climatic variables' time evolution within a fixed environment will be observed. Secondly, the combination of the climatic variables time evolution and displacement dynamics will be observed.

### 1.4.1 Impact of climatic variables evolution within a fixed environment

This section examines the impact of changing climatic variables ( $T_a$ ,  $T_{mrt}$ ,  $RH$  and  $v_a$ ) on heat strain in a consistent exposure environment, as measured by changes in  $T_{core}$  and  $T_{sk}$ . The study measures the effects using both steady and transient approach and investigates the resulting influence on heat stress assessment. Our focus is on outdoor environments, where climate variables tend to fluctuate more rapidly than indoors.

Weather data measurements, taken from a weather station located in the Lyon Confluence urban area at a height of 10 m and without notable obstructions, are utilised to determine the distribution of changes in climatic variables ( $\Delta T_a$ ,  $\Delta T_{mrt}$ ,  $\Delta RH$ ,  $\Delta v_a$ ) over an hour during summer. This data was visualized using a box plot (Figure 1.8).

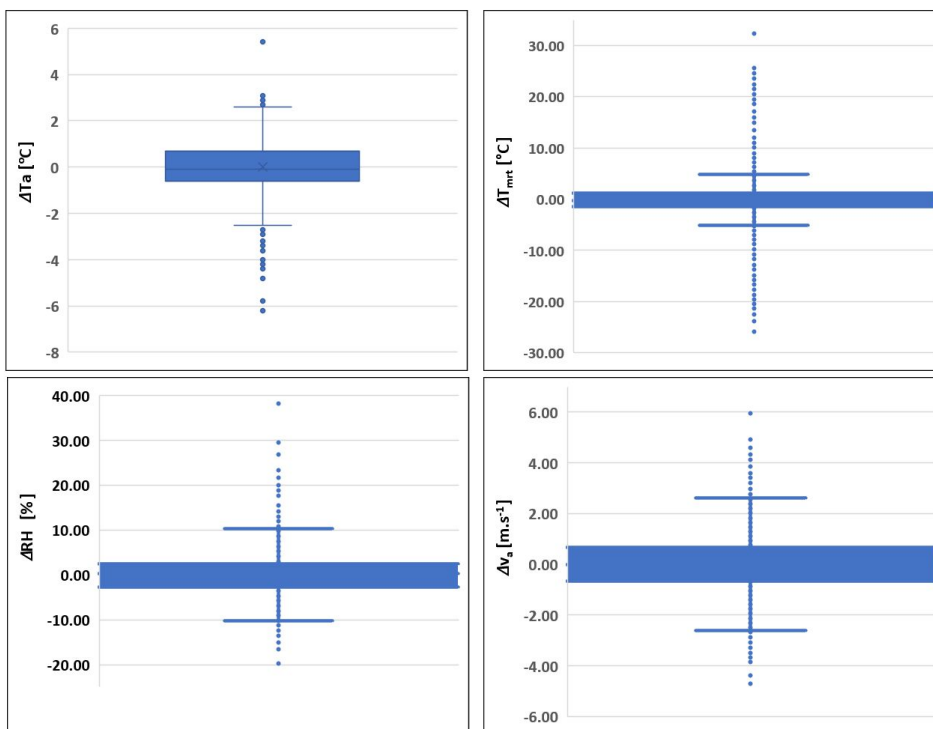


Figure 1.8: Hourly variation of climatic variables  $T_a$ ,  $T_{mrt}$ ,  $RH$ ,  $v_a$  (Lyon Confluence Weather file).

The choice of a one-hour timeframe is due to the fact that weather data are currently provided in hourly intervals. The appropriate timescale for climatic data will be discussed in Section 1.5. As depicted in Figure 1.8, the hourly changes in climatic variables typically fall within the following ranges:  $\pm 2.6$  °C per hour for air temperature ( $T_a$ );  $\pm 5.4$  °C per hour for mean radiant temperature ( $T_{mrt}$ );  $\pm 2.5$  m s<sup>-1</sup> per hour for wind speed ( $v_a$ ); and  $\pm 10\%$  per hour for the relative humidity ( $RH$ ). These ranges are generally consistent, except in certain specific situations. During the entire summer period, deviations beyond these ranges do not exceed 20%.

Figure 1.9 portrays the variations in  $T_a$ ,  $T_{mrt}$ ,  $RH$  and  $v_a$  (both curves and hourly fluctu-

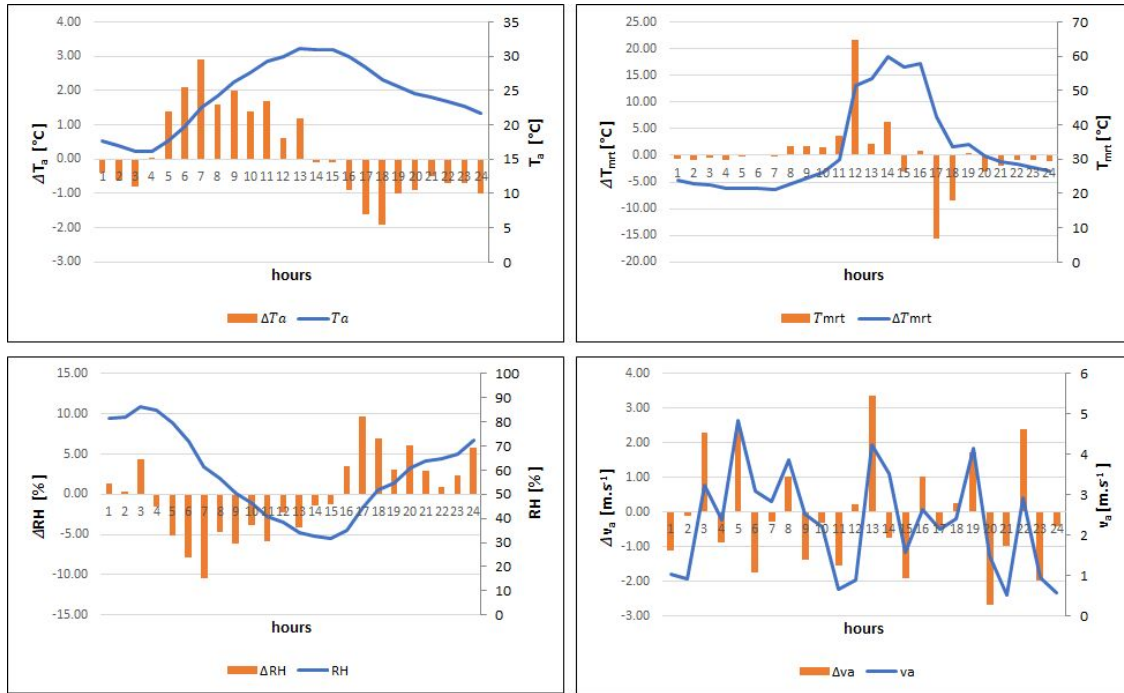


Figure 1.9: Example of  $T_a$ ,  $T_{mrt}$ ,  $RH$ ,  $v_a$  a typical summer day (Lyon Confluence Weather file and computation of the  $T_{mrt}$  based on 4.5.1 model).

ations) on a typical August summer day, with particular focus on the 8th. It reveals that the peak hourly variations for  $T_a$  coincide with sunrise and sunset. For  $T_{mrt}$ , peak occurrences are around noon and during sunset, given there are no obstacles in the analyzed area. The  $RH$  and  $v_a$  values occurring out of range are not affixed to any specific timeframe. Furthermore, it should be noted that the  $v_a$  values and variations pertain to the weather station; they do not accurately represent their real corresponding levels at the pedestrian level. For the sake of analysis,  $v_a$  is kept constant at  $0.1 \text{ m s}^{-1}$ .

Based on weather data, a potential scenario for the change in climate variables during the exposure period of 11 AM to 3 PM on August 8th has been established (Table 1.3).

Table 1.3: Climatic variables evolution scenario within a fixed exposure environment corresponding to the 8th of August from 11AM to 3PM.

	11 AM	12 AM	1 PM	2 PM	3 PM
$T_a$ [°C]	30	31	32	30	29
$T_{mrt}$ [°C]	51	56	60	56	57
$v_a$ [m/s]	0.1	0.1	0.1	0.1	0.1
$RH$ [%]	40	34	33	32	35

Under these conditions, steady-state  $T_{core}$  and  $T_{sk}$  are determined using JOS-3 by applying a constant value of the climatic variables until a steady state is reached. This process typically takes over an hour for the  $T_{core}$ . The calculated  $T_{core}$  and  $T_{sk}$  values are then inputted into the PET Python function to carry out the PET computation. The results can be seen in Table 1.5.

Table 1.4: Behavioural and physiological variables.

Physical activity ratio (*) [-]	1.25
Clothing insulation [clo]	0
Height [m]	1.72
Fat [%]	15
Age [years]	20
Sex [-]	Male

(\*) The ratio of metabolic rate to basal metabolic rate

Table 1.5:  $T_{core}$  and  $T_{sk}$  at steady state for different  $T_a$  values.

	11 AM	12 AM	1 PM	2 PM	3PM
$T_{core}$ [°C]	37.35	37.47	37.62	37.44	37.44
$T_{sk}$ [°C]	36.32	36.54	36.77	36.49	36.51

The comparison between steady-state and transient core ( $T_{core}$ ) and skin temperatures ( $T_{sk}$ ) is conducted using the JOS-3 thermoregulation model, which incorporates hourly changes in air temperature ( $T_a$ ), as detailed in Section 1.3. Figure 1.10 illustrates the comparison between the steady and transient states of  $T_{core}$  and  $T_{sk}$ .

The  $T_{sk}$  response is very rapid, achieving a steady state within just a few minutes. As such, there's a negligible difference between the  $T_{sk}$  calculated using steady and transient methods. However, this is not true for  $T_{core}$  due to its slower dynamic time, needing over an hour to reach a steady state. Consequently, when temperature variation is positive, a steady method overestimates  $T_{core}$  but underestimates it when this variation is negative in the studied scenario. The maximum observed  $T_{core}$  difference between the steady and transient methods is 0.16°C at 2 PM

The difference's impact concerning heat stress is gauged using the PET model. This model calculates a PET to measure heat stress based on a specific core temperature ( $T_{core}$ ), skin temperature ( $T_{sk}$ ), and clothing temperature, which is synonymous with  $T_{sk}$  in this case due to clothing resistance being zero. As there is not a significant difference in  $T_{sk}$  between the steady and transient approaches, the same  $T_{sk}$  temperature is utilised. The two calculated PETs, one with a consistent  $T_{core}$  at 2 PM and the other with a rising  $T_{core}$  increased by 0.16°C, are quite similar: the transient approach yields 37.75°C, while the steady approach results in 37.74°C.

In this particular configuration, the climatic variables of a set environment change on an hourly basis, with the exposure period being at least an hour. Consequently, heat stress assessment can be performed via steady indices like the PET. Notably, there can be swift and significant changes in  $T_{mrt}$  due to solar shading, even within this set environment. However, these quick fluctuations may not be detectable when calculating solar irradiation and  $T_{mrt}$  on an hourly scale.



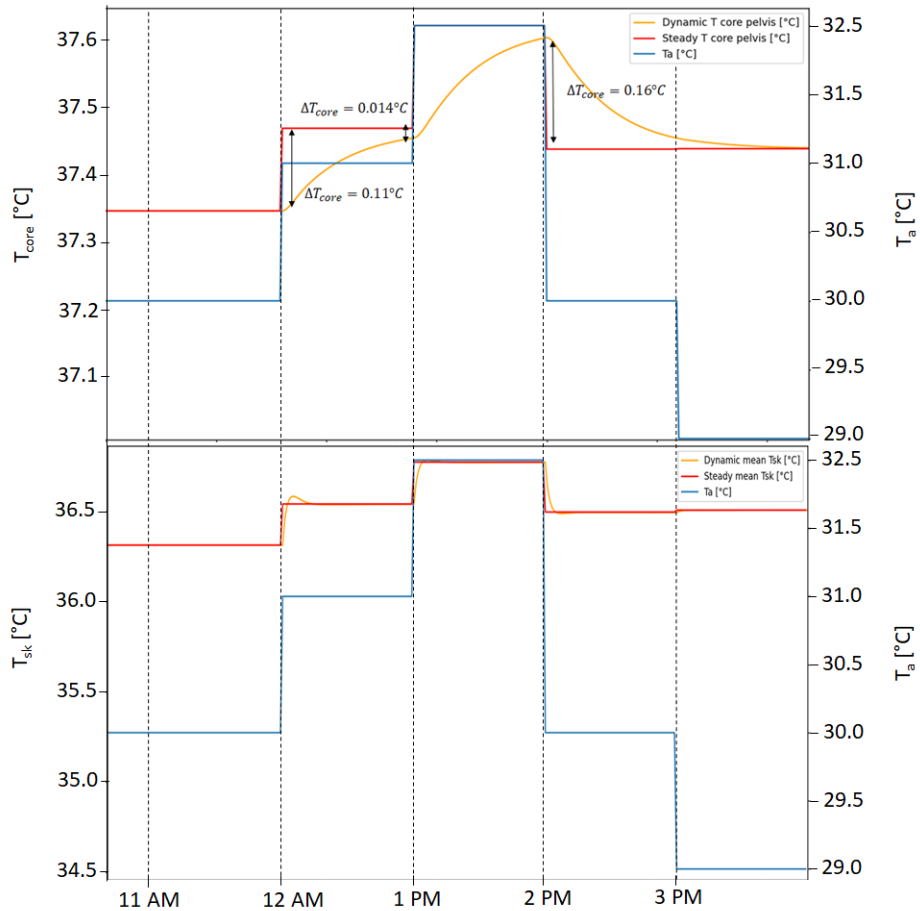


Figure 1.10: Steady and transient  $T_{core}$  and  $T_{sk}$  evolution for climatic variables evolution corresponding to the 8th of August from 11 AM to 3 PM.

### 1.4.2 Impact of cumulative climatic variables time evolution and displacement dynamics

This section seeks to examine the cumulative impact of climatic variables over time and individual movement through varying exposure environments on heat strain development. This involves assessing core temperature ( $T_{core}$ ) and skin temperature ( $T_{sk}$ ) using steady and transient modelling approaches. Additionally, it explores how these factors influence heat stress assessment. The comparative approach previously applied in Section 1.4.1, utilising JOS-3 and the PET, is employed.

A displacement scenario through the four following exposure environments is suggested in Figure 1.11:

- Indoor dwelling environment, where  $\Delta T_a = 2^\circ\text{C h}$  in 3 h,  $T_a = T_{mrt}$  and  $v_a = 0.1 \text{ m s}^{-1}$ .
- An outdoor environment with no wind and under sun exposure, where  $\Delta T_a = 2^\circ\text{C}$ ,  $\Delta T_{mrt} = 10^\circ\text{C}$  and  $v_a = 0.1 \text{ m s}^{-1}$ .
- Outdoor shade environment with no wind, where  $\Delta T_a = 1^\circ\text{C}$ ,  $\Delta T_{mrt} = 2^\circ\text{C}$  and

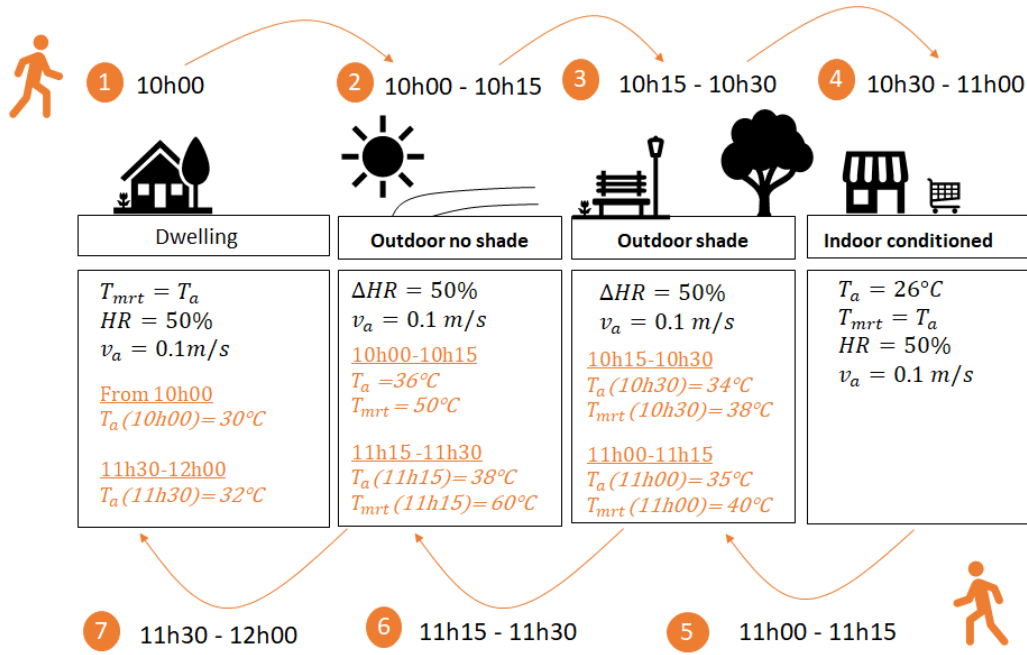


Figure 1.11: Displacement scenario through different exposure environments.

$$v_a = 0.1 \text{ m s}^{-1}.$$

- Indoor conditioned environment, where  $\Delta T_a = 0^\circ\text{C}$ ,  $T_a = T_{mrt}$  and  $v_a = 0.1 \text{ m s}^{-1}$ .

For the purposes of this analysis, the outdoor  $RH$  is kept consistent at 50%.

Figure 1.12 depicts the progression of  $T_{core}$  and  $T_{sk}$ , as calculated by steady and transient approaches. Large changes in  $\Delta T_a$  and  $\Delta T_{mrt}$  over short periods result in a significant gap between steady and transient  $T_{core}$  and  $T_{sk}$  values – exceeding  $1^\circ\text{C}$  for  $T_{core}$  and even more for  $T_{sk}$ . This significantly impacts heat stress evaluation. Transitioning from indoor to outdoor environments causes noticeable increases in  $T_{mrt}$  and  $T_a$ , which results in a slower response from  $T_{core}$  and a faster one from  $T_{sk}$ . This makes the discrepancy between steady and transient approaches more prominent for  $T_{core}$  than  $T_{sk}$ . Also, the reaction differs depending on whether the environment transitions from warm to cool or vice versa. Interestingly, the PET model indicates that PET is more sensitive to  $T_{sk}$  variations than  $T_{core}$ . A discrepancy on the  $T_{core}$  is therefore less relevant than a discrepancy on the  $T_{sk}$  in the PET model. From 11:15 to 11:30 (step 6), when moving from a shaded outdoor environment to one directly exposed to sun,  $T_{mrt}$  increases by  $20^\circ\text{C}$  and  $T_a$  by  $3^\circ\text{C}$ . This leads to the steady approach to overestimate the PET by  $1.04^\circ\text{C}$ . In contrast, from 10:30 to 11:00 (step 4), when transitioning from a shaded outdoor environment to a conditioned indoor one, it results in a significant decrease of  $T_a$ , causing the steady approach to underestimate the PET by  $2.38^\circ\text{C}$ .

These discrepancies should be accounted for in relation to the temperature ranges of the PET assessment scale, which spans between  $4^\circ\text{C}$  and  $6^\circ\text{C}$ . To sum up, the larger the changes in a given period, the greater the discrepancy between steady and transient findings.

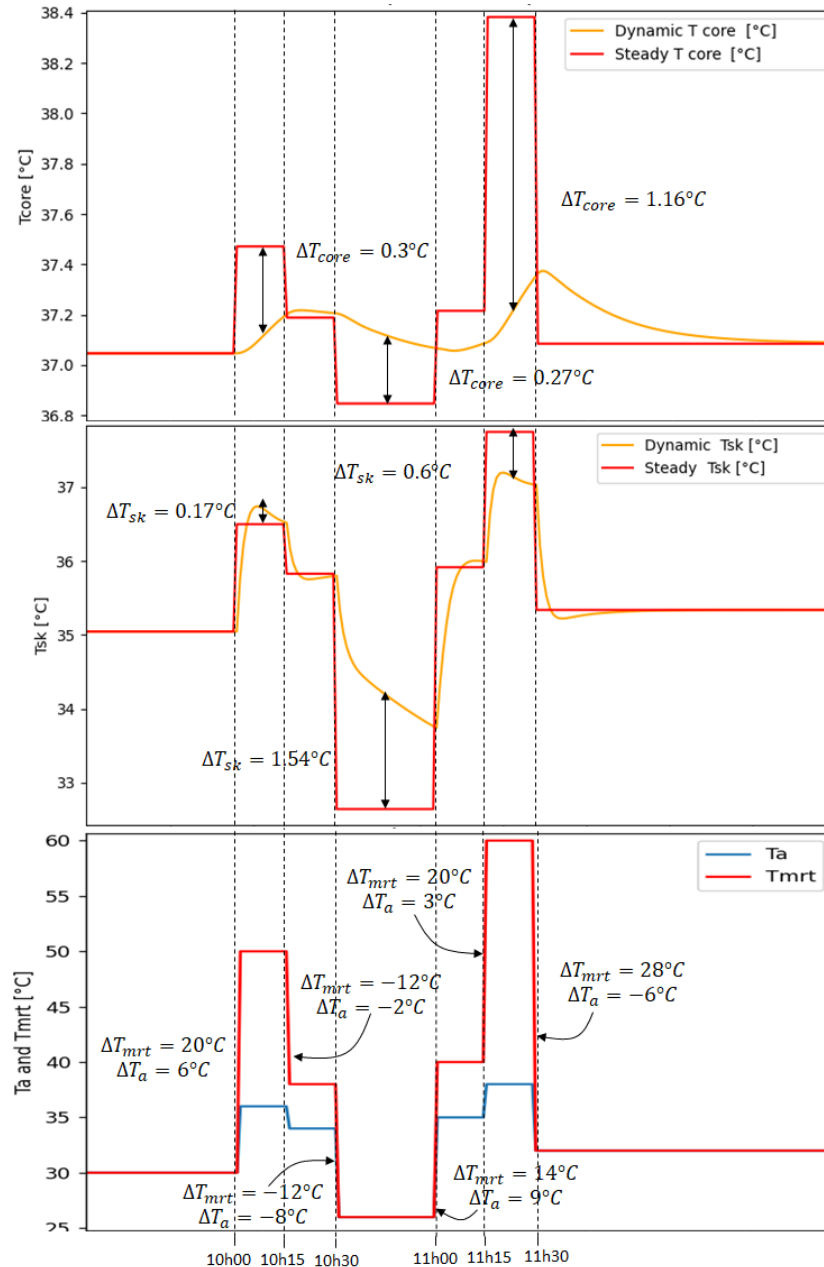


Figure 1.12:  $T_{core}$  and  $T_{sk}$  evolution under exposure environments of Figure 1.11.

### 1.4.3 Conclusions on the applicability of steady and unsteady models

The decision to use either a steady or transient model to evaluate heat stress and strain relies on the fluctuation range of climate variables within a set timeframe. This is affected by a mix of weather and exposure conditions, as well as exposure dynamics.

For the gradual evolution of climate variables, a steady index like PET can be used in heat stress assessment without substantial impact. This principle applies primarily in scenarios where heat stress assessment pertains to a stationary location, an Eulerian exposure approach, in which the hourly variation of climate variables has a negligible effect on PET,

as observed in Section 1.4.1. This kind of heat stress evaluation is beneficial for describing a location's potential for heat stress. However, this approach has limitations. It relies on the calculation of climate variable evolution using hourly averaged values, mainly due to the hourly availability of weather data. Nevertheless, more substantial variations of  $T_{mrt}$  can occur within shortened time intervals, such as 5 min. This is evident, for instance, in the fluctuating solar radiation hitting a surface, which can shift quickly based on the surface's sun exposure. Moreover, even though this approach assesses heat stress relative to a location, it is based on the theoretical heat strain response of an individual who remains continuously in that spot and experiences the unique climatic conditions there under specific metabolic and clothing conditions.

To accurately account for the rapid changes in climatic variables, particularly air temperature ( $T_a$ ) and mean radiant temperature ( $T_{mrt}$ ), a transient approach is essential. This method is more effective in understanding the real-time evolution of thermal strain parameters and, consequently, in determining the associated heat stress. This need is particularly evident when an individual transitions from one thermal environment to another characterized by significant differences in  $T_a$  ( $\Delta T_a$ ) and/or  $T_{mrt}$  ( $\Delta T_{mrt}$ ) within a brief time frame, as discussed in Section 1.11. In such scenarios, the assessment of heat stress and strain is focused on the individual rather than a static location, adopting a Lagrangian exposure approach.

As highlighted previously, this situation is also observed in a fixed place when rapid fluctuation of solar radiation occurs, resulting from the sun's path and the generation of shaded or solar-exposed areas by the surrounding context. As the transient approach is able to better represent the thermoregulatory response of the person through the rapid evolution of thermal environments, it is also currently adopted in heat strain assessment for health purposes.

In this context, we will use the PET steady index for daily and seasonal analysis, allowing us to evaluate the potential heat stress in a location and identify possible heat shelters. To illustrate, we will also use PET to evaluate heat stress along a hypothetical person's daily path. We will use transient indices from the JOS-3 thermoregulation model to evaluate the heat strain a person may experience within a day.

## 1.5 Sensitivity of heat stress and heat strain indices to climatic variables evolution and time step

Under the perspective of using both the PET steady heat stress index and transient heat strain index, the aims of this section are to study:

- The sensitivity of the PET index to climatic variables evolution.
- The impact of input climatic variable time step on the evolution of some transient heat

strain variables using the JOS3 model.

### 1.5.1 Sensitivity analysis of PET to climatic variation

This paragraph undertakes a sensitivity analysis to evaluate the impact of each climatic parameter on the variation of the PET. Useful in discussing the suitable spatial and temporal breakdown for thermal models, the analysis aids in assessing both outdoor and indoor climate variables (within urban microclimate models and BEM). This analysis employs Sobol's method using the SALib Python library (Herman and Usher, 2023) with input parameters such as air temperature ( $T_a$ ), mean radiant temperature ( $T_{mrt}$ ), relative humidity ( $RH$ ), and air velocity ( $v_a$ ).

The study observes  $T_a$  and  $T_{mrt}$  across three distinct subdomains to analyze sensitivity over varying temperatures, ranging from slightly cold to hot. These are marked as R1, R2, and R3 in Table 1.6. Within each domain, the  $T_a$  and  $T_{mrt}$  ranges are pre-determined based on weather file observations. For instance, if  $T_a$  ranges between 10°C and 20°C, the corresponding outdoor  $T_{mrt}$  in an unobstructed area varies between 10°C and 37°C. Additionally, the study explores two  $v_a$  ranges to analyze sensitivity in relation to high and low air velocities, designated as R3 and R4 in Table 1.6.

The summer 2020 weather data from the Lyon Confluence is used to assign value ranges and probability distributions. Both the  $T_a$  and the  $RH$  follow a normal distribution.  $T_{mrt}$  (depicted in Figure 3.10) and  $v_a$  (Figure 1.14) are assigned a triangular distribution, with ranges based on the  $T_a$  ranges. The other individual PET input parameters are set as follows:  $M = 1.37met$ ,  $I_{clo} = 0.5clo$ .

Table 1.6: Ranges of values and probability distribution of climatic variables.

	R1	R2	R3	R4	distribution
$T_a$ [°C]	[10 – 20]	[20 – 30]	[30 – 40]	[30 – 40]	Normal
$T_{mrt}$ [°C]	[10 – 37], 35% <sup>(*)</sup>	[12 – 60], 40% <sup>(*)</sup>	[20 – 65], 85% <sup>(*)</sup>	[20 – 65], 85% <sup>(*)</sup>	Triangular
$v_a$ [m/s]	[0.01 – 2], 50% <sup>(*)</sup>	[0.01 – 2], 50% <sup>(*)</sup>	[0.01 – 2], 50% <sup>(*)</sup>	[2, 5], 10% <sup>(*)</sup>	Triangular
$RH$ [%]	[20 – 90]	[20 – 90]	[20 – 90]	[20 – 90]	Normal

(\*) The “%” stands for the peak location (when the “%” is less than 50 of the peak is on the left).

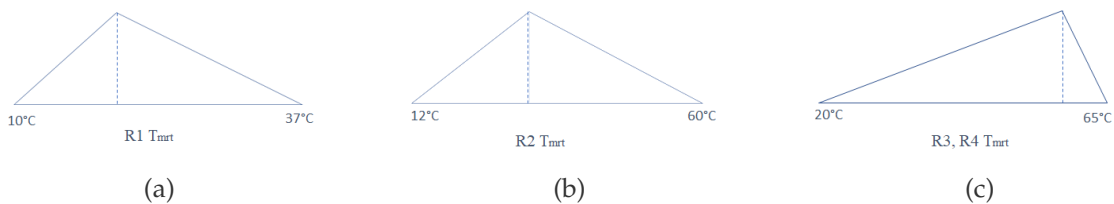


Figure 1.13:  $T_{mrt}$  triangular distribution for the four ranges of climatic variables R1, R2, R3 and R4.

The sensitivity of each climatic variable is represented by three sensitivity indices, the first order, the second order and the total indices (Herman and Usher, 2023). In this specific case:

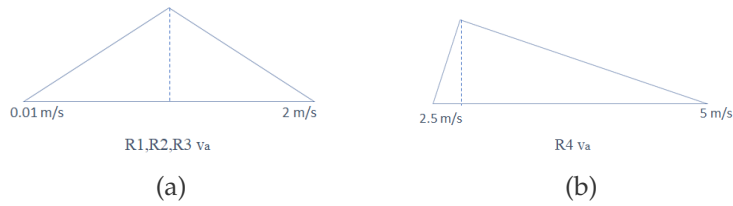


Figure 1.14:  $v_a$  triangular distribution for the four ranges of climatic variables R1, R2, R3 and R4.

- The total order index  $ST$ , measures the contribution to the PET variance caused by a climatic variable including both its first order effect (input varying alone) and all the higher-order interactions.
- The first order index  $S1$ , measures the contribution to the PET variance by a single climatic variable alone.
- The second order index  $S2$ , measures the contribution to the PET caused by the interaction of two climatic variables.

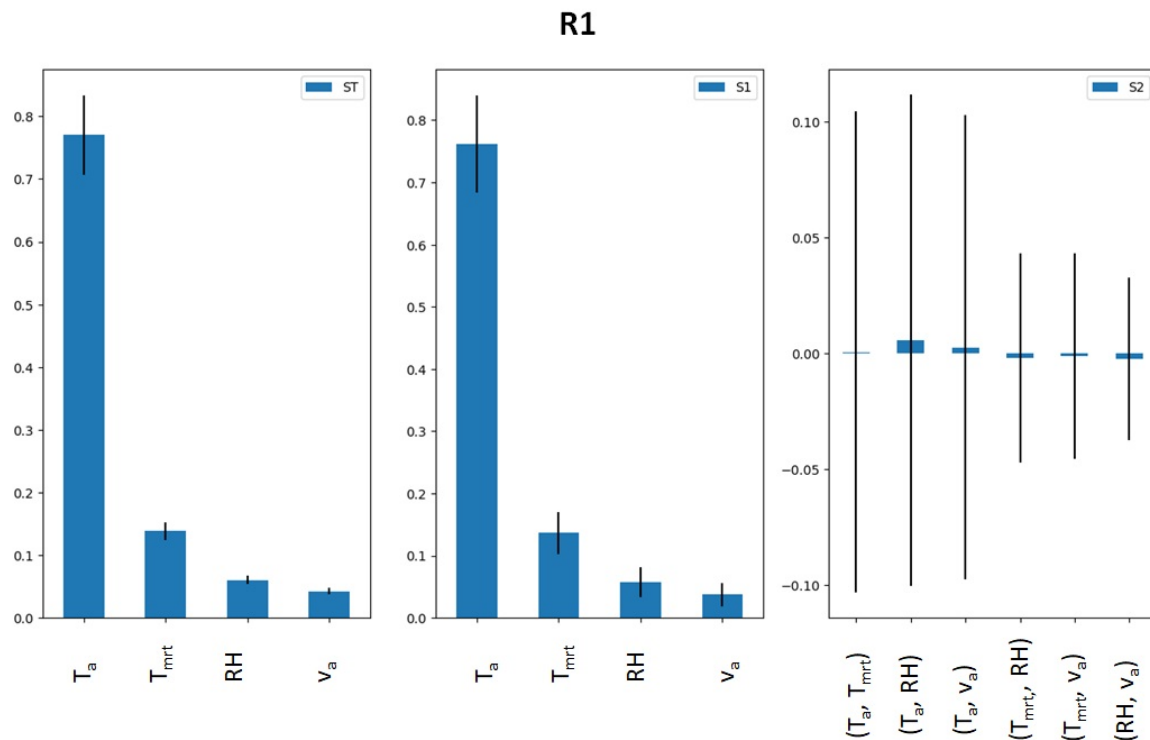


Figure 1.15:  $ST$ ,  $S1$  and  $S2$  indices for Sobol PET Sensitivity analysis for the range R1.

The results of the analysis are depicted in Figures 1.15 to 1.18. The total order index  $ST$  reveals that  $T_a$  contributes most significantly to the PET variance, ranging between 50% and 77% based on other parameter value ranges. The second most influential parameter is  $T_{mrt}$ , impacting 13% to 50%, particularly in high  $T_a$  value ranges. This is due to the  $T_{mrt}$  ranges and their probability distribution. The range of  $T_{mrt}$  values in R2 and R3 is notably larger

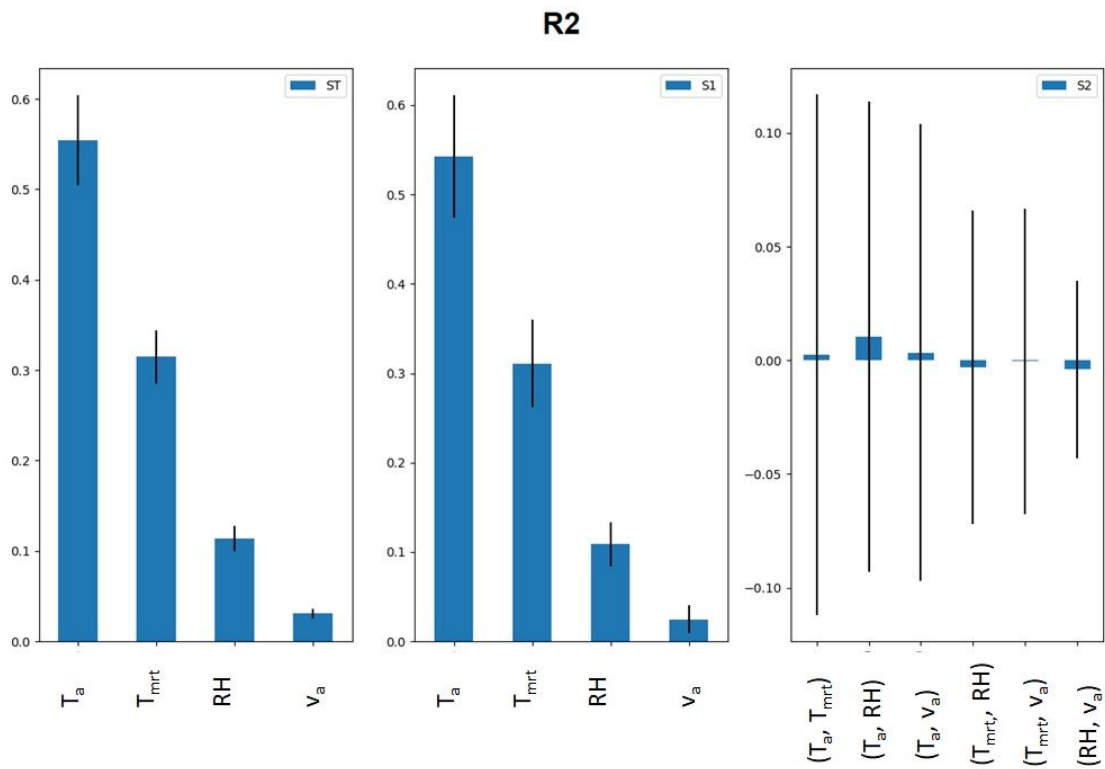


Figure 1.16: ST, S1 and S2 indices for Sobol PET Sensitivity analysis for the range R2.

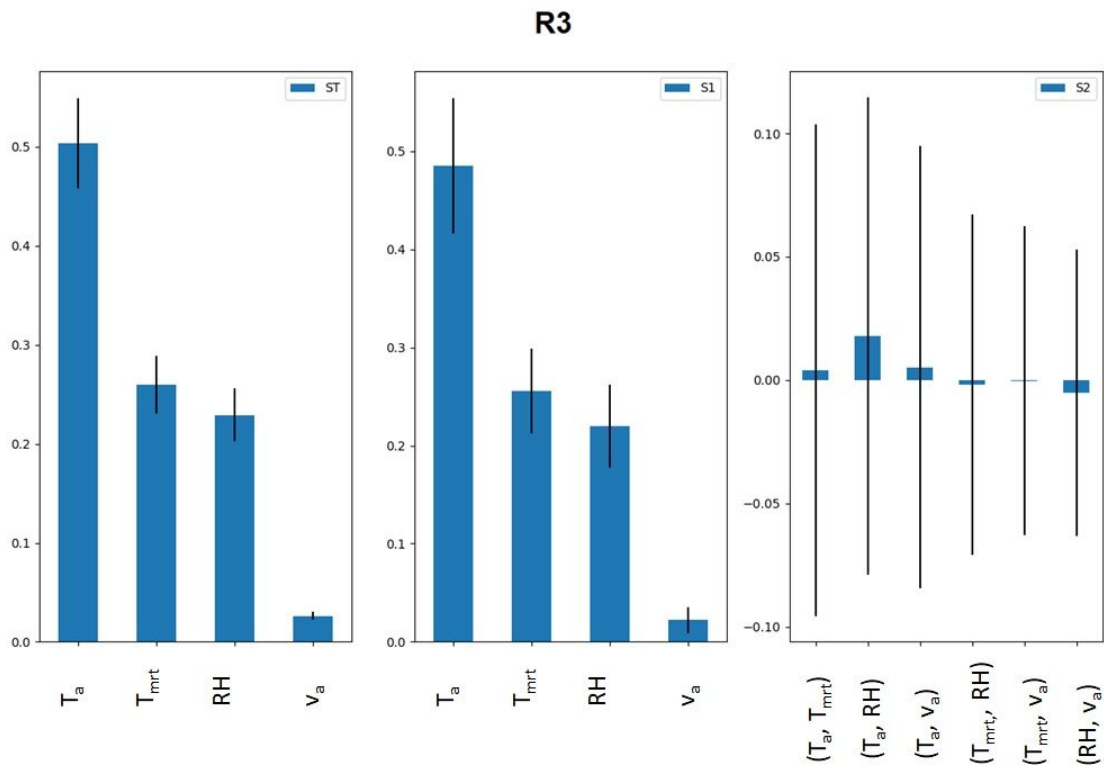


Figure 1.17: ST, S1 and S2 indices for Sobol PET Sensitivity analysis for the range R3.

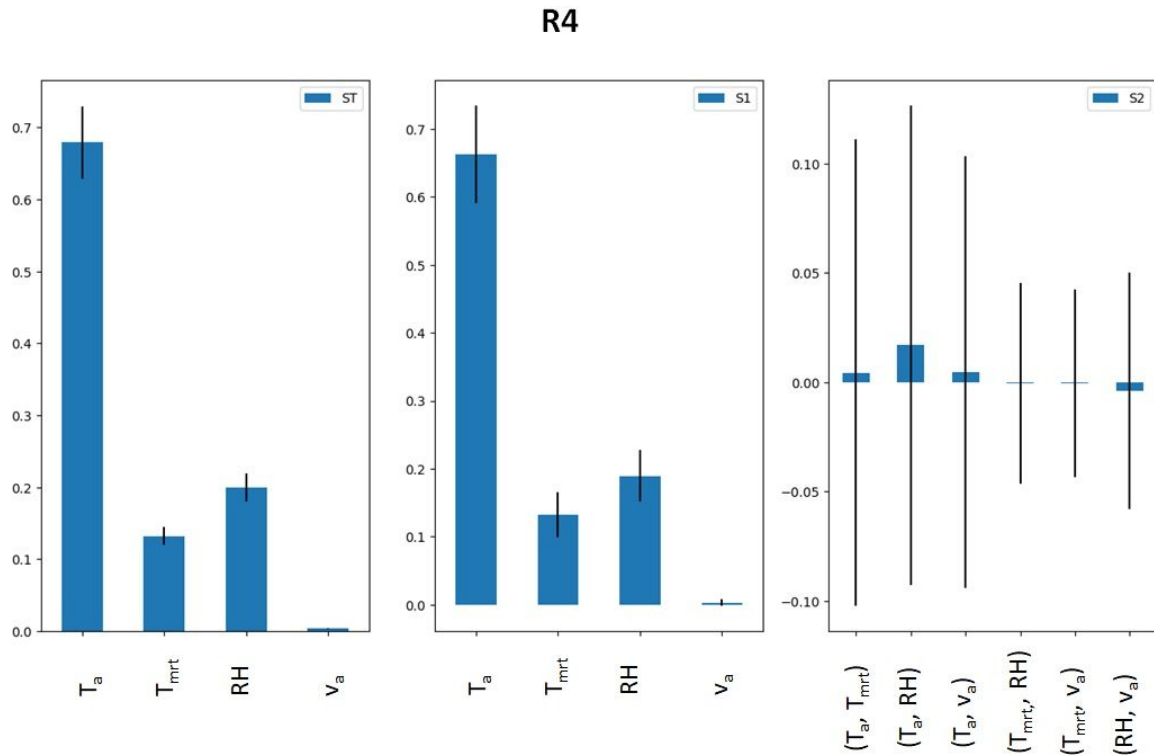


Figure 1.18: ST, S1 and S2 indices for Sobol PET Sensitivity analysis for the range R4.

than in R1.  $RH$  also plays a significant role, with its effect increasing as  $T_a$  values rise. This is due to the combined high values of  $T_a$  and  $RH$ , which restrict the ability to sweat, thereby lessening our capacity to decrease skin temperature ( $T_{sk}$ ) and core body temperature ( $T_{core}$ ). The least impactful parameter is wind speed ( $v_a$ ), contributing roughly 3% for low  $v_a$  levels (R1, R2, R3) and only 0.3% when  $v_a$  exceeds  $2 \text{ m s}^{-1}$ . This is because, beyond a certain wind speed, the body no longer significantly reacts to the wind's effect as the convective exchange between  $T_{sk}$  and  $T_a$  becomes so profound that  $T_{sk}$  tends to align with  $T_a$ . In terms of heat strain, an increased  $v_a$  helps reduce strain when  $T_{sk}$  is greater than  $T_a$ . Conversely, when  $T_{sk}$  is less than  $T_a$ , a higher convective exchange can exacerbate heat strain by increasing  $T_{sk}$  (Deng et al., 2018). This factor is not currently considered in the PET assessment, as discussed in Section 1.3.1.

The S1 indices demonstrate that each parameter individually contributes to the variance in PET. The 'S2' result suggests the maximum combined effect of two parameters is under 2%, specifically regarding  $T_a$  and  $RH$ . This points to the joint impact of high temperatures and humidity on sweating ability and, thus, on related heat stress. Through this sensitivity analysis, we emphasize the significance of the two climate parameters,  $T_a$  and  $T_{mrt}$  in evaluating PET.

Two additional analyses are performed here to assess the effect of a  $1^\circ\text{C}$  increase in ambient temperature ( $T_a$ ) and mean radiant temperature ( $T_{mrt}$ ) on the evolution of the PET (Figure 1.19). Given that the interaction with other climate parameters has a negligible im-



## 1.5. Sensitivity of heat stress and heat strain indices to climatic variables evolution and time step

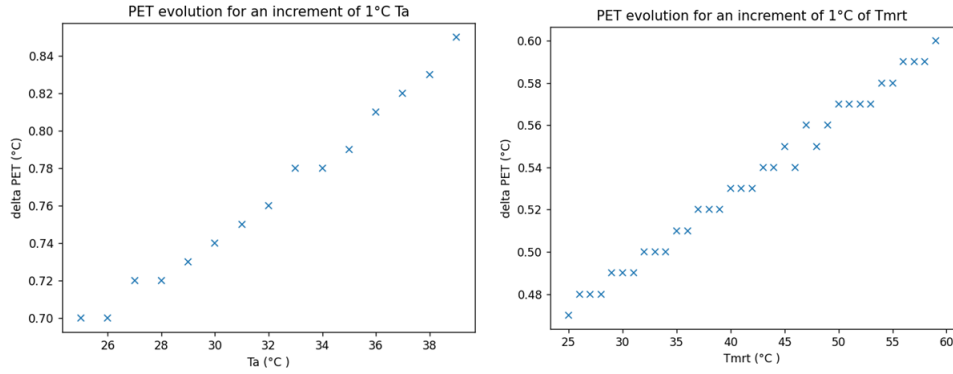


Figure 1.19: Increase of PET with an increase of 1°C of  $T_a$  and 1°C of  $T_{mrt}$

impact on the PET variance, these parameters are set to constant values:  $RH$  at 50%, wind speed ( $v_a$ ) at  $0.15 \text{ m s}^{-1}$ ,  $T_{mrt}$  at  $28^\circ\text{C}$  (for the study of the  $T_a$  increase), and  $T_a$  at  $28^\circ\text{C}$  (for the study of the  $T_{mrt}$  increase).

As seen in Figure 1.19, a  $1^\circ\text{C}$  increase in the ambient temperature ( $T_a$ ) within the range of  $26\text{--}40^\circ\text{C}$  leads to a corresponding rise in the PET between  $0.7^\circ\text{C}$  and  $0.8^\circ\text{C}$ . Likewise, a  $1^\circ\text{C}$  increase in mean radiant temperature ( $T_{mrt}$ ) within the range of  $26\text{--}60^\circ\text{C}$  results in a  $0.48\text{--}0.6^\circ\text{C}$  increase in PET. It is important to note that during a summer day when the sun is at its peak, the  $T_{mrt}$  can vary by more than  $10^\circ\text{C}$  from one location to another based on the sky view factor (Naboni et al., 2017). This variation can alter the PET by around  $5^\circ\text{C}$ . Thus, for an accurate assessment of PET, it is necessary to properly evaluate the  $T_a$  and  $T_{mrt}$ , taking into account the spatial fluctuations within the environment to capture climate parameter variations caused by a diverse exposure environment.

Concerning the impact of  $v_a$  variation on PET variation, Figure 1.20 shows that PET variation is more important for low wind speed and for high values of  $T_{mrt}$ .

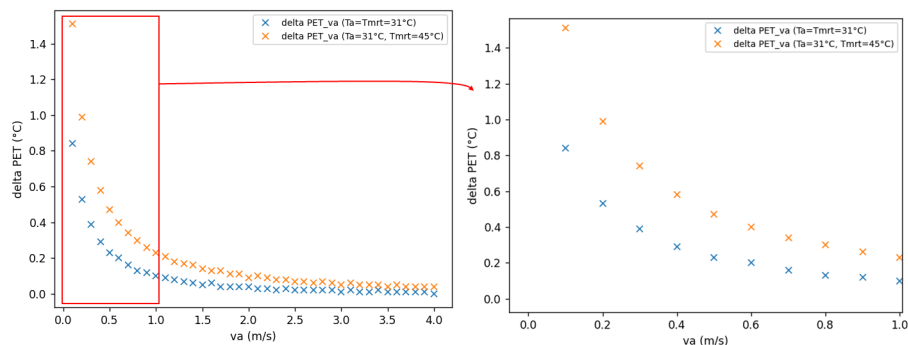


Figure 1.20: Increase of PET with an increase of  $0.1 \text{ m s}^{-1}$  in the case of  $T_a = T_{mrt} = 31^\circ\text{C}$  and  $T_a = 31^\circ\text{C}$  and  $T_{mrt} = 45^\circ\text{C}$ .

### 1.5.2 Impact of input climatic variable time step on physiological variables

In this section, we analyze variations in the  $T_{core}$  using the JOS-3 thermoregulation model. Our objective is to examine the responses and stabilization time of the stated parameters under different exposure conditions. In the initial phase, only  $T_a$  changes over time, with other conditions remaining constant at  $T_{mrt} = 30\text{ }^\circ\text{C}$ ,  $RH = 50\%$ ,  $v_a = 0.1\text{ m s}^{-1}$ , and a physical activity ratio of 1.25. The characteristics of the body are: height 1.7 m, weight 60 kg, and age 30 years. The JOS-3 model retains its default time discretization unit value of 60 s.

#### 1.5.2.1 Response of the $T_{core}$ over different time steps of $T_a$ evolution

The analysis of a  $T_a$  evolution rate of  $3\text{ }^\circ\text{C}$  per hour, considered a high evolution rate according to the weather data analysis in Section 1.4.1, involves examining two distinct input data frequencies.

- The first is based on an hourly time step of 3 hours. The ranges of temperature are 32, 35, and  $38\text{ }^\circ\text{C}$ ;
- The second is based on a 10 min time step during 3 h. The ranges of temperature are  $32\text{ }^\circ\text{C}$  every 10 min the first hour and an evolution of  $0.5\text{ }^\circ\text{C}$  every 10 min the following 2 h.

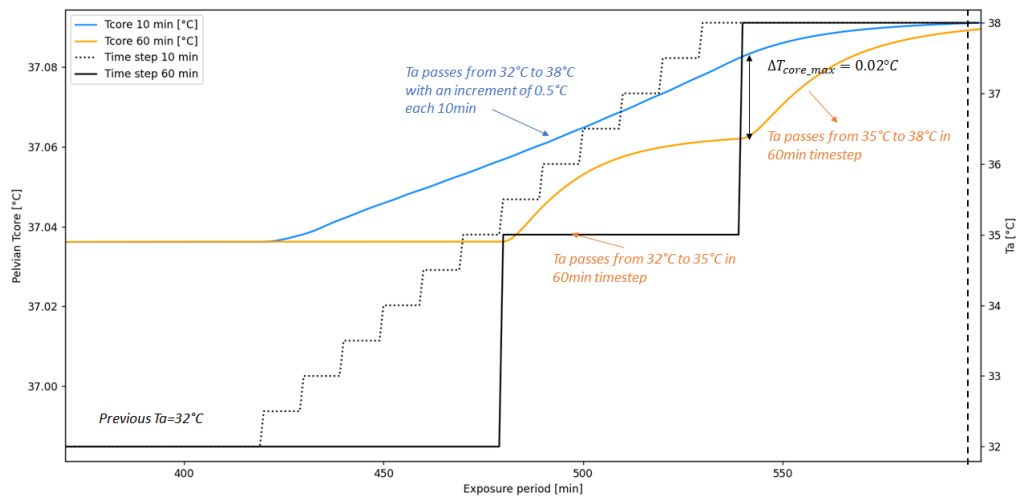


Figure 1.21:  $T_{core}$  evolution for hourly and 10 min  $T_a$  time step.

Figures 1.21 and 1.22 depict the evolution of  $T_{core}$  and the  $T_{sk}$  for two distinct  $T_a$  input frequencies, commencing at the 420th minute, respectively. The figures illustrate similar  $T_{core}$  fluctuations for both methods, with a maximum variation of just  $0.02\text{ }^\circ\text{C}$ . As this is negligible for heat stress assessment, we can conclude that hourly  $T_a$  input data delivery to the JOS-3 model will not significantly impact  $T_{core}$  computation. Interestingly, the effect on  $T_{sk}$  is more prominent, as Figure 1.22 shows a maximum variation of  $0.2\text{ }^\circ\text{C}$ . This variation corresponds

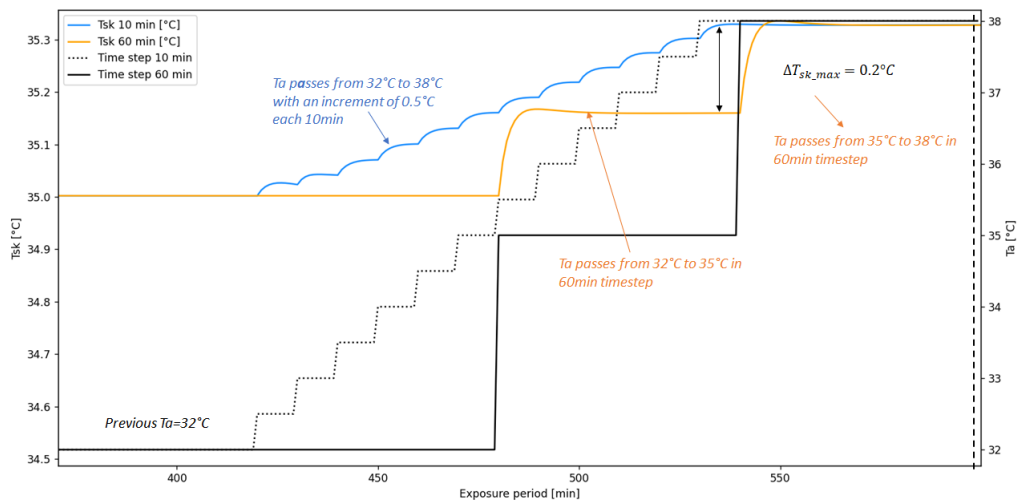


Figure 1.22:  $T_{sk}$  evolution for hourly and 10 min  $T_a$  time step.

to a PET variation of approximately  $0.2^{\circ}\text{C}$ , which still holds little relevance for heat stress assessment. However, shorter time step intervals should be considered for a more detailed analysis of  $T_{sk}$ 's heat stress effects.

### 1.5.3 Conclusions on the sensitivity of heat stress and strain indices to climatic time evolution and time-step

The study outlined in Section 1.5 emphasizes PET's prominent sensitivity to both  $T_a$  and  $T_{mrt}$  variations, particularly noticeable in circumstances with substantial exposure to solar radiation for  $T_{mrt}$ . While sensitivity to variations in airflow ( $v_a$ ) is less distinctive, accurately gauging this airflow in intricate urban spaces is crucial. It allows for a proper understanding of the thermal exchanges between surfaces, subsequently helping to characterize  $T_a$  and the exchanges of LWR.

In conclusion, the sensitivity analysis emphasizes the importance of spatially fragmenting the exposure environment. This fragmentation is required to capture variations in dominant climate parameters when assessing heat stress and strain. The degree of fragmentation solely depends on the variability of the thermal environment generated by the exposure environment. Additionally, the JOS-3 model's response analysis reveals that altering the  $T_a$  time step between 10 min and 1 hour only mildly affects  $T_{sk}$  and barely impacts  $T_{core}$ . Therefore, it is acceptable to use an hour time step when observing the  $T_{core}$  variable.

## 1.6 Selected heat stress and heat strain indices

This section introduces the indices used to evaluate heat stress and strain throughout this work, building upon previously presented analyses. These indices differ based on whether

they are used for seasonal or short-term heat stress analysis.

### 1.6.1 Seasonal analysis indices

For the seasonal analysis only, the Eulerian exposure approach is considered. This means that heat stress is assessed in reference to a fixed place. The reference index used is PET. PET is utilised specifically for global heat stress assessment, as per the scale outlined in Section 1.3.1. Alongside the PET, we introduce supplementary overheating indices. Overheating is defined as a PET greater than 29°C, the point where moderate heat stress arises. The specifics and objectives of these indices are illustrated in Table 1.7.

Index	Definition	Unit	Objective
<b>Global analysis of heat stress (PET assessment scale)</b>			
<b>Heat stress distribution</b>	Distribution of heat stress according to the PET assessment scale over the analysis period or month by month	%	Global heat stress assessment Provides indoors and outdoors heat stress classification based on maximal and minimal PET values
<i>Maximum</i>	<i>Considers the maximal PET over the selected zones</i>		
<i>Minimum</i>	<i>Considers the minimal PET over the selected zones</i>		
<b>Overheating (PET&gt;29°C) zonal analysis</b>			
<b>Maximal overheating duration</b> $OhD_{max}$	Within an overheating episode, it returns the longer one. Overheating episode time range PET>29°C	h	<b>Overheating duration</b> Provides an indication of the maximal overheating duration per zone. This indicator needs to be observed in regards of the number of overheating episodes
<b>Maximal cumulative overheating</b> $OhI_{max}$	$OhI_{max} = Max(\sum_{OhD} Overheat^{\circ C})$ Within an overheating episode, it identifies the one with the maximal overheating cumulative value and returns this value. Where $Overheat^{\circ C} = PET - 29^{\circ C}$ if $PET > 29^{\circ C}$ , otherwise $Overheat^{\circ C} = 0$	°Ch	<b>Overheating intensity</b> Provides an indication of the maximal overheating intensity per zone
<b>Maximal overheating</b> $Oh_{max}$	It returns the maximal overheating within the whole analysis period $Oh_{max} = Max(Overheat^{\circ C})$	°C	<b>Overheating peak</b> Provides an indication of the maximal degree of overheating
<b>Average overheating</b> $Oh_{mean}$	It returns the average overheating within the whole analysis period $Oh_{mean} = Mean(Overheat^{\circ C})$	°C	<b>Average overheating</b> Provides an indication of the mean degree of overheating

Table 1.7: Selected indices for seasonal analysis of heat stress and overheating.

### 1.6.2 Daily analysis indices

We can evaluate both heat stress and heat strain using Eulerian and Lagrangian exposure methods at this time scale. Heat stress is assessed using the PET index and the respective scale found in Table 1.1. Additionally, we measure heat strain using different indices, matching those in Table 1.2, which include  $T_{core}$ ,  $T_{sk}$ ,  $sw_R$ , *SkinWet* and *CO*. We calculate these indices with the JOS-3 thermoregulation model. It is important to note that the provided thresholds for these indices are merely suggestive. They offer more of a comparative than quantitative measure.

## 1.7 Conclusions

The lengthy, intense heatwaves people are enduring raise concerns about both thermal comfort and health. Numerous interacting factors influence how people perceive overheating and its actual health implications. Factors can be categorized into two types: environmental and individual. Environmental factors include external influences, such as physical elements and interpersonal interactions, that affect a person's exposure to the environment. On the other hand, individual factors relate to a person's characteristics, including social, physiological, personal, psychological, and behavioural traits that interact with the external setting.

The significance of these factors fluctuates based on the assessment's objective. For evaluating heat stress and strain, no index comprehensively encompasses all individual and environmental particulars; climate and physical conditions are predominantly considered. This applies to advanced indices that account for the interaction between an individual's physiological response and the climate (PET, UTCI, SET).

The PET index is chosen for heat stress evaluation as it allows consideration of both indoor and outdoor thermal conditions based on the temperature and wind speed observed during Lyon's summer. The JOS-3 thermoregulatory model is selected to calculate heat strain indices. The necessary input climatic variables for the PET and JOS-3 models include  $T_a$ ,  $T_{mrt}$ ,  $v_a$ , and  $RH$ .

Adaptive indoor models, which account for acclimatization, are often used in heat stress assessments to gauge thermal perception. However, these models aren't suitable for high-temperature cases and are thus excluded from this study. The concept of alliesthesia, influenced by an individual's thermal history, also factors into developing heat stress assessment scales. However, the inherent difficulty in creating universal scales due to this variable means it is also omitted from this study.

The decision to use either a steady or transient method for assessing heat stress and strain is debatable. It seems to largely depend on the extent of climate fluctuations and their rate of change. If the heat stress evaluation is conducted in a stable environment (Eule-

rian approach), steady indices are generally adequate, as climate variables' changes result in minimal differences between the transient and steady-state methods. When assessing heat stress related to a moving individual (using a Lagrangian approach), transient models become necessary.

This chapter also explores the sensitivity of thermal stress indices to fluctuations in climate parameters and air temperature time steps in a dynamic approach. Apparently, air temperature ( $T_a$ ) and mean radiant temperature ( $T_{mrt}$ ) are significant parameters when evaluating thermal stress using the PET and JOS-3 indices. When applying a dynamic approach, the relevant time step for monitoring core body temperature ( $T_{core}$ ) is approximately an hour, while for monitoring skin temperature ( $T_{sk}$ ), it is in the order of minutes.

The next chapter aims to identify modelling requirements for indoor and outdoor heat stress evaluation over daily and seasonal periods. It also seeks to define a suitable model and address any challenges associated with assessing the specified climatic variables.

## Chapter 2

# Modelling of urban microclimate and buildings for heat stress assessment

The purpose of this chapter is to outline the specific modelling challenge addressed in this thesis and to define the methodology used. Precisely, it will accomplish the following:

1. It will identify the physical phenomena that need to be modelled to evaluate the climatic variables highlighted in the previous chapter. This is necessary for assessing heat stress and heat strain.
2. It will identify various indoor and outdoor cooling solutions to model for the purpose of gauging their impact on heat stress and heat strain.
3. It will pinpoint the modelling requirements and evaluate the capability of existing buildings and microclimate models to meet those needs.
4. Lastly, it will describe the specific modelling problem, identify any issues, and propose potential solutions.

### Contents

---

<b>2.1 Physical phenomena to be modelled</b>	<b>49</b>
2.1.1 Urban microclimate principles	49
2.1.2 Conclusion on the physical phenomenon to be modelled	59
<b>2.2 Cooling solutions to be modelled in urban spaces and buildings</b>	<b>59</b>
2.2.1 Main observed indoors and outdoors cooling strategies	59
2.2.2 Selected cooling strategies	61
<b>2.3 Modelling thermal environments for heat stress and heat strain assessment</b>	<b>61</b>
2.3.1 Modelling requirements	62
2.3.2 Applicability of BEMs, McMs, UCMs and radiative models for seasonal and daily heat stress assessment	63

---

2.4	Specific problem formulation, expected outcomes and modelling issues . . .	68
2.5	Modelling strategy . . . . .	70
2.5.1	Model architecture . . . . .	70
2.6	Conclusions . . . . .	74

---



## 2.1 Physical phenomena to be modelled

This section aims to identify the physical phenomena that need to be modelled on a block scale to represent the climate variables previously outlined effectively. It offers a summary of urban microclimate phenomena and key physical phenomena that influence urban climate.

### 2.1.1 Urban microclimate principles

This section outlines the various climatic scales, with a primary focus on the urban canopy layer (UCL). It further explores the city's impact on the urban microclimate. Lastly, it introduces the main physical phenomena that regulate heat exchange between the atmosphere and urban elements like buildings and surfaces at the block scale, aiding in selecting the physical phenomena for modelling.

#### 2.1.1.1 Climatic scales

This section explains the physical principles that dictate atmospheric behaviour at various scales, helping to understand the interactions between the urban environment and local climate.

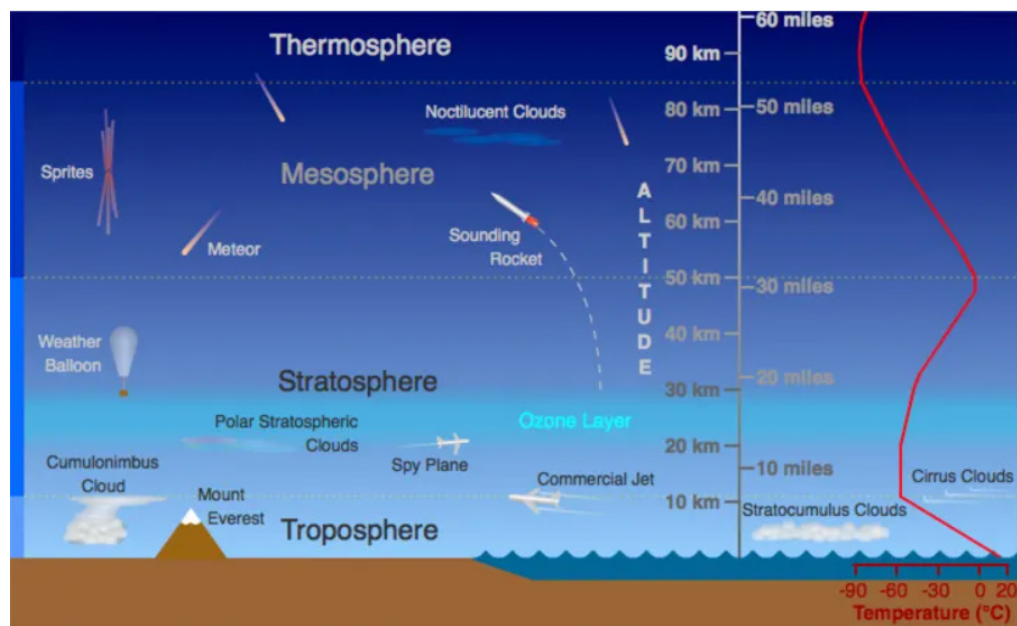


Figure 2.1: The atmosphere structure layer and temperature evolution (Figure from UCAR/Randy Russell).

The Earth's atmosphere primarily comprises nitrogen (78.09%) and oxygen (20.95%). It also contains water in various forms, represented by the specific humidity  $r$ . The state of an atmospheric air volume can be thermodynamically defined by its pressure, temperature, density, and the mass composition of its different components. The atmosphere is divided

into layers, each displaying unique temperature variations (Figure 2.1).

Most meteorological phenomena occur in the troposphere, a region ranging from the Earth's surface to an altitude of about 15 km (Soulhac, 2018). The atmospheric boundary layer (ABL), found within the troposphere, is the lowest segment of the atmosphere and directly interacts with Earth's surface. It has a depth between 100 to 3000 m. Factors such as surface roughness, thermal mixing, and emissions of moisture and air pollutants from the Earth's surface influence the ABL (Oke et al., 2017).

The ABL can be divided into two distinct regions: the mixed layer (ML), which constitutes the upper portion (90% of the ABL), and the surface layer (SL), representing the lower part (10% of the ABL). In the ML, atmospheric properties such as potential temperature, water vapor, wind speed and direction are nearly uniform due to thorough mixing. The thermal effects of the Earth dominate in this layer. In contrast, the flow within the SL is primarily influenced by friction with the Earth's surface. The vertical climate scale of the SL is referred to as the local scale.

During the daytime, the warm and less dense air near the Earth's surface rises buoyantly until it reaches the top of the ABL. The upward movement is then halted by a temperature inversion, beginning the free atmosphere (FA), where the Earth's surface has limited influence. Between the ABL and the FA, an entrainment zone exists where air from both areas mixes during the inversion. At night, the ABL shrinks due to the cooling of the Earth's surface, creating a stagnant layer near the ground that's roughly 200 to 400 m deep. This layer limits vertical mixing and restricts air movement within the ABL. The Urban Boundary Layer (UBL) is the part of the ABL affected by the city. Figure 2.2 presents the internal structure of the UBL and its scaling variables.

The SL is divided into three sublayers: the inertial sublayer (ISL), the roughness sublayer (RSL) and the urban canopy layer (UCL) nestled within the RSL. The ISL typically extends vertically from 20 to 250 m. Within this layer, the influence of turbulent mixing is so profound that mean properties like wind velocity, temperature, and humidity do not vary with horizontal placement; they instead only depend on altitude and time. Under neutral circumstances, the relationship between horizontal wind speed and altitude, denoted by  $u(z)[\text{m s}^{-1}]$ , can be represented by logarithmic profile.

$$u(z) = \frac{u^*}{k} \ln\left(\frac{z - z_d}{z_0}\right) \quad (2.1)$$

Where :

$$\begin{cases} u(z) \text{ is the mean wind velocity at height } [\text{m s}^{-1}] \\ u^* \text{ is the friction velocity } [\text{m s}^{-1}] \\ k \text{ is the Von Karman's constant } (0.42) [-] \\ z_0 \text{ is the aerodynamic roughness length } [\text{m}] \\ z_d \text{ is the zero-plane displacement length } [\text{m}] \end{cases}$$

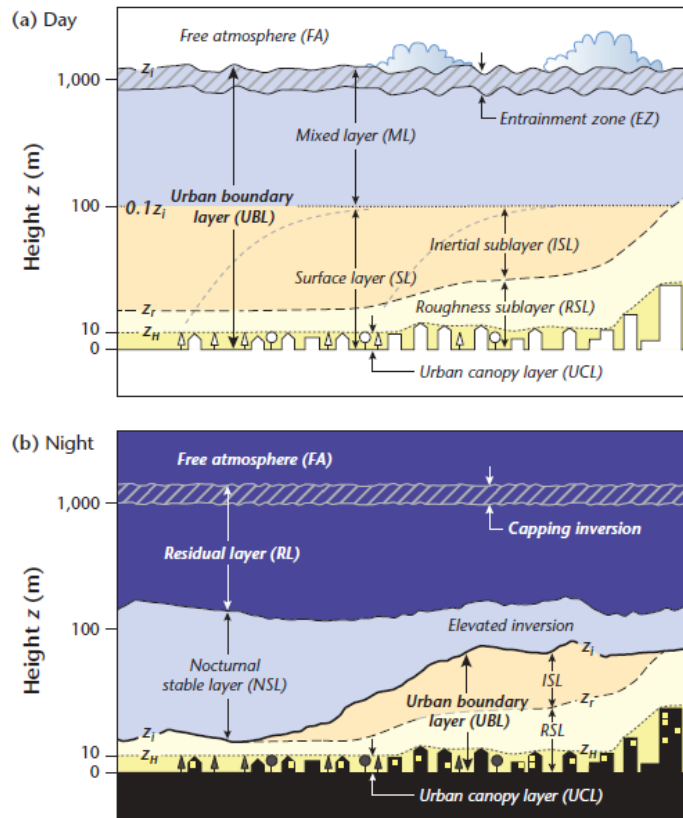


Figure 2.2: Schematic typical layering of the atmosphere over a city (a) by day and (b) by night (Figure from Oke et al., 2017).

$z_0$  depends on the terrain roughness, and  $z_d$  depends on the surface properties including roughness and is the distance by which the height scale has to be adjusted upward to effectively become the ground surface felt by the flow (Oke et al., 2017). Figure 2.3 illustrate the displacement of the logarithmic wind profile when passing over a rural area to an urban area.

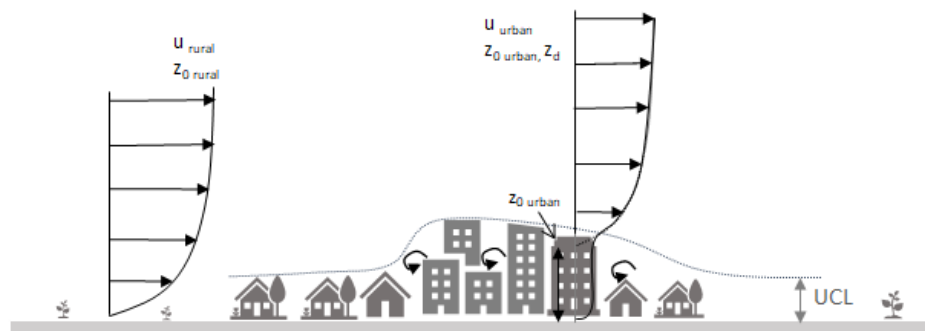


Figure 2.3: Mean wind profile depending on the land use (based on (Merlier, 2015), (Blocken, Stathopoulos, and Carmeliet, 2007)).

The RSL typically extends from the ground to two to five times the height of surrounding buildings or trees, encompassing the UCL. This sub-layer's climate scale referred to as the

micro-scale, experiences both reduced main airflow and increased turbulence. The flow in this layer is influenced by individual elements. Key factors that affect the average flow and turbulence levels are the average height and spacing of the roughness elements, as well as the layout of the street network.

The UCL extends from the ground to the average height of buildings and trees, encompassing both outdoor and building atmospheres (Oke et al., 2017). This layer's flow and thermal properties are influenced by urban features, resulting in intricate micro-scale processes that shape its climate and promote a variety of local microclimatic conditions.

### 2.1.1.2 The influence of the city on the urban climate

Urban climate in the UCL is influenced by several urban features that can be regrouped in two categories (Figure 2.4): The urban form and the urban function (Oke et al., 2017). Urban form encompasses aspects like fabric, cover, and structure.

The fabric represents the natural and artificial surfaces and volumes with their unique thermal, moisture, radiative, and aerodynamic properties. Properties like thermal capacity, conductivity, diffusivity, or inertia outline how much heat can be stored and released into the atmosphere, as well as the timing of this process. For instance, walls with a high thermal capacity can store more heat during the day and slowly release it at night, affecting the pattern of heat transfer. Moisture properties, such as moisture availability, impact the potential for evaporation, which in turn dictates the amount of latent heat released. Surface radiative properties, like albedo and emissivity, impact the radiative fluxes that are reflected, absorbed, or transmitted by surfaces, subsequently influencing their temperatures. Aerodynamic, including surface roughness length, urban shape, leaf area index (LAI), and more, also play an important role. These contribute to shaping the airflow trajectory and the heat exchanges, driven by convection, with the surrounding air.

The urban cover describes how infrastructure is spread across a city. It refers to the proportion of the ground covered by different types of infrastructure (Oke et al., 2017). Key parameters of urban cover include the building plan fraction, which is the ratio of a building's floor space to the lot size it sits on, and the impervious plan fraction, referring to the ratio of impermeable surface areas to the total lot space. Urban cover significantly impacts heat distribution into the atmosphere.

Finally, the urban structure, refers to the volumes and shapes of the urban elements. Some typical properties of the urban structure are the 3D explicit or simplified geometry, the canyon aspect ratio, representing the ratio of the canyon height to the canyon width, the sky view factor, representing the ratio of sky hemisphere visible from the ground, the mean height roughness elements, characterizing the city roughness. The term 'urban structure' pertains to the volume and form of urban elements. Key properties of this concept include 3D, whether explicit or simplified, geometrical patterns, the canyon aspect ratio, which signifies the ratio of height to width, the sky view factor indicating the visible sky

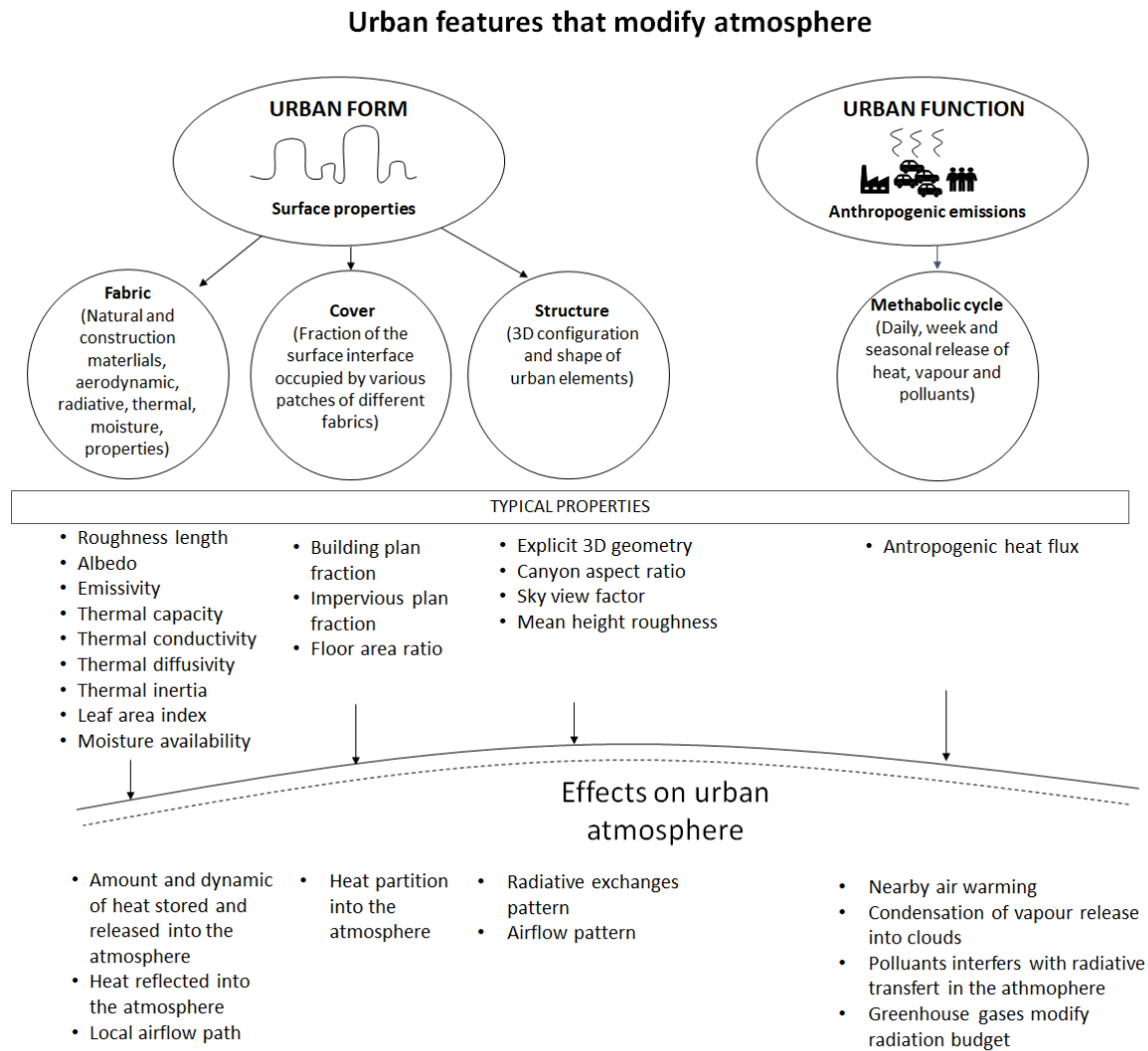


Figure 2.4: Schematic illustration of urban features modifying the atmosphere and their characteristic parameters.

hemisphere from ground-level, and mean height roughness elements that determine the city's coarseness. The urban structure mainly influences the radiative heat exchanges and airflow patterns, which in turn affect advective and convective heat exchanges. For instance, urban canyons, as depicted by long streets surrounded by towering vertical walls (Oke et al., 2017), encourage radiative trapping. This prevents incident solar and LWR on the canyon walls from being reflected back into the atmosphere. The canyon's aspect ratio also impacts its vertical ventilation. Also, trees can reduce the solar radiation on shaded surfaces and affect airflow. In some instances, they can even generate a local breeze, improving the sensation of thermal comfort.

Urban function refers to human activities that impact a city's metabolic cycle, including the emission of heat, steam, and pollutants. These activities affect the city's metabolic cycle on daily, weekly, and seasonal timescales. These cycles warm the surrounding air, condense vapour into clouds, emit greenhouse gases that alter the radiation budget, and release pol-

lutants that disrupt the radiative transfer in the atmosphere.

In conclusion, the interplay between urban form and function alters the urban climate by impacting local heat energy balance.

The city's impact on climate can be analyzed at different urban unit resolutions. Figure 2.5 provides a classification of urban morphological units along with corresponding climatic phenomena, characteristic length scales and climatic scales (Oke et al., 2017).

Urban units	Built features	Green and water features	Urban climate phenomena	Typical horizontal length scales	Climate scale
<b>Facet</b>	Roof, wall, road	Leaf, lawn, pond	Shadows, storage heat flux, dew and frost patterns	10 × 10 m	Micro
<b>Element</b>	Residential building, high-rise, warehouse	Tree	Wake, stack plume	10 × 10 m	Micro
<b>Canyon</b>	Street, canyon	Line of street trees or gardens, river, canal	Cross-street shading, canyon vortex, pedestrian bioclimate, courtyard climate	30 × 200 m	Micro
<b>Block</b>	City block (bounded by canyons with interior courtyards), factory	Park, wood, storage pond	Climate of park, factory cumulus	0.5 × 0.5 km	Local
<b>Neighbourhood or Local Climate Zone</b>	City centre, residential (quarter), industrial zone	Greenbelt, forest, lake, swamp	Local neighbourhood climates, local breezes, air pollution district	2 × 2 km	Local
<b>City</b>	Built-up area	Complete urban forest	Urban heat island, smog dome, patterns of urban effects on humidity, wind	25 × 25 km	Meso
<b>Urban region</b>	City plus surrounding countryside		Urban 'plume', cloud and precipitation anomalies	100 × 100 km	Meso

Figure 2.5: Classification of urban morphological units and their urban climate phenomena, based on horizontal length scale and climate scale. Units from canyon to city are based on a city with about 1M inhabitants (source: Oke et al., 2017).

### 2.1.1.3 Urban and building energy balance

Microclimate in the UCL is governed by the corresponding surface energy balance. This balance uses the energy conservation principle on surfaces and air volumes across all space and time scales.

#### Energy balance of a portion of urban volume

The urban energy balance can be established through a conceptual volume, as shown in Figure 2.6, encompassing the entire urban ecosystem (Oke et al., 2017). In this representation, the vertical heat flux density by conduction across the bottom is neglected. The energy balance of this conceptual volume is conveyed via an equivalent heat flux density across the horizontal surface of Figure 2.6, as detailed below:

$$Q^* + Q_F = Q_H + Q_E + \Delta Q_S + \Delta Q_A \quad (2.2)$$

Where :

- $Q^*$  is the incoming net all-wave radiative flux density [ $\text{W m}^{-2}$ ]
- $Q_F$  is the incoming anthropogenic heat flux density [ $\text{W m}^{-2}$ ]
- $Q_H$  is the outgoing turbulent sensible heat flux density driven by temperature differences between the surface and the atmosphere. This flux minimizes temperature within the atmosphere by mixing warmer and cooler eddies [ $\text{W m}^{-2}$ ]
- $Q_E$  is the outgoing turbulent latent heat flux density, consequence of water vapour transport [ $\text{W m}^{-2}$ ]
- $\Delta Q_S$  is the outgoing net heat storage charge by the fabric of the city trees, ground, materials air contained in the volume [ $\text{W m}^{-2}$ ]
- $\Delta Q_A = Q_{A,out} - Q_{A,in}$  is the outgoing flux density related to net energy added to, or subtracted from, the volume by wind-borne transport (advection) [ $\text{W m}^{-2}$ ]

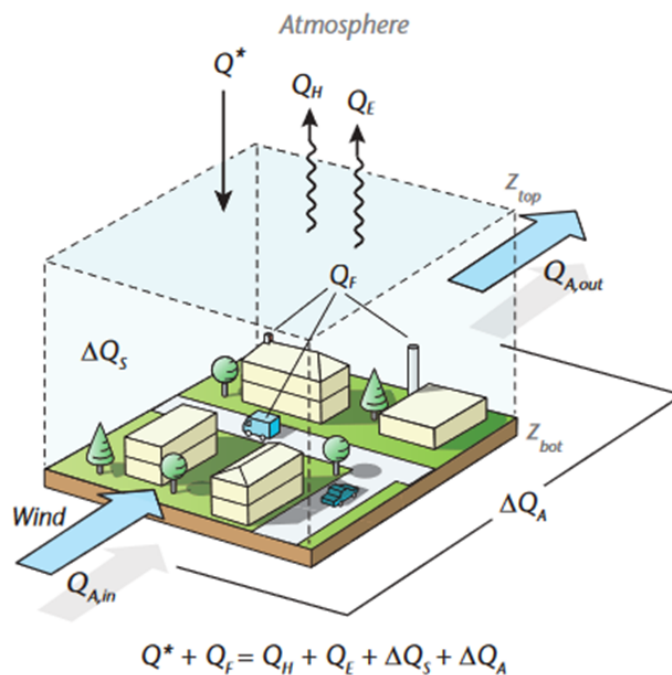


Figure 2.6: Schematic of the fluxes in the surface energy balance of a building-soil-air volume. The volume that extends from the top of the RSL ( $z_{top}$ ) down to a depth where there is no net conduction over the period of interest ( $z_{bot}$ ). (Source: Oke et al., 2017).

The entire balance is affected by environmental and meteorological conditions – such as temperature, humidity, wind speed, and radiative flux – at a volume’s boundary and the features of the urban landscape (Figure 2.7 (a)). Compared to rural areas, urban zones have higher anthropogenic heat flux ( $Q_F$ ) and denser building volumes, with buildings placed closely together. This leads to increased heat storage during daytime heat release at night-

time ( $\Delta Q_s$ ) and an overall increase in radiative flux  $Q^*$ . These features contribute to the UHI phenomenon, seen as higher average temperatures in the UCL than in rural areas. The UHI magnitude, referring to the temperature disparity between urban and rural air, increases after sunset when the air above urban surfaces cools more slowly than in rural air. The rate of nocturnal cooling also relies on the sky view factor; taller buildings and narrower streets minimize the sky's cooling effect. During the daytime, the UHI magnitude is generally smaller and can even be negative due to the shading caused by buildings or heat storage.

### Soil and building heat transfers at block scale

Figure 2.7 (b) presents the energy balance as subdivided into sub-balances pertaining to different urban elements - buildings, ground, and humans.

This thesis specifically aims to create a model for heat exchanges that impact thermal environments and chosen climatic variables ( $T_a$ ,  $T_{mrt}$ ,  $RH$  and  $v_a$ ). We employ a spatial modelling approach for these calculations at the block scale. The chosen air volume at this scale is further divided into air zones, which are illustrated as dotted squares in Figure 2.7 (b).

The heat flux involved in the heat exchange at the building surface and at the soil surface are the following:

- The convective heat flux density,  $\Phi_c$  [ $\text{W m}^{-2}$ ]: Forced convective heat exchange can be 3-4 times higher than LWR heat exchange (Mirsadeghi et al., 2013). This flux density can be expressed by the Newton's law of cooling (positive when entering the surface):

$$\Phi_c = h_c(T_a - T_s) \quad (2.3)$$

$$\text{Where : } \begin{cases} T_s \text{ is the surface temperature [K]} \\ T_a \text{ is the air temperature [K]} \\ h_c \text{ is the convection heat transfer coefficient [W m}^{-2} \text{ K}^{-1}] \end{cases}$$

$h_c$  depends on conditions in the boundary layer, which are impacted by surface geometry, the characteristics of fluid movement, and a range of thermodynamic properties of the fluid such as density, viscosity, thermal conductivity and specific heat. Any study of convection ultimately reduces to a study of the means by which  $h_c$  may be determined (Bergman, 2011). The  $h_c$  can be determined through analytical, numerical, and experimental methods. The analytical method is primarily suitable for specific flow regimes and straightforward geometries, such as plates or cylinders. Numerical methods use CFD to replicate the process of heat transfer in the boundary layer of a wall surface. Meanwhile, experimental methods involve running tests in a scaled wind tunnel or even full-scale experiments, but the latter option can be quite complex to implement. These experiments have led to the development of empirical laws used to compute and assess  $h_c$  in conjunction with both windward and leeward convective heat exchanges on a building's exterior, tailored to differing building heights



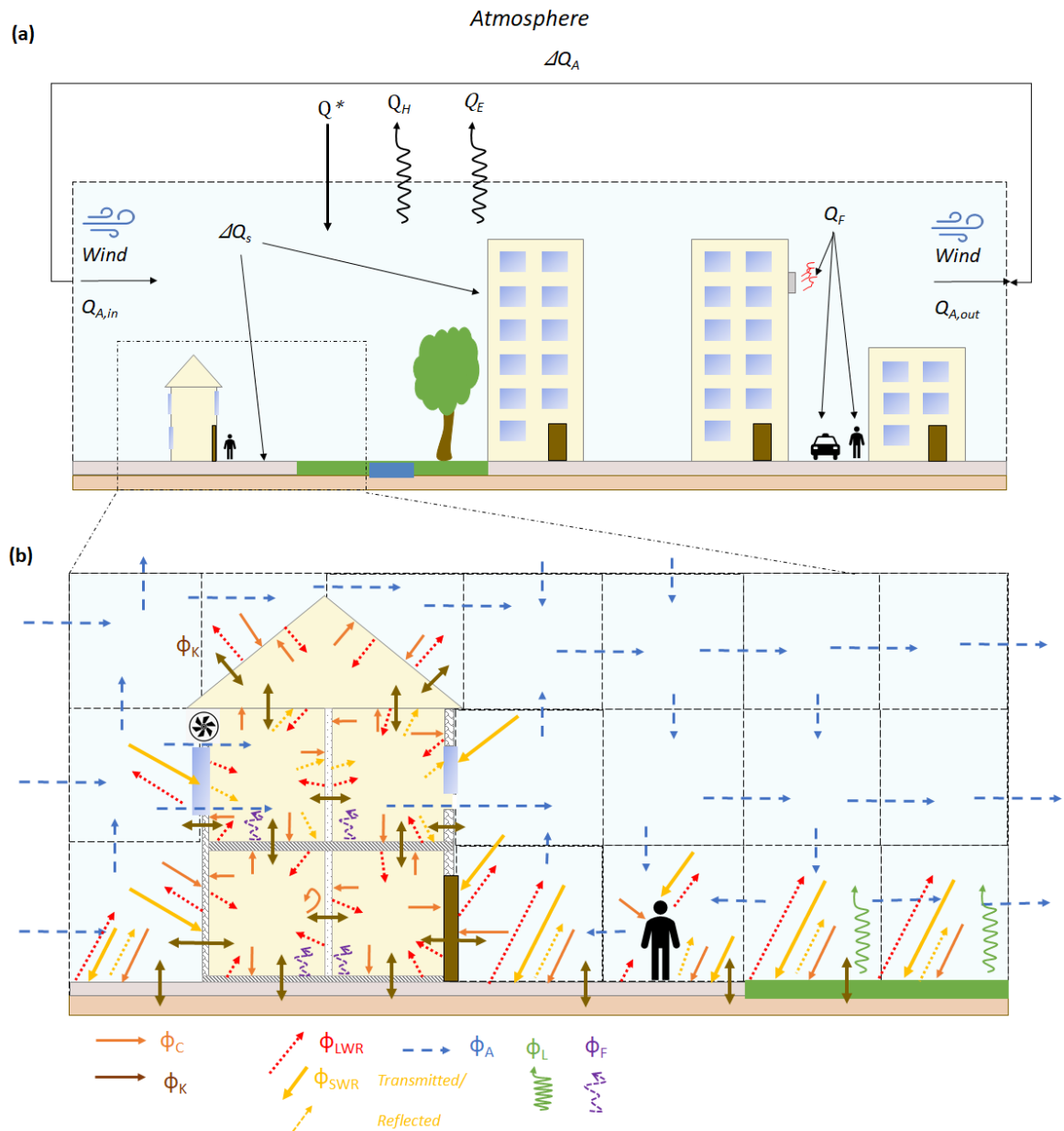


Figure 2.7: (a) Section of Figure 2.6. (b) Fluxes involved in the heat transfers at block scale. The air volume at the block scale is subdivided into air-zones :  $\Phi_A$  is the heat flux density exchanged by the air-zones by advection.  $\Phi_C$ ,  $\Phi_{SWR}$ ,  $\Phi_{LWR}$ ,  $\Phi_K$ ,  $\Phi_F$  and  $\Phi_L$  are respectively the convective heat flux density, the solar heat flux density, the net long wave radiation heat flux density, the conductive heat flux density, the sources/sink heat flux density and the latent heat flux density.

(Mirsadeghi et al., 2013).

- The solar heat flux density or short wave radiation (SWR) heat flux density,  $\Phi_{SWR} [W m^{-2}]$ : this flux results from the direct, the diffuse and the reflected flux from the surrounding surfaces. The solar heat flux reflected by a surface depends on its albedo (solar reflection factor) and on the direct and diffuse solar heat flux incident to the surface. More specifically for buildings, the transmission coefficient of transparent surfaces

(windows) influences the amount of incident solar flux transmitted in the building.

- The infrared radiative heat flux density or long wave radiation (LWR) heat flux density,  $\Phi_{LWR}[\text{W m}^{-2}]$ : for outdoors it is the infrared radiative heat flux exchanged with the sky and the surrounding surfaces and for indoors it is the infrared radiative heat flux exchanged between the indoor surfaces. This flux density depends on the surrounding surfaces temperatures and on the LWR emissivity of the considered and surrounding surfaces.
- The conductive heat flux density crossing a material,  $\Phi_K[\text{W m}^{-2}]$ : this flux depends on the physical nature of the medium expressed by the thermal conductivity  $\lambda[\text{W m}^{-1} \text{K}^{-1}]$  of the material.  $\lambda$  and the material thickness influence its thermal resistance, indicating its ability to restrict heat transfer through conduction (thermal insulation).

Another material property influencing the conductive heat flux is its thermal inertia, depending on the material density  $\rho [\text{kg m}^{-3}]$  and its specific heat  $C_p [\text{J kg}^{-1} \text{K}^{-1}]$ , which represents the ability of the material to store and release heat over time.

- The latent heat flux density,  $\Phi_L[\text{kg m}^{-3}]$ : is generally modelled for vegetation or evaporative soils.

Heat transfer related to air mass transfer is represented in Figure 2.7 (b) by the heat flux density exchanged by advection within air-zones ( $\Phi_A[\text{W m}^{-2}]$ ). This flux is positive when entering an air zone and depends on the mass flow rate ( $mfr[\text{kg s}^{-1}]$ ) and the temperature difference between the air zone and the incoming or outgoing flow. At the building interface, this flux pertains to mechanical ventilation, natural ventilation, and infiltration. For mechanical ventilation, the mass flow rate is usually regulated. In the context of natural ventilation and infiltration, it is necessary to understand that the mass flow rate ( $mfr$ ) that enters a building is contingent on both wind and air buoyancy forces. Moreover, this rate is also influenced by the pressure variance on the building's exterior. When the wind comes into contact with a building, a positive pressure, commonly referred to as "wind pressure", is generated on the side facing the wind. This pressure is typically measured using a pressure coefficient ( $cp$ ). The value of  $cp$  is subject to various factors like the wind's direction, speed, and the point of impact on the building's surface. The  $cp$  value signifies the pressure caused by the wind at a particular point on the building's facade relative to the dynamic wind pressure in an undisturbed airflow region. To measure the  $mfr$ , power pressure calculations related to wind pressure are conventionally employed, as explained in Section 3.2.1.

The heat source or sink,  $\Phi_F[\text{kg m}^{-3}]$ , as shown in Figure 2.7 (b), corresponds to anthropogenic heat flux. Specifically for indoor settings, this is connected to electrical and electronic equipment, human metabolism, energy and water systems, and latent heat emitted from human activity.

Please note that identical flux densities also apply to human beings, where the internal heat source  $\Phi_F$  is created from metabolic heat and the latent heat from respiration and

sweating. These heat exchanges are typically represented using varying levels of complexity in thermal balance models (Chapter 1).

### 2.1.2 Conclusion on the physical phenomenon to be modelled

From the current section, it is clear that to accurately model air temperature ( $T_a$ ) and relative humidity ( $RH$ ), we need to account for convective, advective, radiative, conductive, and latent heat exchanges. Additionally, airflow modelling is crucial due to its impact on convective and advective exchanges and it also helps in providing spatialized variables ( $v_a$ ). Lastly, for assessing the mean radiant temperature ( $T_{mrt}$ ), it is important to model the radiative heat exchanges between the body and surrounding surfaces. More in-depth hypotheses related to the physical phenomena that need to be modelled will be discussed in the following chapter.

## 2.2 Cooling solutions to be modelled in urban spaces and buildings

The aim of this section is to outline various indoor and outdoor cooling strategies for modelling. It provides an overview of primary cooling solutions employed to mitigate heat stress in urban areas and buildings.

### 2.2.1 Main observed indoors and outdoors cooling strategies

To tackle the increasingly prominent issue of urban overheating, outdoor cooling strategies are being employed by various stakeholders. These strategies operate at different scales, from city-wide to individual building measures, and are applied in both public and private spaces. The French Environment and Energy Management Agency (ADEME) categorizes these solutions as follows (ADEME, 2021):

- Grey solutions: These encompass energy systems and urban infrastructure, including coatings, urban furniture, and buildings.
- Green and blue solutions: These are often nature-based solutions utilising vegetation and water.
- Soft solutions: These involve behavioural and urban management adaptive strategies.

Figure 2.8 recaps the main measures implemented in urban spaces and inside buildings, categorized by solution typology and their impact on heat stress and heat strain (ADEME, 2021). The figure illustrates two levels of action impact: exposure-oriented actions and individual-oriented actions.

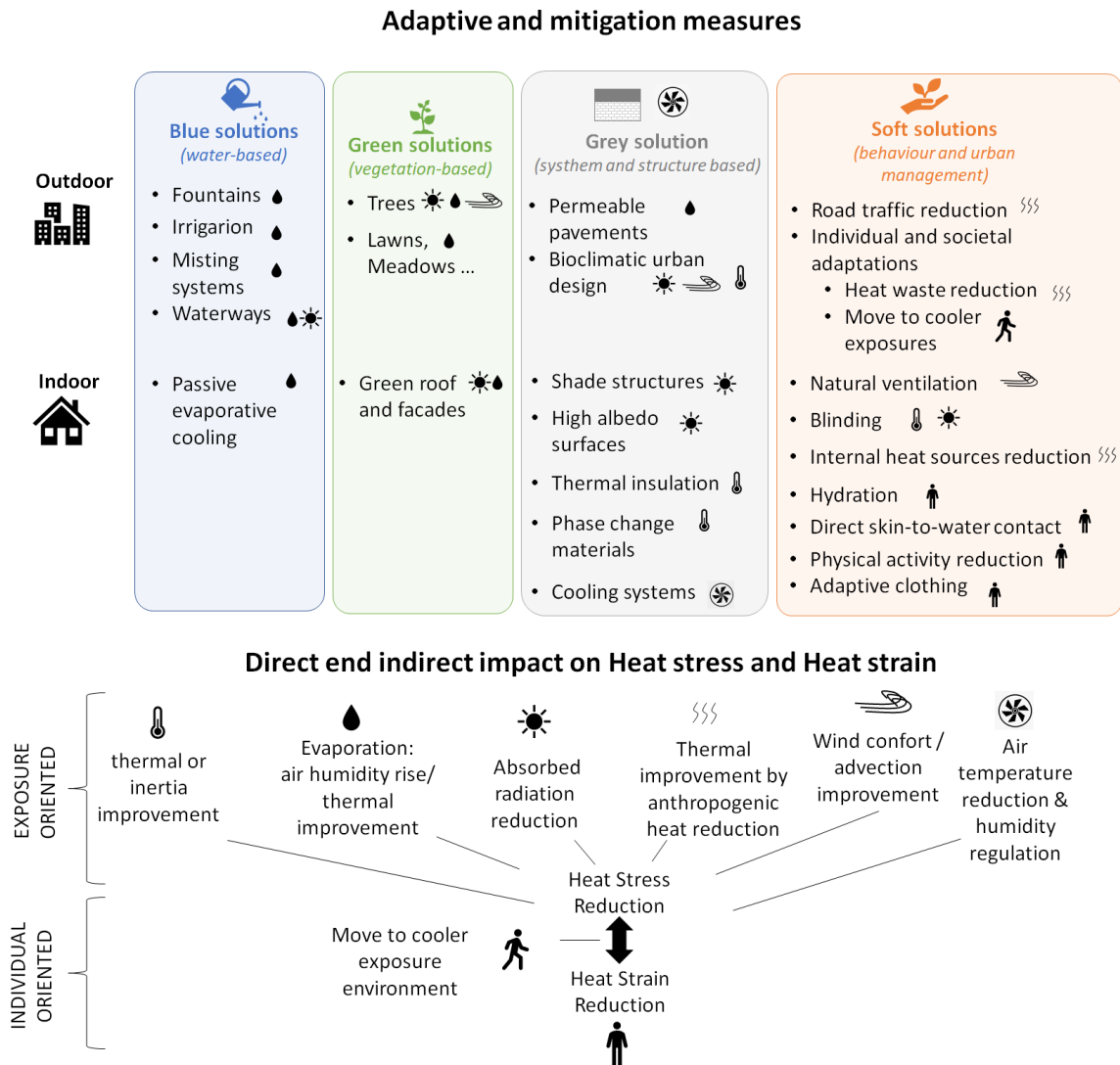


Figure 2.8: Adaptive and mitigation measures and their direct and indirect impact on heat stress and heat strain.

### Exposure oriented actions

Actions that influence exposure levels directly impact heat stress and, subsequently, heat strain individuals experience. This includes blue, green, grey, and some soft solutions. Blue solutions mainly harness the atmosphere’s cooling capacity through evaporation, primarily applied outdoors. When selecting these solutions, one should consider regional water resources, potential high costs, and associated issues (e.g., tiger mosquito). Green solutions, often employed in urban spaces or on building facades, revolve around trees. Trees do not just contribute to evaporative cooling; they also provide shade and a local breeze, enhancing thermal comfort. Grey solutions mainly aim to improve thermal insulation and inertia, reduce absorbed radiation, and enhance airflow paths. Grey solutions may also include making the space mineral without making it impermeable (such as reservoir-structure pavements or permeable surfacing) and infiltrating rainwater. Among these solutions, ur-

ban structure-related ones usually take longer to implement and cost more. Air conditioning system-related solutions are commonly implemented in houses but have adverse environmental effects (e.g., primary energy use, increase of urban overheating due to outdoor heat release). Lastly, soft solutions focus on urban and social policies (including health), as well as changes in individual behaviours (e.g., applying passive cooling solutions in buildings). These solutions also encompass societal adaptations, altering individuals' lifestyles to reduce anthropogenic heat (for instance, modifying work schedules to decrease traffic or avoiding air conditioning installation).

### **Individual oriented actions**

Individual-oriented actions do not alter the overall environment, but they influence personal heat stress and strain through cooling methods directly affecting the body. Examples include staying hydrated, wearing appropriate clothing, reducing physical activities, or moving to cooler environments. Common havens from excessive heat include shaded parks, air-conditioned spaces, or waterfront areas. However, socio-economic factors limit access to these places, underscoring social-spatial inequalities in coping with urban overheating (Allagnat, 2020). Taking into account the real dynamics of individual exposure, shaped by daily routines and adaptive behaviour, allows a more accurate evaluation of the actual heat stress individuals experience.

### **2.2.2 Selected cooling strategies**

This thesis investigates the effects of various cooling strategies on heat stress and strain. It focuses on the most commonly used indoor and outdoor cooling measures. Indoor strategies include window shading and natural ventilation via open windows. Outdoors, common measures include urban greening and replacing impervious soil with trees and permeable soil. In particular, this thesis examines the latter measure. It will also explore individual efforts to mitigate heat, such as relocating to cooler environments.

## **2.3 Modelling thermal environments for heat stress and heat strain assessment**

This section outlines the modelling requirements for a spatialized daily and seasonal heat stress assessment for indoors and outdoors at a block scale. These requirements result from the main objective of the thesis presented and the previous selected physical phenomenon and cooling measures. Based on a selection of urban canopy models UCMs, urban micro climate models McMs, building energy models BEMs, and radiation models, it investigates to what extent the selected models cover the modelling requirements.

### 2.3.1 Modelling requirements

The selected modelling approach should accurately assess the spatialized heat stress in a dwelling and its immediate surroundings across daily and seasonal spans and meet various modelling requirements. Figure 2.9 illustrates the progression from the primary thesis question to the modelling requirements. The central question is, "**How to assess daily and seasonal heat stress in the building and its immediate surroundings considering their mutual interaction?**".

The primary objective in modelling pertains to the development of a numerical modelling method. This method will assess heat stress and strain over daily and seasonal exposure periods, factoring in the interplay of indoor and outdoor thermal environments within residences and their immediate surroundings. Ideally, it would be implemented at a block scale with a spatial resolution that could range from 1 to 30 m.

The model should provide output climatic variables of  $T_a$ ,  $T_{mrt}$ ,  $RH$  and  $v_a$  on a hourly basis. Physical phenomena, such as advective, radiative, convective, conductive, and latent heat flux, will need to be modelled to predict these variables. These heat fluxes should be modelled with an understanding of the interplay between urban atmospheres, buildings, and soil.

Critical urban features to model in relation to the atmosphere include buildings and both permeable and impervious soil areas. It is especially important to accurately model the impact of radiative fluxes, particularly solar flux, on outdoor environments. In addition, modelling should reflect how outdoor radiative fluxes affect individuals, represented by the outdoor  $T_{mrt}$ . This consideration involves modelling the interaction between an individual's surface and surrounding radiation.

Airflow coupling variables involved in heat exchange interactions are the convective heat transfer coefficient ( $h_c$ ), the mass flow rate ( $mfr$ ), and the pressure coefficient ( $cp$ ). For a comprehensive analysis of these interactions, it is crucial to estimate these coupling variables reliably.

Additionally, to assess heat stress accurately, the model must estimate pedestrian wind speed ( $v_a$ ). In terms of the interaction between building occupants and the building itself, the model should simulate common cooling strategies such as natural ventilation, window blinds, ventilation systems, and internal heat sources.

Concerning the model's spatial domain, it should be capable of modelling on a block scale (roughly 300 m  $\times$  300 m), including buildings. The horizontal resolution should reflect the dimensions of differing urban surfaces, encompassing areas from the room to the ground while adjusting for vertical resolution, which represents a pedestrian level and building floors.

The time exposure scale covers the seasonal period with an hourly time resolution, which, as seen in Chapter 1, is acceptable when using unsteady thermoregulation models

for the assessment of heat strain indices. Finally, the modelling approach should integrate a post processing stage providing the identified climatic variables and selected heat stress and heat strain indices identified in Chapter 1.

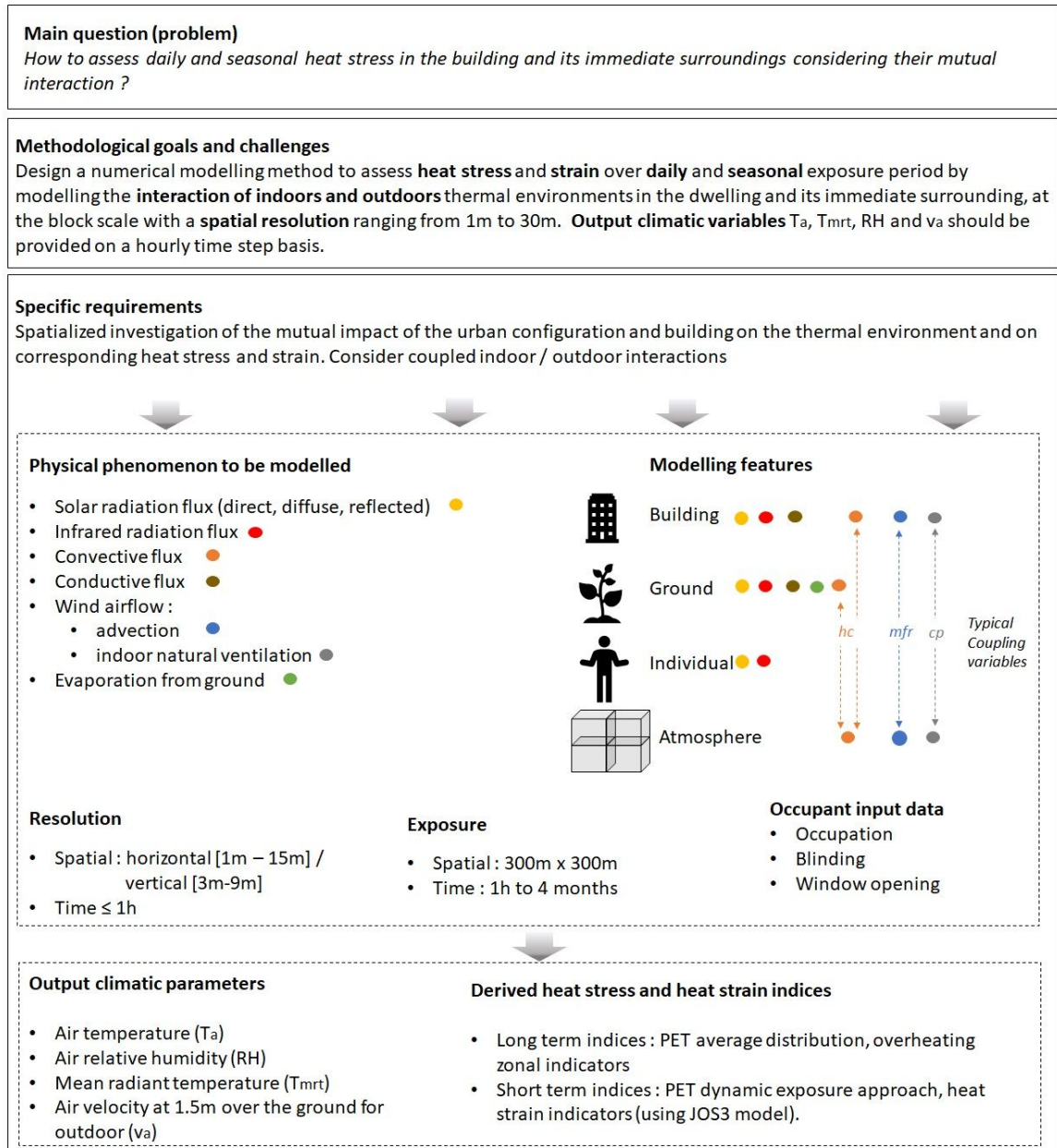


Figure 2.9: Modelling process design: from the main question to the modelling requirements.

### 2.3.2 Applicability of BEMs, McMs, UCMs and radiative models for seasonal and daily heat stress assessment

The aim of this segment is to evaluate how well current UCMs, McMs, BEMs and radiation models correspond to the goals set in this thesis. Additionally, if these models fail to meet

the objectives, we will define the needed requirements to resolve this. We will conduct an analysis using a selection of nine BEMs, McMs, UCMs, and radiation models from building to city scale. :

- For the UCMs: TEB (Masson et al., 2000; Masson, 2000).
- For the McMs: SOLENE Microclimat (Vinet, 2000; Bouyer et al., 2009) and ENVI-met (Bruse and Fleer, 1998), EnviBatE (Bozonnet, 2005; Gros, 2014)).
- For the BEMs: EnergyPlus (Crawley et al., 2000), CitySim Pro (Robinson et al., 2009) and the MyBEM toolchain (Bouquerel et al., 2019).
- For the radiative model: RayMan (Matzarakis and Mayer, 1996) and LadyBug (Sadeghipour Roudsari, Pak, and Viola, 2013).

The four elements outlined in Figure 2.10, which categorize the modelling requirements, are as follows: (i) the modelled physical phenomena, (ii) individual behaviour, (iii) model outputs, and (iv) the model's spatial and temporal scale and resolution.

### **(i) The physical phenomena modelled**

The accuracy of climate model outputs hinges on the model's ability to emulate the physical phenomena occurring in the real world. Therefore, a balance must be struck between representing all of the actual physical phenomena comprehensively and highlighting the vital physical aspects needed to meet the modelling objective. For our current needs, the essential physical phenomena to be modelled encompass sensible and latent heat balances on both indoor and outdoor surfaces. The necessity to account for interactions between indoor and outdoor environments incorporates modelling the advective heat flux and convective heat flux between the air and the adjacent surfaces, taking into account both indoor and outdoor conditions. The exchange of heat between the air and surrounding surfaces comprises radiative fluxes, convective heat flux, conductive heat flux, and latent heat flux, particularly for permeable soil, vegetation, or water ponds. It is important to model low vegetation, trees, or water ponds to represent cooling measures used in urban areas accurately. To predict local wind speed and heat exchanges by advection accurately, it is crucial to model the influence of urban geometry on airflow.

Current models primarily focus either on indoor or outdoor modelling. Among the considered McMs, SOLENE Microclimat, ENVI-met and EnviBatE cover both outdoors and indoors. However, SOLENE Microclimat, ENVI-met, are primarily oriented towards outdoor thermal comfort. These models take into account various urban surfaces such as vegetation, ground, water ponds, and building envelopes. They involve related physical phenomena that contribute to the energy balance. Importantly, all three models incorporate an explicit 3D urban geometry. In both SOLENE Microclimat and ENVI-met, outdoor airflow is modelled using a CFD RANS approach that incorporates turbulence and buoyancy effects (only in Envi-Met). This method significantly extends the computational time. In EnviBatE, employs an empirical zonal model for airflow, which appreciably shortens the computational



### 2.3. Modelling thermal environments for heat stress and heat strain assessment

		BEMs					UCMs		McMs				Radiative models							
		Energy Plus		MyBEM		CitySim Pro		TEB		EnviBatE		SOLENE microclimat		Envi-MET		RayMAN		LadyBug & HoneyBee		
		B	O	B	O	B	O	B	O	B	O	B	O	B	O	B	O	B	O	
MODELED PHENOMENA	<b>Airflow</b>	Nodal	NA	NA	NA	NA	NA	Empirica I	NA	Zonal	NA	CFD Rans	NA	CFD Rans	NA	NA	NA	NA	NA	
	<b>Sensible heat balance</b>	Nodal	NA	Nodal	NA	Nodal	Nodal	Nodal	Nodal	Nodal	Nodal	Finite volume	Nodal	Finite volumes	Nodal	NA	NA	NA	NA	
	<b>Latent Heat balance</b>	Nodal	NA	NA	NA	Nodal	Nodal	NA	Nodal	Nodal	Nodal	Finite volume	NA	Finite volumes	NA	NA	NA	NA	NA	
	<b>Surface Heat balance</b>																			
	<i>Ground / floor</i>	x	NA	x	x	x	x	x	x	x	x	x	x	x	x	x	NA	NA	NA	NA
	<i>Wall, Roofs, windows</i>	x	NA	x	x	x	x	x	x	x	x	x	x	x	x	x	NA	NA	NA	NA
	<i>Vegetation</i>	x	NA	NA	x	NA	x	NA	NA	NA	NA	x	NA	x	x	NA	NA	NA	NA	NA
	<i>Water ponds</i>	NA	NA	NA	NA	NA	x	NA	NA	NA	NA	x	NA	x	NA	NA	NA	NA	NA	NA
	<b>Outdoor SWR</b>																			
	<i>Direct (sky)</i>		x		x		x		x		x		x		x		x		x	x
	<i>Diffuse (sky)</i>		x		x		x		x		x		x		x		x		x	x
	<i>Reflected ground</i>		x		x		x		x		x		x		x		x		x	x
	<i>Reflected Building, mask, vegetation</i>		x		x		x		x		x		x		x		NA		NA	x
	<i>Sky and surface view factor</i>		x		x		x		x		x		x		x		x		x	x
	<b>Indoor Transmitted SWR</b>	Distributed on surfaces		On floor		Distributed on surfaces		NA		On floor & reflected on surfaces		Distribute d on surfaces		NA						
<b>Outdoor LWR</b>																				
<i>With the sky</i>		x		x		x		x		x		x		x		x		x	x	
<i>With ground</i>		x		x		x		x		x		x		x		x		x	x	
<i>With Buildings</i>		x		x		x		x		x		x		x		NA		NA	x	
<i>With vegetation</i>		NA		x		x		x		NA		x		x		NA		NA	NA	
<b>Indoor LWR</b>	Between surfaces & Heat load		Heat load		Heat load		NA		Between surfaces & Heat load		NA		NA		NA					
<b>Model Geometry</b>	Explicit 3D	Explicit 3D	Explicit 3D	Explicit 3D	Implicit	Explicit 3D	Explicit 3D	Explicit 3D	Explicit 3D	Explicit 3D	Explicit 3D	Explicit 3D	Explicit 3D	Explicit 3D	Explicit 3D	Explicit 3D	Explicit 3D	Explicit 3D	Explicit 3D	
<b>INDIVIDUAL BEHAVIOUR</b>	<b>Exposure path</b>	NA	NA	NA	NA	NA	NA	NA	NA	NA	NA	NA	NA	NA	NA	NA	NA	NA	NA	
	<b>On building</b>																			
	<i>Blinding</i>	x		x		NA		NA		NA		NA		NA		NA		NA		
	<i>Opening windows</i>	x		x		NA		NA		NA		NA		NA		NA		NA		
	<i>Occupation</i>	x		x		x		NA		x		NA		NA		NA		NA		
<b>MODEL OUTPUTS</b>	<b>Climatic output</b>																			
	<i>Ta</i>	x	x	x	x	x	x	x	x	x	x	x	x	x	x	x	x	x	Input	Input
	<i>RH</i>	x	x	x	x	x	x	x	x	x	x	x	x	x	x	x	x	x	Input	Input
	<i>va</i>	Fixed	NA	NA	NA	NA	x	NA	x	NA	x	NA	x	NA	x	NA	x	NA	Input	Input
	<i>T<sub>int</sub></i>	x	NA	NA	x	NA	x	x	x	x	x	x	x	x	x	NA	x	x	x	x
<b>EXPOSURE</b>	<b>Temporal</b>	Hour to year	Hour to year	Hour to year	Hour to year	Hour to year	Hour to year	Hour to year	Hour to year	Hour to year	Hour to 15 days	Hour to 15 days	Hour to 15 days	Hour to year	Hour to year	Hour to year	Hour to year	Hour to year	Hour to year	
	<b>Spatial</b>	Room to Building	Room to block(300mx300 m)	Building to District (~1km <sup>2</sup> )	District to Town	Room to District (~1km <sup>2</sup> )	Block (300mx300m)	Block (300mx300m)	Block (300mx300m)	Block(300m x300m)	Block(300m x300m)	Block(300m x300m)	Block(300m x300m)	Building to District (~1km <sup>2</sup> )	Building to District (~1km <sup>2</sup> )	Building to District (~1km <sup>2</sup> )	Building to District (~1km <sup>2</sup> )	Building to District (~1km <sup>2</sup> )	Building to District (~1km <sup>2</sup> )	
<b>RESOLUTION</b>	<b>Temporal</b>	hour	Adaptative	hour	hour	hour	hour	hour	hour	hour	5 min	30 min	hour	hour	hour	hour	hour	hour	hour	
	<b>Spatial</b>	< 1 m	m	m	100 m	m	m	m	m	m	m	0.5 m	m	< 1 m	< 1 m	< 1 m	< 1 m	< 1 m	< 1 m	

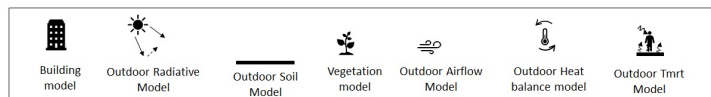


Figure 2.10: BEM and urban microclimate models comparison.

time. A SWR radiative model, present in SOLENE Microclimat and Envi-met, handles direct, diffuse, and multi-reflecting radiation from buildings, vegetation, and soil, but only outdoors. For indoor scenarios, SWRs are projected onto the floor and, reflected off other surfaces in EnviBatE and dispersed across surfaces in SOLENE Microclimat. Both SOLENE Microclimat and Envi-Met utilise a unique model to evaluate radiative exchanges with the

human body for  $T_{mrt}$  assessment. Envi-BatE's SWR model is grounded on the SOLENE Microclimat model.

For the three mentioned McMs, LWR fluxes account for the radiant heat from the sky and radiant heat exchange between surfaces. Inside LWR, fluxes are only modelled in EnviBatE. The building model in these McMs is a nodal model with fewer modelling options compared to more detailed nodal BEMs like EnergyPlus or MyBEM.

Among the considered BEMs, EnergyPlus offers a wide variety of cooling strategy modelling options, such as ventilation, shading, and cooling systems. However, there are certain approximations made while modelling the building's interaction with its outdoor environment. For example, empirical laws are used for convective heat exchange coefficients, LWR heat exchanges are either oversimplified or ignored entirely, and air temperature data is imported directly from external weather files. Further, outdoor temperatures are not spatialized. Models like MyBEM and CitySimPro provide a more consistent modelling approach for both indoor and outdoor environments, aiming to more accurately evaluate indoor energy consumption by comprehensively considering the radiative conditions of the outdoor environment. They do this by explicitly modelling the 3D urban geometry. These models also integrate outdoor radiative models, considering the effect of the surface cover on the direct, diffuse, and multi-reflected SWR and LWR heat exchanges. However, they do not model airflow both indoors and outdoors. Radiative models such as RayMan, Lady-Bug, and HoneyBee are specifically designed to calculate outdoor radiative heat exchanges for thermal comfort purposes. These models use a simplified representation of the human body and its position to compute the outdoor mean radiant temperature ( $T_{mrt}$ ).

In UCMs like TEB, which are either multi-layer or single-layer, the urban structure is represented by parameters indicative of a neighbourhood, such as building height, street width, and depth. Furthermore, these models distinguish between different types of surfaces, such as natural surfaces, vegetation, roads, roofs, walls, etc. They also incorporate a simplified building energy model (BEM), which comprises a thermal zone and a wall that exchanges heat with the external environment. In these UCMs, air and surface heat exchanges occur through a system of aerodynamic resistances, which are affected by wind conditions and atmospheric stability. The wind velocity within the canyon is calculated using empirical relationships, while temperature and humidity are determined by the heat balance at the surface and top of the canyon. However, UCMs have a limitation: their capacity to realistically model spatial thermal environments.

### **(ii) The individual behaviour**

This criteria addresses both the individual's exposure and the impact the occupant's behaviour has on the building's thermal environment. As discussed in Chapter 1, considering an individual's exposure path provides a more accurate assessment of experienced heat stress, particularly within a dynamic environment. However, when evaluating heat stress associated with a specific location, the dynamic exposure path becomes irrelevant. None

of the current Models and Building Environment Models (McMs and BEMs) incorporate a dynamic exposure path; they only account for climate variables associated with a specific location. While most advanced BEMs such as EnergyPlus and MyBEM can simulate occupant actions that influence a building's thermal environment, they still do not cover a variety of cooling strategies utilised by occupants when under heat stress, such as local evaporative cooling or the use of a local fan.

#### **(iii) The model outputs**

Chapter 1 establishes that the critical variables to evaluate heat stress include  $T_a$ ,  $RH$ ,  $T_{mrt}$ , and  $v_a$ . Therefore, it is key to have a model that can compute these outputs in both indoor and outdoor environments. However, no single model can encompass the range of these climate outputs in both environments. Only CFD and zonal-based models are able to compute airflow, and they only work outdoors (Evi-mET, SOLENE Microclimat, EnviBatE) due to the absence of control over window openings in the respective building model. This lack of control limits the precise prediction of indoor airflow. Additionally, any errors or approximations in managing indoor/outdoor airflow exchanges could influence the  $T_a$  and  $HR$  assessment. When considering outdoor  $T_{mrt}$ , it is only computed by McMs, radiative models, and BEMs with an external radiative model, as they explicitly consider the outdoor environment. Indoors,  $T_{mrt}$  is often calculated via simplified models that do not take into consideration the individual's location. There are models that directly provide steady heat stress indices for indoor environments (EnergyPlus) or for outdoor environments (Envi-met, SOLENE Microclimat and RayMan).

#### **(iv) Model spatial and time exposure scale and model spatial and time resolution**

Among the chosen models, EnviBatE, EnviMet, and SOLENE Microclimat are best suited for block scale evaluations. CitySimPro, RayMan, LadyBug, and Honey Bee are capable of handling scales ranging from block to district, while TEB is designed for district to town scale. Aside from TEB, the models can achieve a spatial resolution of one meter, which makes them ideal for assessing individual heat stress. In terms of temporal exposure and resolution, models such as Envi-met and SOLENE Microclimat are better equipped for short simulation periods due to their extensive computational times. Contrarily, other models are capable of handling seasonal or annual exposure periods. To summarize, out of the chosen models, EnviBatE, CitySimPro, and MyBEM meet the requirements for both temporal and spatial exposure and resolution.

This analysis shows that current models aren't capable of accurately representing all climate variables necessary for assessing indoor and outdoor heat stress while also considering the relationship between indoor and outdoor spaces.

Couplings between BEMs and UCMs (UWG and TRNSYS (Palme et al., 2017), UWG and EnergyPlus (Salvati, Roura, and Cecere, 2015)) or chaining between BEMs and McM (SOLENE Microclimat and BuildSysPro (Merlier et al., 2019), EnviMET and EnergyPlus (Yang et al., 2012), OpenFoam (RANS) and TRNSYS (Dorer et al., 2013)) have been attempted with

the objective to better consider the impact of the outdoor environment on building energy consumption (Lauzet, 2019). Among those coupling, the ones coupling McM with BEM may be most suitable for our needs, as McM offer a spatial representation of the thermal environment. However, the CFD computations used in these combinations are unsuitable for seasonal simulation periods.

Hence, a targeted modelling approach, able to meet the needs outlined in Section 2.3.1, needs to be developed.

## 2.4 Specific problem formulation, expected outcomes and modelling issues

Section 2.3 highlights the need for a custom modelling approach. This approach should include both indoor and outdoor spatial representation of climatic variables, adhering to the modelling needs outlined in Section 2.3.1.

The need to simulate both indoor and outdoor thermal conditions necessitates a combined modelling approach that handles building interiors and their immediate microclimate.

Moreover, to simulate airflow without the extensive computation times of CFD, a zonal modelling approach seems optimum for outdoor environments. A pressure-based modelling approach can effectively handle indoor environments, simulating the advective heat exchange between the outdoors and indoors, as well as different indoor zones. A zonal outdoor model coupled with a nodal indoor model is suitable, given that the zonal structure can portray heat stress on an individual scale. Remarkably, the outdoor zonal model can project average wind speed at the pedestrian level.

These initial considerations lead to the formulation of this thesis's specific modelling problem.

### Specific problem formulation

The specific problem at hand involves creating and integrating a microclimate zonal model (McZM) with a BEM to establish a spatial depiction of heat stress during various seasonal and daily periods. It is designed to assess heat stress using both Eulerian and Lagrangian exposure approach. The effectiveness of this spatial approach used in the zonal model is determined by its ability to distinguish differing levels of heat stress across various zones. The aim is to identify priority areas where cooling interventions are needed and designate heat shelter zones.

The overall efficacy of the coupled McZM and BEM model approach is evaluated in terms of its capability to meet modelling requirements. This specifically includes its ability

to model some commonly used indoor and outdoor cooling strategies. The intention is to allow for a comparative study of heat stress reduction achieved by implementing varied indoor and outdoor cooling strategies, not just in terms of overall heat stress but also in relation to spatially delineated heat stress.

Furthermore, the effectiveness of the integrated McZM and BEM modelling method is evaluated based on possible enhancements in indoor air temperature forecasting. This is in comparison to predictions given when using oversimplified external conditions of outdoor air temperature or external convective heat transfer coefficients  $h_{c_{ext}}$ .

### **Expected outcomes**

Expected outcomes of the thesis include identifying the advantages and constraints of a combined McZM and BEM approach in assessing seasonal and daily heat stress and strain. This modelling approach is expected to:

- Provide a zonal representation of the indoor and outdoor thermal environments in order to identify potential heat shelters and the most heat stressed zones.
- Compare and assess the effectiveness of cooling strategies in reducing heat stress.
- Assess heat stress related to individual displacement.

The thesis also identifies expanded research perspectives relating to the modelling approaches of combined indoor and outdoor thermal environments, as well as heat stress indices and their connected models.

### **Modelling issues**

The modelling issues addressed in this thesis include:

- The implementation of an outdoor airflow zonal model capable of considering the impact of the urban geometry and the surface properties on the airflow. This model should consider different wind speeds and directions and ensure mass conservation between zones.
- The definition of an appropriate zoning form and resolution adapted for heat stress assessment.
- The ability to ensure thermal and airflow coupling between indoors and outdoors. This refers to the model's ability to accurately forecast the McZM and BEM airflow coupling variables ( $mfr$ ,  $cp$ ,  $h_{c_{ext}}$ ) over time. It is essential for maintaining consistent airflow both indoors and outdoors. Moreover, it models natural ventilation, mechanical ventilation, and infiltrations well, including convective heat exchanges between the building envelope and outdoor air zones.

## 2.5 Modelling strategy

To address the thesis's specific issue and resolve identified modelling challenges, the strategy involves establishing an airflow zonal model. This model will utilise mass flow rate ( $mfr$ ) predictions drawn from steady-state Reynolds-Averaged Navier-Stokes (RANS) CFD simulations. The simulations will depict an urban form representative and a range of inlet wind speeds and directions.

The CFD simulations will provide the data set needed to implement predictive models of the average  $mfr$  at the air zone volume interface, accommodating any wind speed and direction. These averaged  $mfr$  values will then be used to calculate the advective heat traversing the outdoor air zones.

The same set of RANS CFD simulations will also be utilised to calculate the average external convective heat transfer coefficient ( $h_{c_{ext}}$ ) on the ground and the building's external surfaces, as well as the  $cp$  on these surfaces. Like the  $mfr$ , predictive models will be put in place for  $h_{c_{ext}}$  and  $cp$  computations.

To address the zoning structure and resolution issue, the recommended approach is to determine the appropriate scale for identifying heat shelters or areas of thermal tension which correspond to individuals' living spaces. This means that the model zoning aligns with the rooms or floors of a building and extends outside to coincide with the building's exterior. As such, outdoor air zone surfaces match the corresponding building surfaces.

The dynamic resolution of the coupled airflow and energy balance equations, along with the computation of SWR fluxes, results in extended computational times. In order to decrease these times, our modelling strategy includes separating the airflow and SWR calculations from the energy balance computations.

We've therefore divided the process into three stages: an initial stage that pre-calculates radiative and airflow, a second stage that dynamically resolves the energy balance within the BEM and McZM and a final stage of post-processing.

This modelling approach is implemented using the MyBEM toolchain, which conveniently pre-integrates a solar flux pre-calculation model, view factor for LWR flux calculation, and dynamic resolution of the building's energy balance through a BEM. The thesis aims to develop a McZM, coupled it with the BEM in the MyBEM toolchain, and implement necessary post-processing for calculating heat stress indices.

### 2.5.1 Model architecture

The global model architecture of the coupled McZM and BEM is subdivided into different components with different levels of coupling shown in Figure 2.11.

### Model components overview

The different model components are:

1. **The solar radiation model:** it allows the calculation of the incident solar radiation on surfaces in the outdoor environment (building, ground, individual)
2. **The long-wave radiation model:** it allows the calculation of long-wave exchanges between surfaces in the outdoor environment (building, ground) and the long-wave irradiation received by an individual standing outdoors.
3. **The outdoor airflow model:** it allows for the calculation of outdoor airflow ( $v_a$  and  $mfr$ ),  $h_{c_{ext}}$  on exterior surfaces (building, ground) and  $cp$  on building surfaces. This model also includes the energy balance resolution between air zones by ensuring the mass conservation.
4. **The outdoor soil model:** it consists of three kinds of soil (impervious soil, evaporative bare soil, low vegetative soil). This model is coupled with the outdoor airflow model through a surface energy balance. The two outdoor airflow and soil models form the McZM.
5. **The building dynamic energy model (BEM):** it allows the calculation of airflow in the building related to natural ventilation, infiltration, and mechanical ventilation using a nodal method. This model is coupled with the BEM and the McZM.
6. **The indoor airflow model:** it allows the calculation of airflow in the building related to natural ventilation, infiltration, and mechanical ventilation, using a nodal method. This model is coupled with the BEM and the McZM.
7. **The outdoor mean radiant temperature model:** it computes the outdoor mean radiant temperature of a standing person.

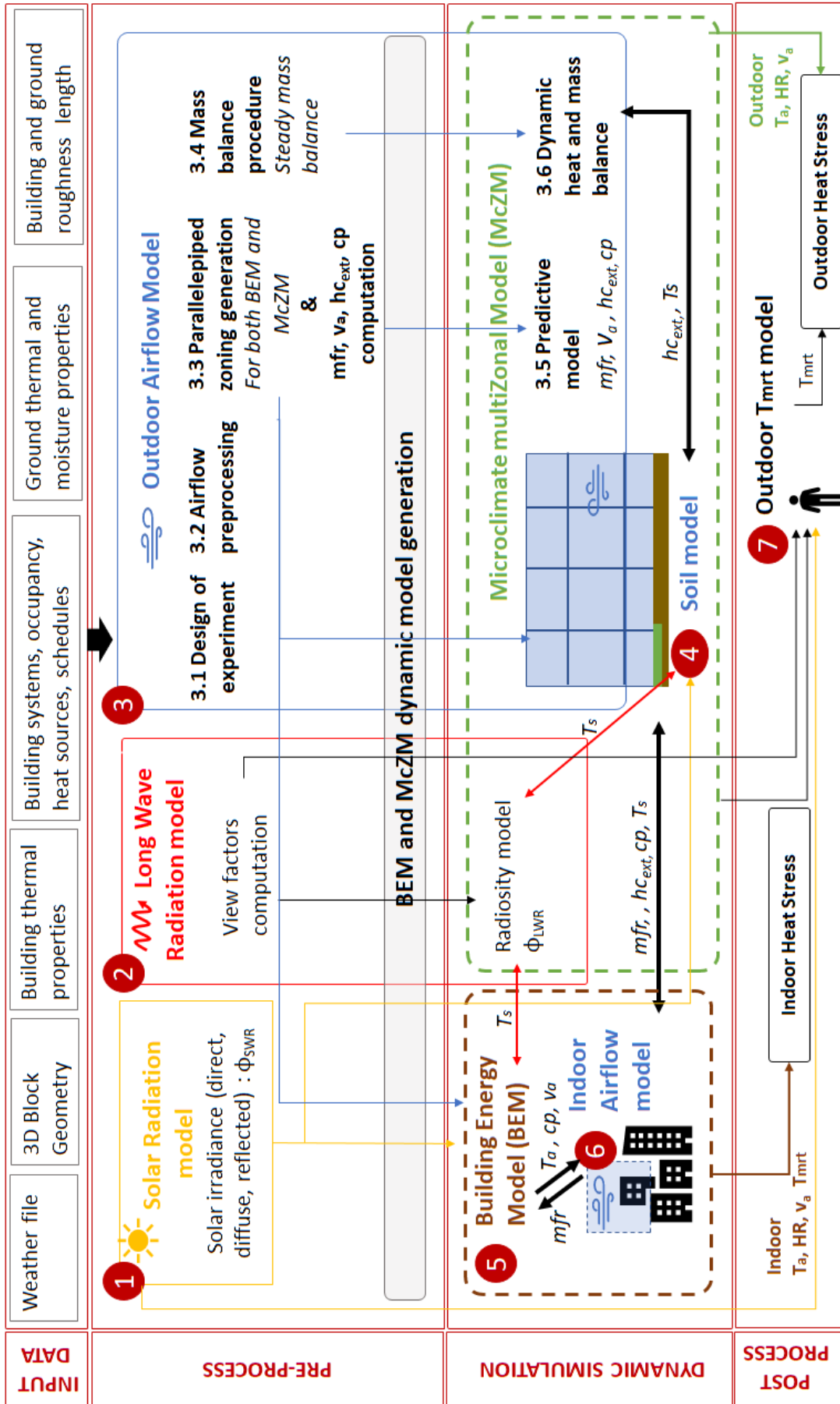


Figure 2.1.1: Global model architecture: model components vision. The double arrow indicates that the models are coupled and the one-way arrow indicates that the data is going from one model to another in the direction of the arrow.



---

## Modelling workflow

### Pre-processing stage

The pre-processing stage is divided into a radiative pre-processing, airflow pre-processing and the BEM and McZM dynamic model generation. The radiative pre-processing involves calculating the incident solar flux on surfaces and the form factors used for the calculation of long-wave radiative flux. The airflow pre-processing involves calculating the airflow for a range of wind directions and velocities, generating the zoning of the BEM and McZM and performing a first mass balance adjustment to correct any imbalances generated during the zoning creation.

The pre-processing stage is split into three sections: radiative pre-processing, airflow pre-processing, and the construction of BEM and McZM dynamic models. Radiative pre-processing involves determining the solar flux incident on surfaces and the view factors needed to compute LWR flux. Calculating airflow for varying wind directions and speeds, creating the zoning of the BEM and McZM, and performing an initial mass balance adjustment to rectify any imbalances from the zoning creation process are all part of the airflow pre-processing. The final stage of pre-processing involves using the PyRosette package to generate the BEM and McZM models in Modelica automatically. The PyRosette package, specifically developed for the Merrubi project (2014–2018) <sup>1</sup> to automate building model construction in Modelica, now incorporates new features that allow for automatic microclimate model generation. Pre-processed irradiation and airflow data serve as inputs for the dynamic simulation.

The pre-processing stage uses several types of input data, including weather data, the 3D layout of the outdoor environment and building, the building's thermal setup (including properties of surfaces thermal bridges), information about the building's usage (like configuration of the heating or cooling system, heat sources, and schedules for occupancy and usage), properties of surface roughness, and wind and turbulence profiles at the inlet.

### Dynamic simulation stage

The dynamic simulation consists of running the coupled BEM and McZM over a specific simulation period. These dynamic models are formulated in the Modelica language within the Dymola environment. The equations that make up the dynamic building and urban microclimate models are solved using the Differential Algebraic System Solver (DASSL), which is a high-order, multi-step solver with implicit step-size control. This solver is frequently used for the numerical solution of implicit systems of differential and algebraic equations. To negate the effects of default parameterized initial conditions on the energy balance, an initialization period (roughly 15 days of simulation) is required. The dynamic simulation yields outputs that are used in the post-processing stage, including the air temperature ( $T_a$ )

---

<sup>1</sup>Mrrubi or "Methods for exploiting the valuable resources of the bioclimatic building within its urban context" is a research project founded by the French Research Agency

and relative humidity ( $RH$ ) in each air zone, the mean radiant temperature ( $T_{mrt}$ ) in each indoor air zone, and the surface temperatures ( $T_s$ ) of the building and soil surfaces, which are essential for calculating the outdoor  $T_{mrt}$  in the post-processing stage.

### Post-processing stage

Post-processing involves computing heat stress indices such as PET for each zone in the zoning. This calculation relies on climatic data such as  $T_a$ ,  $RH$ ,  $v_a$ , and  $T_{mrt}$ . Aside from the external mean radiant temperature ( $T_{mrt_{ext}}$ ), the other climatic variables are derived from the dynamic simulation results. ( $T_{mrt_{ext}}$ ) is calculated via a specific model that takes into account the surface temperatures  $T_s$ , view factors, and incident solar radiation from the dynamic simulation and the radiative pre-processing stage.

Model components 1, 2, and 6 belong to the MyBEM modelling chain (EDF software), while components 3, 4, 5, and 7 were developed specifically for this thesis.

Figure 2.12 provides a detailed overview of the software and data formats used at each step of the modelling workflow.

## 2.6 Conclusions

This chapter presents the physical principles that regulate the urban microclimate, along with an overview of the cooling measures used in buildings and urban areas. This information enables the identification of physical phenomena and effective cooling tactics, laying down the groundwork for modelling requirements for a spatial and temporal heat stress assessment.

The chapter then conducts a multi-criteria analysis featuring commonly used UCMs, McMs, BEMs and radiative models. The analysis underscores the need to establish a customised modelling approach. This approach would facilitate a spatial portrayal of heat stress climatic variables both indoors and outdoors over a season or a day. The analysis also leads to the identification of a specific problem and the proposition of a modelling strategy.

Part II of this thesis outlines the development and validation of a modelling strategy. It is divided into two chapters: Chapter 3, which discusses the components and validation methods for outdoor and indoor airflow models, and 4, which focuses on the SWR, LWR, BEM, soil, and  $T_{mrt}$  model components and their respective validation methods.

Due to the complex interaction of physical phenomena and governing parameters in urban microclimates, validating microclimate models through real measurements can be challenging. It necessitates the definition of a specific experimental protocol for a validation case where model parameters and boundary conditions are well understood. Thus, this thesis opts to assess the accuracy of the McZM using a modular comparative approach, referencing established models or experimental data.

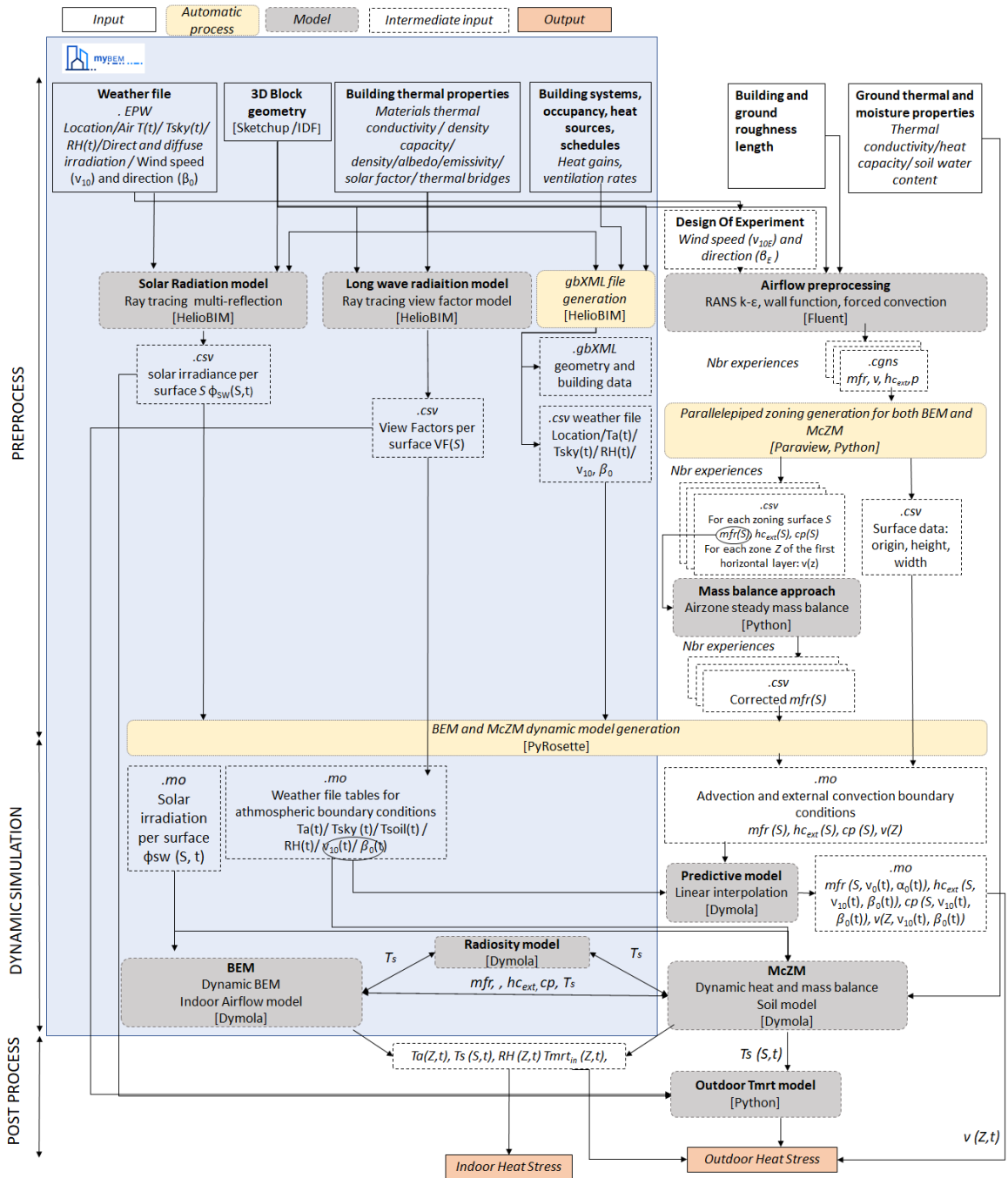


Figure 2.12: Global model architecture : data workflow.



## **Part II**

# **Coupled Microclimate Zonal Model and Building Energy Model**



# Chapter 3

## Outdoor and indoor airflow models

This chapter aims to delineate the components of the outdoor and indoor airflow model within the coupled McZM and BEM framework, as shown in Figure 2.11's components (3) and (6). It proposes a validation methodology for each model component via comparison to experimental data or numerical simulations. Further, it provides an outline for parameterizing these airflow models, intended for use in the Confluence Ydeal Square case study discussed in Chapter 5.

### Contents

---

<b>3.1 Outdoor airflow model</b>	<b>80</b>
3.1.1 Site description	80
3.1.2 Model description	81
3.1.3 Model validation	98
<b>3.2 Natural ventilation model</b>	<b>105</b>
3.2.1 Physical principles of natural ventilation	105
3.2.2 Model description	106
3.2.3 Model verification	111
<b>3.3 Conclusions</b>	<b>113</b>

---

### 3.1 Outdoor airflow model

This section presents the outdoor airflow model component from the coupled McZM and BEM (Featured as component (3) in Figure 2.11), forming the primary contribution of this thesis. It also outlines the method of validating the CFD simulation implemented in the modelling procedure. To exemplify the pre-processing phase, we use the Ydeal Square block in Confluence as the site. The same location is adopted for the application case study detailed in Part III (Chapter 5)). A detailed synopsis of the site follows in the upcoming sub-section.

#### 3.1.1 Site description

The Ydeal Square block in the Lyon Confluence district comprises five buildings including offices, retail outlets, student residences and dwellings (Figure 5.1).

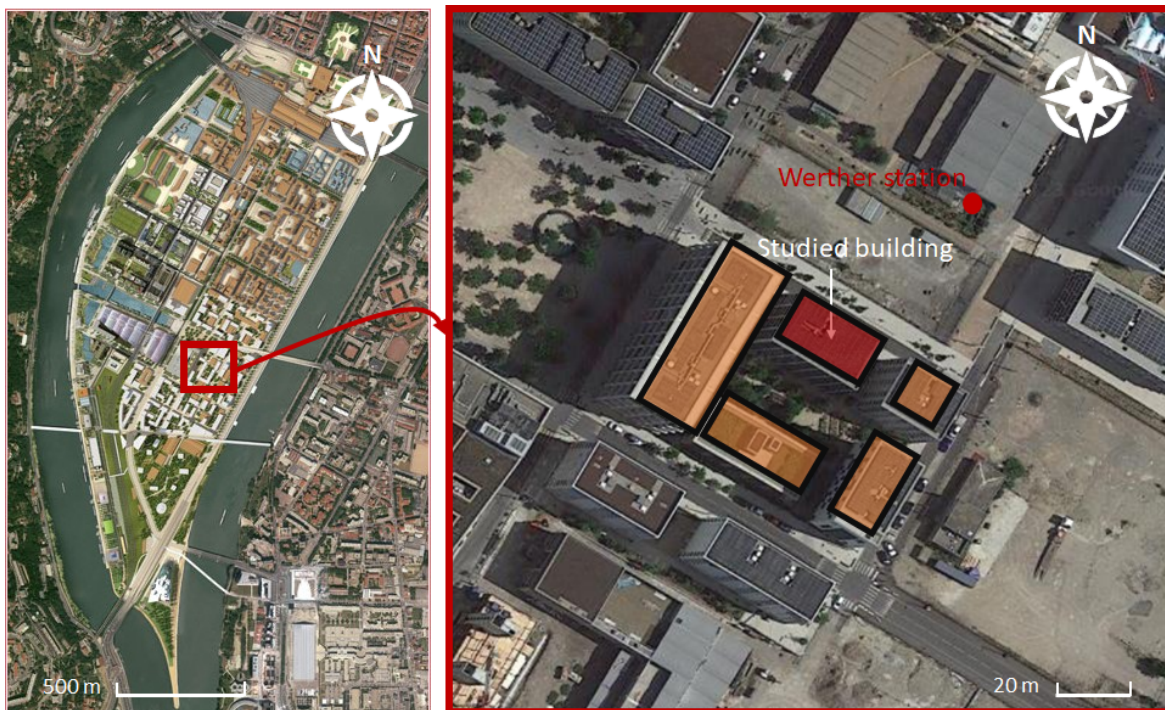


Figure 3.1: Confluence Ydeal Square: global view of the square and view of the target building and weather station.

This site exemplifies recent trends in eco-neighbourhood projects in urban planning. The on-site weather station, positioned northeast on top of the Maison de la Confluence building, about 10 m high, makes it particularly conducive for the McZM model application. The North-South prevailing winds, depicted in Figure 3.2, are unaffected by urban geometry since most of the new buildings were not yet constructed during that period. Figure 3.3 demonstrates this by comparing wind direction distributions between the Confluence



station and the Bron meteorological station, situated outside the urban scope, from July to mid-September 2020.

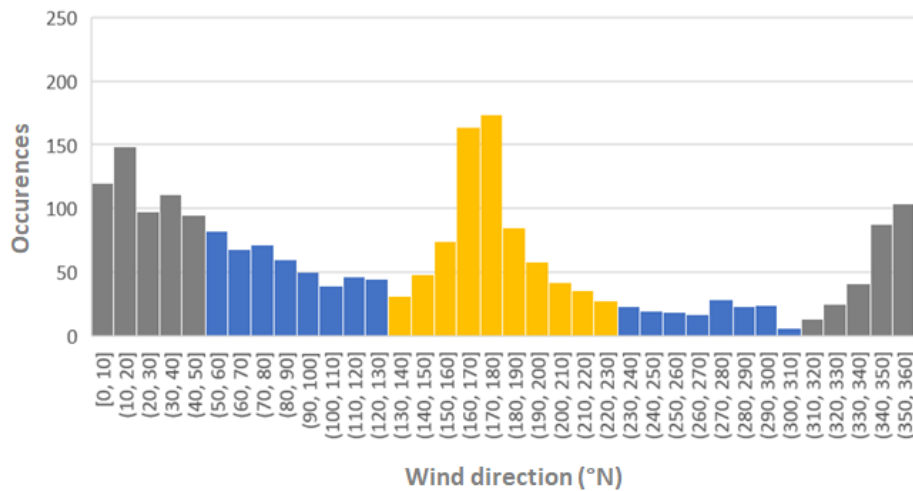


Figure 3.2: Confluence wind direction distributions from June to September 2020. Yellow bars represent Southeast to Southeast wind direction. The blue bars represent Southwest to Northwest and Northeast to Southeast wind direction. The gray bars represents Northwest to Northeast wind direction. The  $y$  axis represents the wind direction occurrences and the  $x$  axis represents the wind direction ranges in degrees from North.

### 3.1.2 Model description

The airflow model consists of two main phases: pre-processing and dynamic simulation.

The pre-processing stage is justified by the need to conduct simulations over long periods (such as the summer season) that would not be feasible with reasonable computation times using dynamic flow resolution. This stage includes:

1. The design of the experiment, where a weather file analysis is performed in order to identify the wind speed and wind direction ranges using a Sobol method.
2. The airflow pre-processing, where a steady RANS realizable  $k - \varepsilon$  ( $rk - \varepsilon$ ) CFD simulation is performed for different wind speeds and directions.
3. The zoning generation and computation, where a parallelepiped zoning is generated and the average  $mfr$  is computed for each air zone surface, the average  $v_a$  is computed for each air zone at pedestrian level, the average  $h_{c_{ext}}$  is computed for each exterior building and soil surface, and the average  $cp$  is computed for each exterior building surface.
4. The mass balance procedure, where a balancing method is implemented to correct the mass imbalance induced by the zoning generation.

5. The choice of the interpolation model to predict the outcome variables, where an analysis of predictive models leads to the choice of interpolation for the  $mfr$ ,  $v_a$ ,  $h_{c_{ext}}$  and  $cp$  prediction corresponding to a general wind speed and direction.

The dynamic simulation stage conducts a dynamic heat and mass balance for the coupled McZM and BEM. The subsequent sections detail the various steps of these two stages.

### 1. Design of experiment

The initial step encompasses outlining the experimental design (DOE) for the CFD simulations targeting airflow pre-processing. The resultant variables to be utilised as input data for the dynamic zonal model include:

- The average mass flow rates crossing the zoning surfaces ( $mfr$  [ $\text{kg s}^{-1}$ ]).
- The average external convective heat transfer coefficient ( $h_{c_{ext}}$  [ $\text{W m}^{-2} \text{K}^{-1}$ ]) at the building envelope surfaces and outdoor ground surfaces.
- The average pressure coefficients ( $cp$ ) corresponding to the building facades.

Additionally, the mean velocity ( $v_a$ ) is computed for each outdoor air zone during the post-processing stage in Figure 2.11 for the calculation of the PET index. To set the input variables for the design of experiment (DOE), it is essential to pinpoint the parameters affecting the three dependent variables as well as identify which parameters alter and which remain constant. The three dependent variables are influenced by a range of parameters, including geometry, surface properties (like roughness and porosity), inlet velocity profile (which includes shape, direction, and speed), surface temperatures, and other environmental conditions (such as temperature and pressure). Within these parameters, the temperatures, wind speed, and wind direction show time-dependent variations in the dynamic model.

The impact of surface temperatures is considered negligible compared to the influence of wind for the  $mfr$  and  $cp$  variables. The prevailing assumption is that the flow is primarily driven by wind forces rather than buoyancy forces. Though this presumption is plausible in urban settings with high wind speeds, it becomes dubious when wind speed averages around  $2 \text{ m s}^{-1}$ . Mei et al. (2022) critically reviewed urban buoyancy-driven flow and modelling methods, introducing buoyancy parameters to gauge the dominance of wind-driven forces over buoyancy-driven ones. The buoyancy parameter data, distributed across various urban configurations and surface temperature increases, demonstrates that buoyancy consistently dominates at wind speeds below  $1.5 \text{ m s}^{-1}$ .

Regarding the influence of the surface temperature on  $h_{c_{ext}}$ , we assume that the predominant convection type is forced convection. However, as shown in the analysis of the Richardson number presented in Appendix C, both natural and forced convection are present. In conclusion the hypothesis consisting in neglecting natural convection encounters limitations

with high-temperature differences (around 18 K) between air and surface, combined with low inlet wind speed (less than  $0.1 \text{ m s}^{-1}$ ).

Assuming that the airflow path is only influenced by the wind speed and the geometry and roughness properties, the input variables selected to define the experimental plan are the wind direction  $\beta$  and wind speed  $v_{10}$  at 10 m height at the weather station. After identifying these variables, it is crucial to specify their variability range. This is done by cross-analyzing the wind speeds and directions from the meteorological data file to be implemented in the dynamic simulation.

Figure 3.3 illustrates the distribution of wind speeds and directions based on data collected by the Confluence weather station from June to September 2020. This distribution reveals several varying areas where a design of experiment (DOE) can be set up. The maxi-

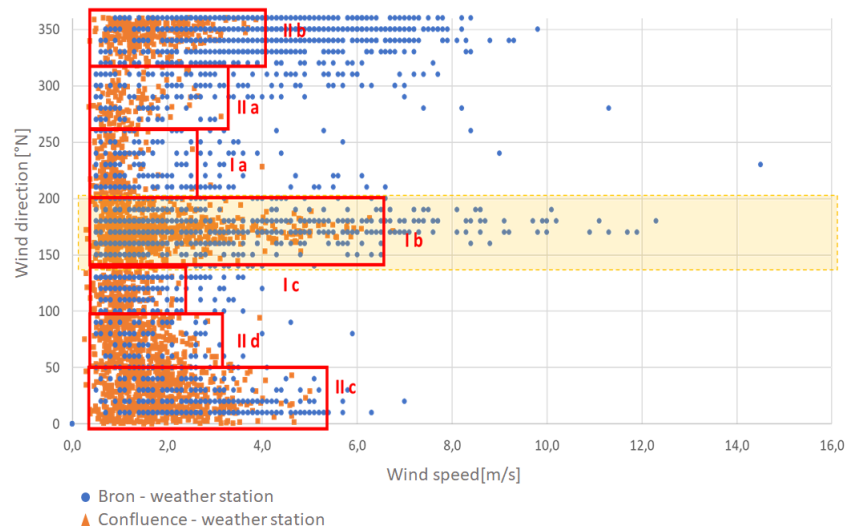


Figure 3.3: Segmentation of the DOE based on the Wind speed and orientation distribution for the Confluence urban weather station and Bron rural weather.

mum and minimum values for each DOE are derived from this figure, segmented by wind speed and direction for both the Confluence urban weather station and Bron rural weather data. The density of data points for each experimental design was determined by prior observations of airflow at various domain locations, with wind speed and direction varied independently. As illustrated in Appendix D, a nearly linear relationship can be established between the inlet wind speed and the mass flow rate ( $mfr$ ) crossing a surface for a given wind direction.

Given the nearly linear relationship between outcome variables ( $mfr$ ,  $h_{c_{ext}}$ ,  $cp$ ) and wind velocity at a specific point for a particular wind orientation (Appendix D), we can initially choose a point density equivalent to one velocity point per wind orientation. The domain's geometric complexity does not offer a broad rule for adjusting wind orientation variations. A recommended strategy is to change the wind orientation by an average of  $5^\circ$ , thus providing a detailed representation of airflow variation. With these presuppositions, we can

form a design of experiment (DOE) using Sobol sequences (from the Sobol Python library by John Burkardt and Corrado Chisari), which generate pseudo-random numbers with definite statistical properties and enable a substantial decrease in variance. We can fine-tune this density later based on the predictive model's quality. The setup of all experimental designs is depicted in E.

The case study from Chapter 5 focuses on wind directions between  $150^\circ\text{N}$  and  $190^\circ\text{N}$ . This range records the most occurrences of wind direction, as illustrated in Figure 3.2. Nineteen CFD simulations are conducted to analyze the varying wind speeds and directions.

## 2. Airflow pre-processing

The airflow pre-processing is performed by CFD using a steady RANS approach together with a  $rk - \epsilon$  turbulence model and a standard wall function to model the near-wall flow region. The computational domain size is defined accordingly to the recommendations of CFD simulation best practice guidelines (Tominaga et al., 2008, Blocken, 2015, Blocken et al., 2009). Table 3.2 provides a summary of the features of the chosen mesh alongside recommendations from relevant literature.

In the Ydeal Square case study, the computational domain encompasses a study area made up of five buildings around the target building, as well as a surrounding area, made up of blocks that signify distant hurdles. While these hurdles play a significant role in the airflow model, they will not be included in the final dynamic energy balance model. The transition from the square's actual geometry to a simplified cubic form is illustrated in Figure 3.4.

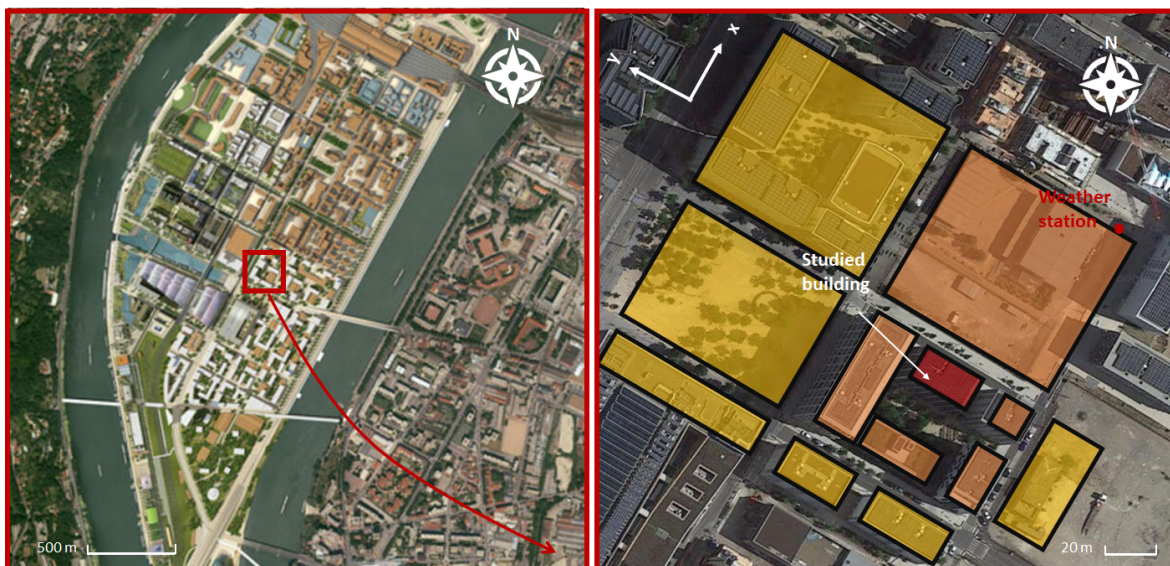


Figure 3.4: Confluence district plan and zoom on the Ydeal square block. Horizontal view.

The corresponding CFD domain is shown in Figure 3.5, where the main buildings are

represented within the dashed square area.

Table 3.1: Computational domain recommendation and adopted values.

Computational domain properties	Recommendations	Adopted value
Blockage ratio	$< 3\%$	3%
Lateral and top boundary	$\geq 5H_{max}$ away from the building	$5H_{max}$
Outflow boundary top boundary	$\geq 10H_{max}$ away from the building	$10H_{max}$

Table 3.2: Meshing recommendation and adopted values.

Mesh properties	Recommendations	Adopted value
Resolution near the buildings	Approximately 1/10 of the building scale	Building edges from 0.5 m to 1 m (smallest dimension 10 m)
Nbr. of cells per building side	$\geq 10$	Respected
Nbr. of cells before 2m height (for an accurate estimation of pedestrian wind speed)	3 to 4	Respected
First cell height	$> K_s \approx 10z_0$	Respected
Growth Rate	$< 1.3$	1.2
Mesh type	Prisms for the boundary layer surfaces and tetrahedral for the remaining cells.	Tetrahedral
Total mesh number		1 833 812
$y^*$ (for wall function)	$20 < y^* < 500$	Respected

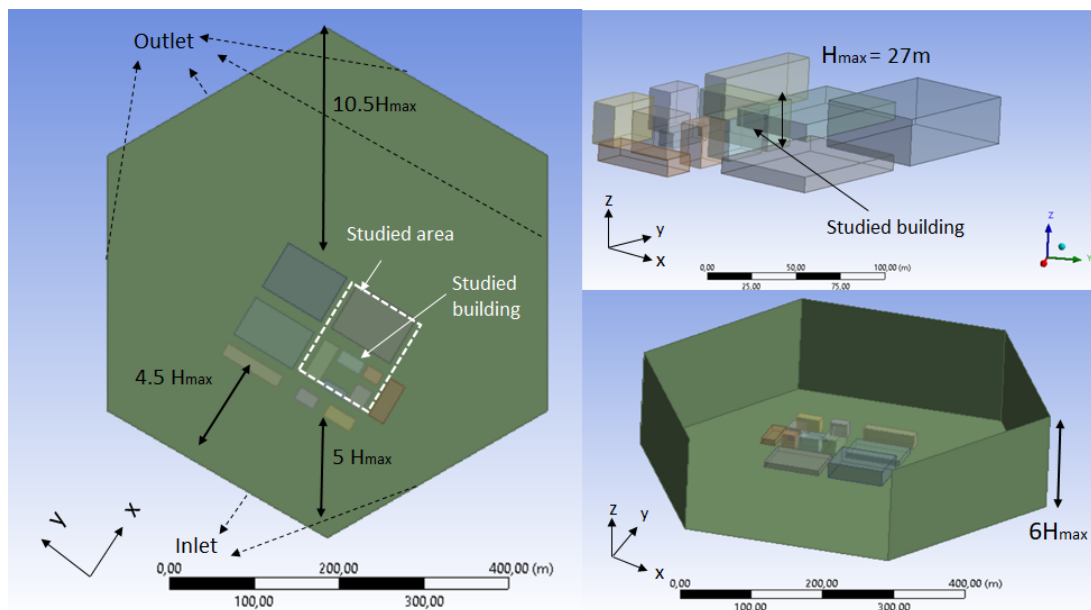


Figure 3.5: CFD domain.

$y^*$  in Table 3.2 is an adimensional number corresponding to (3.1):

$$y^* = \frac{\rho C_\mu^{1/4} K^{1/2} y}{\mu} \quad (3.1)$$

Where :

- $y$ : is the normal distance from the wall to the center of the first cell adjacent to the wall [m]
- $K$ : is the turbulent kinetic energy [ $\text{m}^2 \text{s}^{-2}$ ]
- $C_\mu$ : is a coefficient equal to 0.09 [-]
- $\rho$ : is the air density [ $\text{kg m}^{-3}$ ]
- $\mu$ : is the air dynamic viscosity [ $\text{kg m}^{-1} \text{s}^{-1}$ ]

The meshing is shown in Figure 3.6. Boundary conditions are described in Table 3.3.

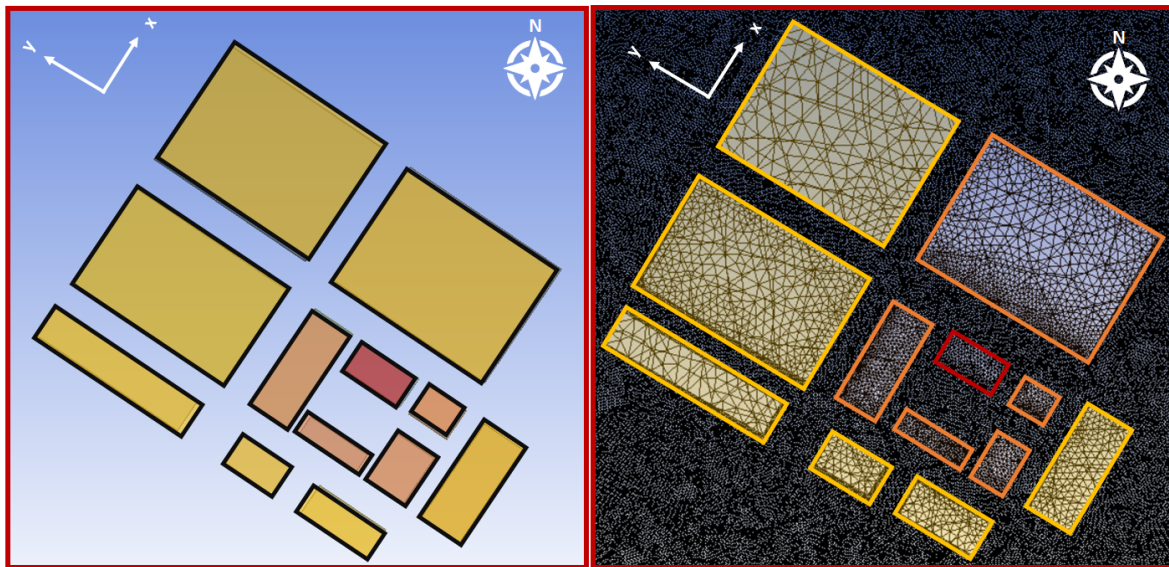


Figure 3.6: Geometry to and mesh for the CFD computation. Horizontal view.

The air is considered an incompressible perfect gas with a fixed temperature. The buoyancy effect is not considered. To compute the heat transfer coefficient, the hypothesis of 20 °C temperature difference between the inlet air, wall, and ground surface is considered. This difference corresponds to what can be observed between the air temperature and the wall temperature during the day when the sun is high.

Table 3.3: Adopted boundary conditions.

Boundary conditions	Kinematic	Temperature
Inlet	$u_x(z) = u^*/k \ln((z + z_0)/z_0) \cos(\alpha_w)$ $u_y(z) = u^*/k \ln((z + z_0)/z_0) \sin(\alpha_w)$ $K(z) = u^{*2}/C_\mu^{1/2}$ $\epsilon(z) = u^{*3}/k(z + z_0)$	$Ta = 22^\circ\text{C}$
Outlet	Pressure outlet	$Ta = 22^\circ\text{C}$
Top and sides	Symmetry	
Ground	$z_0 = 0.03 \text{ m}$	$Ts = 42^\circ\text{C}$
Walls	$z_0 = 10^{-9} \text{ m}$	$Ts = 42^\circ\text{C}$

The atmospheric boundary layer friction velocity  $u^*$  is calculated from a specific velocity  $v_{10}$  at reference height 10 m as:

$$u^* = k \frac{v_{10}}{\ln((z + z_0)/z_0)} \quad (3.2)$$

$$\text{Where : } \begin{cases} k: \text{ is the von Karman constant } = 0.42 \\ v_{10}: \text{ is wind velocity at 10 m height } [\text{m s}^{-1}] \\ z: \text{ is the height considered } [\text{m}] \\ z_0: \text{ is the roughness length } [\text{m}] \end{cases}$$

For the calculation of the turbulent kinetic energy  $K$ ,  $C_\mu$  is a constant generally taken equal to 0.09 and  $\alpha_w$  represents the wind direction in the orthonormal coordinate system  $x$ ,  $y$ ,  $z$ .

When using the wall function the equivalent sand-grain roughness height  $k_s$  is used instead of  $z_0$ .  $k_s$  refers to small-scale surface roughness. In Ansys/Fluent CFD code, the following relation relates  $k_s$  and  $z_0$ :

$$k_s = 9.793 \frac{z_0}{C_s} \quad (3.3)$$

Where  $C_s$  is a configurable roughness constant set here to 1.  $z_0$  values are fixed by referring to the updated Davenport-Wieringa roughness classification (Blocken, 2015). As the directing most influencing obstacles in the computed domain are explicitly modelled, it was decided to consider for the ground  $z_0 = 0.03 \text{ m}$  corresponding to the country with low vegetation (e.g. grass). For the walls a hypothesis of smooth walls is considered.

A CFD simulation is performed for each pair of control variables (wind speed and orientation) defined in the DOE described in Section 3.1.2.

The resolution method used is a pressure and velocity coupled scheme. The software employed for conducting the CFD simulation is Ansys Fluent 2020. The convergence is

examined with respect to the residual criteria of a minimum order of magnitude of  $10^{-4}$  recommended by Tominaga (2008). In our case, it was set to  $10^{-4}$  for the mass balance and  $10^{-6}$  for velocity components, energy, turbulence, and viscosity.

### 3. Zoning generation and computation

This step requires constructing a coarser mesh (or zoning) from the detailed mesh utilised in CFD computations. Shifting to a coarser mesh with pre-computed flow fields aids in decreasing simulation time during the resolution of the energy balance.

The zoning, in this case, is represented by parallelepipeds arranged within a cartesian coordinate system of  $x$ ,  $y$ , and  $z$  parameters. The arrangement aligns with the urban layout, particularly with the buildings. This ensures that the zoning division correlates with the thermal zoning applied to the building model. Typically, the first zoning level's height, represented by  $z$ , aligns with the ground floor height of common buildings, usually measuring between 2.5 m and 3 m. We refer to this as the pedestrian level. This height is also suitable for studying the thermal comfort of an upright individual. CFD simulation produces cell data, which is then imported into Paraview 5.9.1. Automatic zoning is generated with this data, facilitated by a Python program running within Paraview. The zoning is created using operations such as "clip" and "slice." Whenever a slice cuts through a cell in the CFD mesh, interpolation is utilised to work out the cut portion's corresponding cell value. Towards every slice of the zoning, a surface  $mfr$ , an averaged  $h_{c_{ext}}$  and an averaged  $cp$  are calculated. Only the averaged  $h_{c_{ext}}$  on the building envelope and soil surfaces and the averaged  $cp$  on the building envelope surfaces are considered. Horizontal slices are also formed mid-height of the first level of the air zones (at 1.5 m height) to compute the mean value of  $v_a$ .

This zoning does not adapt to the evolution of flow profiles, making the airflow inconsistent in each zone. Despite this inconsistency, the zoning approach is still valid because its primary goal is not to model the flow profile in each zone but rather to estimate the advective heat exchanges between zones. Each zone is viewed as a control volume with uniform air temperature, density, and velocity. Ultimately, quadrilateral zoning is simpler to apply than zoning based on arbitrary shapes. Figures 3.7 and 3.8 depict the zoning formation for the Ydeal Square case study.

Following the establishment of the zoning, the trio of outcome variables detailed in Section 3.1.2 ( $mfr$ ,  $h_{c_{ext}}$  and  $cp$  averages) are calculated for each zoning surface. Moreover, the average  $v_a$  for pedestrian-level air zones is computed for every CFD simulation result gained from Section 3.1.2. The zoning surfaces are represented in a Python dictionary. This data is sequentially processed to maintain mass conservation in each air zone and across the entire domain.



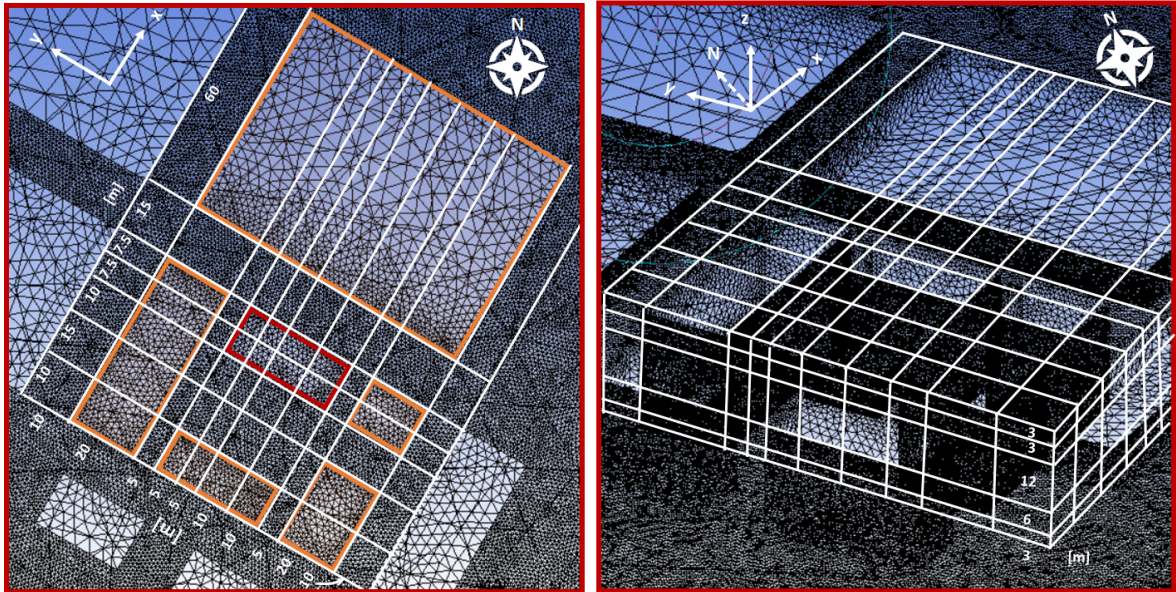


Figure 3.7: Transition from the fine mesh to a coarser zoning. Horizontal view and 3D view showing the vertical sections.

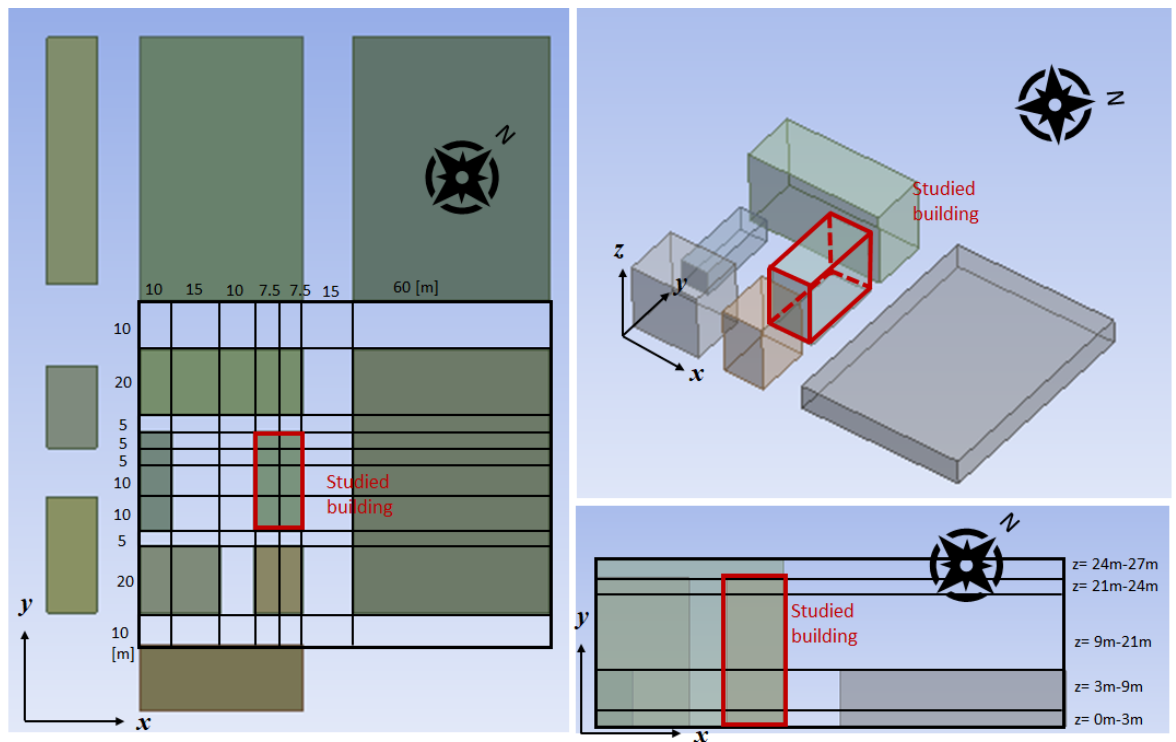


Figure 3.8: Zoning implemented in the Ydeal Square case study (Confulence), horizontal view, vertical view and 3D view.

#### 4. Mass balance procedure

The mass conservation principle mandates that the amount of air entering a control zone, depicted here as an air zone in the zoning, should equal the amount of air exiting. This

principle is upheld in each control volume during the CFD resolution. Imbalances can occur during the transition from a fine CFD mesh to zoning due to the spatial discretization not aligning perfectly. These imbalances are addressed through a balancing procedure. This procedure entails maintaining the pre-computed CFD mass flow rates corresponding to the upper faces of air zones - represented as  $mfr_{n_{up}}$  (where  $n = x, y, z$ ). This maintenance is performed if an imbalance, denoted as  $\Delta mfr$ , is observed in the air zone (as illustrated in Figure 3.9). The lower face mass flow rates ( $mfr_{n_{down}}$ ) are then adjusted as necessary. This correction involves the use of a weighting coefficient that is proportional to the mass flow rate per surface, computed accordingly:

$$c_n = \frac{|mfr_{n_{down}}|}{\sum_{i=x,y,z} |mfr_{i_{down}}|}, \text{ where: } n = x, y, z \quad (3.4)$$

The updated mass flow rates  $mfr_{n_{down(bal)}}$  on the down faces are then calculated as follows:

$$mfr_{n_{down(bal)}} = mfr_{n_{down}} + c_n \Delta mfr \quad n = x, y, z \quad (3.5)$$

where:

$$\Delta mfr = \sum_{i=x,y,z} mfr_{i_{up}} - \sum_{i=x,y,z} mfr_{i_{down}} \quad (3.6)$$

It should be noted that  $\Delta mfr > 0$  when oriented in the positive direction of the  $x$ ,  $y$ , and  $z$

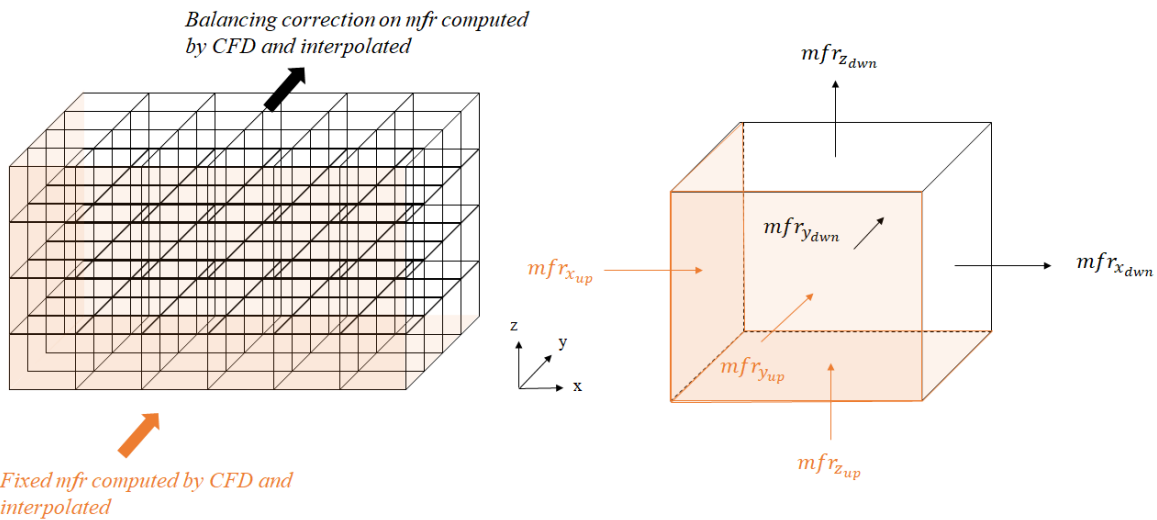


Figure 3.9: Schematic view of the balancing approach (independent of the wind flow direction).

axes. In fact, the assignment of up and down faces is based on the reference of the  $x$ ,  $y$ , and  $z$  axes rather than the direction of air flow (Figure 3.9).

The balancing procedure guarantees that the mass flow rates on the air sides next to firm surfaces are truly zero, making corrections if required. This process also ensures corrections made on downward-facing surfaces are reflected in the upward-facing surfaces of subsequent areas. Consequently, this could lead to unnecessary flow rate corrections in down-

stream zones. Thus, it is critical to assess the effects of this correction on a precise spatial scale to determine its impact on the overall flow.

We evaluate the influence of the mass flow rate balancing procedure on the overall mass flow crossing an air zone in a scenario where the wind speed at 10 m is  $2 \text{ m s}^{-1}$ , coming from the south. Figure 3.10c visually represents the overall mass flow rate across the air zones: (a) post-zone creation, (b) post-balance technique implementation, and (c) the corresponding correction percentage. It is important to note that the cells' scale in Figure 3.10c does not correspond to the actual geometry size - each cell indicates an air zone, not its size.

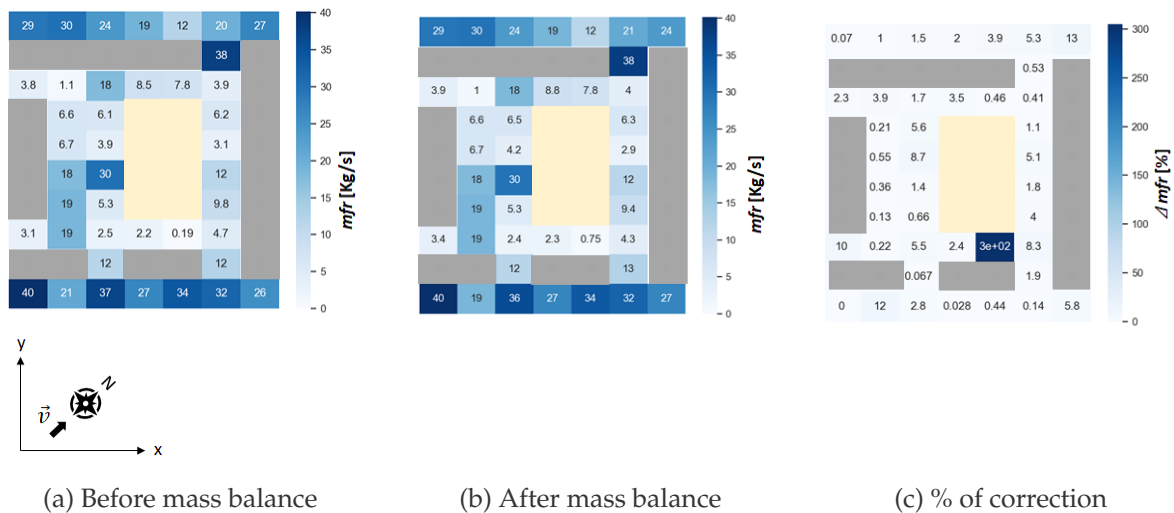
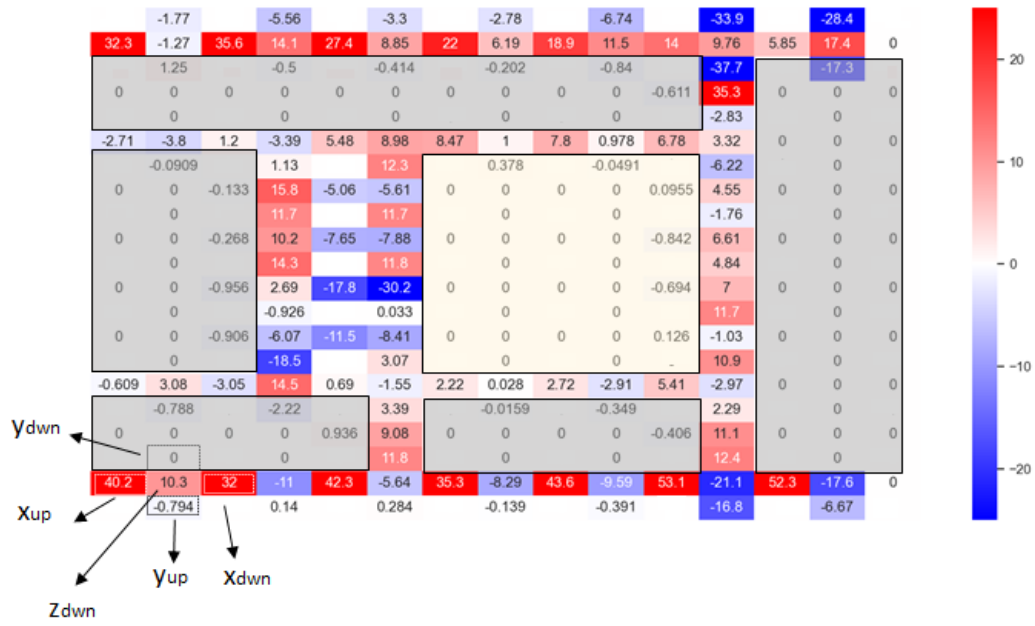


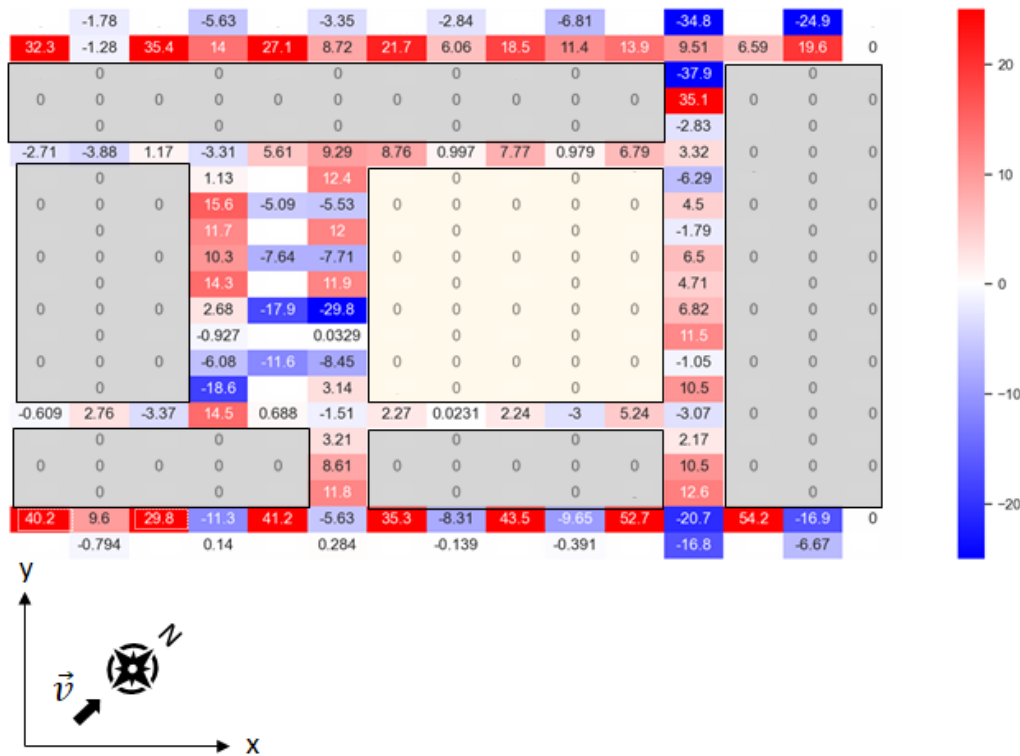
Figure 3.10: Net mass flow rates crossing air zones at pedestrian level [0 m – 3 m] (a) before mass balance (b) after mass balance, and (c) % of correction on the pedestrian level [0 m–3 m],  $v_{10} = 2 \text{ m s}^{-1}$  and wind blowing from South.

The figure shows a higher correction percentage at the building edges and domain boundaries where the mesh is coarser. Figure 3.11 illustrates this with the mass flow rates on the upper and lower surfaces for faces x and y, as well as the mass flow rate traversing the lower surface of face z both (a) before and (b) after the balancing operation. These corrections mainly relate to previously existing imbalances from zoning generation. There is negligible correction propagation from upper to lower zones in this particular case study, and it is not dependent on wind orientation.

The balancing procedure is also implemented during the dynamic simulation stage when solving the enthalpy balance. A similar process is used when enabling natural ventilation in the building (refer to the airflow model in Section 3.2). In this scenario, the mass flow rate at the contact points of the openings switches from zero (indicative of closed doors or windows) to a non-null value  $mfr_{nNV}$  (indicative of open doors or windows). This extra term, produced by natural ventilation, is incorporated into the mass flow rate balance at the lower air surface (on x or y for vertical openings) next to the opening. An additional correction equivalent to the  $mfr_{nNV}$  value is applied to the other two down air surfaces to ensure a zero net balance for the entire air zone. This correction follows the same principle as



(a) mfr before balancing



(b) mfr after balancing

Figure 3.11:  $mfr$  [ $\text{kg s}^{-1}$ ] crossing the x and y up air surfaces and the x,y,z down air surfaces for the pedestrian level [0m – 3m],  $v_{10} = 2 \text{ m s}^{-1}$  and wind blowing from South (a) before balance and (b) after balance.

the underlying balancing process detailed above, employing the weighting coefficient rule. However, since the mass flow rates generated by window openings are very small compared to the mass flow rates crossing the surfaces of the air zones adjacent to the opening ( $\approx 1/100$ ), the corrections made have negligible impact on the initial exterior airflow.

## 5. Choice of the interpolation to predict the outcome variables

This stage is focused on choosing the best method for predicting the output variables ( $mfr$ ,  $h_{c_{ext}}$ ,  $cp$ ). Three predictive models are considered: multiple polynomial regression, Gaussian regression (GPR), and linear interpolation.

Multiple polynomial regression is implemented via Python's `sklearn` library. The optimal polynomial degree is determined through a parametric comparison of scores for various polynomial degrees, done using the `GridSearchCV` function. This preliminary study recommends a polynomial degree of 2 for  $mfr$ ,  $h_{c_{ext}}$ , and  $cp$ .

The Gaussian regression model is designed using the `sklearn` library's `GaussianProcessRegressor` class. Currently, our model assumes a Gaussian process with a zero mean, not influenced by any specific kernel structure. As a result, the Gaussian Process Regressor estimates the data's covariance structure directly, with the learning algorithm determining the optimal covariance structure during training.

The linear interpolation model assumes a linear relationship between the inlet velocity ( $v_{10}$ ) and the outcome variable for a fixed wind direction ( $\beta$ ), as outlined in Section 3.1.2. This is utilised, for instance, in the case of the mass flow rate ( $mfr$ ). The same methodology applies to the prediction of  $h_{c_{ext}}$  and  $cp$ . The function relating  $mfr$  to  $v_{10}$  exhibits a linear or straight-line form:

$$mfr = f(\beta_w)v_{10} \quad (3.7)$$

where  $f(\beta_w)$  represents the slope of the line, which varies depending on the wind direction  $\beta_w$ . For each value of  $\beta_w$  and  $v_{10}$ , the slope  $f(\beta_w)$  is calculated:

$$f(\beta_w) = \frac{mfr}{v_{10}} \quad (3.8)$$

A linear interpolation is then performed between known values of  $\beta_w$  and  $f(\beta_w)$  to predict the values of  $f_{\text{pred}}(\beta_p)$  for any wind direction  $\beta_p$ . The predicted mass flow rate  $mfr_{\text{pred}}$  for a given  $v_{10_p}$  is then obtained as follows:

$$mfr_{\text{pred}} = f_{\text{pred}}(\beta_p)v_{10_p} \quad (3.9)$$

To select the optimal prediction approach, the input variables  $v_{10}$  and their corresponding outcome variables ( $mfr$ ,  $h_{c_{ext}}$ ,  $cp$ ) determined from the CFD simulation are divided into a training dataset (comprising two-thirds of the total simulations) and a test dataset (one-third of total simulations).

The comparison of the models is based on the mean relative error (MRE), which is calculated in equation equation 3.10:

$$MRE = \frac{\sum_{j=1}^N RE_j}{N} \quad (3.10)$$

where  $N$  is the number of surfaces in the zoning and  $RE_j$  is the relative error of on the surface  $j$  defined as:

$$RE_j = \frac{\sum_i^n (|y_{j,i} - y_{j,i_{pred}}|)}{\sum_i^n (|y_{j,i}|)} \times 100 \quad (3.11)$$

where  $n$  is the number of test data sets,  $y_{j,i}$  is the CFD calculated outcome variable on the surface  $j$  corresponds to the  $i$  test data set and  $y_{j,i_{pred}}$  is the predicted outcome variable on the surface  $j$  corresponding to the  $i$  test data set.

A comparison of the three predictive models under consideration indicates that linear interpolation provides superior forecasts (Table 3.4). Thus, we have opted for linear interpolation as our chosen methodology.

Table 3.4: Mean surfaces relative error.

MRE	<i>mfr</i>	$h_{c_{ext}}$	<i>cp</i>
Polynomial multiple regression	23.6%	Ground: 6.6% Wall: 14.4% Roof: 9.2%	21.7%
Gaussian regression	23.1%	Ground: 10.5% Wall: 20.1% Roof: 10.1%	29.8%
Linear interpolation	3.6%	Ground: 10.9% Wall: 3.9% Roof: 1.6%	3.8%

## 6. Dynamic heat and mass balance

The dynamic heat and mass balance model solves the enthalpy balance by ensuring mass balance equilibrium at each time step based on the principle described in section 3.1.2. Indeed, applying the predicted *mfr* at the zone interfaces, rather than directly using *mfr* calculated by CFD, introduces imbalances that require dynamic correction. Also, the dynamic balance model ensures the mass balance when natural ventilation is activated, as described in section 3.1.2.

Let's consider an orthonormal zoning consisting of  $N_x$  zones along the  $x$  axis,  $N_y$  zones along the  $y$  axis, and  $N_z$  zones along the  $z$  axis. Let  $Z_{i,j,k}$  denote the thermal zone located in the orthonormal space at position  $i$  along the  $x$  axis, position  $j$  along the  $y$  axis, and position  $k$  along the  $z$  axis, where  $i = [1, N_x]$ ,  $j = [1, N_y]$  and  $k = [1, N_z]$ . Let  $N_{Sad_{i,j,k}}$  denote the number of building surfaces or soil surfaces  $Sad_{i,j,k}$  adjacent to the air zone  $Z_{i,j,k}$ .  $N_{Sad_{i,j,k}}$

has a minimal value of zero when the air zone is not adjacent to a building or to the soil, and has a maximum value of 5 when the air zone is surrounded by building surfaces or a soil surfaces. The sensible heat balance in zone  $Z_{i,j,k}$  can then be expressed as follows:

### Sensible heat flux

$$\rho V_{i,j,k} C_a \frac{dT_{a_{i,j,k}}}{dt} = Adv_{up_{i,j,k}} + Adv_{dn_{i,j,k}} + Adv_{mix_{i,j,k}} + \sum_{m=0}^{N_{Sadj}} S_m h_{c_{extm}} (T_{s_m} - T_{a_{i,j,k}}) \quad (3.12)$$

Where :

- $\rho$  is the air zone density [ $\text{kg m}^{-3}$ ]
- $V_{i,j,k}$  is the volume of the air zone  $Z_{i,j,k}$  [ $\text{m}^3$ ]
- $C_a$  is the specific heat of air [ $\text{J kg}^{-1} \text{K}^{-1}$ ]
- $Adv_{up_{i,j,k}}$  is the total advective heat exchanged by the upper air surfaces of the  $Z_{i,j,k}$  air zone, with the down air surface of the previous air zones  $Z_{i-1,j,k}$ ,  $Z_{i,j-1,k}$  and  $Z_{i,j,k-1}$  [ $\text{W}$ ]
- $Adv_{dn_{i,j,k}}$  is the total advective heat exchanged by the down air surfaces of the  $Z_{i,j,k}$  air zone, with the up air surface of the next air zones  $Z_{i+1,j,k}$ ,  $Z_{i,j+1,k}$  and  $Z_{i,j,k+1}$  [ $\text{W}$ ]
- $Adv_{mix_{i,j,k}}$  is an additional advective heat related to the air mixture between  $Z_{i,j,k}$  and the adjacent air zones [ $\text{W}$ ]
- $S_m$  is the area of the  $Sadj_{m_{i,j,k}}$  surface, with  $m = [1, N_{Sadj_{i,j,k}}]$  [ $\text{m}^2$ ]
- $h_{c_{extm}}$  is heat transfer coefficient of the  $Sadj_{m_{i,j,k}}$  surface, with  $m = [1, N_{Sadj_{i,j,k}}]$  [ $\text{W m}^{-2} \text{K}^{-1}$ ]
- $T_{s_m}$  is the temperature of the  $Sadj_{m_{i,j,k}}$  surface, with  $m = [1, N_{Sadj_{i,j,k}}]$  [ $\text{K}$ ]
- $T_{a_{i,j,k}}$  is the air zone  $Z_{i,j,k}$  air temperature [ $\text{K}$ ]

The total advective heat flux exchanged by the upper air surfaces is expressed as follows:

$$Adv_{up_{i,j,k}} = Adv_{up_i} + Adv_{up_j} + Adv_{up_k} \quad (3.13)$$

Where :

- $Adv_{up_i}$  is the advective heat exchanged by the upper air surfaces of the  $Z_{i,j,k}$  air zone through the  $x$  axis [ $\text{W}$ ]
- $Adv_{up_j}$  is the advective heat exchanged by the upper air surfaces of the  $Z_{i,j,k}$  air zone through the  $y$  axis [ $\text{W}$ ]
- $Adv_{up_z}$  is the advective heat exchanged by the upper air surfaces of the  $Z_{i,j,k}$  air zone through the  $z$  axis [ $\text{W}$ ]

$Adv_{up_i}$  for the  $Z_{i,j,k}$  air zone is calculated as follows :

$$Adv_{up_i} = \begin{cases} C_a mfr_{up_i} T_{a_{i-1,j,k}}, & \text{for } mfr_{up_i} > 0 \text{ (heat flux enters into the air zone)} \\ -C_a mfr_{up_i} T_{a_{i,j,k}}, & \text{for } mfr_{up_i} < 0 \text{ (heat flux exit the air zone)} \end{cases} \quad (3.14)$$

Where  $mfr_{up_i}$  is the mass flow rate crossing the upper surface  $i$  of the  $Z_{i,j,k}$  air zone.  $Adv_{up_j}$  and  $Adv_{up_k}$  are calculated as  $Adv_{up_i}$  respectively along the  $y$  axis and along the  $z$  axis. The total advective heat flux exchanged by the down air surfaces is expressed as follows:

$$Adv_{down_{i,j,k}} = Adv_{down_i} + Adv_{down_j} + Adv_{down_k} \quad (3.15)$$

Where :

$$\begin{cases} Adv_{down_i} \text{ is the advective heat exchanged by the down air surfaces of the } Z_{i,j,k} \\ \text{air zone through the } x \text{ axis [W]} \\ Adv_{down_j} \text{ is the advective heat exchanged by the down air surfaces of the } Z_{i,j,k} \\ \text{air zone through the } y \text{ axis [W]} \\ Adv_{down_z} \text{ is the advective heat exchanged by the down air surfaces of the } Z_{i,j,k} \\ \text{air zone through the } z \text{ axis [W]} \end{cases}$$

$Adv_{down_i}$  for the  $Z_{i,j,k}$  air zone is calculated as follows:

$$Adv_{down_i} = \begin{cases} -C_a mfr_{down_i} T_{a_{i,j,k}}, & \text{for } mfr_{up_i} > 0 \text{ (heat flux exit the air zone)} \\ C_a mfr_{down_i} T_{a_{i+1,j,k}}, & \text{for } mfr_{up_i} < 0 \text{ (heat flux enters into the air zone)} \end{cases} \quad (3.16)$$

Where  $mfr_{down_i}$  is the mass flow rate crossing the down surface  $i$  of the  $Z_{i,j,k}$  air zone.  $Adv_{down_j}$  and  $Adv_{down_k}$  are calculated as  $Adv_{down_i}$  respectively along the  $y$  axis and along the  $z$  axis.

The advective heat flux related to the air mixture between air zone  $Z_{i,j,k}$  and the adjacent air zones considers any recirculation present at the interface between two air zones (Figure 3.12) and is expressed as follows:

$$\begin{aligned} Adv_{mix_{i,j,k}} = & C_a [mfr_{mix_{up_i}} (T_{a_{i-1,j,k}} - T_{a_{i,j,k}}) + mfr_{mix_{up_j}} (T_{a_{i,j-1,k}} - T_{a_{i,j,k}}) + \\ & mfr_{mix_{up_k}} (T_{a_{i,j,k-1}} - T_{a_{i,j,k}}) + mfr_{mix_{down_i}} (T_{a_{i+1,j,k}} - T_{a_{i,j,k}}) + \\ & mfr_{mix_{down_j}} (T_{a_{i,j+1,k}} - T_{a_{i,j,k}}) + mfr_{mix_{down_k}} (T_{a_{i,j,k+1}} - T_{a_{i,j,k}})] \end{aligned} \quad (3.17)$$



$$\text{Where : } \left\{ \begin{array}{l} mfr_{mix_{up_i}} \text{ is the recirculation mass flow rate on the upper surface of } Z_{i,j,k} \\ \text{air zone through the } x \text{ axis [kg s}^{-1}\text{]} \\ mfr_{mix_{up_j}} \text{ is the recirculation mass flow rate on the upper surface of } Z_{i,j,k} \\ \text{air zone through the } y \text{ axis [kg s}^{-1}\text{]} \\ mfr_{mix_{up_k}} \text{ is the recirculation mass flow rate on the upper surface of } Z_{i,j,k} \\ \text{air zone through the } z \text{ axis [kg s}^{-1}\text{]} \\ mfr_{mix_{down_i}} \text{ is the recirculation mass flow rate on the down surface of } Z_{i,j,k} \\ \text{air zone through the } x \text{ axis [kg s}^{-1}\text{]} \\ mfr_{mix_{down_j}} \text{ is the recirculation mass flow rate on the down surface of } Z_{i,j,k} \\ \text{air zone through the } y \text{ axis [kg s}^{-1}\text{]} \\ mfr_{mix_{down_k}} \text{ is the recirculation mass flow rate on the down surface of } Z_{i,j,k} \\ \text{air zone through the } z \text{ axis [kg s}^{-1}\text{]} \end{array} \right.$$

Each surface of the an air zone is composed on n facets corresponding to the CFD meshing. The recirculation mass flow in each surface on a general surface S is calculated during the zoning generation as follows:

$$mfr_{mix_S} = \rho \min \left( \sum_{n=1}^{Nf} |V_n^- S_n|, \sum_{n=1}^{Nf} |V_n^+ S_n| \right) \quad (3.18)$$

$$\text{Where : } \left\{ \begin{array}{l} mfr_{mix_S} \text{ is the recirculation mass flow rate of the surface S of the air zone [kg s}^{-1}\text{]} \\ V_n^- \text{ is the velocity exiting the facet n of the surface S [m s}^{-1}\text{]} \\ V_n^+ \text{ is the velocity entering the facet n of the surface S [m s}^{-1}\text{]} \\ Nf \text{ is the number n of facet of the surface S [-]} \\ S_n \text{ is the area of the facet n [m}^2\text{]} \end{array} \right.$$

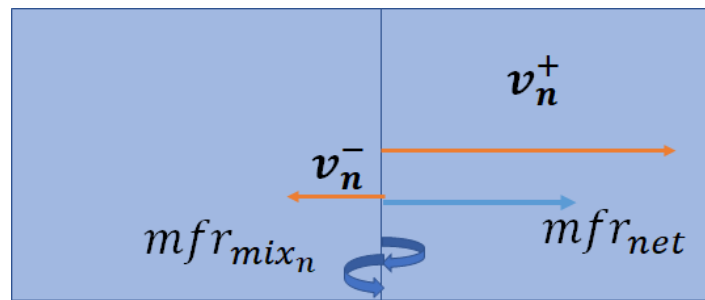


Figure 3.12: Schematic view of the mfr exchange in an air zone.

Similarly to the  $mfr$ , the  $mfr_{mix}$  is also predicted during the dynamic simulation using linear interpolation. As for the sensible heat flux, the latent heat flux is expressed as follows:

### Latent heat flux

$$Lm_a \frac{dr_{i,j,k}}{dt} = \sum_n L_{Adv_{up,n}} + \sum_n L_{Adv_{dwn,n}} + \sum_n L_{Adv_{mix,n}} + S_l \quad (3.19)$$

Where :

- $L$  is the latent heat of vapourization of water [ $J\ kg^{-1}$ ]
- $m_a$  is the dry air mass [kg]
- $r$  is the specific humidity [ $kg_{water}/kg_{dry\ air}$ ]
- $L_{Adv_{up,n}}$  is the latent flux exchanged by advection through the up air surfaces [W]
- $L_{Adv_{dwn,n}}$  is the latent flux exchanged by advection through the down air surfaces [W]
- $L_{Adv_{mix,n}}$  is the latent heat flux related to the air mixture between air zone  $Z_{i,j,k}$  and the adjacent air zones [W]
- $S_l$  is a source of latent heat (e.g. from evaporation) [W]

$L_{Adv_{up,n}}$ ,  $L_{Adv_{dwn,n}}$  and  $L_{Adv_{mix,n}}$  are calculated as for equations 3.14, 3.16 and 3.17 by replacing the temperature  $T$  with the specific humidity  $r$  and the air specific heat  $C_a$  with  $L$ , the latent heat of vaporization of water.

The set of equations is written in Modelica language and solved in Dymola using the DASSL solver, presenting the advantage of being quite stable for a wide range of models as it is an implicit, high order, adaptive time step solver.

### 3.1.3 Model validation

#### 3.1.3.1 Airflow on an isolated building model

This paragraph confirms the accuracy of the numerical CFD settings used for the flow model described in section 3.1.2 by comparing a steady RANS  $rk-\epsilon$  model to measurements from a wind tunnel experiment on an isolated cube. This chosen experiment was carried out by the Architectural Institute of Japan (AIJ) and considers a simple rectangular building shape (Meng and Hibi, 1998).

#### Experiment description

The model building deployed in the experiments has dimensions of 160 mm in height and 180 mm in both width and depth (Figure 3.14a). The wind profile is supplied as part of the experiment (Meng and Hibi, 1998). Figure 3.14 shows the points where the wind speed was measured.

#### Model setting

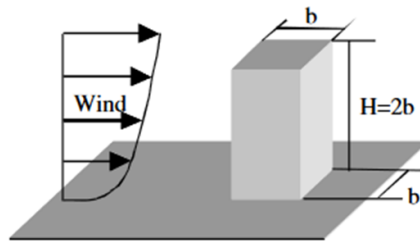
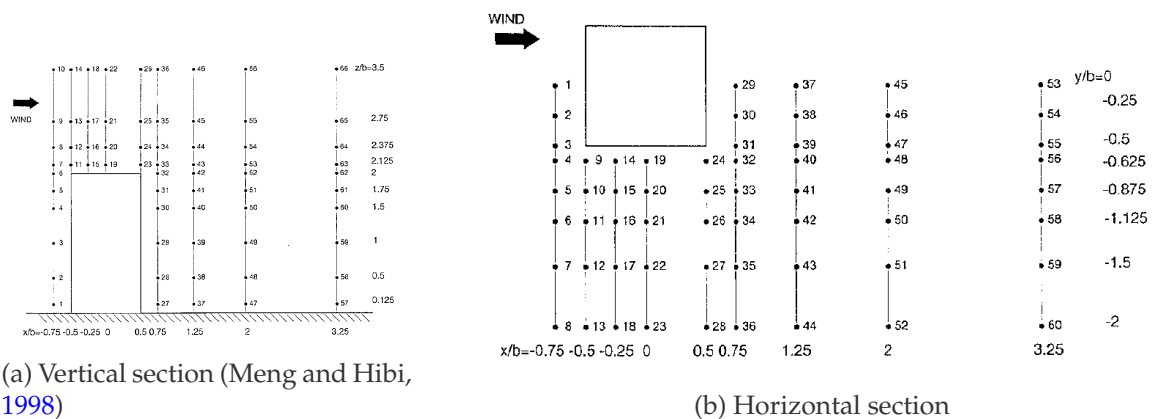


Figure 3.13: Schematic representation of the square prism experiment (Meng and Hibi, 1998).



(a) Vertical section (Meng and Hibi, 1998)

(b) Horizontal section

Figure 3.14: Measuring points for the (a) vertical section and the two (b) horizontal sections at  $z=0.125b$  and  $z=1.25b$  (from Meng and Hibi, 1998).

The Reynolds number ( $Re$ ), calculated using the reference width of the model building and mean wind speed at the eave  $U_0$  of  $4.49 \text{ m s}^{-1}$ , is approximately  $5 \times 10^4$ . In cases where  $Re > 10^4$ , we can assume that changing the scale from a small-scale experiment to a larger-scale building does not significantly affect the overall flow. This assumption is satisfactory for sharp shapes, where flow separation is less  $Re$ -dependent than in circular shapes.

Hence, for the CFD modelling, a rectangular prism with dimensions of 20 m height 10 m depth is chosen. The wind profile from the experiment is replicated using a logarithmic law. The domain size, meshing, and convergence criteria follow the recommendations of the CFD simulation best practices guidelines (Tominaga et al., 2008, Blocken, 2015, Blocken et al., 2009). The grid cell size on the prism's side is 1 m, totalling 342,924 cells. The model setup is depicted in Figure 3.15. A simulation was executed using Fluent, which employs the RANS  $rk - \varepsilon$  turbulence model and a coupled resolution method. Convergence was accomplished with a convergence criterion of  $10^{-4}$  for mass balance and  $10^{-6}$  for velocity components, energy, turbulence, and viscosity.

## Results and discussions

The metric applied for comparing the simulated results with the experimental data is the

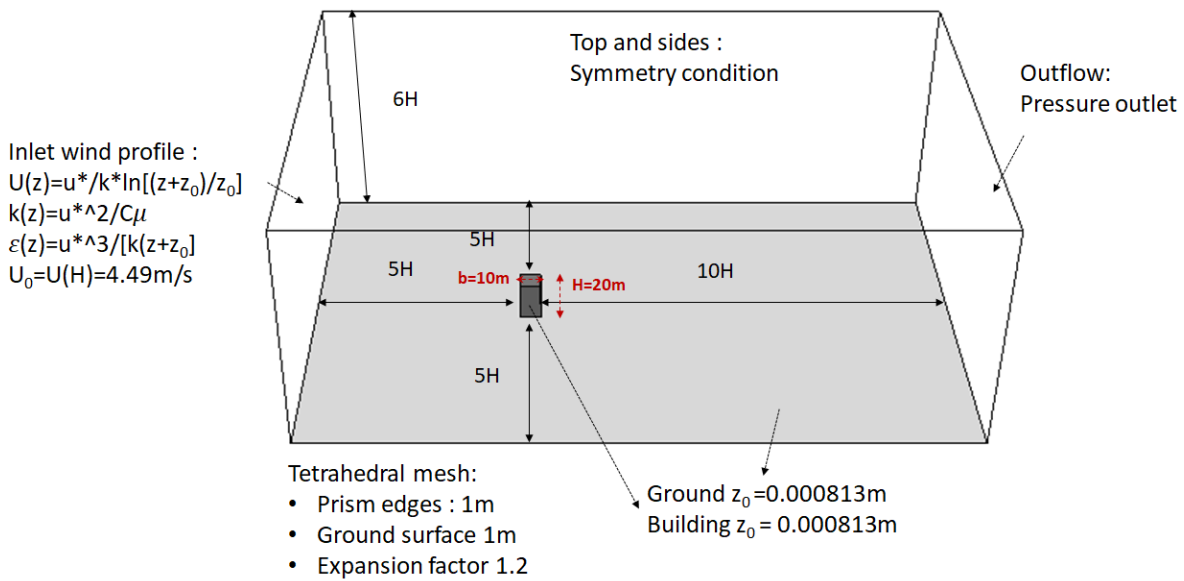


Figure 3.15: CFD setting for the reproduction of the square prism experiment (Meng and Hibi, 1998).

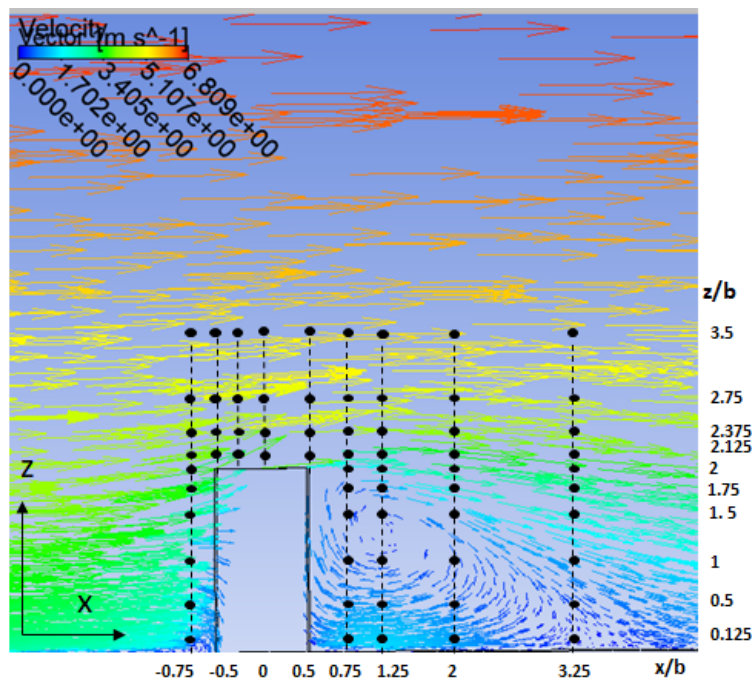


Figure 3.16: Vertical section: Airflow simulated by CFD RANS  $rk - \varepsilon$  in the reproduction of the square prism experiment (Meng and Hibi, 1998).

RNMSE, along with the average error relative to the inlet wind velocity  $U_0$  at height  $H=2b$ . Figure 3.16 displays the vertical section measurements points along with the corresponding airflow simulated by CFD RANS  $rk - \varepsilon$ . The corresponding measured and simulated velocity components normalized by the inlet wind speed  $U/U_0$ ,  $V/U_0$  and  $W/U_0$  are captured in Figures 3.17 and 3.18.



Figure 3.17: Wind profile for XZ vertical section (Part I : from  $x = -0.75b$  to  $0.5b$ ). Average RNMSE on  $x = 0.89$ , on  $y = 7.08$  on  $z = 1.70$ . Average error relative to  $U_0$  on  $x = 9.6\%$ , on  $y = 0.9\%$  on  $z = 4.9\%$ .



Figure 3.18: Wind profile for XZ vertical section (Part II : from  $x=0.75b$  to  $3.25b$ ). Average RNMSE on  $x = 0.89$ , on  $y = 7.08$  on  $z = 1.70$ . Average error relative to  $U_0$  on  $x = 9.6\%$ , on  $y = 0.9\%$  on  $z = 4.9\%$ .

The results demonstrate general concurrence between the measured and simulated wind speed. However, the RANS model's capacity to accurately replicate the downstream recirculation has certain constraints, as it overestimates the recirculation size (Merlier, 2015). Negative velocity values recorded from  $x = 0.75$  to  $x = 3.25$  in the CFD findings indicate a substantially larger recirculation produced by the RANS model compared to actual measurements, which show recirculation ending at  $x = 2$ . Complete results for all experimental measurement points can be found in Appendix F.

### 3.1.3.2 Convective heat transfer coefficient on a cube immersed in a turbulent boundary layer

This paragraph seeks to affirm the validity of the numerical model and settings utilised in calculating the convective heat transfer coefficient ( $h_c$ ) on a cube exposed to high-Reynolds number flow. This is done by comparing it with a similar numerical simulation conducted by Defraeye, Blocken and Carmeliet (2010).

The outcomes of this numerical simulation act as a standard reference. They have been cross-verified with another simulation that applied Low Reynolds Number Modelling (LRNM) to an identical 10 m cube setup within an ABL, as executed by Defraeye, Blocken and Carmeliet (2010).

At first, LRNM was validated by Defraeye, Blocken and Carmeliet (2010) by comparing its results with those from a wind tunnel experiment involving a 15 mm cube (Meinders, Hanjalic, and Martinuzzi, 1999) placed in a turbulent channel flow at moderately low Reynolds number ( $4.5 \times 10^3$ ). Results provided by LRNM ( $rk_\epsilon$  model) showed good agreement with the experimental data in estimating the  $h_c$  profiles on the windward surface of the cube. However, considerable discrepancies were found for the top and the side surfaces of the cube.

The comparative analysis conducted between LRNM and the wall function method simulations on a 10 m cube situated within an ABL, involved Reynolds numbers ranging from  $3.5 \times 10^4$  to  $3.5 \times 10^6$ . Results demonstrated a qualitatively similar  $h_c$  distribution. However, a consistently higher  $h_c$  was observed when the wall function model was used (Defraeye, Blocken, and Carmeliet, 2010). While LRNM provides more accurate results, it is highly demanding in terms of numerical cost, given its need for an extensive meshing process. The inability to employ a LRNM in building physics problems generally leads to the alternative use of wall functions for  $h_c$  estimation.

#### Model settings

A cube, signifying a building in the ABL, is represented with a height (H) of 10 m. The mesh refinement close to the wall is adjusted so that the value of  $y^*$  ranges from 30 to 600.

The dimensions of the three-dimensional computational domain and simulation settings are depicted in Figure 3.19, based on the design by Defraeye, Blocken and Carmeliet (2010). To calculate  $h_c$ , an air reference temperature of  $10^\circ\text{C}$  is employed, with the wall surface temperature set at  $20^\circ\text{C}$ . The influence of buoyancy and radiation is disregarded. Both simulations were executed with Fluent utilising a steady RANS  $rk - \varepsilon$  turbulence model and a standard wall function. The convergence criteria were established at  $10^{-4}$  for mass balance and  $10^{-6}$  for components like velocity, energy, turbulence, and viscosity.

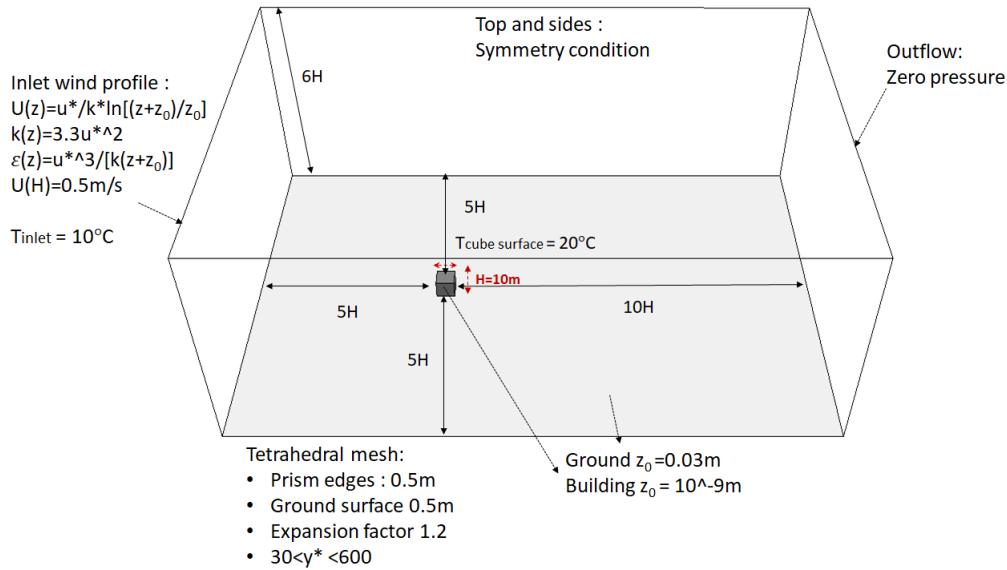


Figure 3.19: Domain and size and simulation setting for the simulation of the single cube immersed in a turbulent boundary layer using RANS  $rk - \varepsilon$  turbulence model (Defraeye, Blocken, and Carmeliet, 2010).

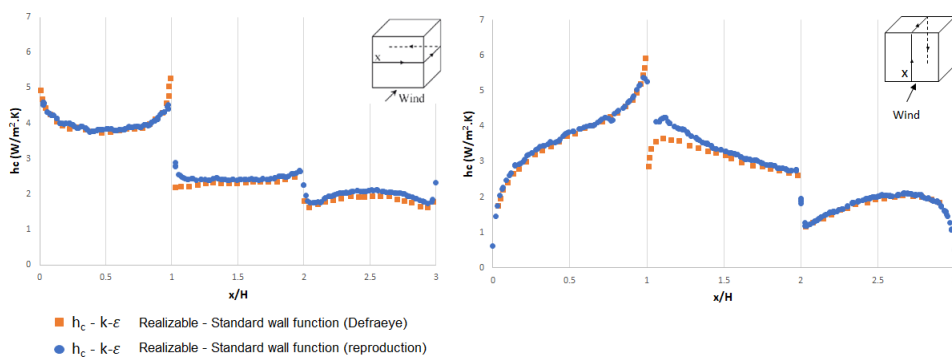


Figure 3.20: Comparison of the  $h_c$  distribution on the surfaces of the cube resulting from a DCF RANS  $rk - \varepsilon$  turbulence model and using a standard wall function for the Defraeye, Blocken and Carmeliet (2010) numerical simulation and the simulation reproduced in this thesis.

## Results and discussions

Results in figure 3.20 show a good agreement between  $h_c$  profiles simulated by Defraeye,



Blocken and Carmeliet and the reproduced one.

## 3.2 Natural ventilation model

### 3.2.1 Physical principles of natural ventilation

Natural ventilation through openings in buildings is the motion of air resulting from pressure differences, which are driven by a combination of wind forces, buoyancy forces and turbulent fluctuation.

Wind-driven ventilation relies on the movement of air induced by external wind pressure: when wind encounters obstacles such as buildings, dynamic pressure is converted into static pressure. This phenomenon leads to the creation of areas of positive pressure (overpressure) on the windward side, while areas of negative pressure (under pressure or suction) are formed on the leeward side. The pressure difference between the windward and leeward sides of the building creates airflow through openings. The over pressure on the windward side forces air into the building, while the under-pressure zone on the leeward side facilitates air exhaust. The resulting pressure difference from wind force can be empirically expressed as follows (Equation 3.20):

$$\Delta P_w = \Delta c_p \frac{1}{2} \rho v_{ref}^2 \quad (3.20)$$

$$\text{Where : } \begin{cases} \Delta P_w \text{ is the pressure difference from wind force [Pa]} \\ \Delta c_p \text{ is the difference in wind pressure coefficient [-]} \\ v_{ref} \text{ is the wind speed at a reference height [m s}^{-1}\text{]} \\ \rho \text{ is the air density [kg m}^{-3}\text{]} \end{cases}$$

The wind pressure coefficient can be determined either experimentally or numerically at a single point on a building's facade or by averaging pressure over the entire facade. For turbulent flow, occurring at high Reynolds numbers and sharp-edged geometries, the average pressure coefficient on a facade can be approximately considered independent of wind speed and dependent only on wind direction, building geometry, building porosity, and its surroundings. In our approach, linear interpolation is used to obtain the average pressure coefficients of the facades from pre-computed sets of pressure coefficients. These estimates are computed using CFD via the RANS  $rk - \varepsilon$  turbulence model, considering different wind directions. The reference velocity in these calculations is the velocity measured at a height of 10 m, which aligns with the input velocity's height in the dynamic model.

In the case of buoyancy-driven ventilation, air movement is dictated by differences in air density, resulting from variations in air temperature and the height between openings. The pressure gradient created from these temperature and height differences between the inlet

and outlet can be formulated in the following manner (Equation 3.21):

$$\Delta P_b = \Delta \rho g h \quad (3.21)$$

$$\text{Where : } \begin{cases} \Delta P_b \text{ is the pressure gradient [Pa]} \\ \Delta \rho \text{ is the inlet/outlet air density difference [kg m}^{-3}\text{]} \\ g \text{ is the gravitational constant (9.81) [m s}^{-2}\text{]} \\ h \text{ is the inlet/outlet height difference [m]} \end{cases}$$

When there is a temperature difference between indoor and outdoor environments, a bidirectional buoyancy-driven flow, where air moves both ways, is observed. Figure 3.21 depicts a typical vertical airflow profile for this kind of flow in the absence of wind. This happens when the indoor temperature is higher than the outdoor temperature, causing warm, less dense air in the room to rise and be replaced by cooler, denser air from outside.

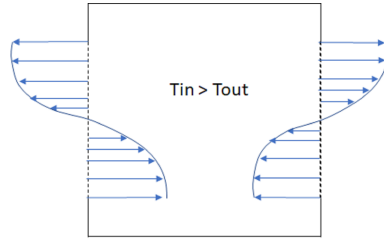


Figure 3.21: Vertical airflow velocity profiles for two-way buoyancy-driven flow in the absence of wind forces (adapted from Truong, 2012).

### 3.2.2 Model description

The airflow model is a pressure-based node model used in building thermal zones and the interface between indoor and outdoor thermal zones. It uses models from the International Building Performance Simulation Association (IBPSA) library in Modelica. The airflow transfers comply with the three conservation principles: momentum, mass, and energy. Each node pressure calculation assumes a stationary and non-compressible fluid. Thus, the airborne transfers are dictated by the Bernoulli equation.

The calculation of static pressure happens at each node. We compute the airflow between two nodes using an empirical law that associates pressure differences between two nodes with the corresponding cross-flow volume of air. The governing equations underlie this are (Wetter, 2006):

$$\dot{V} = \begin{cases} K_{Flow} \Delta P^m, & \text{for } \Delta P \geq 3/2 \Delta P_{0,\epsilon} \\ -K_{Flow} (-\Delta P)^m, & \text{for } \Delta P \leq -3/2 \Delta P_{0,\epsilon} \\ K_{Flow} \Delta P_{0,\epsilon}^{m-1} \Delta P, & \Delta P \in [-\Delta P_{0,\epsilon}/2, \Delta P_{0,\epsilon}/2] \end{cases} \quad (3.22)$$

$$\text{Where : } \left\{ \begin{array}{l} \dot{V} \text{ is the volume flow rate } [\text{m}^3 \text{ s}^{-1}] \\ K_{Flow} \text{ represents the flow characteristics and} \\ \text{as a consequence, on the type of aperture } [\text{m}^3 \text{ s}^{-1} \text{ Pa}^{-m}] \\ \Delta P \text{ is the static pressure difference over the apertures } [\text{Pa}] \\ m \text{ is a flow exponent } \in [0.5, 1] \text{ with} \\ m = 0.5 \text{ for turbulent flow and } m = 1 \text{ for laminar flow } [-] \\ \Delta P_{0,\epsilon} \text{ is a user specified numerical parameter } [\text{Pa}] \end{array} \right.$$

$\Delta P_{0,\epsilon} \ll 1$  is introduced to avoid numerical problems occurring for  $m < 1$  when  $\Delta P \rightarrow 0$  and the derivative  $d\dot{V}/d\Delta P \rightarrow \infty$ . A good numerical stability has been observed for  $\Delta P_{0,\epsilon} = 0.1 \text{ Pa}$ .

In the intervals  $\Delta P \in (-3/2\Delta P_{0,\epsilon}, -1/2\Delta P_{0,\epsilon})$  and  $\Delta P \in (1/2\Delta P_{0,\epsilon}, 3/2\Delta P_{0,\epsilon})$  the built-in Dymola function `spliceFunction` is used to ensure continuity between the equations 3.22 (Wetter, 2006).

The airflow model developed for the coupled BEM and McZM uses two models of the IBPSA Modelica library aiming to reproduce the flow characteristic through a small orifice and through a large vertical open aperture, described below.

### 3.2.2.1 Orifice model

The flow through an orifice with cross section area  $S$  is deduced from the Bernoulli equation and is given by equation 3.23:

$$\dot{V} = C_d S \sqrt{2/\rho} \Delta P^m \quad (3.23)$$

$$\text{Where : } \left\{ \begin{array}{l} C_d \in (0, 1) \text{ is a discharge coefficient } [\text{kg}^{0.5} \text{ m}^{-0.5} \text{ Pa}^{-m} \text{ s}^{-1}] \\ S \text{ is the section of the orifice } [\text{m}^2] \\ \rho \text{ is the air density set constant to } 1.2 [\text{kg m}^{-3}] \\ \Delta P \text{ is the static pressure difference over the apertures } [\text{Pa}] \\ m \text{ is the flow exponent } \in [0.5, 1] \end{array} \right.$$

### 3.2.2.2 Large vertical open aperture model

This model calculates steady-state bidirectional airflow through doors or windows. It represents the aperture with a height  $h$  and a width  $w$  separating two air volumes: Room A and Room B (figure 3.23).

In room A, the air density and the static pressure varies with height  $z$  according to the

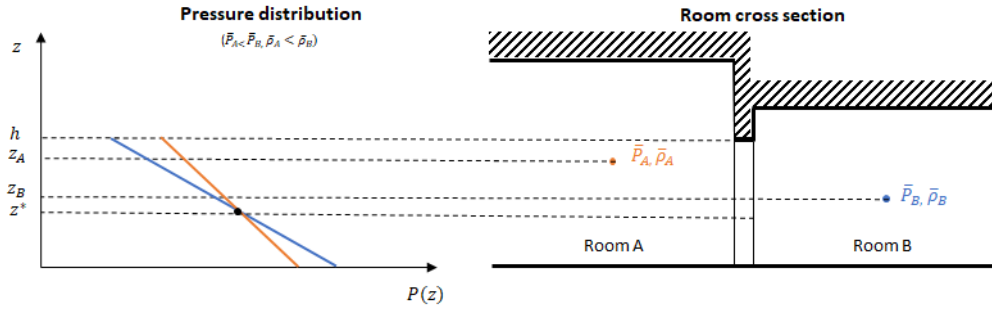


Figure 3.22: Schematics of pressure distribution of two rooms connected by a large vertical aperture of height  $h$ . (Adapted from Wetter, 2006).

following equations:

$$\rho_A(z) = \bar{\rho}_A \left( 1 - \frac{(z - z_A) T'_A}{\bar{T}_A} \right) \quad (3.24)$$

$$P_A(z) = \bar{P}_A + g \int_0^{z_A} \rho_A(s) ds - g \int_0^z \rho_A(s) ds \quad (3.25)$$

Where  $g = 9.81 m/s^2$ ,  $\bar{\rho}_A$ ,  $\bar{T}_A$  and  $\bar{P}_A$  are the air density, the air temperature and the static pressure at height  $z = z_A$  and  $T'_A = dT_A(z)/dz$ .

Equations 3.24 and 3.24 yields to:

$$P_A(z) = \bar{P}_A + g \bar{\rho}_A (z_A - z) + g \bar{\rho}_A \frac{T'_A}{2 \bar{T}_A} (z^2 - 2zz_A + z_A^2) \quad (3.26)$$

The static pressure difference between rooms A and B at height  $z$  can be expressed as:

$$\Delta P_{AB} = P_A(z) - P_B(z) = \bar{P}_A - \bar{P}_B + g(\bar{\rho}_A(z_A - z) - \bar{\rho}_B(z_B - z)) + g \bar{\rho}_A \frac{T'_A}{2 \bar{T}_A} (z^2 - 2zz_A + z_A^2) - g \bar{\rho}_B \frac{T'_B}{2 \bar{T}_B} (z^2 - 2zz_B + z_B^2) \quad (3.27)$$

Equation 3.27 solutions, if they exist, are called the neutral height  $z^*$ . In the absence of temperature gradients, equation 3.27 is simplified and the neutral height is:

$$z^* = \frac{\bar{P}_A - \bar{P}_B + g(\bar{\rho}_A z_A - \bar{\rho}_B z_B)}{g(\bar{\rho}_A - \bar{\rho}_B)} \quad (3.28)$$

The volume flow rate from A to B through the height element  $dz$  is:

$$\dot{V}_{AB}(z)/dz = \begin{cases} C_d \sqrt{2/\rho_A(z)} \Delta P_{AB}^m(z) w dz, & \text{for } \Delta P_{AB}^m(z) > 0 \\ -C_d \sqrt{2/\rho_A(z)} (-\Delta P_{AB}^m(z)) w dz, & \text{for } \Delta P_{AB}^m(z) \leq 0 \end{cases} \quad (3.29)$$

The net flow from A to B and from B to A over the aperture height  $h$  is given by equation

3.30 and equation 3.31 respectively.

$$\dot{V}_{AB} = \int_0^h \max(0, d\dot{v}_{AB}(z)/dz) dz \quad (3.30)$$

$$\dot{V}_{BA} = \int_0^h \min(0, d\dot{v}_{AB}(z)/dz) dz \quad (3.31)$$

A discretized model is used to solve equations 3.30 and 3.31. The height  $h$  is then discretized into  $n$  compartments (where  $n \in \mathbb{N}$ ) and the orifice equation 3.23 is used to compute the flow. The air density used in this case is approximated to the average air density of the two air volumes

### 3.2.2.3 Boundary conditions model

The IBPSA library includes a model for predefined boundary conditions like pressure, specific enthalpy, temperature, and density. This model has been updated to account for dynamic boundary conditions. Consequently, a wind pressure term from equation 3.32 has been incorporated into the boundary reference pressure.

$$P_w = cp \frac{1}{2} \rho v_0^2 \quad (3.32)$$

$$\text{Where : } \begin{cases} P_w \text{ is the wind pressure [Pa]} \\ cp \text{ is the pressure coefficient [-]} \\ \rho \text{ is the air density set constant to } 1.2 \text{ [kg m}^{-3}\text{]} \\ v_0 \text{ is the weather file wind speed at the reference height (} z = 10 \text{ m) [m s}^{-1}\text{]} \end{cases}$$

Air temperatures in each air zone are also updated for each computational time step with the air temperatures computed in the heat balance of the coupled BEM and McZM.

### 3.2.2.4 Assembled airflow model

The prior sub-models are merged into a comprehensive airflow model. This model reflects the cumulative influence of cracks, open windows, open doors, and the air renewal system on the overall airflow. This model applies to the top-floor dwelling outlined in Chapter 5. Figure 3.23 provides a floor plan, marking the location of windows, doors, cracks, and the air renewal system. The air renewal system reciprocates with the air in the outdoor space next to Room 1's rooftop.

The specific settings of the model are listed in Table 3.5. The  $SC_d$  value for cracks aligns with the average infiltration rate permitted for new buildings according to French regula-

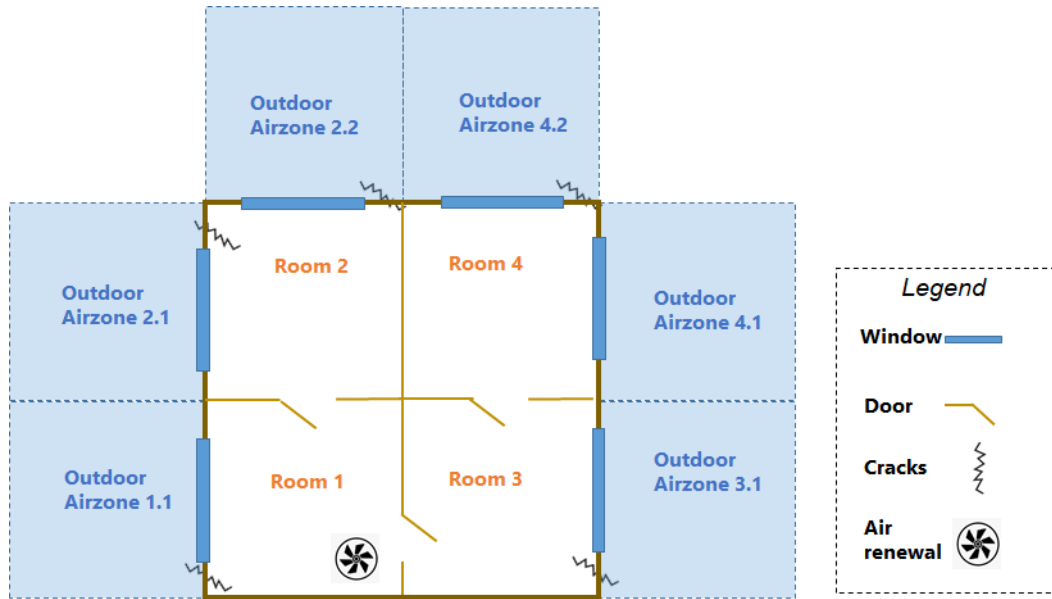


Figure 3.23: Schematic view of the assembled air flow components in a 4 rooms apartment.

tions<sup>1</sup>. Large openings are typically characterized by an  $m$  close to 0.5, while smaller cracks have been found to have values near 0.65 (Walton, 1989; Wetter, 2006; Dols and Polidoro, 2020). The  $C_d$  value shifts based on various factors - including differences in temperature, varying inclination angles, the type of surrounding field, and the height of roughness - but is generally assumed to hover around 0.61 (Orme, Liddament, and Wilson, 2010). Research involving a seven-story building has shown that the  $C_d$  values tend to be higher on the top floor (Baxevanou, Fidaros, and Tsangrassoulis, 2017). For the current model, a  $C_d$  value of 0.65, which is typically applicable to a top-floor apartment, has been decided on.

Table 3.5: Airflow model parameters.

Model parameters	Window	Door	Crack	Air Renewal
Opening width [m]	0.5	0.5	-	-
Opening height [m]	0.125	2.2	-	-
$SC_d$ (for 6 cracks) [ $\text{kg}^{0.5}\text{Pa}^{-\text{m}}\text{s}^{-1}$ ]	-	-	0.007	-
$C_d$ [ $\text{kg}^{0.5}\text{m}^{-0.5}\text{Pa}^{-\text{m}}\text{s}^{-1}$ ]	0.65	0.65	-	-
$m$ [-]	0.5	0.5	0.65	-
Air renewal flow rate [kg/s]	-	-	-	0.05

The model's boundary conditions are wind  $cp$  and air zone temperatures. The airflow model is coupled with the BEM/McZM air zone model. At each step, this model uses wind  $cp$  and air zone temperatures from the BEM/McZM model as input data. It then computes the mass flow rates through openings under a steady-state regime. These rates are employed to resolve the energy balance in the BEM/McZM air zone model.

<sup>1</sup>Article 17- Arrêté du 26 octobre 2010 relatif aux caractéristiques thermiques et aux exigences de performance énergétique des bâtiments nouveaux et des parties nouvelles de bâtiments

### 3.2.3 Model verification

The IBPSA Modelica airflow model's validity has been confirmed by its comparison with the CONTAM airflow model (Wetter, 2006). This comparison predominantly highlights buoyancy-driven airflow rates passing through orifices and open doors. Several reasons make CONTAM an apt comparison. First, like Modelica, CONTAM uses a nodal method with comparable pressure models. Second, CONTAM has already been numerically and experimentally validated (Haghighat and Megri, 1996). Lastly, it is widely utilised in building ventilation systems studies and has been paired with EnergyPlus (Justo Alonso, Dols, and Mathisen, 2022) and TRNSYS (Dols, Emmerich, and Polidoro, 2016).

This section sets out to compare the mass flow rates obtained from the airflow model assembled for the McZM, as detailed in Section 3.2.2, with those computed using the CONTAM model.

#### Case study configuration

The case study refers to a theoretical dwelling that shares the same structure as the top-floor dwelling of the examined building (Figure 3.4). The dwelling plan is reported in Figure 3.24

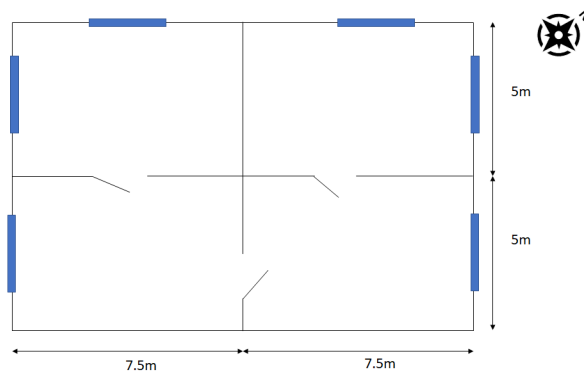


Figure 3.24: Plan 2D and dimensions of the studied dwelling.

Here, the impact of obstacles on airflow and, consequently, on  $cp$  values is excluded. We rely on theoretical  $cp$  values, representing an isolated building.

We examine two configurations incorporating windows and doors: one maintains a consistent temperature  $T = 20^{\circ}\text{C}$  across air zones, while the other presents a temperature differential  $\Delta T = 10^{\circ}\text{C}$  between indoor ( $T = 30^{\circ}\text{C}$ ) and outdoor ( $T = 20^{\circ}\text{C}$ ) environments. Table 3.6 details the boundary conditions and opening parameters.

#### Model setting

In the initial configuration featuring consistent temperatures, both Modelica and CONTAM utilise an orifice model. For the second scenario, CONTAM employs the Single Open model.

Table 3.6: Airflow model parameters for the two comparison configurations.

Boundary conditions		Opening parameters	
Absolute pressure [Pa]	101325	$Cd$ [ $\text{kg}^{0.5}\text{m}^{-0.5}\text{Pa}^{-\text{m}}\text{s}^{-1}$ ]	0.78
wind speed [ $\text{m s}^{-1}$ ]	2	$m$ [-]	0.5
wind direction [ $^{\circ}\text{N}$ ]	225	$h_{\text{window}}$ [m]	1
$cp$ North-East	-0.6	$w_{\text{window}}$ [m]	0.25
$cp$ North-West	-0.1	$h_{\text{door}}$ [m]	2.2
$cp$ South-West	0.6	$w_{\text{door}}$ [m]	0.3

The input model parameters mirror both the boundary conditions and the parameters for the opening, as depicted in Table 3.6.

### Results and discussions

The metric for this comparison model utilises the relative error ( $RE$ ). Figure 3.25 presents the derived mass flow rates along with their associated  $RE$ , which is computed by dividing the difference in mass flow rates by the rate calculated in CONTAM and then multiplying by 100.

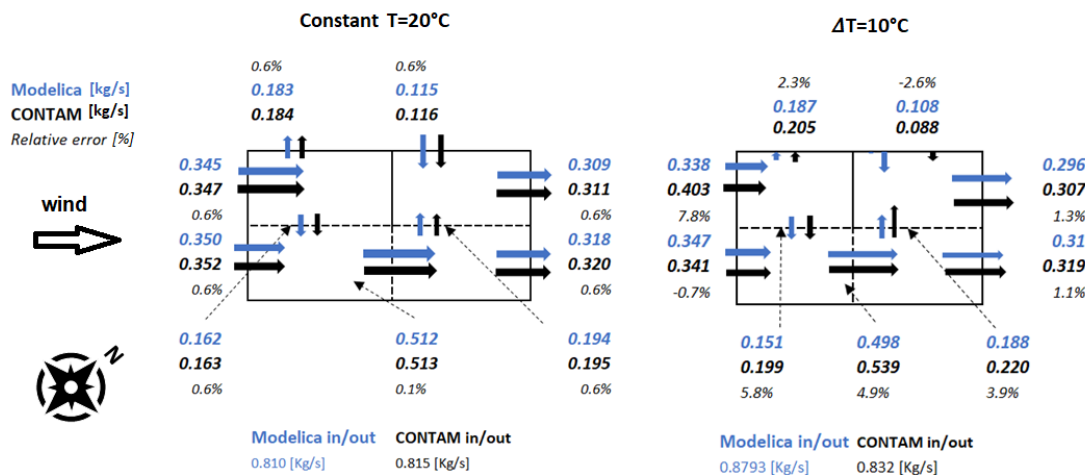


Figure 3.25: Mass flow rates computed with Modelica and CONTAM models for an isothermal configuration and a difference of temperature configuration.

The flow direction prediction in the Modelica model aligns with the results provided by CONTAM. A comparative validation of the orifice power law and the windows model (with flow reversal) shows close correspondence between the Modelica and CONTAM models under steady isothermal conditions, with a negligible  $RE$  of around 0.6%. However, results diverge when temperature differences exist between various air zones. For example, when the temperature difference ( $\Delta T$ ) is  $10^{\circ}\text{C}$  in some openings, the flow rate discrepancy can reach 8%. This variability can be attributed to the different approximations used in the Modelica models. In the Modelica model, the air density utilised is the average of the air density in adjacent opening zones, whereas the CONTAM model uses the calculated density



corresponding to the inflowing air. Additionally, CONTAM's resolution method employs a symbolic approach, while the Modelica model uses a method of discretization. Despite the noted divergence, the overall in and out mass flow rate is acceptable, with the RE remaining under 5%.

This comparison allowed us to verify the equations and couplings between the pressure models used in the indoor airflow model developed within the framework of the McZM.

### 3.3 Conclusions

This chapter discusses outdoor and indoor airflow models, as well as their validation and verification methods.

The outdoor airflow modelling method uses pre-calculated mass flow rate ( $mfr$ ) from CFD RANS simulations. This results in detailed airflow predictions and significantly trims computation time for dynamic enthalpy and surface balance in combined building and microclimate models. Nevertheless, this method assumes neutral atmospheric stability and that the airflow is chiefly wind-driven. It does not account for airflow induced by buoyancy or turbulence. This oversight is tolerable for high wind speeds and certain geometric configurations conducive to airflow but not for slower wind speeds. This limitation should be taken into account in future developments. Lastly, although the RANS modelling approach yields satisfactory results for high wind speeds, it is less precise for lengthy recirculation flows (Merlier, 2015).

To verify the accurate handling of CFD simulations using Fluent, measurements from wind tunnel experiments of flow around an isolated parallelepiped are reproduced using the same turbulence model (RANS  $rk - \epsilon$ ) used for the McZM airflow model. The ability to reproduce numerical simulations from the literature of external heat transfer coefficients ( $h_{c_{ext}}$ ) using a RANS  $rk - \epsilon$  turbulence model and a standard wall function is also discussed. If the RANS  $rk - \epsilon$  model using LRNM correctly provides accurate predictions for convective heat transfer coefficient on windward faces, it is not the case for other faces of the building. Additionally, convective heat transfer coefficient obtained using a standard wall function, introduces an additional level of approximation compared to high-resolution, LRNM.

The  $h_{c_{ext}}$  calculation is premised on the concept of forced convection. Under forced convection, our undertaken methodology strives to enhance the accuracy in estimating  $h_{c_{ext}}$ , as opposed to relying on empirical formulas pertinent to certain geometries or the standard  $h_{c_{ext}}$  values stipulated by regulatory bodies.

In addition, the dynamic simulation predicts average  $mfr$ , average  $h_{c_{ext}}$  for the building envelope and outdoor soil, average pressure coefficient ( $cp$ ) for the building envelope, and average airzone air velocity ( $v_a$ ) at the pedestrian level. These predictions are based on linear interpolations of results from CFD simulations, which introduces an additional approximation level compared to direct results from CFD simulations. Lastly, a balancing

approach is employed to ensure mass conservation, which does not alter overall airflow.

We have developed a model for indoor airflow pressure, referred to here as the natural ventilation model, which has been coupled to the McZM and BEM. This coupling process involves resolving both the energy and mass balances. Verification of this model was achieved by replicating the airflow model with the CONTAM tool, ultimately yielding very similar results. To validate the relevance of input parameters related to the type of opening and surface area, a comparison of these airflow rates with actual measurements in buildings would be beneficial. This would also allow verification of the suitability of the power laws chosen in the model for the observed flow types.

The radiative, BEM, soil and outdoor *Tmrt* model components and their validation approach will be discussed in the following chapter.

# Chapter 4

## Radiative, BEM, Soil and $T_{mrt}$ models

This chapter aims to explain the SWR, LWR, BEM, soil, and  $T_{mrt}$  model elements of the combined McZM and BEM (refer to components (1), (2), (4), (5), and (7) of Figure 2.11). It also includes a validation or verification study for each model. This is accomplished through comparison with either experimental data or numerical simulations.

### Contents

---

<b>4.1</b>	<b>Solar radiation model</b>	<b>116</b>
4.1.1	Model description	116
4.1.2	Model comparison	117
<b>4.2</b>	<b>Long Wave radiation model</b>	<b>120</b>
4.2.1	Model description	120
4.2.2	Model comparison	122
<b>4.3</b>	<b>Outdoor soil model</b>	<b>124</b>
4.3.1	Hydrological modelling approaches for soil models	124
4.3.2	Model description	125
4.3.3	Model validation	131
<b>4.4</b>	<b>Building energy model (BEM)</b>	<b>133</b>
4.4.1	Model description	133
4.4.2	Model comparison	136
<b>4.5</b>	<b>Indoor and Outdoor <math>T_{mrt}</math> model</b>	<b>139</b>
4.5.1	Model presentation	139
4.5.2	Outdoor $T_{mrt}$ model comparison	142
<b>4.6</b>	<b>Conclusions</b>	<b>146</b>
4.6.1	Chapter conclusions	146
4.6.2	General conclusions of part II	147

---

## 4.1 Solar radiation model

### 4.1.1 Model description

The HeliobIM software (Bouquerel et al., 2021) is used to calculate the irradiance on a building envelope, ground, and various elements of an urban scene. The inputs for HeliobIM include the site location, direct and diffuse solar radiation fluxes (sourced from a weather file, such as TMY2 or Energyplus EPW), and the 3D geometry of the site. The software also utilises data on longitude, latitude, and time zone to determine the sun's position.

HeliobIM can consider the effects of solar shading and reflections caused by the structure and reflective surface properties of a district. This is accomplished by using a Monte-Carlo ray-tracing algorithm, which calculates four types of irradiance, namely direct-direct, direct-reflected, diffuse-direct, and diffuse-reflected (Lindsay et al., 2016), as illustrated in Figure 4.1).

The Monte-Carlo ray-tracing algorithm dispatches rays in an evenly distributed manner across the hemisphere. These rays then reach the light sources originating from the sun and dispersing from the sky via successive reflections.

To cut down on computation time, direct irradiance is determined by the model at about 144 critical sun positions across the year, equating to one day every 30 days and one position per hour throughout sunlight hours. The model then interpolates the remaining days prior to applying the weather file. The procedure to calculate solar irradiance on an hourly basis across a year consumes less than a minute. The sun moves  $15^\circ$  each hour, and between two days at the same time, it shifts roughly  $0.11^\circ$  around the solstices and  $0.40^\circ$  near the equinoxes. Thus, the maximum change over 30 days will be  $12^\circ$  or less. For files with hour-long time steps, a 30-day time span appears to be appropriate because the angular error stays below that of two time steps. The solar irradiance is computed for each surface of the

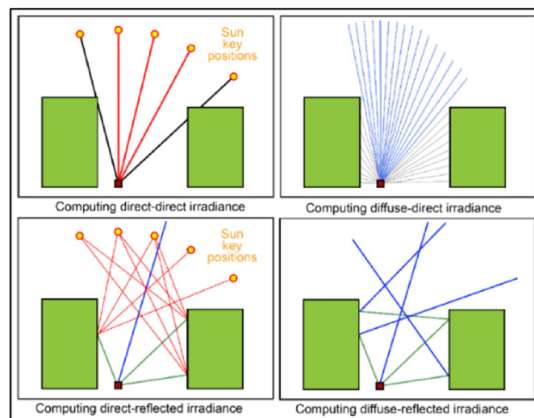


Figure 4.1: Four components of solar irradiance calculated by HeliobIM (Bouquerel et al., 2021).

building envelope (opaque walls, roofs, openings...) at the hourly time step provided by the weather file. From HelioBIM, it is possible to export the building information modelling (BIM) as a gbXML file, and the results of the solar calculation as CSV files. These data are used by the dynamic models in stage 4) and 5).

#### 4.1.2 Model comparison

The SWR model outlined in Section 4.1 was previously validated through a study of photovoltaic panels (Chiodetti et al., 2018). This particular study did not evaluate the impact of shading, as the PV panels were unobstructed. As such, this section seeks to corroborate the solar radiation model (SWR) described in 4.1 by comparing it with an equivalently validated Monte-Carlo ray-tracing model.

The model's ability to accurately calculate shade is evaluated by examining solar radiation within a canyon. This involves comparing the results from the solar radiation model in HelioBIM with those from a backward Monte-Carlo code developed at CETHIL. This code, used in other validation cases (Galtier et al., 2022), serves as a reference. The backward Monte-Carlo code generates numerous random paths from each probe location, where the radiative powers are assessed.

#### Case study configuration

The case study replicates the DIAMS project <sup>1</sup> case study setup as described by Gresse et al. (2023). Figure 4.2 and in Table 4.1 depict the study's geometry, weather data boundary conditions, and the radiative properties of its surfaces. The investigation focuses on the ground surface C and two canyon-facing facades: north-facing wall A and south-facing wall B.

Table 4.1: SWR radiative surface properties and direct and diffuse solar flux for the SWR study configuration.

Albedo		
Ground	0.15	
Walls A and B	0.4	
Roofs	0.2	
Horizontal flux [ $\text{W m}^{-2}$ ]	Direct	Diffuse
6:30 AM	194.2	128.0
12:30 PM	603.5	263.1
5:30 PM	112.5	115.3

<sup>1</sup>DIAMS is a collaborative research project that aims to define and test methods adapted to urban environments for exploiting satellite data to provide accurate, large-scale information on surface and air temperatures. It involves the research centers CEREMA, CETHIL, ONERA, KERMAP and ICube.

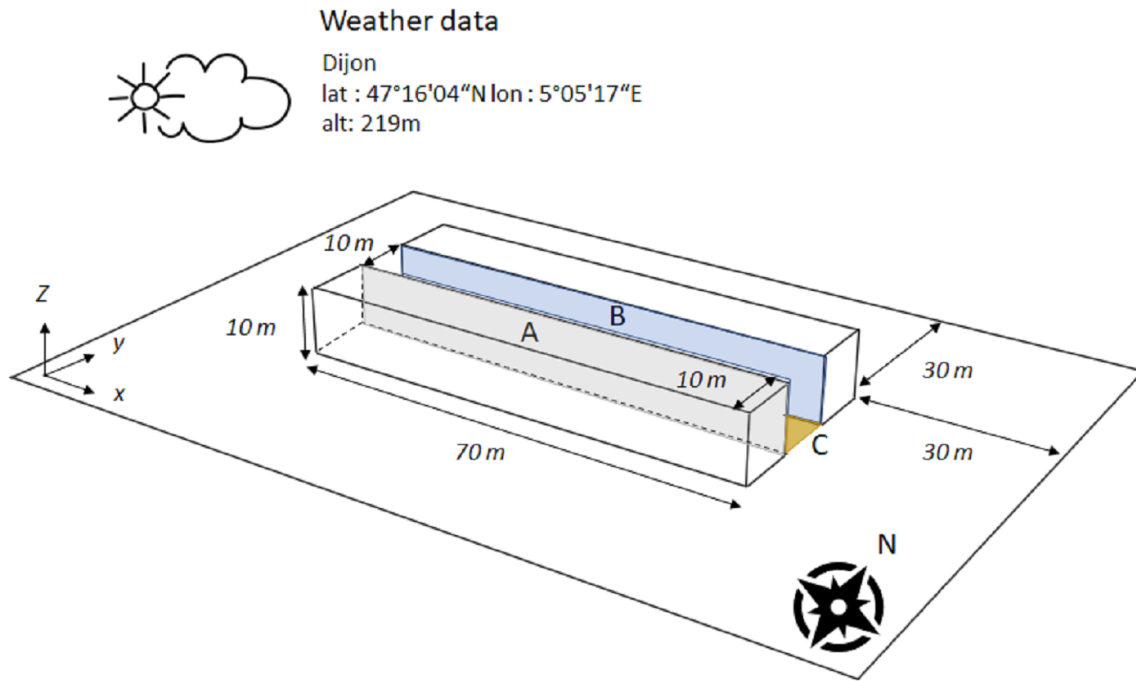


Figure 4.2: Simple canyon geometry configuration.

### Model setting

The geometry depicted in Figure 4.2 was replicated in SketchUp and imported into HeliobIM. To examine the vertical and horizontal irradiance profiles (refer to Figure 4.3), surfaces A, B, and C were discretized. The DIAMS Monte-Carlo model configuration utilised a fine meshing approach, providing 20 points for horizontal profiles (1, 2, and 3) and 141 points for vertical profiles (4, 5, 6).

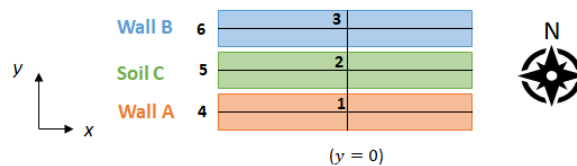


Figure 4.3: Illustration of the 3 vertical (1,2,3) and 3 horizontal (4,5,6) profiles for the 3 surfaces A, B and C.

In the HeliobIM model configuration, we use a coarser orthonormal mesh, comprising seven points for horizontal profiles and five points for the vertical profile (Figure 4.4). This mesh corresponds to a  $10 \times 2$  m surface discretization along the x- and z-axes for walls A and B and a  $10 \times 2$  m surface discretization along the x and y-axes for ground C. This is representative of the air zone surfaces in the McZM and BEM, aligning with the thermal zone divisions in the building and urban pedestrian space. It is important to note that HeliobIM software does not support fine discretization like the DIAMS model because it was not designed for that purpose. Radiative surface properties used in the Monte-Carlo and

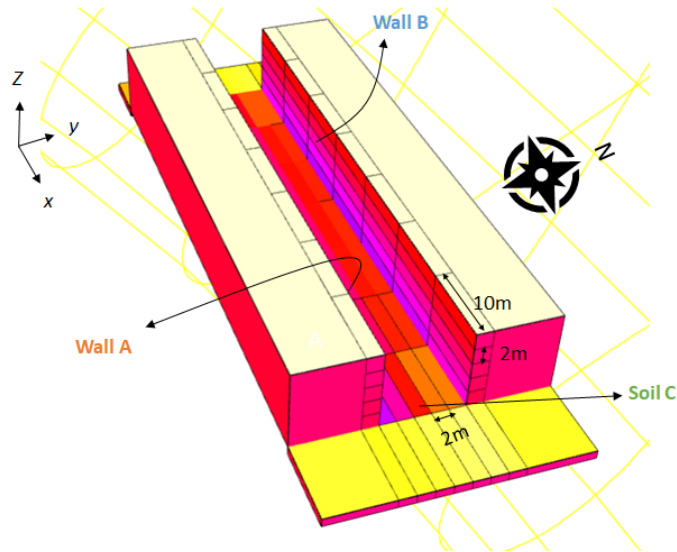


Figure 4.4: Reproduction of the DIAMS canyon configuration in Heliobim.

Heliobim model are ones specified in Table 4.1. The simulation runs at three different times of the day on July 18th at 6:30 AM, 12:30 AM and 5:30 PM. In both models, air is considered to be a transparent medium.

## Results and discussions

The metric used to evaluate the two model discrepancies is the relative error ( $RE[\%]$ ) calculated as follows:

$$RE = 100|(I_{MCa} - I_{HeB})|/I_{MCa} \quad (4.1)$$

Where :

- $I_{MCa}$  is the solar irradiance calculated with the Monte-Carlo model [ $W m^{-2}$ ]
- $I_{HeB}$  is the solar irradiance calculated with the Heliobim model [ $W m^{-2}$ ]

Figure 4.5 shows the average of solar irradiance, on the three surfaces A, B and C at 6:30 AM, 12:30 AM and 5:30 PM on July the 18th for the Monte-Carlo model and for the Heliobim model.

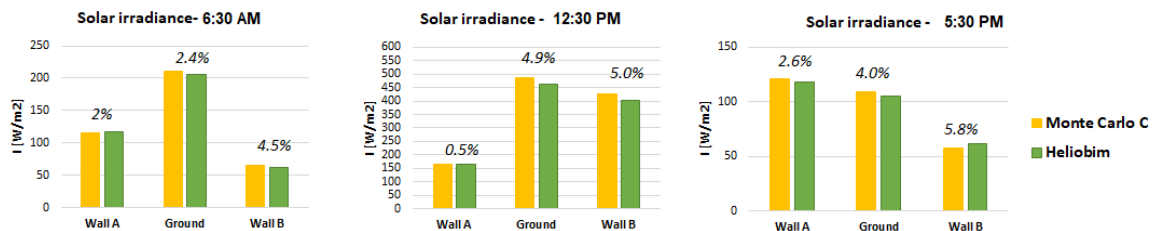


Figure 4.5: Average irradiance on the A, B, C surface at different periods of the day and corresponding RE at 6:30 AM, 12:30 AM and 5:30 PM on July the 18th.

Figure 4.5 demonstrates that the outcomes from Heliobim align closely with the detailed

Monte-Carlo model. However, there are instances of relative errors peaking at less than 6%. Such discrepancies are more evident when the sun is low, and surfaces experience higher direct solar flux.

To pinpoint the reasons behind these discrepancies, we analyze the vertical and horizontal irradiance profiles illustrated in Figure 4.6.

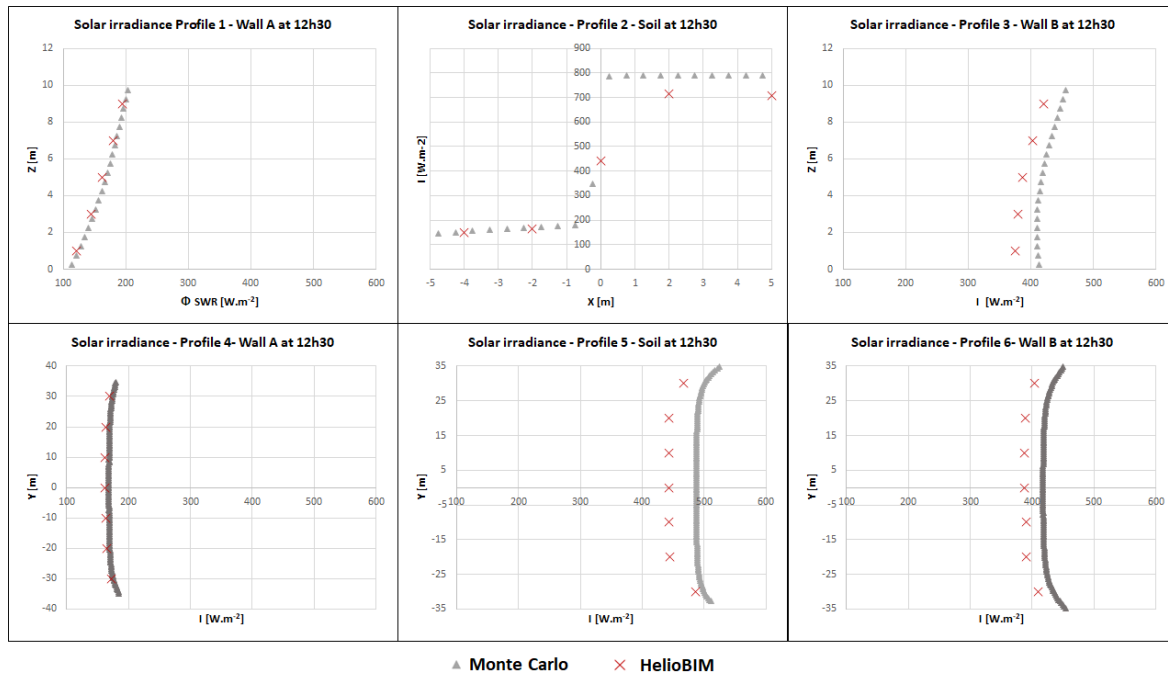


Figure 4.6: Solar irradiance profile on the A, B, C surfaces at different periods of the day on July the 18th.

The main error occurs when the direct solar radiation is the higher (profile 3 on wall B and the up side of the profile 2). These sources of error can be explained by the approximation associated with the interpolation of sun positions. In fact, as described in section 4.1, HelioBIM interpolates the sun's position. Another reason for discrepancies can be the shift between the sun position at each hourly time step and the horizontal direct solar flux provided with a 30-minute offset.

## 4.2 Long Wave radiation model

### 4.2.1 Model description

The method used to calculate the LWR heat flux in the coupled McZM and BEM is the radiosity method. The external environment is considered as a closed enclosure composed of the grey surfaces (ground, building surfaces) able to receive and to emit the LWR heat flux and the sky only able to emit.



For the grey surfaces, the net LWR heat flux is calculated as follows:

$$\Phi_{LWR} = \epsilon M^0 - \alpha E \quad (4.2)$$

$$\text{Where : } \begin{cases} \Phi_{LWR} \text{ is the net radiative LWR heat flux on the surface [W m}^{-2}\text{]} \\ \epsilon \text{ is the emissivity of the grey surface [-]} \\ M^0 \text{ is the radiant exitance of a black body [W m}^{-2}\text{]} \\ E \text{ is the irradiation received from the surrounding surfaces [W m}^{-2}\text{]} \end{cases}$$

$\Phi_{LWR}$  is positive when the surface emits more energy than it receives. This equation involves the computation of view factors, indeed, the long wave irradiation received by a surface  $i$  ( $E_i$ ) results from the sum of the radiosities emitted by the surrounding surfaces  $j$  (where  $j = [1, \dots, n]$  and  $n$  is the number of surface) multiplied by the view factor  $F_{ij}$  as follows :

$$E_i = \sum_{j=1}^n F_{ij}(\epsilon_j M_j^0 + \rho_j E_j) \quad (4.3)$$

The LWR heat flux from the sky is calculated using the Equation 4.2 with  $\alpha = 0$ . The sky temperature is also needed to compute  $M^0$ .

In the coupled McZM and BEM modelling approach, view factors are calculated by the HeliobIM software using the Monte Carlo ray-tracing method in the pre-processing stage. HeliobIM is also used to set parameters for the surfaces' radiative attributes, such as emissivity and reflection coefficients, as well as to determine the sky temperature. Sky temperature is computed based on two distinct formulas, which depend on the known or unknown status of humidity levels.

When humidity is known, the following empirical equation is used (Aubinet, 1994):

$$T_{sky} = 94 + 12.6 \log(v_p) - 13Ci + 0.341T_a \quad (4.4)$$

$$\text{Where : } \begin{cases} T_{sky} : \text{ is the sky temperature [K]} \\ v_p : \text{ is air the vapour pressure [mbar]} \\ Ci : \text{ is the clearness index (ratio of the received irradiance} \\ \text{on a horizontal plane to the extraterrestrial irradiance} \\ \text{received on a horizontal plane [-]} \\ T_a : \text{ is the air temperature [K]} \end{cases}$$

When humidity is not known, the following empirical equation is used:

$$T_{sky} = 273 - 29.9 - 19.9Ci + 1.09T_a \quad (4.5)$$

Note that the  $C_i$  is set to zero during the night, meaning that in the current implementation,  $T_{sky}$  can be overestimated (from 0 °C to 13 °C).

The net LWR heat flux is calculated during the dynamic simulation stage. To minimize the computation time needed to solve equation 4.2, a streamlined model has been created. This can be optionally activated in both McZM and BEM dynamic resolutions. In this model, the outdoor LWR exchanges take place solely among the building surfaces, the ground, and the sky. Any LWR exchanges between buildings are disregarded. Frayssinet's thesis (2018) demonstrates that this assumption is justified due to the slight underestimation of summer surface temperatures, as well as the reduction of the computational time by more than a factor of 3 when the simplified model is used. Thus, the net flux of surface  $i$  can be expressed as follows:

$$\phi_{LWR,i} = \epsilon_i \sigma [F_{i,sky}(T_{s,i}^4 - T_{sky}^4) + F_{i,grd}(T_{s,i}^4 - T_{s,grd}^4)] \quad (4.6)$$

$$\text{Where : } \left\{ \begin{array}{l} F_{i,sky} : \text{is view factor between } i \text{ surface and the sky } [-] \\ F_{i,grd} : \text{is view factor between } i \text{ surface and the ground } [-] \\ T_{sky} : \text{is the sky temperature } [K] \\ T_{s,i} : \text{is the temperature of the surface } i [K] \\ T_{s,grd} : \text{is the temperature of the ground, approximated in the} \\ \text{simplified model with the air temperature } [K] \end{array} \right.$$

In Chapter 5's application study, we use a simplified model that excludes the building-to-building LWR heat exchange. A linearization of equation 4.6 is performed. Additionally, we estimate the soil surface temperature using air temperature for the LWR heat exchanges.

For the purposes of model comparison (discussed in Section 4.2.2), we consider a global model that includes LWR radiation exchanges between outdoor surfaces.

## 4.2.2 Model comparison

This section validates the LWR model from Section 4.2 by comparing it with a pre-validated model. The same Monte-Carlo model as the solar radiation one (Galtier et al., 2022), which was previously used in the DIAMS project to compute LWR fluxes, was utilised.

### Case study configuration

The comparative study uses the case study presented in Section 4.1.2. The surfaces' radiative properties are reported in Table 4.2.

Table 4.2: SWR radiative surfaces properties.

	Emissivity	Transmissivity	Surface temperature [°C]
Ground	0.9	0	17
Walls A and B	0.9	0	25
Roofs	0.9	0	25
LWR flux [ $\text{W m}^{-2}$ ]			
Sky	394.4		

### Model setting

The geometry and meshing detailed in Figure 4.4 pertain to the model, while the profiles in focus are those illustrated in Figure 4.3. Table 4.2 outlines the LWR radiative surface properties utilised in both the Monte-Carlo model and within the McZM's LWR model. The model's simulation is set for July 18th at 12:30 PM. It is important to note that the assumptions in this model include an isotropic sky and air as a nonparticipating medium in LWR exchanges.

### Results and discussions

The metric used for the average long wave irradiation is the  $RE$ . In addition, the metric used for the long wave irradiation profiles is the maximal  $RE$  ( $RE_{Max}$ ).

Averaged long wave irradiation reported in Figure 4.7 show a good agreement between the Monte Carlo model and the LWR model of the McZM presented in section 4.2 with an average relative error inferior to 0.6%.

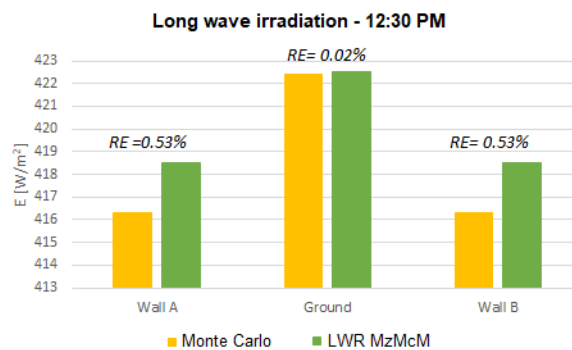


Figure 4.7: Average long wave irradiation for the Monte-Carlo method and the LWR model of the McZM and the RE July 18th at 12:30 PM.

The vertical and horizontal profiles (Figure 4.8) display significant discrepancies that can be attributed to the varying modelling approaches and discretization levels used by the two models. The Monte-Carlo approach contrasts with the radiosity method, and the models use different meshing densities. The Monte-Carlo model employs a detailed mesh with 140 points on the y-axis and 20 points on the z-axis. In contrast, the LWR model of the McZM

uses seven points on the y-axis and 5 points on the z-axis.

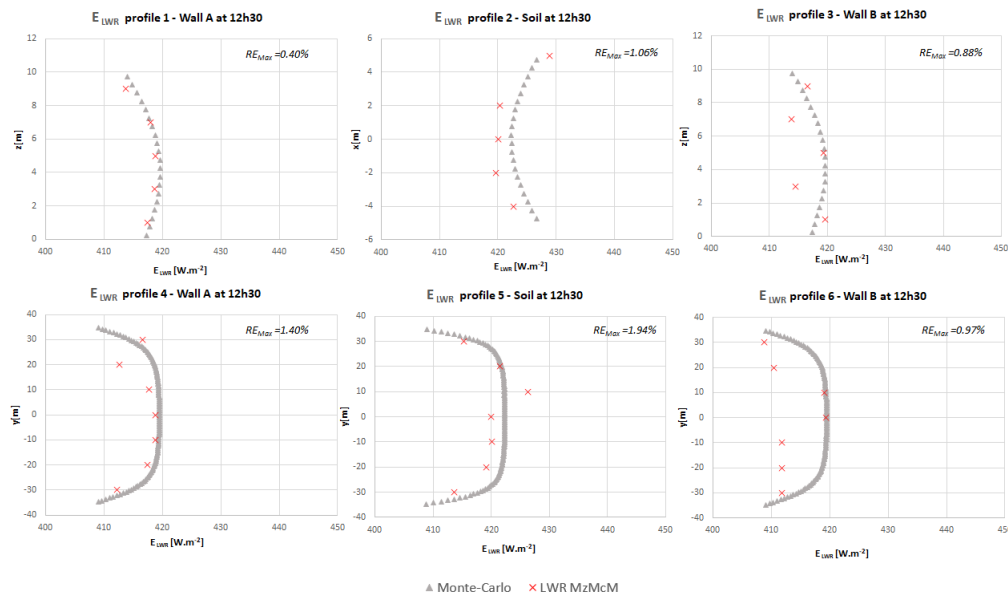


Figure 4.8: Comparison of the long wave irradiation profiles and RE: Monte Carlo model and LWR model of the McZM.

## 4.3 Outdoor soil model

### 4.3.1 Hydrological modelling approaches for soil models

Various hydrological modelling approaches can be used to determine the evaporation flux in urban soil models, which results from air-to-soil interactions (Musy, 2012):

#### Parameterization of evaporation flux

Effective evaporation flux is estimated as a fraction of potential evaporation proportionate to the water stored at the soil surface. This parameterization draws inspiration from rural hydrology studies and does not account for potential impacts of urban mineral surface warming on evaporation flux (Musy, 2012, Rodriguez, Andrieu, and Morena, 2008).

#### Hydro-energetic model

This model takes into account the interaction between energy and hydrological balances to represent surface water fluxes. Different modelling approaches can be distinguished:

- Simplified modelling of potential evaporation using the Penman-Monteith equation (see Appendix H), incorporating net radiation, air temperature, wind speed, and saturation vapour pressure. Actual evaporation is then deduced based on the water content at the soil surface. This modelling approach is used for example in SOLENE-Microclimat soil model (Vinet, 2000; Bouyer et al., 2009) or in Chalhoub (2017) heat

and moisture soil model.

- Modelling evaporation through a thermo-hydraulic balance within the soil using the  $\alpha$  method based on a bulk aerodynamic formulation for evaporation (Mahfouf and Noilhan, 1991) and the force-restored method (Dickinson, 1988) for soil heat water content. The force-restored method utilizes a prognostic temperature equation that precisely reproduces the response to periodic heating and uniform thermal properties. This approach was utilized in the ISBA-2L and ISBA-3L soil models (Noilhan and Mahfouf, 1996).
- Modelling evaporation by explicitly solving the Fourier and Darcy laws within the soil. This approach is employed in a more recent ISBA scheme coupled with the TEB scheme (Lemonsu, Masson, and Berthier, 2007).

For the McZM's specific purposes, considering various energy balance couplings, we prefer models that are easy to solve numerically. Accordingly, we use a simplified model of potential evaporation in the McZM soil model, employing the Penman-Monteith equation, which will be described below.

#### 4.3.2 Model description

To record ground-level surface temperatures hourly over a three-to-four-month period (specifically, the summer season), three soil models have been created using Modelica and operated in Dymola Figure Figure 4.9). These models are integrated with the McZM through surface balance:

- (A) An impervious soil model where only 1D thermal conduction, radiative and sensible exchanges at the surface are calculated.
- (B) A bare soil model, which includes the exchanges present in Model A, along with latent exchanges related to soil evaporation. The soil evaporation potential is estimated based on the Penman-Monteith formula and is adjusted based on the volumetric water content using a two-reservoir model (Chalhoub et al., 2017; Chalhoub and Philippe, 2015).
- (C) A soil model with small vegetation (where the shade effect is not considered), exhibiting the same exchanges as Model B, with the difference that the evaporation potential from foliage is calculated by approximating the leaf surface temperature with the air temperature in the Penman-Monteith formula.

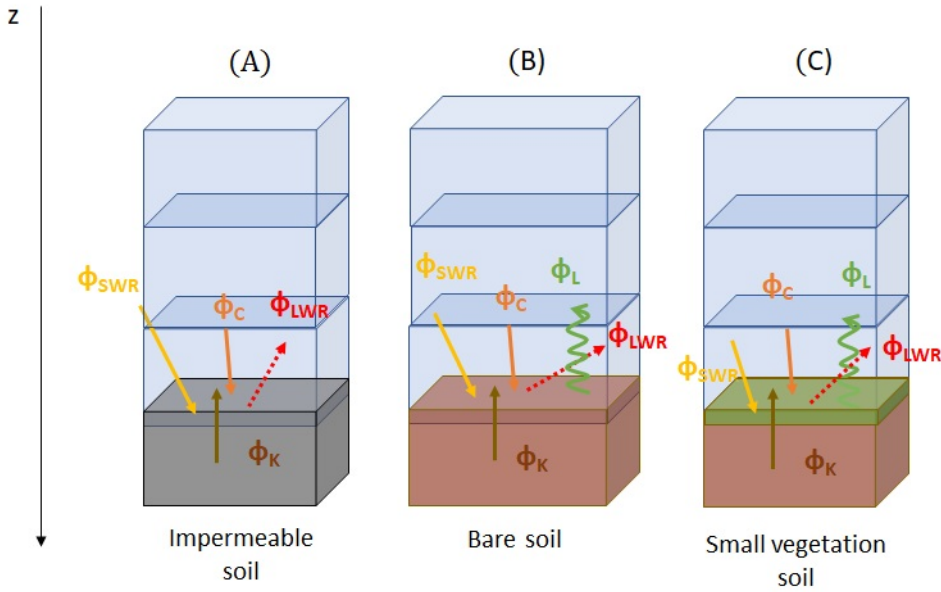


Figure 4.9: Outdoor soils models.

### Heat surface balance

The surface heat balance for the soil (A) and the soils (B) and (C) is described respectively by equations 4.7 and 4.8 respectively:

$$\Phi_{SWR} + \Phi_c = \Phi_{LWR} + \Phi_K \quad (4.7)$$

$$\Phi_{SWR} + \Phi_c = \Phi_{LWR} + \Phi_K + \Phi_L \quad (4.8)$$

Where :

- $\Phi_{SWR}$  is the SWR flux absorbed by the surface, depending on the albedo and the solar irradiance pre-computed in HeliobIM (see Section 4.1) [ $W m^{-2}$ ]
- $\Phi_{LWR}$  is the net LWR flux calculated with the model described in section 4.2 [ $W m^{-2}$ ]
- $\Phi_c$  is the convective heat flux [ $W m^{-2}$ ]
- $\Phi_K$  is the conductive heat flux [ $W m^{-2}$ ]
- $\Phi_L$  is the latent heat flux [ $W m^{-2}$ ]

The convective heat flux  $\Phi_c$  is computed using equation 2.3 where:  $T_a$  [ $^{\circ}C$ ] is the air temperature of the air zone adjacent to the soil,  $T_s$  [ $^{\circ}C$ ] is the soil surface temperature, and  $h_c$  [ $W m^{-2} K^{-1}$ ] is the external convective heat transfer coefficient, obtained from pre-computed simulations of CFD RANS  $rk - \epsilon$  as described in Section 3.1.2 and expressed in the following equations as  $h_{c_{ext}}$ .

The conductive heat flux  $\Phi_K$  is computed by solving the heat equation (4.9) using a finite volume method based on the floor model available in the BuildSysPro Modelica library

(Plessis, Kaemmerlen, and Lindsay, 2014).

$$\rho C_p \frac{\partial T}{\partial t} = -\lambda \frac{\partial^2 T(z, t)}{\partial z^2} \quad (4.9)$$

$$\text{Where : } \begin{cases} \rho \text{ is the soil density [kg m}^{-3}\text{]} \\ C_p \text{ is the soil specific heat [J kg}^{-1}\text{ K}^{-1}\text{]} \\ T \text{ is the temperature in the material [K]} \\ \lambda \text{ is the thermal conductivity of the material [W m}^{-1}\text{ K}^{-1}\text{]} \end{cases}$$

The latent heat flux  $\Phi_L$  [W m<sup>-2</sup>] corresponds to  $LE_v$ , where  $L$  is the latent heat of vapourization of water [J kg<sup>-1</sup>] and  $E_v$  [kg m<sup>-2</sup> s<sup>-1</sup>] is the soil evaporation, also expressed in [mms<sup>-1</sup>] assuming a density of 1000 kg m<sup>-3</sup> for water.  $E_v$  is obtained from equation 4.10 as a function of the evaporation potential  $E_0$  [mms<sup>-1</sup>], precipitation  $P_r$  [mms<sup>-1</sup>], and a coefficient  $\beta$ .  $\beta$  is a weighting coefficient obtained from equation 4.11 used to regulate the soil evaporation level that depends on the volumetric soil water content as described in the further section (Chalhoub et al., 2017).

$$E_v = P_r + \beta(E_0 - P_r) \quad (4.10)$$

$$\beta = \begin{cases} 1 - e^{-\frac{6.68\theta_1 h_1}{\theta_1^*}} & \text{for } P_r < E_0 \\ 1 & \text{for } P_r \geq E_0 \end{cases} \quad (4.11)$$

The evaporation potential  $E_0$  is calculated for model (B) based on the saturation vapour pressure at the surface temperature of the soil using the Penman-Monteith equation, expressed as equation 4.12 (developed in Appendix H).

$$E_0 = \frac{1}{L} \left[ \frac{\rho_a C_a}{r_a + r_c} \frac{(v_{p_s}^* - v_{p_a})}{\gamma} \right] \quad (4.12)$$

$$\text{Where : } \begin{cases} L \text{ is the latent heat of vapourization of water [J kg}^{-1}\text{]} \\ \rho_a \text{ is the air density [kg m}^{-3}\text{]} \\ C_a \text{ is the specific heat of air [J kg}^{-1}\text{ K}^{-1}\text{]} \\ r_a \text{ is the aerodynamic resistance [s m}^{-1}\text{]} \\ r_c \text{ is the crop resistance [s m}^{-1}\text{]} \\ v_{p_s}^* \text{ is the saturation vapour pressure at surface temperature [kPa]} \\ v_{p_a} \text{ is the vapour pressure at air temperature [kPa]} \\ \gamma \text{ is the psychrometric constant (0.063 kPa K}^{-1}\text{)} \end{cases}$$

In this equation, the evaporation potential is determined based on the saturation vapour pressure  $v_{p_s}^*$  [kPa] at the surface temperature of the soil.

In model (B)  $r_a$  is deduced from the  $h_{c_{ext}}$  values interpolated from the CFD preprocessing

described in 3.1.2 as follows:

$$r_a = \frac{\rho_a C_a}{h_{c_{ext}}} \quad (4.13)$$

In model (C), where the foliage surface temperature is unknown, the vapour pressure used is assumed to correspond to that of the air temperature, and equation 4.14 is used. This equation also incorporates a term for canopy resistance specific to vegetation. In equations 4.12 and 4.14.

$$E_0 = \frac{1}{L} \left[ \frac{\Delta(\Phi_{SWR} + \Phi_{LWR}) + \frac{\rho_a C_a (v_{p_a}^* - v_{p_a})}{r_a}}{\Delta + \gamma(1 + \frac{r_c}{r_a})} \right] \quad (4.14)$$

Where :

- $L$  is the latent heat of vaporization of water [ $\text{J kg}^{-1}$ ]
- $\Delta$  is the slope of the saturation vapour pressure curve (equation 4.15) [ $\text{kPa K}^{-1}$ ]
- $\Phi_{SWR}$  is the net short wave radiation [ $\text{W m}^{-2}$ ]
- $\Phi_{LWR}$  is the net long wave radiation [ $\text{W m}^{-2}$ ]
- $\rho_a$  is the air density [ $\text{kg m}^{-3}$ ]
- $C_a$  is the specific heat of air [ $\text{J kg}^{-1} \text{K}^{-1}$ ]
- $r_a$  is the aerodynamic resistance [ $\text{s m}^{-1}$ ]
- $r_c$  is the crop resistance [ $\text{s m}^{-1}$ ]
- $v_{p_a}^*$  is the saturation vapour pressure at air temperature [ $\text{kPa}$ ]
- $v_{p_a}$  is the vapour pressure at air temperature [ $\text{kPa}$ ]
- $\gamma$  is the psychrometric constant ( $0.063 \text{ kPa K}^{-1}$ )

Where :

$$\Delta = \frac{4098 v_{p_a}^*}{(T_a)^2} \quad (4.15)$$

Where  $T_a[\text{K}]$  is the air temperature. In model (C), as the  $h_{c_{ext}}$  at the foliage surface is unknown,  $r_a$  is obtained according to the FAO formulation (Allen, Pereira, and Smith, 1988), illustrated in Figure 4.10:

$$r_a = \frac{\ln\left(\frac{z_{ref} - z_d}{z_{0m}}\right) \ln\left(\frac{z_{ref} - z_d}{z_0 h}\right)}{k^2 v_{ref}} \quad (4.16)$$

where  $z_{ref}[\text{m}]$  is the height above the ground level where wind speed, air temperature and air humidity are measured,  $v_{ref}[\text{m s}^{-1}]$  is the wind speed at  $z_{ref}$  the  $k(0.42)$  is the Von Karman constant,  $z_d[\text{m}]$  is the zero plane displacement height,  $z_{0m}[\text{m}]$  is the roughness length governing momentum transfer and  $z_0 h[\text{m}]$  is the roughness length governing the transfer of heat and vapour. For a wide range of crops  $z_d$  and  $z_{0m}$  can be estimated from the crop height  $h_{veg}[\text{m}]$  by the following equations:

$$z_d = \frac{2}{3} h_{veg} \quad (4.17)$$

$$z_{0m} = 0.123 h_{veg} \quad (4.18)$$



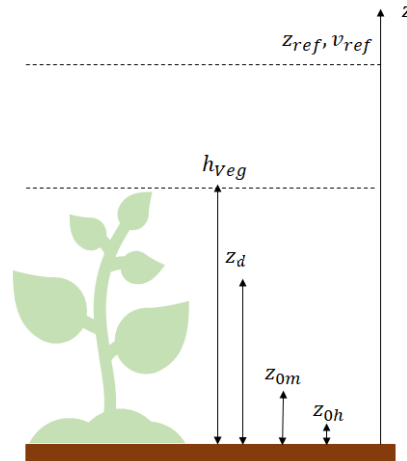


Figure 4.10: Schematic view of the displacement height and roughness length for low vegetation model (C) ( $z_{0h}$  not at scale).

$z_{0h}$  can be approximated by:

$$z_{0h} = 0.1z_{0m} \quad (4.19)$$

In both models (B) and (C),  $r_c [\text{s m}^{-1}]$  is obtained using the following relation (Chalhoub et al., 2017):

$$r_c = \frac{r_1}{0.5LAI} \quad (4.20)$$

Where  $r_1$  is the stomatal resistance of a single leaf, considered in the model (C) of  $\approx 100 \text{ s m}^{-1}$ ,  $LAI$  is the leaf area index, and if not known can be estimated using the following relation by Allen (Allen et al., 1989):

$$LAI = 5.5 + \ln(h_{veg}) \quad (4.21)$$

The use of the Jarvis expression (1976) for the calculation of stomatal resistance could have been an alternative as a replacement for the canopy resistance in equation 4.14.

### Soil water balance

The water balance soil model, depicted in Figure 4.11, is a dual-reservoir model proposed by Chalhoub (2017). This configuration, consisting of two soil layers, each functioning as a reservoir, balances modelling complexity and computational time with the phenomena being studied. It effectively takes into account the influence of rainfall and soil water content budget on total evaporation potential without necessitating the resolution of the water diffusion equation in the soil. Each reservoir is defined by the following characteristics:

- an initial volumetric water content  $\theta_{1_0}$  and  $\theta_{2_0}$  in  $[\text{cm}^3 \text{ cm}^{-3}]$ ,
- a height  $h_1$  and  $h_2$  in  $[\text{mm}]$ ,

- a soil moisture storage capacity  $\theta_1^*$  and  $\theta_2^*$  in [mm], calculated based on the residual volumetric water content  $\theta_r$  and the saturated volumetric water content  $\theta_s$  of the soil according to the following relation:

– reservoir 1:  $\theta_1^* = (\theta_s - \theta_r)h_1$ ,

– reservoir 2:  $\theta_2^* = (\theta_s - \theta_r)h_2$ .

$\theta_r$  and  $\theta_s$  are generally predicted using empirical functions depending on the soil composition and distribution of its components. Rawls et al.(1982) established mean values and standard deviation of  $\theta_r$  and  $\theta_s$  for 11 type of soil textures (Chalhoub et al., 2017) that can be used when data are not available. The evolution of the volumetric water content in the first reservoir follows the following law:

$$\frac{d\theta_1}{dt} = \frac{P_r - E_v}{h_1} \quad (4.22)$$

If  $\theta_1^*$  is reached, the water excess percolates into reservoir 2 until  $\theta_2^*$  is reached, and reservoir 2 fills according to the following law:

$$\theta_2(t) = \frac{\theta_1(t)h_1 - \theta_1^*}{h_2} + \theta_2(t - 1) \quad (4.23)$$

The water content of reservoirs 1 and 2 can never drop below  $\theta_r$ .

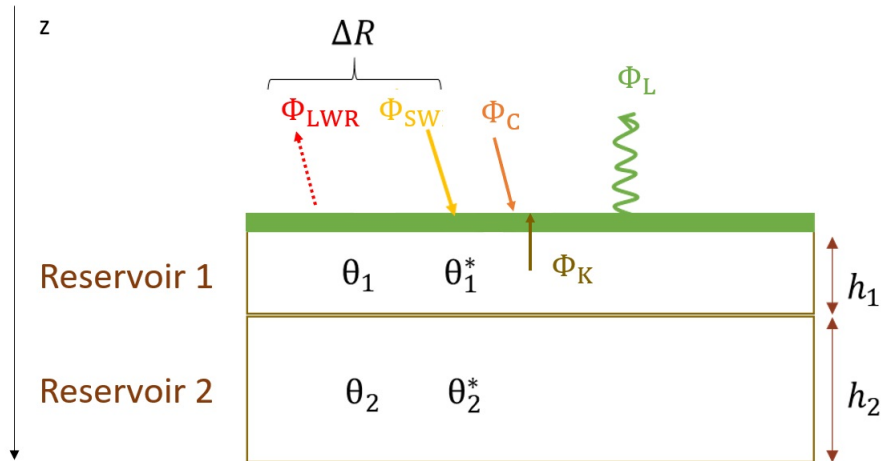


Figure 4.11: Two reservoirs water balance model.

### Soil thermal conduction

The soil thermal conduction is modelled solving the heat equation 4.9 with the finite volume method. The thermal conductivity and the heat capacity are assumed to be constant.

### 4.3.3 Model validation

This section focuses on the validation of the soil model (B) through comparison with experimental measurements of surface temperatures on a bare soil (Bittelli et al., 2008). The BuildSysPro library's soil model (A) has been validated in the comprehensive BEM model and, therefore, does not require extra validation in this thesis. Soil model (C) was not validated in this thesis due to insufficient experimental data related to vegetation arrangement, which is essential for validating latent heat exchanges and shading effects tied to vegetation presence. Hence, only soil models (A) and (B) will be utilised in subsequent work.

### Experiment description

Bittelli et al. (2008) conducted an experimental field trial in Holtville, California, from October 2 to 17, 2003. They studied the dynamics of soil during a drying cycle on a bare plot of soil measuring 50x100m<sup>2</sup>.

The soil type was Imperial-Glenbar silty clay loam. Experimental conditions included air temperature, *RH*, net radiation measured over the soil, irrigation, average wind speed, and some hydraulic properties like soil composition, density, and water-holding capacity. These conditions are detailed in Table 4.3.

Table 4.3: Soil properties used in model (B).

Soil properties	
Thickness	2 m
Composition	40% sand 40% silt 20% clay
Bulk density [kg m <sup>-3</sup> ]	1160
$\theta_s$ [m <sup>3</sup> m <sup>-3</sup> ]	0.56
Soil water capacity [m <sup>3</sup> m <sup>-3</sup> ]	[0.17-0.35]

### Model setting

Soil thermal properties (thermal conductivity and heat capacity), which were not explicitly provided, were set based on average data found in the literature for similar soil types. The thermal conductivity  $\lambda$  [W m<sup>-1</sup> K<sup>-1</sup>] being situated between 0.75 and 2.4 W m<sup>-1</sup> K<sup>-1</sup> depending on soil properties, hydric status and temperature, an average value of 1.5 was fixed. The soil specific heat is fixed at 2500 J kg<sup>-1</sup> K<sup>-1</sup>, corresponding to a soft grey fine sandy clay (Hamdhan and Clarke, 2010).

The experiment provides measurements of air temperature, *RH*, and net radiation, which serve as the boundary conditions for the soil model and establish initial conditions. We chose a constant wind speed of 5 m s<sup>-1</sup>, falling within the range of wind speeds recorded

at our weather station. We also set a boundary temperature condition of  $10^{\circ}\text{C}$  at a height of 2 m above the ground, in line with the setup for the DIAMS impervious soil model. For this experiment, we didn't prescribe a specific depth; we opted for a 2m depth to maintain consistency between the impervious and permeable bare soil models. Geothermal heat pump data from Virginia Tech<sup>2</sup> is relied upon for the soil temperature at this depth, which feeds into the boundary conditions. We also discretized the conduction model with a node spacing of 2 cm. The chosen soil properties used in the model (B) can be found in Table 4.3.

## Results and discussions

Figure 4.13 illustrates the observed and predicted soil temperatures at a depth of 2 cm, including the observed air temperature at the experimental station set up over bare soil. Figure 4.13 displays the variations in surface temperatures; the greatest variations align with periods of increased solar radiation during the day. The model accurately mirrors the trend of the surface temperature, with an average deviation of 6.2%. This discrepancy can be attributed to the model's inherent simplifications and approximations linked to our precise understanding of the soil's thermal and hydric properties. Additionally, it is important to note that soil model (B) is especially sensitive to changes in velocity. However, the model uses an average velocity, in contrast to the wind speed in the experiment, which constantly fluctuates and occasionally exceeds  $8\text{ m s}^{-1}$ . To conclude, soil model B strikes a balance between accurate results and the need for input parameters. Although a more complex model might demand more input data and computing resources, which may be unavailable or challenging to acquire during an experiment, it would also entail higher computational costs and be harder to implement numerically.

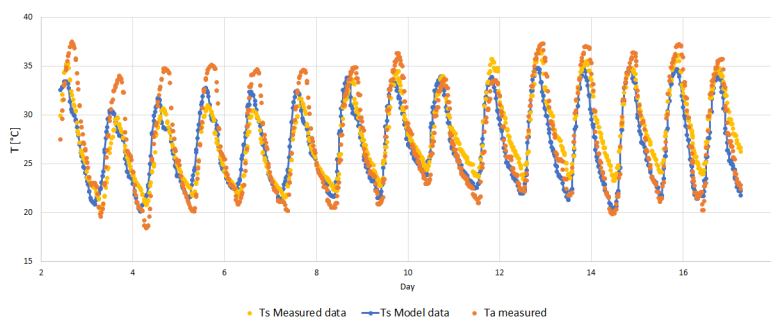


Figure 4.12: Measured and modelled soil temperatures at a depth of 2 cm and measured air temperature from 2 - 17 October 2003 (Hotville, California).

---

<sup>2</sup><https://www.builditsolar.com/Projects/Cooling/EarthTemperatures.htm>

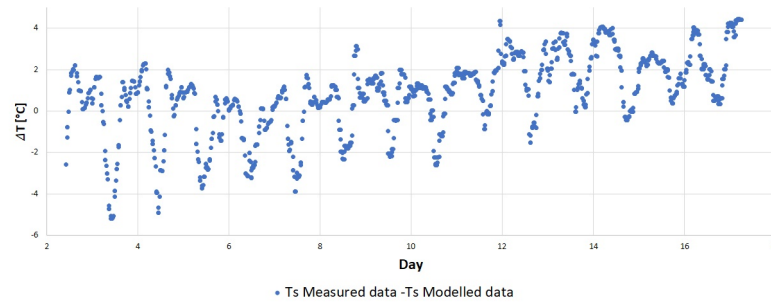


Figure 4.13: Measured and modelled soil temperature differences at a depth of 2 cm from 2 - 17 October 2003 (Hotville, California).

## 4.4 Building energy model (BEM)

### 4.4.1 Model description

The BEM is automatically generated by a Python-based program, PyRosette, which is part of the MyBEM toolchain. PyRosette uses output data from HelioBIM, which includes BIM and view factor files in gbXML format, a weather file, and solar fluxes in .csv format. This data is utilised to generate a building model in the Modelica language, which can be run in Dymola. The BEM uses modules from the BuildSysPro library (Plessis, Kaemmerlen, and Lindsay, 2014) as well as specific models developed under Dymola. The building model divides the structure into several air volumes, each isolated from the other and the external air by either opaque walls or glazed windows. Each air volume represents a thermal zone. The link between two thermal zones is established via heat transfer (conduction) or both heat and mass transfer (openings in walls or mechanical ventilation systems). The comprehensive building model can be broken down into two parts: a model for the walls and windows and a model for the air zone.

### Wall and window models

Walls are seen as opaque surfaces that divide thermal zones and permit heat transfer via conduction. Windows, on the other hand, are seen as clear surfaces in the walls that permit heat transfer through conduction and SWR. The wall and window model solves indoor and outdoor surface balance, and applies the unidirectional Fourier conduction equation:

$$\Phi_{SWR} + \Phi_{LWR} + \Phi_c + \Phi_K = 0 \quad (4.24)$$

$$\text{Where : } \begin{cases} \Phi_{SWR} \text{ is the solar flux absorbed by the surface [W m}^{-2}\text{]} \\ \Phi_{LWR} \text{ is the net surface long wave radiative flux [W m}^{-2}\text{]} \\ \Phi_c \text{ is the convective heat flux [W m}^{-2}\text{]} \\ \Phi_K \text{ is the conduction heat flux crossing the surface [W m}^{-2}\text{]} \end{cases}$$

### Outdoors $\Phi_{SWR}$

$\Phi_{SWR} = I(1 - a)$ , where  $I$  is the incident irradiation [ $W m^{-2}$ ] and is calculated using the solar radiation model presented in Section 4.1, and  $a$  is the albedo of the surface. The solar flux transmitted by windows  $\Phi_{SWRt} = \tau_w \Phi_{SWR}$ , where  $\tau_w[-]$  is the solar transmission coefficient of the media.

### Indoors $\Phi_{SWR}$

It is supposed that all the transmitted solar flux is distributed on the floor.

### Outdoors $\Phi_{LWR}$

The LWR flux for outdoor surfaces is computed according to the described model of Section 4.2.

### Indoors $\Phi_{LWR}$ and indoors $\Phi_c$

$\Phi_{LWR}$  and  $\Phi_c$  are calculated using equation 2.3, where  $h_c$  corresponds to a global heat exchange coefficient  $h_{c_{in}}$  integrating the effects of the convective and long wave heat exchanges. The value of this global heat exchange coefficient is provided by ISO 6946 norm<sup>3</sup>, which provides the method for calculating the thermal resistance of building components and walls. A value of  $h_{tot_{in}}$  is provided for each wall typology: vertical wall, floor, ceiling.

### Outdoors $\Phi_c$

$\Phi_c$  is expressed by equation 2.3 and it is calculated using interpolated values of the  $h_c$  pre-computed with CFD, as presented in Section 3.1.2.

### Outdoors and indoors $\Phi_k$

$\Phi_k$  is expressed by the Fourier law on the x-axis direction:

$$\Phi_k(x, t) = -\lambda \frac{\partial T(x, t)}{\partial x} \vec{n}\vec{x} \quad (4.25)$$

Where :  $\left\{ \begin{array}{l} \frac{\partial T}{\partial x} \text{ is the temperature gradient over the x-axis in the material [K m}^{-1}\text{]} \\ \lambda \text{ is the thermal conductivity of the material [W m}^{-1}\text{ K}^{-1}\text{]} \end{array} \right.$

The application of Fourier's combined with the conservation of energy, leads to the heat equation:

$$\rho C_p \frac{\partial T(x, t)}{\partial t} = \lambda \frac{\partial^2 T(x, t)}{\partial x^2} \quad (4.26)$$

---

<sup>3</sup>Composants et parois de bâtiments — Résistance thermique et coefficient de transmission thermique — Méthodes de calcul

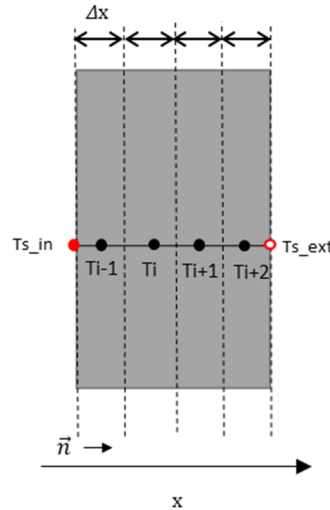


Figure 4.14: Example of spatial discretization along the x-axis.

Where :  $\left\{ \begin{array}{l} \rho \text{ is the density of the material } [\text{kg m}^{-3}] \\ C_p \text{ is the specific heat of the material at constant pressure } [\text{J kg}^{-1} \text{K}^{-1}] \end{array} \right.$

The heat equation is solved by numerical discretization of the computational domain and by temporal resolution of the associated differential system. The finite volume method is applied for the spatial discretization. The heat equation can then be expressed using the electrical analogy as follows (Figure 4.14, and 4.27):

$$\rho c_p \Delta x \frac{dT_i}{dt} = \frac{\lambda}{\Delta x} (T_{i-1} - T_i) + \frac{\lambda}{\Delta x} (T_{i+1} - T_i) \quad (4.27)$$

The boundary conditions are the indoor and outdoor surface temperatures.

### Air zone model

For a building with  $N$  thermal zones and  $n_w$  surfaces surrounding each thermal zone, the model solves the sensible and latent heat balance and the mass balance for the dry air in the zone  $i$  (Equations 4.28, 4.29 and 4.30).

The air renewal model is activated by assigning a value of air changes per hour (ACH) in the building model. This involves the exchange of air volumes within the building and the neighbouring external thermal zone. However, this model does not take into account the mass transfer between the building's internal air volumes nor the transfer between openings within the same thermal zone. To address inter-volume mass transfers, a unique airflow model has been developed and coupled this building model in Section 3.2.

$$\left\{ \begin{array}{l} \rho_i C_a V_i \frac{dT_i}{dt} = \sum_{n=1}^N C_a m f r^{in}(i, n) (T_n - T_i) + \sum_{j=1}^{n_w(i)} S_j h_{c,j} (T_{s,ij} - T_i) + P_s + S_s \end{array} \right. \quad (4.28)$$

$$\left\{ \begin{array}{l} m_{a,i} \frac{dr_i}{dt} = \sum_{n=1}^N m f r^{in}(i, n) (r_n - r_i) + \frac{P_l}{L} + \frac{S_l}{L} \end{array} \right. \quad (4.29)$$

$$\left\{ \begin{array}{l} \sum_{n=0}^N m f r^{in}(i, n) = \sum_{n=1}^N m f r^{out}(n, i) \end{array} \right. \quad (4.30)$$

Where :

$$\left\{ \begin{array}{l} \rho_i \text{ is the air density of the zone } i \text{ [kg m}^{-3}\text{]} \\ C_a \text{ is the air heat capacity [J kg}^{-1}\text{ K}^{-1}\text{]} \\ V_i \text{ is the air volume of the zone } i \text{ [m}^3\text{]} \\ T_i \text{ is the air temperature of the zone } i \text{ [K]} \\ T_n \text{ is the air temperature of the zone } n \text{ [K]} \\ m f r^{in}(i, n) \text{ is the air mass flow rate from thermal zone } n \\ \text{entering thermal zone } i \text{ [kg s}^{-1}\text{]} \\ m f r^{out}(i, n) \text{ is the air mass flow rate exiting thermal zone } i \\ \text{and entering thermal zone } n \text{ [kg s}^{-1}\text{]} \\ P_s \text{ is the sensible heat or cooling power generated by systems [W]} \\ P_l \text{ is the latent heat or cooling power generated by systems [W]} \\ S_s \text{ is the sensible internal heat source [W]} \\ S_l \text{ is the latent internal heat source [W]} \\ m_{a,i} \text{ is the dry air mass of the zone [kg]} \\ r_i \text{ is the specific humidity of the zone [kg}_{\text{water}}\text{/kg}_{\text{dry air}}\text{]} \\ L \text{ is the latent heat of vapourization of water [J kg}^{-1}\text{]} \end{array} \right.$$

#### 4.4.2 Model comparison

The BuildSysPro library building model has been validated on multiple occasions, primarily focusing on temperatures inside the building and heating power needs. We are interested in the interaction between the building and its external environment. Therefore, this section examines the outdoor surface temperatures yielded by merging the solar radiation, the LWR, and the building model discussed in sections 4.1, 4.2 and 4.4. These results are compared with the surface temperatures provided by the Traboule model. The latter, utilised in the DIAMS project, employs a radiative model based on a finite volume method and a unidirectional finite volume method to calculate the conduction flux through a solid volume (Schmitt et al., 2023).



### Case study configuration

The case study's configuration mirrors the geometry outlined in Section 4.1.2. Table 4.4 lists the thermal properties of the walls and soil. The radiative properties correspond to those detailed in Tables 4.1 and 4.2.

Table 4.4: Conduction study configuration.

Thermal properties				
<b>Surface Layers</b> (from outside to inside)	e [cm]	$\lambda$ [W m <sup>-1</sup> K <sup>-1</sup> ]	$\rho$ [kg m <sup>-3</sup> ]	$C_p$ [J kg <sup>-1</sup> K <sup>-1</sup> ]
<b>Walls A, B, Roofs</b>				
Insulation	5	0.03	50	1200
Concrete	30	1.7	2100	1000
<b>Ground</b>				
<i>Asphalt</i>	5	0.7	2400	880
<i>Untreated Aggregate</i>	35	1.8	1660	960
<i>General ground</i>	160	0.5	1900	800
<b>Boundary conditions</b>				
Inside $T_s$	25°C			
$T_s$ ground at 2 m deep	20°C			
$h_{c,out}$	30	[W m <sup>-2</sup> K <sup>-1</sup> ]		
<b>Initial conditions</b>				
Wall, roof and ground $T_s$	20°C			

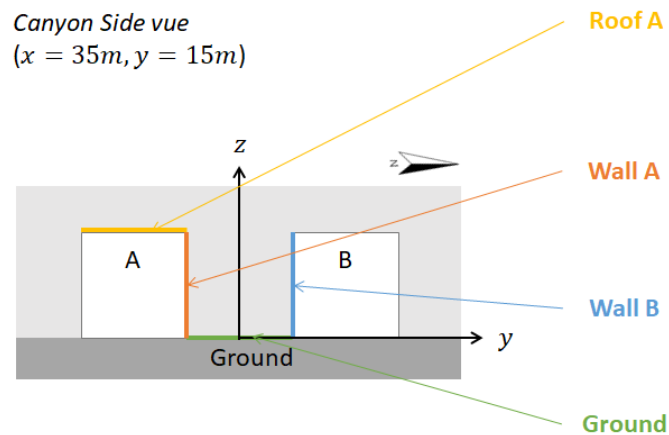


Figure 4.15: Canyon side view.

### Model setting

The model geometry mirrors that of the canyon, as depicted in Figure 4.2, without any discretization. The radiative and thermal properties of walls and soil employed in the Traboule and BuildSysPro BEM models adhere to the specifications outlined in Tables 4.1, 4.2, and 4.4.

The simulation spans from July 13 to 19 and utilises a uniform input weather file derived from measurements taken by the Dijon weather station. It is worth noting that the ground is depicted using the building wall model found in Section 4.4.

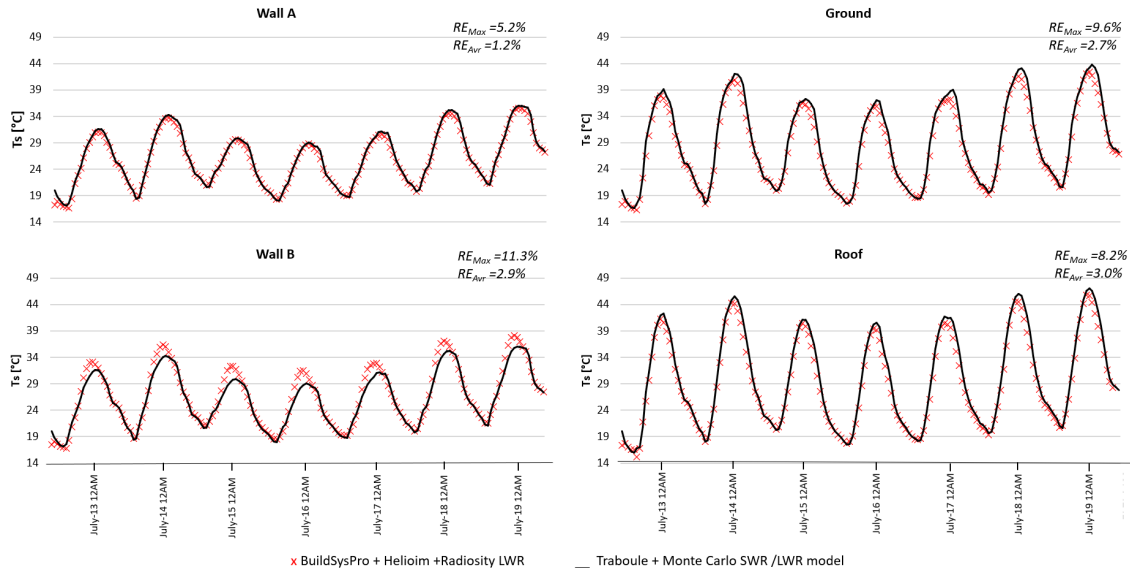


Figure 4.16: Surface temperatures on Wall A, Wall B, Roof A and Ground.

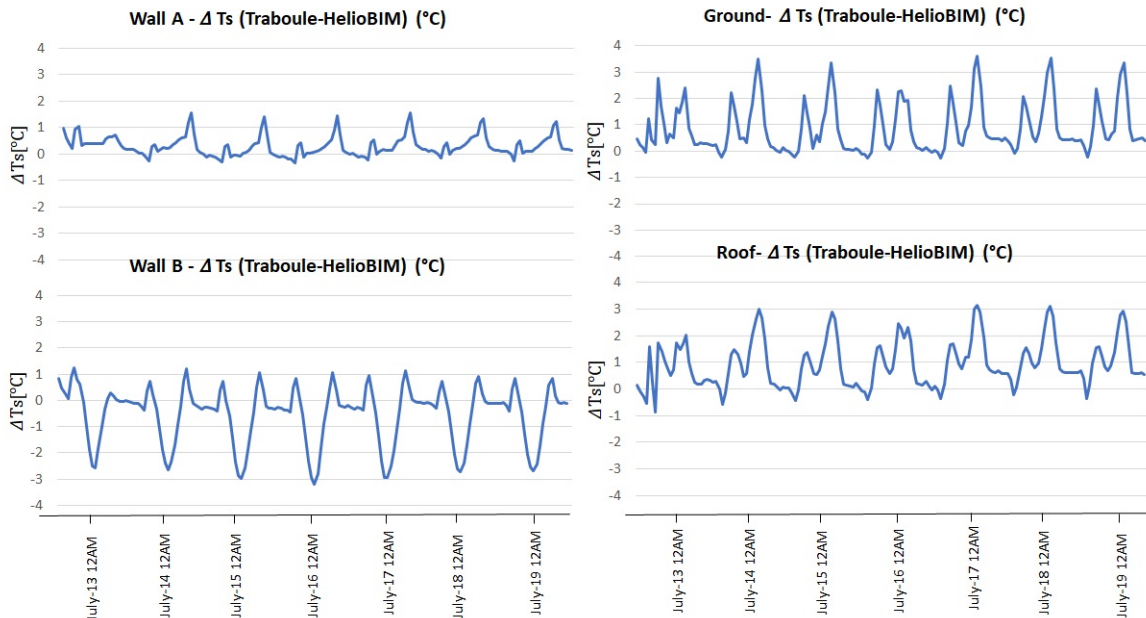


Figure 4.17: Differences of surface temperatures ( $T_s$  Traboule -  $T_s$  HelioBIM) on Wall A, Wall B, Roof A and Ground.

## Results and discussions

The metric used for the model comparison is the  $RE$ . Figure 4.17 highlights that the largest absolute difference in surface temperatures is seen on the ground and roof, reaching up to 3.6 °C. When considered in the context of the  $RE$ , these values are acceptable.

Figure 4.16 illustrates that the average surface temperatures for Wall A, Wall B, Roof A, and the ground are consistent across both models. The average relative error,  $RE_{Avr}$ , ranges from 1.2% to 3.0%. The highest relative error,  $RE_{Max}$ , peaks at 11.3% on Wall B when solar radiation is at its maximum. This discrepancy can be somewhat attributed to the different spatial discretization of the first solar-exposed layer of the wall.

The SWR and LWR fluxes are detailed in Appendix G.

## 4.5 Indoor and Outdoor $T_{mrt}$ model

### 4.5.1 Model presentation

#### Indoor $T_{mrt}$

Calculating the mean radiant temperature ( $T_{mrt}$ ) requires an understanding of the body's radiation environment. Simplified calculations for standing and seated persons based on tabulated view factors can be used for indoor environments. Additionally,  $T_{mrt}$  can be calculated by measuring both the internal temperature of a black globe ( $T_g$ ) and the air temperature ( $T_a$ ).

The zone-averaged method, surface-weighted method, and angle factor method are commonly used to calculate indoor  $T_{mrt}$  for thermal comfort models (Crawley et al., 2000).

The zone-averaged method assumes that a person is located at the centre of the space and determines the  $T_{mrt}$  based on this. On the other hand, the surface-weighted method calculates  $T_{mrt}$  as a weighted average, considering the surface nearest to the individual. Lastly, the angle factor method uses the angles between the person and various surfaces in the room to calculate  $T_{mrt}$ . This method provides a more accurate prediction of thermal comfort at a specific location within the space, but it requires knowledge of the angle factors. It represents the mean of surrounding surface temperatures, weighted according to their respective angle factors. Models like EnergyPlus offer the convenience of selecting any of these three approaches to calculate the mean radiant temperature.

In this thesis, the zone average model is utilised in the BEM, as the focus of the heat stress study is to compare different thermal zones rather than specific locations of individuals within a room. This means that the resulting  $T_{mrt}$  corresponds to a weighted average of the interior surface temperatures, taking into account their respective areas. This approach avoids making any assumptions about the room's configuration or the individual's place-

ment within the thermal zone.

### Outdoor $T_{mrt}$

Measuring the radiation environment outdoors around the body can be challenging. To facilitate this process, several simplified measurement methods have been proposed. The most commonly used are the six-directional technique, as recommended by VDK 3787 (1998) and the globe thermometer technique, outlined in ISO 7726 (ISO 1985, 1998).

Hoppe (1992) introduced the six-directional method, which simplifies surroundings into six perpendicular parts: the four cardinal points and above and below (Holmer et al., 2015; Kántor, Lin, and Matzarakis, 2014). The  $T_{mrt}$  on a standing person is calculated using this method by modelling the body as a rectangular box. This box emits the same amount of LWR as the combined short and LWR fluxes received from the six directions.

In the rectangular box model representing a standing body, assumed surface fractions ( $w_i$ ) are as follows: 0.06 for both upward and downward exposure and 0.88 for vertical exposure, which is split into four equal parts of 0.22 (Holmer et al., 2015; Fanger, 1972). The mean radiant flux absorbed by the body is calculated by summing up the SWR and LWR absorbed by each face  $i$ . Each absorption is multiplied by the surface fraction of a standing body as follows :

$$\phi_{net_{box}} = \sum_{i=1}^6 w_i (\alpha_{body} I_i + \epsilon_{body} E_i) \quad (4.31)$$

$$\text{Where : } \left\{ \begin{array}{l} \phi_{net_{box}} \text{ is the mean radiant flux absorbed by the body [W m}^{-2}\text{]} \\ w_i \text{ is the surface fraction of the standing body [-]} \\ \alpha_{body} \text{ is the body absorption coefficient for SWR (0.7) [-]} \\ I_i \text{ is the short wave irradiation incident the surface } i \text{ [W m}^{-2}\text{]} \\ \epsilon_{body} \text{ is the body absorption coefficient for LWR (0.97) [-]} \\ E_i \text{ is the long wave irradiation incident the surface } i \text{ of the body [W m}^{-2}\text{]} \end{array} \right.$$

The  $T_{mrt}$  [°C] is then calculated as follows:

$$T_{mrt} = \sqrt[4]{\phi_{net_{box}} / (\epsilon_{body} \sigma)} - 273.15 \quad (4.32)$$

Where  $\sigma$  is the Stefan-Boltzmann's constant ( $5.67 \times 10^{-8} \text{ W m}^{-2} \text{ K}^{-4}$ ).

Sophisticated methods employ a cylindrical model of the human body, as seen in Holmer et al. (2015). This shape offers the advantage of reducing discontinuities in flux at the corners of a box shape. Such a model is used in SOLWEIG (Dissegna et al., 2021). Other models, like the one in SOLENE Microclimate (Vinet, 2000), incorporate clothing resistance in calculating radiant flux absorbed by the body. Here, a projection factor is used to account for the radiation received based on body posture.

Furthermore, the RayMan model (Matzarakis, Rutz, and Mayer, 2007), highly referenced in various studies (e.g. Charalampopoulos et al., 2013, Abreu-Harbich, Labaki, and Matzarakis, 2014, Ndetto and Matzarakis, 2015, Yang and Matzarakis, 2016), uses a body modelling approach based on a projection factor. In this model, the body is depicted as a point divided into upper and lower hemispheres. This paper will use the RayMan model as a point of comparison in the succeeding section.

The outdoor ( $T_{mrt_{out}}$ ) calculation method developed in the McZM is inspired by the experimental six-directional method, involving measuring SWR and LWR in six directions (North, South, West, East, up, and down). According to the six-directional method, the  $T_{mrt}$  for a standing person is calculated by modelling the human body as a rectangular box following specific surface fractions ( $w_i$ ): 0.06 for the top and bottom and 0.22 for the vertical surfaces (Holmer et al., 2015). The specifics of the box used in the McZM are outlined in Table 4.5. To achieve a spatial representation of  $T_{mrt}$  at a pedestrian's level, a box is positioned at each zone's centre (Figure 4.18). This box is set 1.1 m above the floor, representing the centre of gravity for the human body (Fanger, 1972, Jendritzky, 1990).

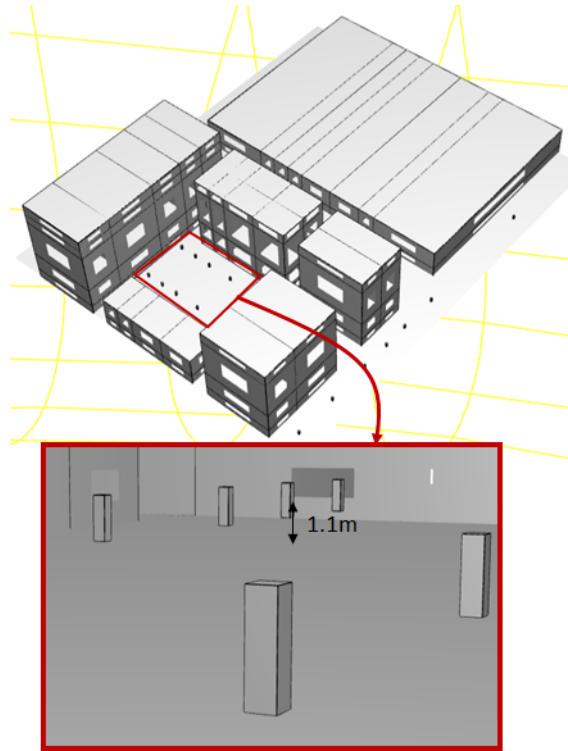


Figure 4.18: Rectangular boxes for  $T_{mrt_{out}}$  modelling.

The  $T_{mrt_{out}}$  is calculated using the following formula:

$$T_{mrt_{out}} = \left[ \sum_{i=1}^6 w_i \left( \sum_{j=1}^n \epsilon_j T_{s_j}^4 F_{ij} + \frac{\alpha_{body} I_i}{\epsilon_{body} \sigma} \right) \right]^{1/4} \quad (4.33)$$

Where :

- $T_{mrt_{out}}$  is the outdoor mean radiant temperature [K]
- $n$  is the number of surfaces surrounding the body [-]
- $\epsilon_{body}$  is the body absorption coefficient for LWR (0.97) [-]
- $w_i$  is the surface fraction of the body [-]
- $\alpha_{body}$  is the body absorption coefficient for SWR (0.7) [-]
- $\epsilon_j$  is the emissivity of the surrounding surface  $j$  [-]
- $T_{s_j}$  is the surrounding surface temperature [K]
- $F_{ij}$  is the view factor of the of the body surface  $i$  and surrounding surface  $j$  [-]
- $I_i$  is the global diffuse and direct short wave irradiation incident the body surface  $i$  [ $W m^{-2}$ ]
- $\sigma$  is the Stefan-Boltzmann constant =  $5.67 \times 10^{-8} W m^{-2} K^{-4}$

In HelioBIM,  $I_i$  and the  $F_{ij}$  values are computed using the ray-tracing method, and the input includes 3D geometry and a weather file. The weather file includes direct and diffuse solar radiation data, as well as sky temperature. The latter can be derived from available atmospheric radiation data. The temperatures of surrounding surfaces are determined through a dynamic McZM simulation and later utilised in the  $T_{mrt_{out}}$  post-process via a Python program.

Table 4.5: Body Box dimensions.

	Body Box dimensions
Length	0.33 m
Width	0.33 m
Height	1.21 m
horizontal surface	$(0.109 \times 2 = 0.218) m^2$
vertical surface	$(0.399 \times 4 = 1.597) m^2$
Total surface	1.815 $m^2$
horizontal surface fraction $w_i$	$(0.218/1.815 = 0.06) m^2 m^{-2}$
vertical surface fraction $w_i$	$(1.597/1.815 = 0.22) m^2 m^{-2}$

#### 4.5.2 Outdoor $T_{mrt}$ model comparison

This section aims to compare the methods used for  $T_{mrt}$  calculation in both the McZM and the RayMan model, especially given that there's no experimental validation for the former. Numerous validation studies indicate RayMan's high accuracy in estimating  $T_{mrt}$  for PET assessment purpose (Matzarakis, Rutz, and Mayer, 2007, Hwang, Lin, and Matzarakis, 2011).

### RayMan model description

The  $T_{mrt}$  in RayMan model results from the long wave radiation and the solar diffuse and diffusely reflected radiation  $D_i$  ( $T_{mrt}$  in equation 4.34) and from an additional direct solar radiation term (Equation 4.35) (Matzarakis, Rutz, and Mayer, 2009) resulting on a total mean radiant temperature  $T_{mrt}^*$ .

The outdoor environment is split into upper and lower hemispheres by a plane ( $x, y$ ), situated 1.1 m above ground. This plane signifies the human body's weight centre (Fanger, 1972, Jendritzky, 1990). The view factors are calculated using pixel map of the solid and free sky elements distribution.

Matzarakis, Rutz, and Mayer's (2009) calculation of direct radiation ( $I_{Dir}$ ) on a horizontal surface is based on Jendritzky et al. (1990) methodology, which considers the degree of cloudiness. Valko's model (Matzarakis, Rutz, and Mayer, 2009; Valko, 1966) is employed to calculate diffuse solar radiation ( $D$ ), taking into account cloud cover and deriving from the linear combination of a fully isotropic and an anisotropic component. Furthermore, the long-wave atmospheric radiation is computed via the Angstrom formula (Matzarakis, Rutz, and Mayer, 2009), depending on air temperature and vapour pressure. In the case of LWR emitted from a solid surface, it is quantified as the sum of the surface's radiated heat flux and reflected atmospheric radiation.

$$\left\{ \begin{array}{l} T_{mrt} = \left[ \frac{1}{\sigma} \sum_{i=1}^n (E_i + \alpha_{body} \frac{D_i}{\epsilon_{body}}) F_i \right]^{0.25} \\ T_{mrt}^* = \left[ T_{mrt}^4 + \frac{f_p \alpha_{body} I_{Dir}}{\epsilon_{body} \sigma} \right]^{0.25} \end{array} \right. \quad (4.34)$$

$$\left\{ \begin{array}{l} T_{mrt}^* = \left[ T_{mrt}^4 + \frac{f_p \alpha_{body} I_{Dir}}{\epsilon_{body} \sigma} \right]^{0.25} \end{array} \right. \quad (4.35)$$

Where :

- $n$  is the number of surfaces surrounding the body [-]
- $T_{mrt}$  is the mean radiant temperature with no direct solar radiation [K]
- $T_{mrt}^*$  is the mean radiant temperature with direct solar radiation [K]
- $\sigma$  is the Stefan-Boltzmann constant =  $5.67 \times 10^{-8}$  [W m<sup>-2</sup> K<sup>-4</sup>]
- $E_i$  is the long wave radiation emitted from the surface  $i$  [W m<sup>-2</sup>]
- $D_i$  is the diffuse solar radiation and the diffusely reflected global radiation,  $i$  [W m<sup>-2</sup>]
- $\alpha_{body}$  is the SWR absorption coefficient of the irradiated body surface [-]
- $\epsilon_{body}$  is the emission coefficient of the human body [-]
- $F_i$  is the view factor of the surface  $i$  [-]
- $I_{Dir}$  is the direct solar irradiation on a surface perpendicular to the incident radiation direction [W m<sup>-2</sup>]
- $f_p$  is a surface projection factor depending on the zenith angle and the body posture (3787, 1998; Jendritzky, 1990) [-]

### Case study configuration

The comparison seeks to calculate the outdoor mean radiant temperature ( $T_{mrt}$ ) on August 12th, 2020, in an unobstructed environment located in Lyon. This calculation is premised on a clear sky, a constant ground temperature of 30°C, an albedo of 0.2, and an emissivity of 1.

### Model configuration

In both the RayMan model and the McZM, the emission coefficient of the human body ( $\epsilon_{body}$ ) is set at 0.97, while the absorption coefficient ( $a_{body}$ ) is set at 0.7. The coordinates are 4°50' longitude and 45°46' latitude, with the time zone (UTC+h) being 1. The RayMan model calculates the mean  $T_{mrt}$  by computing the hourly horizontal diffuse solar radiation ( $D$ ), the direct radiation ( $I_{Dir}$ ) on a horizontally-oriented surface as shown in Figure 4.19a, and the atmospheric radiation for the 12th of August from 0 AM to 11 PM. This radiation data is then inputted into the McZM to compare the corresponding  $T_{mrt}$ .

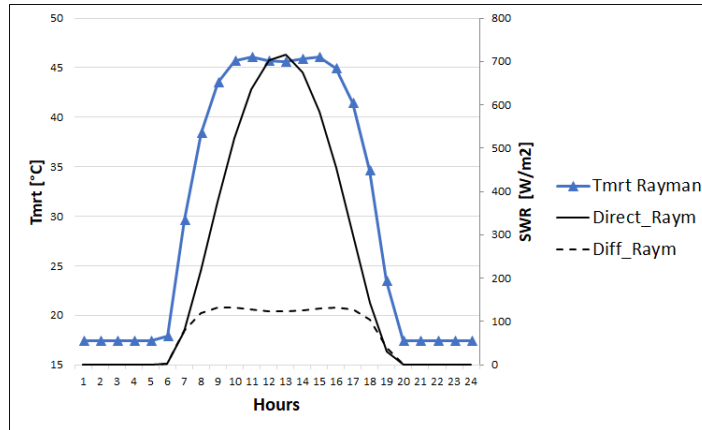
### Results and discussions

Figure 4.19b illustrates the direct and diffuse solar radiation incident on the six surfaces of a body-box using the McZM mean radiant temperature model. This figure also provides the corresponding total  $T_{mrt}$ . A comparison of  $T_{mrt}$  calculated using the RayMan model and the McZM model is visible in Figure 4.19c. The variations between both models stem from their unique methods of modelling an individual and accounting for the impact of SWR on the person. The McZM calculates  $T_{mrt}$  using view factors derived from explicit body-box geometry. In contrast, the RayMan model uses view factors calculated based on pixel distribution and applies a projection factor to the  $I_{Dir}$  (Direct Solar Radiation). The distinctive techniques employed by both models significantly affect the overall evolution of  $T_{mrt}$ . Figures 4.19a and 4.19b demonstrate this, showing the relationship between the evolution of  $T_{mrt}$  and the trend of direct and diffuse solar radiation.

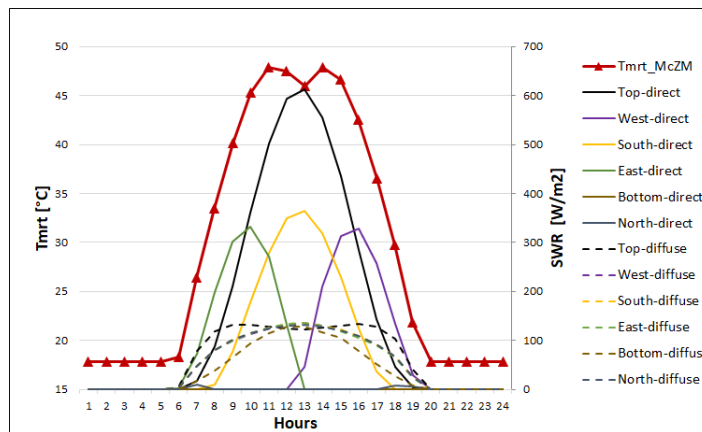
Figure 4.19c demonstrates that the influence of LWR on  $T_{mrt}$  is consistent across both models. This is evident at night when LWR is the sole contributor to  $T_{mrt}$ . Daytime differences in  $T_{mrt}$  can be attributed to distinct manners of redistributing direct and diffuse solar flux in both models. In the McZM model, lower  $T_{mrt}$  values are notable from 7 AM to 10 AM and 3 PM to 8 PM. This aligns with reduced values of diffuse solar radiation on the bottom and lateral faces of the body-box compared to the RayMan model. Conversely, from 11 AM to 1 PM, the total direct solar irradiation averaged across East, West, North, South, and top surfaces in the McZM model exceeds equivalent solar irradiation in the RayMan model.

To conclude, we have initially verified the accurate ranges and trends of  $T_{mrt}$  by the

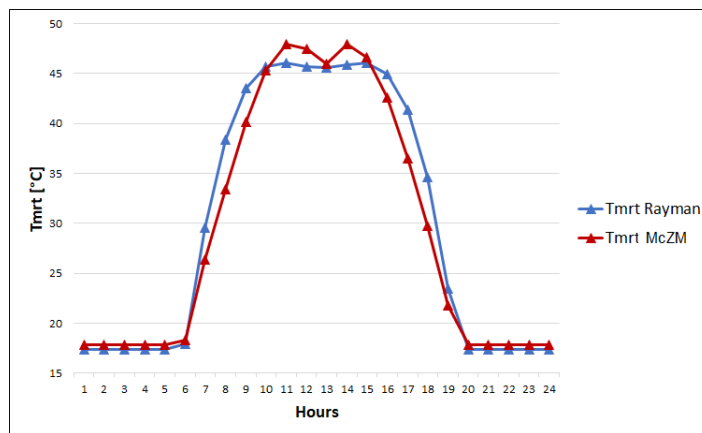




(a) Direct and Diffuse solar radiation and  $T_{mrt}$  in RayMan - The 12th of August 2020.



(b) Direct and Diffuse solar radiation incident the 6 surface of the box in the  $T_{mrt}$  McZM - The 12th of August 2020.



(c)  $T_{mrt}$  with RayMan model and with McZM - The 12th of August 2020.

Figure 4.19: Daily solar radiation and  $T_{mrt}$  evolution for (A) RayMan model, (B) McZM and (C) comparison between  $T_{mrt}$  evolution for RayMan and McZM.

McZM model. For now, this is sufficient for using the McZM model to compare scenarios involving construction or outdoor design. However, further progress will require additional validation using experimental data. Though not covered in this thesis, it remains a crucial area for future research.

## 4.6 Conclusions

### 4.6.1 Chapter conclusions

This chapter focuses on the presentation of the SWR, LWR, soil, BEM and  $T_{mrt}$  models' components of the coupled McZM and BEM.

The SWR model, based on Monte-Carlo ray tracing and sun position interpolation, is especially fitting for long-term solar calculation simulations due to its ability to greatly reduce computational time for incident radiation on surfaces. Nevertheless, the model's drawback is its limitation to accurately capture solar fluctuations between two interpolation points. For a more comprehensive solar analysis, it is preferable to use a model that does not approximate the sun's position. While the SWR model gives adequate results in comparison to the Monte-Carlo ray tracing-based solar model, inconsistencies can arise when predicting radiation between two interpolation points that precede and follow a peak or trough value.

The LWR model, which uses the radiosity method, includes a calculation of view factors during the pre-processing phase and can accommodate the LWR exchanges between building surfaces. However, for instances involving several hundred surfaces, it is advised to use a simplified model focused only on LWR exchanges with the sky and ground to cut down computation time. This simplification has minimal effect on surface temperatures. Comparisons between this LWR model and a validated one based on the ray-tracing method indicate a strong agreement between both models.

The outdoor soil model offers three configurations: the impervious soil setup, which involves only sensible, radiative, and conductive heat fluxes in balancing the surface, as well as bare soil and low vegetation configurations, which incorporate the latent heat flux in the balance through an evaporation potential using the Penman-Montheith equation. However, a limitation of the latter two configurations is that they assume a model with non-zero evaporation potential, unable to represent a completely dry soil scenario. In addition the low vegetation model has not been validated. An experiment replicating surface temperatures on bare soil in a rural area indicates reliable surface temperature predictions, with an average relative deviation of 6.2%. For further model refinement, adapting the hydric model to various soil types, especially those found in urban environments, would be beneficial. Additionally, the model's sensitivity to aerodynamic resistance and other factors merits exploration.

The BEM model incorporates components from the BuildSysPro library. A limitation of

this model is the exclusive distribution of transmitted SWR flux to the floor. This uneven distribution of solar flux impacts temperature levels within rooms. Despite the BuildSysPro library undergoing validation, a comparison was conducted with the wall model and another yet-to-be-validated model. Both models use the same method to calculate heat conduction, aiming to verify the outdoor surface heat balance and the subsequent surface temperatures. The comparison reveals highly similar results.

The simplified indoor  $T_{mrt}$  model, which involves averaging surface temperatures weighted by surface area, is suitable when the analysis is more focused on heat stress instead of thermal comfort. This model assumes that individuals are not confined to a specific area. The outdoor  $T_{mrt}$  model has the benefit of taking into account the individual's geometry (represented as a rectangular prism) and the changes in SWR and LWR with the surrounding environment. This provides a more accurate estimation of the  $T_{mrt}$ . However, it is worth noting the limitations concerning the rectangular prism body shape. This geometric shape exhibits flux discontinuities at the prism's edges. By comparing with the RayMan model, we can confirm the correct  $T_{mrt}$  scale and the correct  $T_{mrt}$  trend relative to the incident SWR and LWR heat flux.

#### 4.6.2 General conclusions of part II

In the second part of this thesis, we present a coupled McZM and BEM model. This model helps tackle the spatial representation of heat stress, ensuring a continuity between indoor and outdoor airflow and energy balance. By integrating BEM and McZM, we facilitate the spatialization of heat stress over short and long durations, with simulations manageable in range (between 8 to 12 hours on an Intel 5 laptop).

The model calculates necessary climatic variables for heat stress evaluation on an hourly basis. These include  $v_a$ , computed during pre-processing;  $T_a$  and  $RH$ , computed during the dynamic simulation; and  $T_{mrt}$ , computed in the post-processing stage.

The outdoor zonal model can accurately simulate airflow, taking into account the local urban landscape, including buildings and their surroundings, for varying wind speed and direction. Continuity between outdoor and indoor airflow is achieved through a pressure-based model that's integrated with both the outdoor McZM and indoor BEM. Furthermore, a thermal and airflow coupling is ensured between indoors and outdoors.

This second part also offers initial verification and validation of the model's components. Nonetheless, it does not tackle the validation of sensible and latent heat balance in air zones, which involves radiative, convective, and conductive couplings. The comprehensive validation of the model could be a future focus within the ongoing DIAMS project, which seeks to compare microclimate models linked with building models. An equally important and ambitious goal is establishing an experimental protocol that can validate the complete modelling chain (Figure 2.11).

The modelling approach introduced in Part II of this thesis is applied to a case study discussed in Part III. The first objective of this section is to demonstrate the significance of our spatialized approach in assessing heat stress over daily and seasonal exposure periods. The second objective is to examine the impacts of various indoor and outdoor cooling strategies on heat stress. We analyze the results using both an Eulerian approach for seasonal and daily heat stress evaluations as well as a Lagrangian approach for daily heat stress and strain assessments.

## **Part III**

# **Application of McZM coupled with BEM to a case study**



# Chapter 5

## Case study on Confluence Ydeal Square

The current chapter presents an applied case study, demonstrating the outcomes achievable with the model detailed in part II of this thesis.

Referring to the specific modelling problem formulated in Section 2.4, this chapter exemplifies the model's capacity to:

- Assess spatialized heat stress over seasonal and daily exposure and to provide heat strain indices over daily exposure.
- Compare the impact of certain indoor and outdoor cooling measures on heat stress and heat strain. A base scenario is compared with a natural ventilation scenario and a scenario where outdoor impermeable soil is replaced with a permeable one.

The heat stress analysis incorporates both Eulerian and Lagrangian exposure approaches. The Eulerian approach is utilised for both seasonal and daily exposure periods, whereas the Lagrangian method is only employed for daily exposure, taking into account a probable individual path. This method is also used to demonstrate certain heat strain indices identified in Chapter 1.

Before delving into the heat stress analysis, this chapter underscores the significance of employing a coupled McZM and BEM modelling approach. It examines the impact on indoor air temperatures when simplified boundary conditions for outdoor air temperature and external convective heat transfer coefficient are considered.

### Contents

---

5.1	Case study configuration . . . . .	153
5.1.1	Boundary conditions of the McZM . . . . .	153
5.1.2	Model geometry . . . . .	154

---

5.1.3	Building settings . . . . .	155
5.1.4	Soil settings . . . . .	157
5.1.5	Numerical setting . . . . .	157
5.1.6	PET and JOS-3 setting . . . . .	158
<b>5.2</b>	<b>Analysis framework and simulated scenarios . . . . .</b>	<b>158</b>
5.2.1	Preliminary comparative analysis of the McZM . . . . .	158
5.2.2	Heat stress and heat strain analysis framework . . . . .	160
<b>5.3</b>	<b>Results : Modelling approaches comparison . . . . .</b>	<b>164</b>
5.3.1	Comparison between $S_{McZM}$ and $S_{h_{c}const}$ . . . . .	164
5.3.2	Comparison between $S_{McZM}$ and $S_{T_{ws}}$ . . . . .	168
5.3.3	Conclusion on the modelling comparison . . . . .	171
<b>5.4</b>	<b>Results: base scenario . . . . .</b>	<b>171</b>
5.4.1	Daily exposure analysis . . . . .	171
5.4.2	Seasonal exposure analysis . . . . .	179
5.4.3	Conclusions on the base scenario results . . . . .	185
<b>5.5</b>	<b>Results : cooling strategy comparison . . . . .</b>	<b>186</b>
5.5.1	Daily exposure analysis . . . . .	186
5.5.2	Seasonal analysis . . . . .	189
5.5.3	Conclusions on cooling strategy effects . . . . .	192
<b>5.6</b>	<b>Conclusions . . . . .</b>	<b>195</b>

---



## 5.1 Case study configuration

The case study involves the Ydeal Square block located in Lyon’s Confluences district (see Figure 5.1). The block, comprised of five buildings, was constructed in 2020, thereby complying with the RT 2012 standards, which are the French thermal regulations. However, to serve the purpose of our study, we examined scenarios where insulation is minimal to investigate how partial insulation affects the assessment of heat stress.



Figure 5.1: Confluence Ydeal Square: global view of the square and view of the target building and weather station.

### 5.1.1 Boundary conditions of the McZM

The necessary boundary conditions for our case study comprise meteorological and land surface elements. The meteorological elements include air temperature ( $T_a$ ), relative humidity ( $RH$ ), direct and diffuse solar irradiation, sky temperature ( $T_{sky}$ ), and wind characteristics (speed and direction). The land surface boundary condition is the deep ground temperature.

In the case study, the boundary conditions for  $T_a$  and  $RH$  were derived from data collected by the Confluence weather station. Thus, at every time step, the same  $T_a$  and  $RH$  were applied to the lateral edges as well as the top of the McZM domain (5.2). The boundary conditions for direct and diffuse solar radiation were pre-determined by the HelioBIM model (Section 4.1). The European Commission’s Photovoltaic Geographic Information System database supplied the direct and diffuse radiation data used by HelioBIM. The boundary condition for wind speed is based on data provided by the Confluence weather station, as

detailed in Section 3.1.2. The wind direction ranges between  $150^{\circ}N$  to  $196^{\circ}N$ . This range is determined by the dominant wind patterns observed from June to September 2020. Helio-BIM calculates the sky temperature using the method described in Section 4.2.

The ground temperature, 2 m deep, is set as the monthly average air temperature, which ranges from  $22.31^{\circ}C$  to  $20.31^{\circ}C$  in stages from June to September.

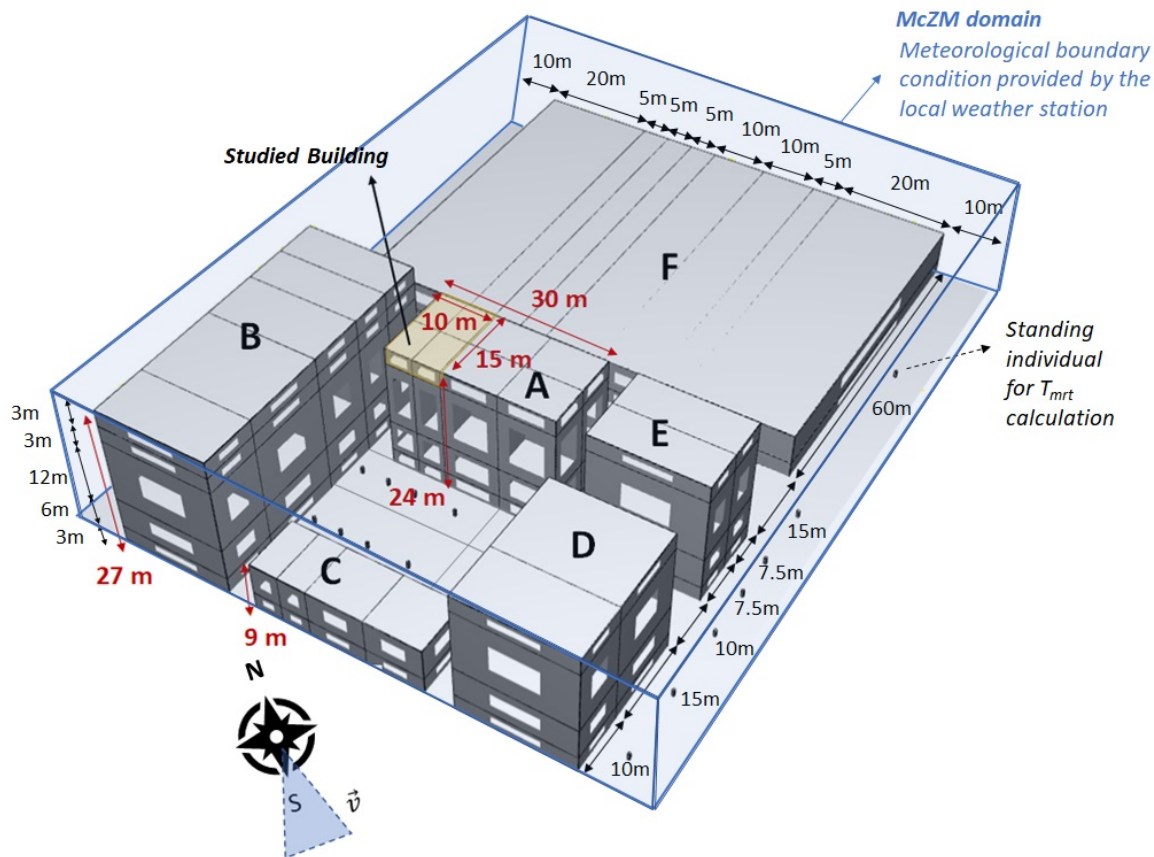


Figure 5.2: 3D illustration of the case study building geometry and dimensions in the McZM domain.  $T_a$  and  $RH$  and wind speed boundary conditions are provided by the data measured at the Confluence weather station. Wind speed direction varies within the ranges from  $150^{\circ}N$  to  $196^{\circ}N$  and direct and diffuse solar radiation are provided by the European Commission’s Photovoltaic geographical information system database.

### 5.1.2 Model geometry

Figure 3.7 illustrates how the actual geometry of the block simplifies into a parallelepiped shape, cut according to a normalized zoning scheme. Figure 5.2 gives a 3D perspective of the area in focus. The original structure of the studied building (Building A) comprises a ground floor and six additional floors, each holding between three and seven dwellings. Loggias with glazed areas make up 80% of the exterior envelope, excluding the roof. For this analysis, we focus on the topmost dwelling facing Building B, which is divided into four thermal zones that represent its four rooms. The other uppermost dwellings follow a less segmented zoning. To streamline the dynamic simulation and, therefore, reduce its du-

ration, we've minimized superfluous thermal zones by merging intermediate floors. Therefore, we merge the first and second floors and the third, fourth, and fifth floors. Lastly, to represent the loggias' effect on dampening solar radiation entering the rooms, we reduced the glazed surface area from 80% to 70% of Building A's external envelope, excluding the roof.

Table 5.1: Studied dwelling dimensions.

Dimensions	Per room	Total dwelling
Surface[m <sup>2</sup> ]	37.5	150
Volume[m <sup>3</sup> ]	112.5	450

### 5.1.3 Building settings

#### Building thermal configuration

Two thermal configurations are considered:

- RT2012: thermal configuration corresponding to an interior insulated building (insulation thickness of 18cm) consistent with the French thermal regulation RT2012 in terms of insulation, thermal bridges and infiltration criteria (Table 5.2).
- LowRth: this configuration aims to represent the thermal configuration of building constructed in the 1970s, before the application of thermal regulation, and where a complete refurbishment is applied on roofs and windows and a small insulation is applied to exterior walls, representing the vetoustity of the insulation (detailed in Table 5.3).

Note that indoor albedo and indoor emissivity are not used in the BEM. In fact, the transmitted SWR heat flux is considered to be completely absorbed by the interior floor.

Table 5.2: Building thermal properties for the insulated building.

RT2012	$R_{Th}$ [m <sup>2</sup> K W <sup>-1</sup> ]	$h_{c_m}$ [W m <sup>-2</sup> K <sup>-1</sup> ]	$a_{ext}$	$sf$ [%]	$\epsilon_{ext}$
Exterior wall(*)	5.58	7.69	0.4	-	0.9
Roof(*)	8.99	10	0.3	-	0.9
Glazing	1.24	-	-	66	-
Floor	0.212	5.8	-	-	0.9

(\*) Plus thermal bridges represent 14% of total thermal losses

Table 5.3: Building thermal properties for the low-insulated building.

LowRth	$R_{Th}$ [m <sup>2</sup> K W <sup>-1</sup> ]	$h_{c_{in}}$ [W m <sup>-2</sup> K <sup>-1</sup> ]	$a_{ext}$	$sf$ [%]	$\epsilon_{ext}$
Exterior wall <sup>(*)</sup>	0.66	7.69	0.4	-	0.9
Roof <sup>(*)</sup>	8.99	10	0.3	-	0.9
Glazing	1.24	-	-	66	-
Floor	0.212	5.8	-	-	0.9

(\*) Plus thermal bridges represent 6% of total thermal losses

Where :

$$\left\{ \begin{array}{l} R_{Th} \text{ is the thermal resistance of the building envelope component} \\ \text{(wall, roof, glazing and floor) [m}^2 \text{ K W}^{-1}\text{]} \\ h_{c_{in}} \text{ is the indoor total heat transfer coefficient accounting for the convective} \\ \text{and LWR heat exchanges [W m}^{-2} \text{ K}^{-1}\text{]} \\ a \text{ is the albedo of the building opaque envelope component [-]} \\ sf \text{ is the solar factor of the building glazing component [-]} \\ \epsilon \text{ is the long wave radiation emissivity of the opaque envelope component [-]} \end{array} \right.$$

$h_{c_{ext}}$  values are calculated with a linear interpolation of the convective heat transfer coefficients pre-computed in the CFD simulations for different wind speeds and directions.

$R_{Th}$  represents the thermal resistance related to heat conduction across the envelope and indoor heat convection. This value is influenced by the component's thermal conductivity  $\lambda$  [W m<sup>-1</sup> K<sup>-1</sup>], its thickness and  $h_{c_{in}}$ .

As outlined in Section 5.1.2, several real-world building geometries - such as floors and rooms—are consolidated into one thermal zone. This leads to a loss of an equivalent volume of 324 m<sup>3</sup> for the floor and a negligible 6 m<sup>3</sup> for the interior walls. To offset the loss of intermediate floor thermal mass, we calculated an equivalent specific heat to add an equivalent thermal mass to the intermediate floor:

$$C_{peq} = C_p (V_{floor} + V_{add_{floor}}) / V_{floor} \quad (5.1)$$

Where :

$$\left\{ \begin{array}{l} C_{peq} \text{ is the equivalent specific heat of the material at constant pressure [J kg}^{-1} \text{ K}^{-1}\text{]} \\ V_{floor} \text{ is the volume of the floor modelled in the building model [m}^3\text{]} \\ V_{add_{floor}} \text{ is the total volume loss after merging floors and rooms [m}^3\text{]} \\ C_p \text{ is the specific heat of the material at constant pressure [J kg}^{-1} \text{ K}^{-1}\text{]} \end{array} \right.$$

## Systems and occupancy

The terms “systems” and “occupancy” refer to the settings of energy systems, such as heating, cooling, and mechanical ventilation, as well as individual behaviours or automatic

settings that impact the overall energy balance, such as shading or opening windows and doors. These terms also incorporate building gains, which are power inputs derived from human presence or the operation of electronic or household appliances. Although the model can consider latent gains, only sensible gains are accounted for in this particular case study.

We consider two configurations - one signifying the absence of natural ventilation ( $NV_{off}$ ) and the other indicating its presence ( $NV_{on}$ ). In the latter, the natural ventilation model from section 3.2.2 is implemented. Both configurations share the same mechanical ventilation rate and internal gains, as outlined in Table 5.4.

Table 5.4: Building systems and occupancy.

<b>Systems and occupancy</b>	$NV_{off}$	$NV_{on}$
Window shutter	70% <sup>(*)</sup>	
Mechanical ventilation [ACH]	0.34 <sup>(**)</sup>	
Natural ventilation <sup>(***)</sup>	-	
door open surface [m <sup>2</sup> ]		0.55
window open surface [m <sup>2</sup> ]		0.25
Internal gains [W m <sup>-2</sup> of floor area]	4	

(\*) To compensate reduction of effective incoming radiation induced by loggias in the real case configuration

(\*\*) Based on French regulatory thresholds

(\*\*\*) Other airflow model setting are described in 3.2

#### 5.1.4 Soil settings

Two soil models are considered for the ground configuration:

- Mineral soil: impervious soil (soil model (A) in Section 4.3.2).
- Bare soil: evaporative soil (soil model (B) in Section 4.3.2).

The thermal properties of these two soils are reported in Table 5.5.

Note that 2 m depth for the soil was selected as the reference in the DIAMS case study described in section 4.4.2 and in the Section 4.3.3.

#### 5.1.5 Numerical setting

The following settings were used for the coupled dynamic McZM and BEM simulation performed in Dymola. The initial conditions of air temperature and specific humidity were set to 20 °C and 8kg<sub>water</sub>/kg<sub>air</sub>, respectively. To ensure the influence of initial conditions was eliminated, a prelude simulation of 20 days was conducted prior to the crucial period from June 20 to September 20. The overall simulation lasted for roughly 10 hours using a laptop

Table 5.5: Ground thermal properties.

	$R_{Th} [m^2 KW^{-1}]$	$a$	$\epsilon$
<b>Mineral soil</b>	1.49	0.05 <sup>(**)</sup>	0.9
<i>Bitumen (0.02 m )</i>			
<i>Concrete (0.12 m)</i>			
<i>Ground (2 m)<sup>(*)</sup></i>			
<b>Bare soil</b>	1.34	0.3 <sup>(***)</sup>	0.9
<i>Ground (2m)<sup>(*)</sup></i>			

(\*) The ground composition described in Section 4.3.3

(\*\*) Oke, 1987

(\*\*\*) averaged value from Rosenberg, Blad, and Verma, 1983

running an 11th Gen Intel(R) Core(TM) i5-1145G7 1.50 GHz processor and utilising 15.7GB of RAM. A set of pre-calculation steps, which included CFD simulations for 19 experiments, took about 3 hours per experiment. Calculating solar radiation and form factors, in contrast, required less than a minute.

### 5.1.6 PET and JOS-3 setting

PET and JOS-3 models are used for heat stress and heat strain assessment respectively. Input parameters set for the PET and JOS-3 models are reported in Table 5.6.

Parameters	Values
Clothes resistance [clo]	0.5
Indoor wind velocity [ $m s^{-1}$ ]	0.15
Age [year]	23
Body mass [kg]	75
Height [m]	1.8

Table 5.6: Input parameters used for the PET and JOS-3 model.

The rest of the parameters are set to their default values <sup>1</sup>.

## 5.2 Analysis framework and simulated scenarios

### 5.2.1 Preliminary comparative analysis of the McZM

A preliminary analysis has been carried out to assess how certain simplifications in building model boundary conditions might enhance indoor air temperature predictions. Two such simplifications are compared with the McZM model. The first simplification involves substituting the variable assumptions for external convective heat transfer coefficients with fixed

---

<sup>1</sup>The default values are available in the pythermalcomfort library documentation : <https://pythermalcomfort.readthedocs.io/en/latest/reference/pythermalcomfort.html>

$h_c$  values. The second one entails replacing the assumptions about external air temperature with temperature values recorded at the weather station.

### Modelling options

Three modelling options are considered (Figure 5.3):

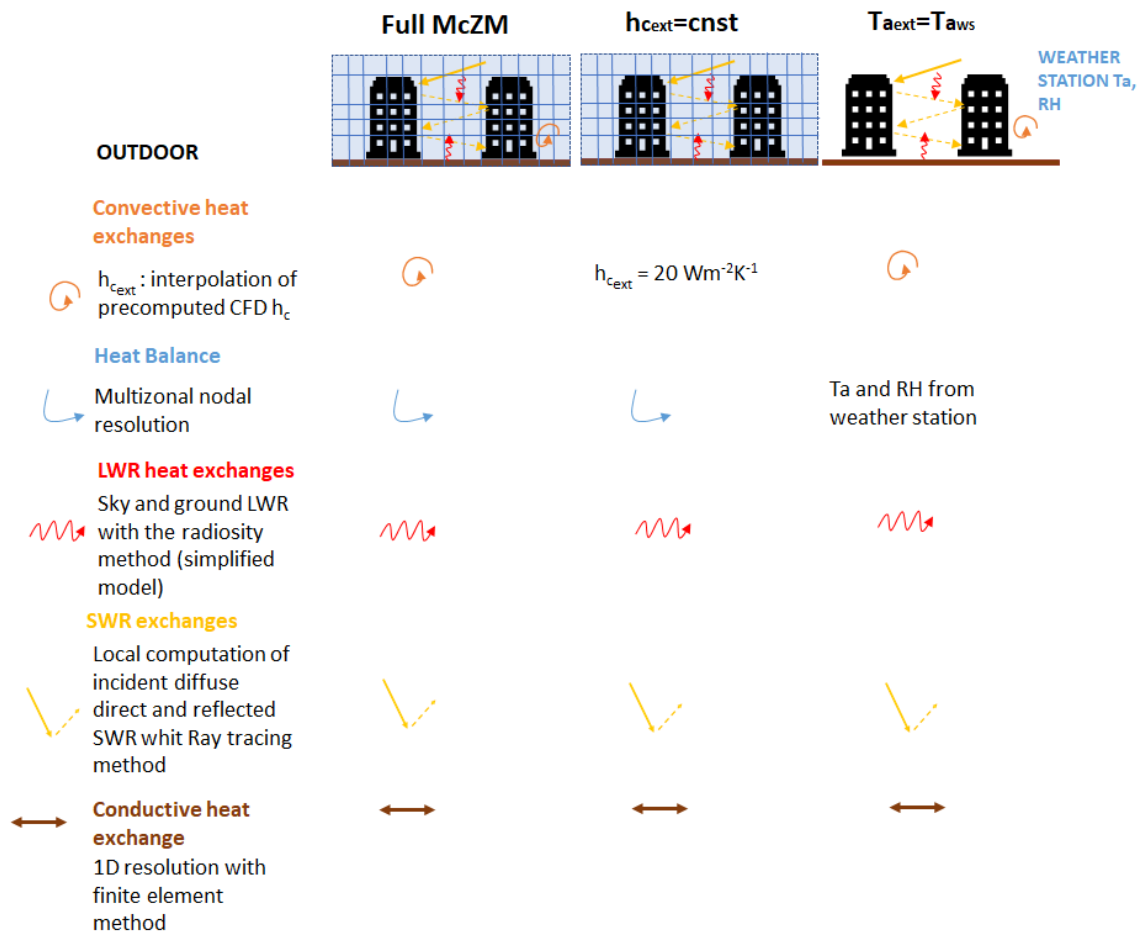


Figure 5.3: Three modelling options scenarios for the outdoor heat flux:  $S_{McZM}$  corresponding to the original McZM,  $S_{h_{c_{ext}}=cnst}$  corresponding to constant  $h_{c_{ext}}$  values and  $S_{T_{a_{ws}}}$  corresponding to weather station  $T_a$  and RH.

- The full McZM: corresponding to the default McZM modelling options described in Chapter 3, where the  $h_{c_{ext}}$  at each time step results from an interpolation of the convective heat transfer coefficients pre-computed with the CFD, and where the outdoor air temperature is computed in each air zone using a nodal multizonal resolution method.
- The  $h_{c_{ext}}=cnst$  model: where the interpolated  $h_{c_{ext}}$  is replaced by a unique constant value of  $20 \text{ W m}^{-2} \text{ K}^{-1}$  according to ISO-13789 standards.
- The  $T_a=T_{a_{ws}}$ : where no spatialized approach is adopted for outdoor air temperature

and humidity. Uniform values of air temperature and humidity are adopted, corresponding to the values measured at the weather station.

### Simulated scenarios

In line with the three aforementioned modelling methods, we execute three simulation scenarios -  $S_{McZM}$ ,  $S_{h_c \text{ cnst}}$  and  $S_{T_{ws}}$ . These tests are conducted using the RT2012 building thermal setup, the mineral soil thermal arrangement, and the  $NV_{off}$  system with occupancy, as detailed in Table 5.7.

The thermal configuration of the RT2012 building underscores how boundary conditions, such as outdoor temperature and external heat transfer coefficients, influence indoor temperatures, even in a well-insulated building.

Table 5.7: Simulated modelling approaches.

	$S_{McZM}$	$S_{h_c \text{ cnst}}$	$S_{T_{ws}}$
Building thermal configuration	RT2012	RT2012	RT2012
Ground thermal configuration	Mineral soil	Mineral soil	Mineral soil
Systems and occupancy	$NV_{off}$	$NV_{off}$	$NV_{off}$
Modelling options (*)	Full McZM	$h_{c \text{ ext}} = \text{cnst}$	$T_a = T_{a \text{ WS}}$

(\*) described in section 5.3

### 5.2.2 Heat stress and heat strain analysis framework

The assessment of heat stress and strain is performed considering two different exposure perspectives (Eulerian and Lagrangian) and two different exposure periods (seasonal and daily). Figure 5.4 provides a comprehensive framework for global heat stress and strain analysis.

#### Daily analysis

As illustrated in figure 5.4, for the daily analysis, heat stress is assessed under the both Eulerian and Lagrangian exposure perspective offering a spatial view of the PET. Heat strain is assessed only under the Lagrangian perspective as heat strain indices are specifically related to the individual. Associating them with a fixed location would be illogical unless the individual is assumed to stay stationary throughout the entire observation period.

#### Seasonal analysis

As illustrated in figure 5.4, for the seasonal analysis, only the Eulerian exposure perspective is considered. Adopting a Lagrangian method would necessitate the development of



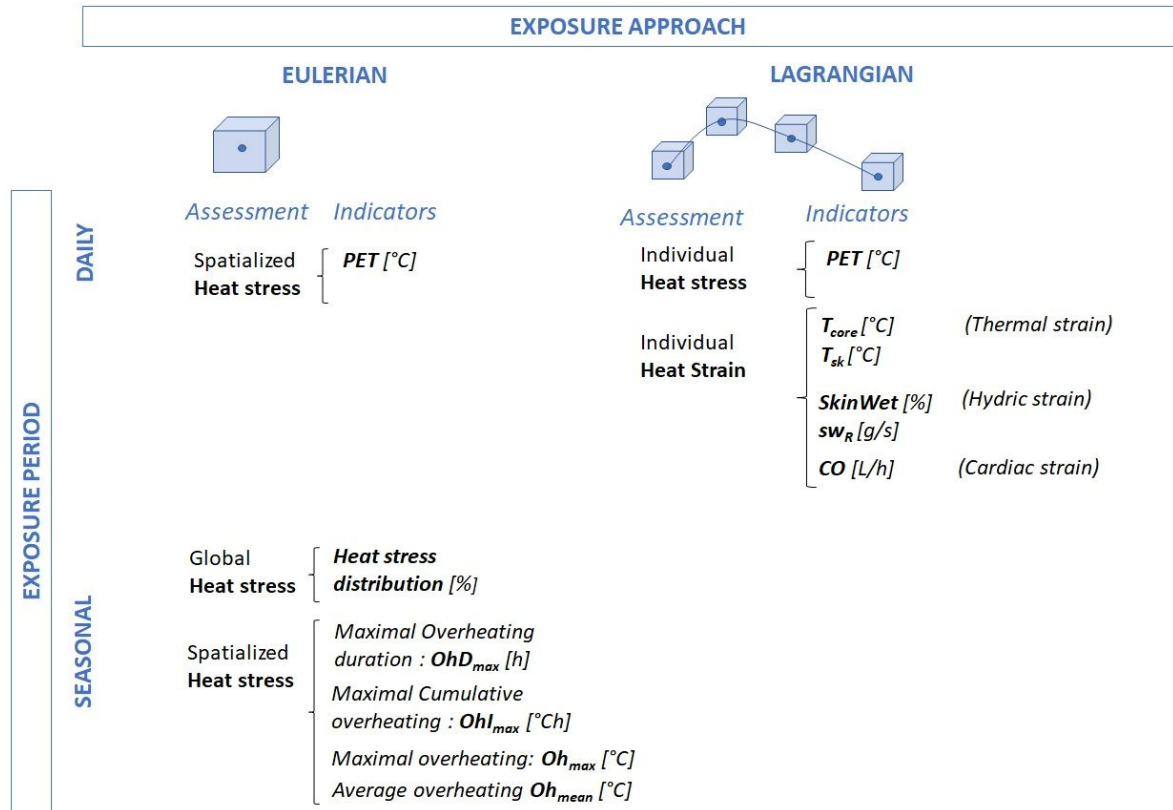


Figure 5.4: Heat stress and heat strain analysis framework.

intricate dynamic path models.

It is important to note one limitation of the seasonal heat stress assessment, related to the fact that the thermoregulation models, which generates heat stress and strain indices, are not designed for long-term analysis, as stated in Chapter 1. The indices used for seasonal analysis, derived from PET (Section 1.6), are restated in Table 5.8.

### Simulated scenarios

The simulated scenarios address two primary objectives:

- Illustrate the relevance of the spatialized approach adopted in the zonal model in regard to the capability to assess heat stress differences from one zone to another and identify heat shelters.
- Illustrate the effects of some indoor and outdoor cooling measures on heat stress assessment and on the selected heat strain indices.

The heat stress and heat strain analysis framework is applied by simulating three scenarios related to the previously mentioned building and ground settings (Table 5.9). These scenarios are analyzed and compared for a comprehensive understanding:

Index	Calculation	Unit	Objective
<b>Global analysis of heat stress (PET assessment scale)</b>			
<b>Heat stress distribution</b>	Distribution of heat stress according to the PET assessment scale over the analysis period or month by month	%	Global heat stress assessment Provides indoors and outdoors heat stress classification based on maximal and minimal PET values
<i>Maximum</i>	<i>Considers the maximal PET over the selected zones</i>		
<i>Minimum</i>	<i>Considers the minimal PET over the selected zones</i>		
<b>Overheating (PET&gt;29°C) zonal analysis</b>			
<b>Maximal overheating duration</b> $OhD_{max}$	Within an overheating episode, it returns the longer one. Overheating episode time range PET>29°C	h	<b>Overheating duration</b> Provides an indication of the maximal overheating duration per zone. This indicator needs to be observed in regards of the number of overheating episodes
<b>Maximal cumulative overheating</b> $OhI_{max}$	$OhI_{max} = Max(\sum_{OhD} Overheat^{\circ C})$ Within an overheating episode, it identifies the one with the maximal overheating cumulative value and returns this value. Where $Overheat^{\circ C} = PET - 29^{\circ C}$ if PET>29°C, otherwise $Overheat^{\circ C} = 0$	°Ch	<b>Overheating intensity</b> Provides an indication of the maximal overheating intensity per zone
<b>Maximal overheating</b> $Oh_{max}$	It returns the maximal overheating within the whole analysis period $Oh_{max} = Max(Overheat^{\circ C})$	°C	<b>Overheating peak</b> Provides an indication of the maximal degree of overheating
<b>Average overheating</b> $Oh_{mean}$	It returns the average overheating within the whole analysis period $Oh_{mean} = Mean(Overheat^{\circ C})$	°C	<b>Average overheating</b> Provides an indication of the mean degree of overheating

Table 5.8: Selected indices for seasonal analysis of heat stress and overheating.

- Base scenario ( $S_{Base}$ ): where the LowRth thermal configuration and  $NV_{off}$  energy management configuration are applied indoors and the impermeable soil model is applied outdoors.
- Natural ventilation scenario ( $S_{NV}$ ): where the LowRth thermal configuration and  $NV_{on}$  energy management configuration are applied indoors in the top floor studied dwelling, and the impermeable soil model is applied outdoors. Note that in this scenario, natural ventilation is always activated.
- Vegetalization scenario ( $S_{Veg}$ ): where the LowRth thermal configuration and  $NV_{off}$  energy management configuration are applied indoors and a bare soil is applied outdoors.

The  $S_{Base}$  scenario is used as a reference scenario to perform the global analysis of heat stress and heat strain over the two exposure frames and periods.

The  $S_{Base}$  scenario is subsequently contrasted with the two scenarios,  $S_{NV}$  and  $S_{Veg}$ , to emphasize the impact of cooling measures on heat stress.

It is worth noting that a thermal configuration with minimal thermal resistance on the walls better accentuates the interaction between indoor and outdoor temperatures, in addition to highlighting the influence of cooling scenarios.

Table 5.9: Simulated cooling scenarios.

	$S_{Base}$	$S_{NV}$	$S_{Veg}$
Building thermal configuration	LowRth	LowRth	LowRth
Ground thermal configuration	Mineral soil	Mineral soil	Bare soil
Systems and occupancy	$NV_{off}$	$NV_{on}$	$NV_{off}$

### 5.3 Results : Modelling approaches comparison

This section contrasts the results from three modelling scenarios:  $S_{McZM}$ ,  $S_{h_c, cnst}$  and  $S_{T_{ws}}$ . We aim to assess how model assumptions regarding external  $h_c$  and external air temperature influence indoor air temperatures.

The analysis focuses on the 12th of August, on the air zones R1, R2, R3 and R4 of the studied dwelling. A 2D plan of the corresponding indoors (R1, R2, R3, R4) and outdoors air zones (Z1\_SW, Z2\_SW, Z2\_NW, Z4\_NW, Z4\_NE, Z3\_NE) walls (W1\_SW, W2\_SW, W2\_NW, W4\_NW, W4\_NE, W3\_NE) and roofs (Roof1, Roof2, Roof3, Roof4) is provided in Figure 5.5.

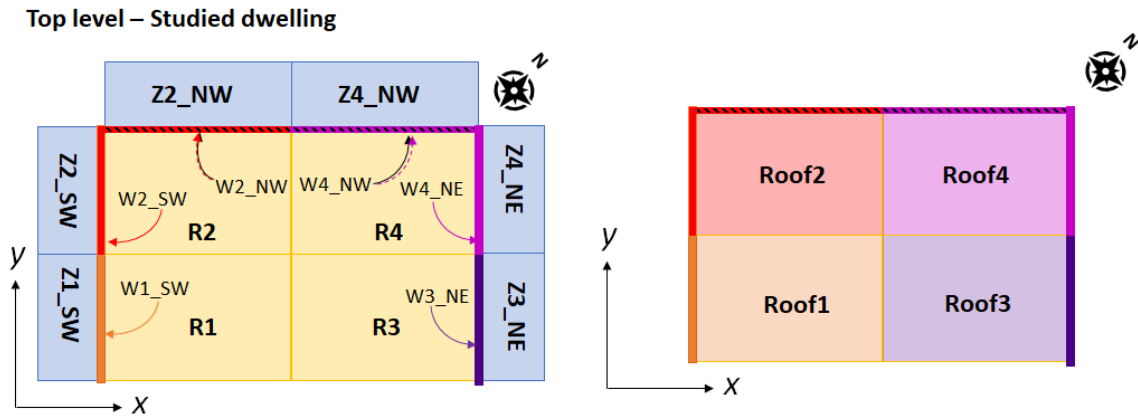


Figure 5.5: 2D plan of the studied dwelling : indoor and outdoor air zones, exterior walls and roofs.

#### 5.3.1 Comparison between $S_{McZM}$ and $S_{h_c, cnst}$

The  $h_{c, ext}$  has an important role on the convective heat exchanges between air and surfaces. Understanding the interplay among outdoor air temperatures, surface temperatures, and the convective heat flux is pivotal. Figure 5.6 depicts these relationships under two modelling options  $S_{McZM}$  and  $S_{h_c, cnst}$ . It outlines the progression of the following: (a) the external convective heat transfer coefficient  $h_{c, ext}$ , (b) the air temperature in the outdoor air zones adjacent to the walls of the studied dwelling ( $T_{a, ext}$ ), (c) the temperature of the studied dwelling's exterior wall surfaces ( $T_{s, ext}$ ), (d) the convective heat flux between the exterior walls of the studied dwelling and the adjacent air zones ( $\Phi_{c, ext}$ ).  $\Phi_{c, ext}$  is positive when directed from the wall towards the outer air. These results are for August 12th. Note that curves unmarked by a cross represent the  $S_{McZM}$  outcomes, while those marked with a cross represent the  $S_{h_c, cnst}$  outcomes.

In the  $S_{h_c, cnst}$  scenario, depicted in Figure 5.6 (a), the  $h_{c, ext}$  value is twice that of the maximum pre-calculated CFD  $h_{c, ext}$  value for the surveyed top-floor dwelling. This significantly affects both the outdoor air and surface temperatures.

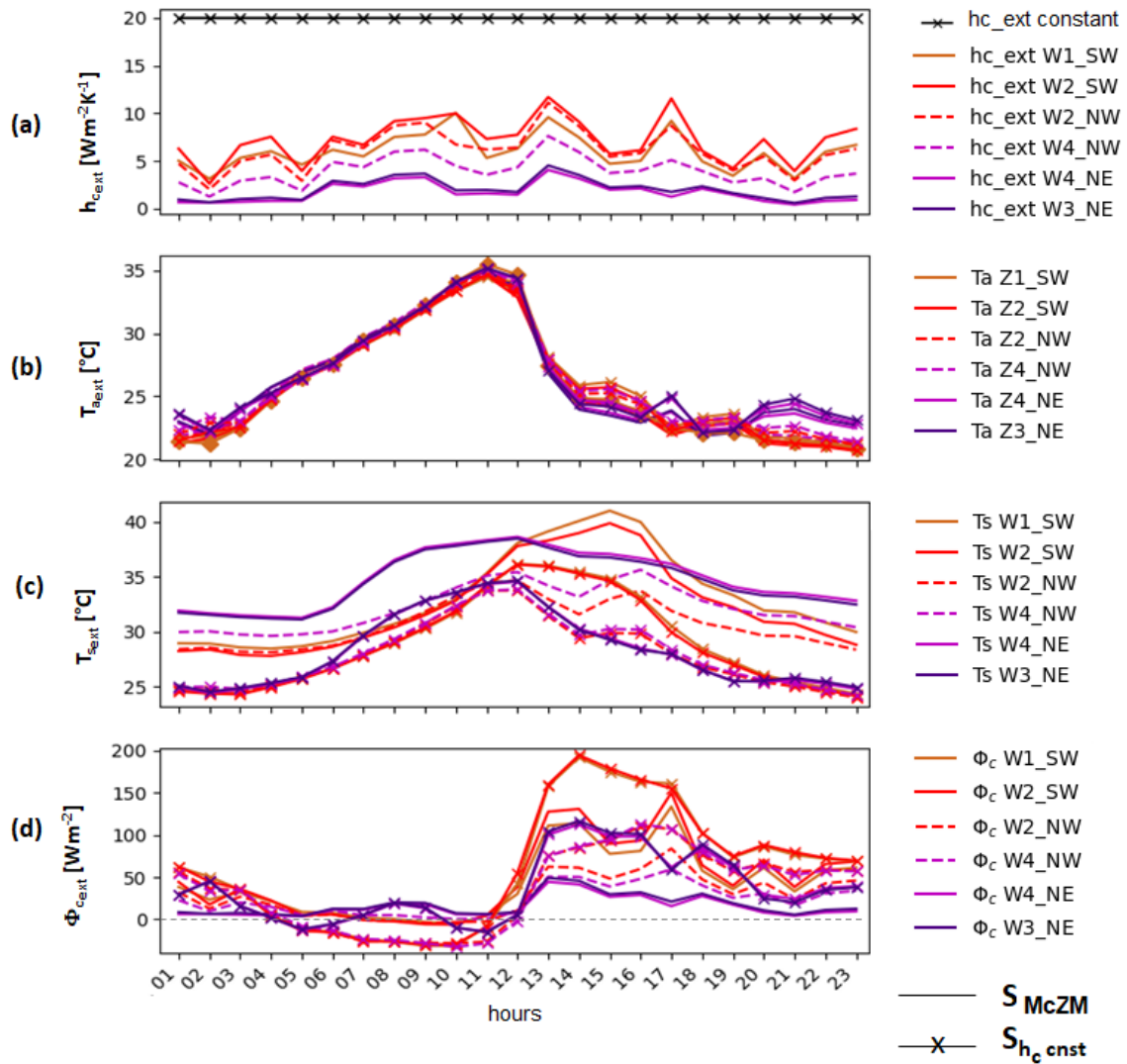


Figure 5.6:  $S_{McZM}$  and  $S_{h_{c}cnst}$  the 12th of August : evolution of (a)  $h_{c_{ext}}$ , (b) Air temperatures in the outdoor air zones adjacent to walls  $T_{a_{ext}}$ , (c) outdoor walls surfaces temperature  $T_{s_{ext}}$  (d) Convective heat flux between exterior walls surfaces and adjacent air zones  $\Phi_{c_{ext}}$ .

A high value of  $h_{c_{ext}}$  contributes to an increase in convective heat exchanges, but it also tends to lessen the temperature difference between the air and surface, thereby reducing the convective heat flux. On the other hand, lower values of  $h_{c_{ext}}$ , such as those found in  $S_{McZM}$ , lead to decreased convective heat flux and a slower convergence of surface and air temperatures. Referring to Figure 5.6 (d), it is noticeable that during the night, when surface temperatures are close to air temperatures (as shown in Figure 5.6 (b) and (c)), convective heat flux decreases. Furthermore, the influence of  $h_{c_{ext}}$  on convective heat exchange diminishes. However, higher  $h_{c_{ext}}$  values speed up the convergence of air and surface temperatures. When air and surface temperatures are closely matched, as in the case of  $S_{h_{c}cnst}$  between 5 AM and 12 AM (Figure 5.6 (b) and (c)), the convective flux gradually lessens and inverses on most surfaces when the air temperature surpasses the surface temperature (Figure 5.6 (d)). The trend reverses when the surface temperature rises due to increased solar

radiation. Specifically, the surface temperatures of walls exposed to sunlight will increase during the day. This spike in temperature prompts an increase in convective exchanges, further heightened by higher values of  $h_{c_{ext}}$ .

Figure 5.7 illustrates the effects of heat balance dynamics on the differences in air and surface temperatures between the two scenarios,  $S_{McZM}$  and  $S_{h_{c_{cnst}}}$ . This figure highlights four key measurements under both scenarios: (a) the evolution of the  $h_{c_{ext}}$ , (b) the difference in air temperatures ( $\Delta T_{a_{ext}}$ ) in outdoor areas adjacent to the dwelling's walls, (c) the difference in the surface temperatures of the dwelling's outdoor walls and roofs ( $\Delta T_{s_{ext}}$ ), and (d) the difference in indoor air temperature in the dwelling ( $\Delta T_{a_{in}}$ ). The temperature differences shown in the figure are derived by subtracting the temperatures of the  $S_{h_{c_{cnst}}}$  scenario from those of the  $S_{McZM}$  scenario. These results are for August 12th.

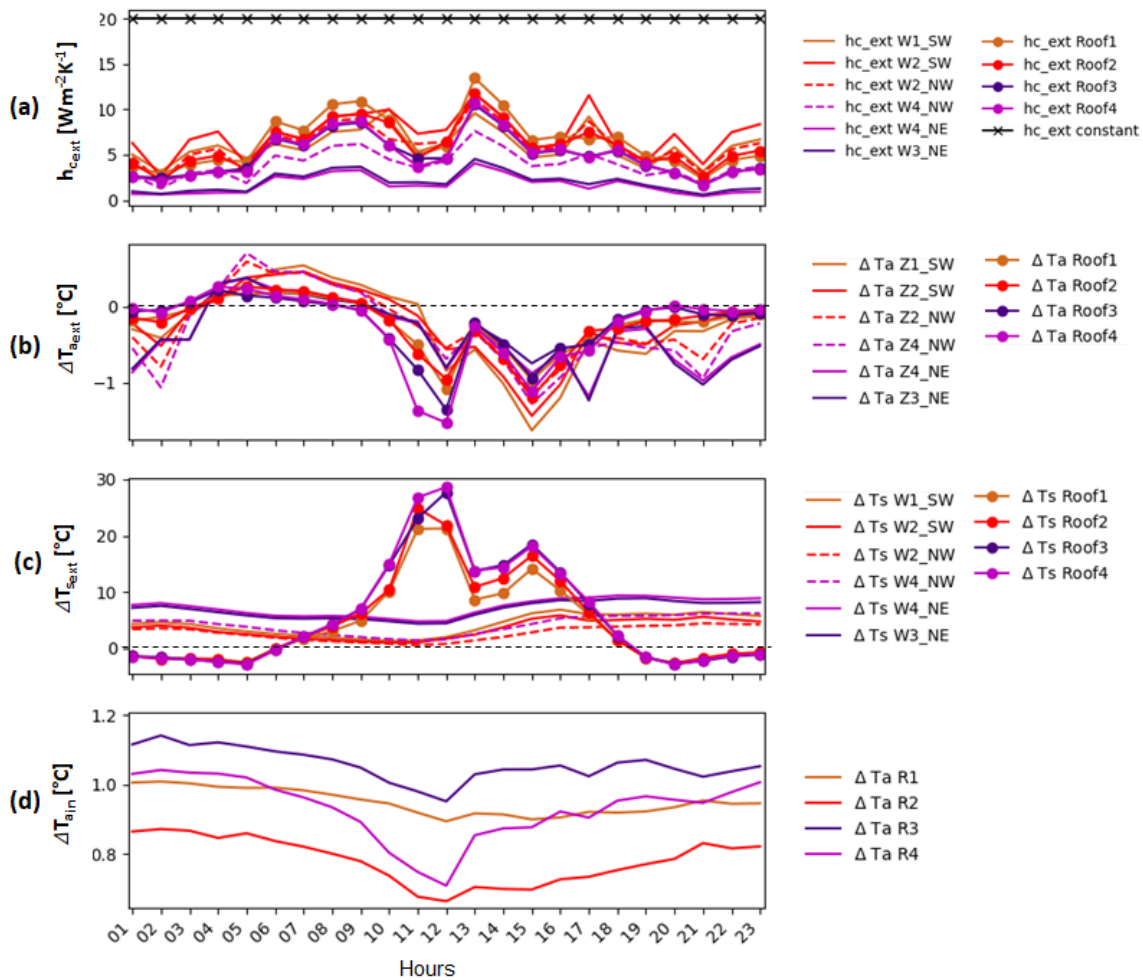


Figure 5.7:  $S_{McZM}$  and  $S_{h_{c_{cnst}}}$  the 12th of August :evolution of (a)  $h_{c_{ext}}$ , (b) outdoor air temperatures difference of air zones adjacent to walls  $\Delta T_{a_{ext}}$ , (c) outdoor walls and roofs surface temperature difference  $\Delta T_{s_{ext}}$  (d) indoor air temperature difference Delta  $\Delta T_{a_{in}}$ .

Figure 5.7 (b) shows that from 1 AM to 3 AM and from 10 AM to 11 PM, the outdoor air temperatures in  $S_{McZM}$  are lower than the ones in  $S_{h_{c_{cnst}}}$  (with a difference reaching  $1.56\text{ }^{\circ}\text{C}$ ) due to lower convective exchanges in  $S_{McZM}$ , as highlighted in Figure 5.6 (d). Conversely,

from 4 AM to 9 AM the trend is reversed, with outdoor air temperatures in  $S_{McZM}$  exceeding the ones in  $S_{h_{c}cnst}$  (with a difference reaching  $0.7^{\circ}\text{C}$  in rooms R2 and R4). This is explained by the combined effect of the reduced advective heat exchanges with the other air zones, especially at 5 AM (note that the  $h_{c_{ext}}$  is proportional to the inlet wind speed, which is proportional to the advected mass flow rate) and the inversion of the convective heat exchange in the  $S_{h_{c}cnst}$ , as highlighted in Figure 5.6 (d).

Figure 5.7 (c) shows that surface temperatures on the roof are slightly superior on the  $S_{h_{c}cnst}$  at night than on the  $S_{McZM}$  scenario, as the  $\Delta T_{s_{ext}}$  is negative.

Figure 5.8 examines two scenarios to explain the given phenomena: One relates to the temporal progression of the surface temperature on Roof1, the second pertains to the changing air temperature adjacent to Roof1, and the third involves the evolution of the convective heat flux between Roof1 and the surrounding air zone. The figure indicates a gradual decrease in both surface and air temperatures in each scenario starting from midnight. Until 6 PM, the surface temperature remains higher than the air temperature in both cases. From 7 PM onwards, however, the air temperature surpasses the surface temperature.

To explain this phenomena, Figure 5.8 compares for the two scenarios: (a) the evolution of the surface temperature on Roof1, (b) the evolution of the air temperature of the zone adjacent to the Roof1 and (c) the evolution of the convective heat flux between the Roof 1 and the adjacent air zone. The figure indicates a gradual decrease in both surface and air temperatures in each scenario starting from 12 PM. Until 6 PM, the surface temperature remains higher than the air temperature in both cases. From 7 PM onwards, however, the air temperature surpasses the surface temperature. This is accounted for by the cooling effect of LWR exchange with the sky as the sun sets, particularly impacting roofs. As a result, the surface temperature drops below the air temperature, reversing the direction of the convective heat flux. Additionally, the external convection coefficient ( $h_{c_{ext}}$ ) in the  $S_{h_{c}cnst}$  scenario is considerably higher than in the  $S_{McZM}$  scenario, amplifying convective heat exchange. Consequently, Roof1's surface temperature in the  $S_{h_{c}cnst}$  scenario increases due to the elevated temperatures of the adjacent air zones. This leads to higher roof surface temperatures at night in the  $S_{h_{c}cnst}$  scenario than in the  $S_{McZM}$  scenario, with a difference peaking at  $-3^{\circ}\text{C}$ .

In contrast, as depicted in Figure 5.7 (c), from 6 AM to 6 PM, solar radiation and reduced convective exchanges cause significantly higher roof surface temperatures in  $S_{McZM}$  compared to  $S_{h_{c}cnst}$ . This swapping of trends between day and night is evident on roofs but not on outdoor wall surfaces, which consistently maintain higher temperatures in  $S_{McZM}$ .

As depicted in Figure 5.7 (d), the influence of the two scenarios on indoor air temperature is subtle, with no excess of  $1.2^{\circ}\text{C}$  and minor fluctuations throughout the day, around  $0.1^{\circ}\text{C}$ . This can be attributed to the highly insulated building envelope, which lessens the impact of external convective heat exchanges.

Figure 5.7 emphasizes the significant discrepancies between surface and air temperatures, primarily in air zones, walls, roofs, and east-facing rooms. These areas experience the

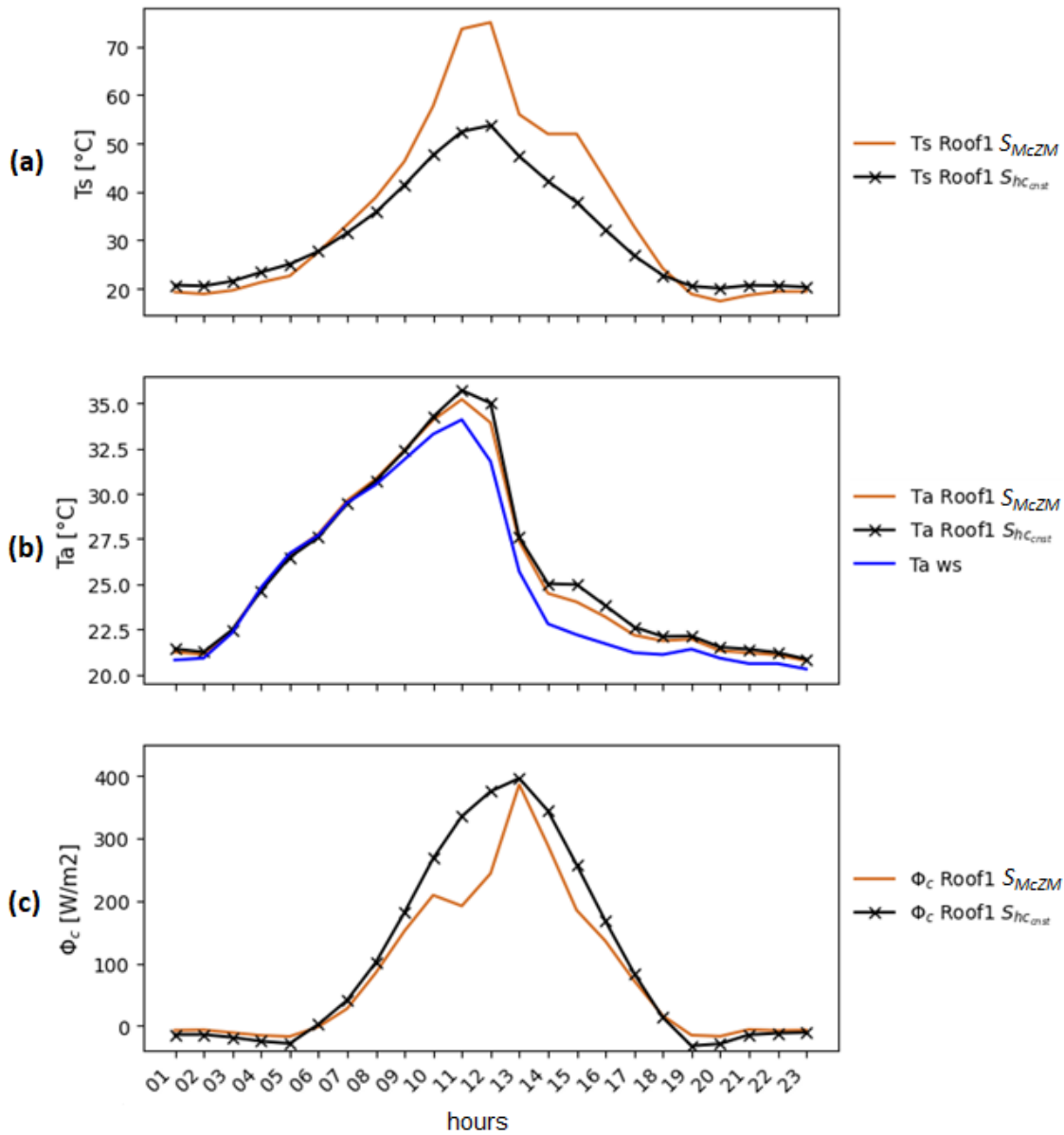


Figure 5.8:  $S_{McZM}$  and  $S_{hcconst}$  the 12th of August : evolution of (a) Roof1 surface temperature  $T_s$ , (b) air temperature of air zone adjacent to Roof1 ( $T_a$  Roof1) and air temperature at the weather station ( $T_a$  ws) (c) Convective heat flux between Roof1 and the adjacent air zone  $\Phi_c$  (positive from the surface to the air).

most overheating due to their high solar exposure and limited wind access.

### 5.3.2 Comparison between $S_{McZM}$ and $S_{Tws}$

In both the  $S_{McZM}$  and  $S_{Tws}$  scenarios, the indoor-outdoor air exchange and heat transfer coefficient remain constant. The only difference is the outdoor air temperature, which, in turn, influences the indoor-outdoor heat flux and indoor air temperature.



Figure 5.9 shows for the two modelling options  $S_{McZM}$  and  $S_{Tws}$  : the (a) inlet wind speed (V speed) and wind direction (V dir), (b) the outdoor air temperature of the air zones adjacent to the exterior walls of the studied dwelling ( $T_{a_{ext}}$ ), (c) the outdoor walls surface temperatures ( $T_{s_{ext}}$ ), (d) the indoor air temperature ( $T_{a_{in}}$ ).

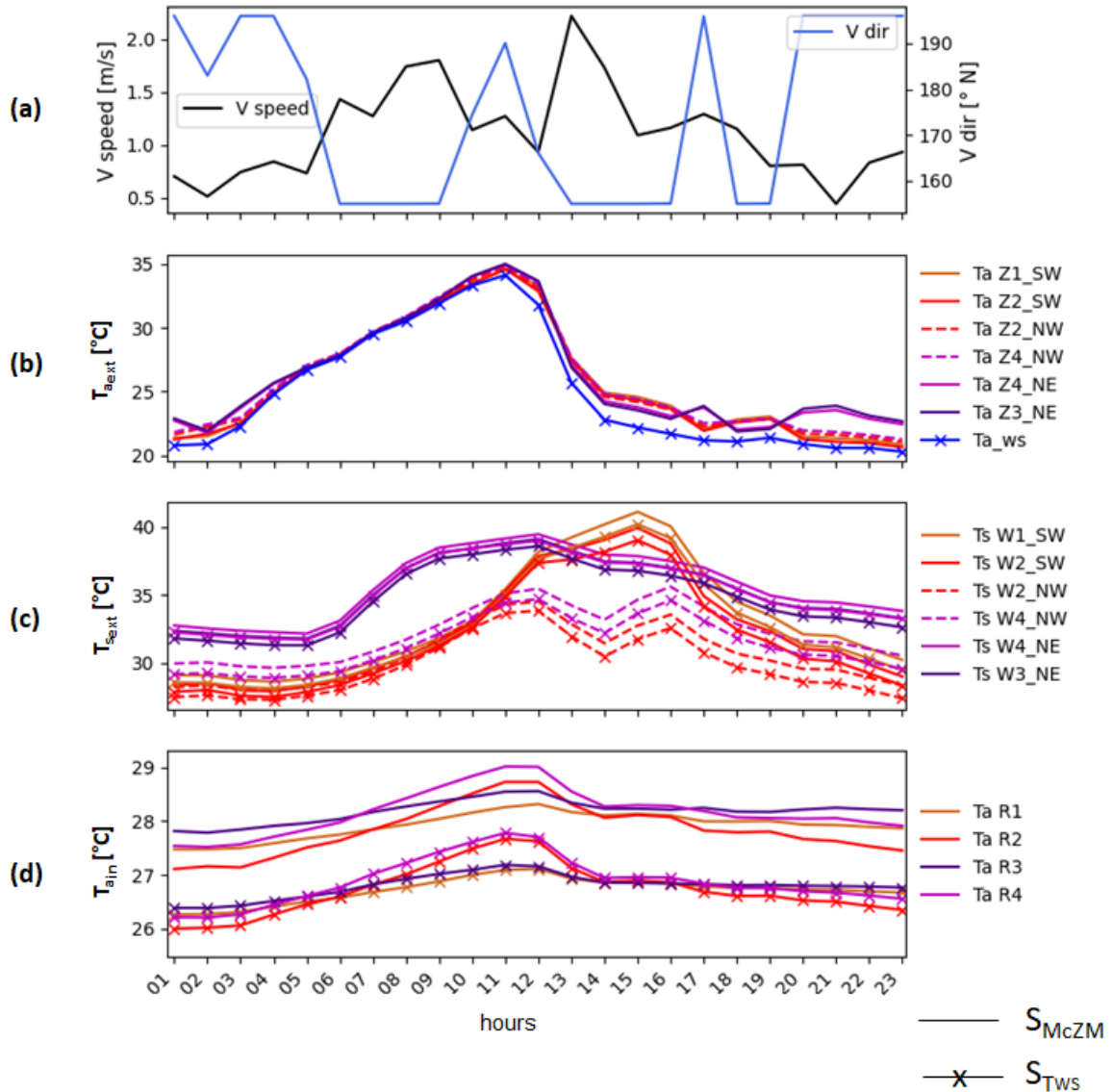


Figure 5.9:  $S_{McZM}$  and  $S_{Tws}$  the 12th of August : (a) inlet wind speed (V speed) and wind direction (V dir) (b) outdoor air temperatures of air zones adjacent to walls ( $T_{a_{ext}}$ ), (c) outdoor walls surfaces temperature ( $T_{s_{ext}}$ ) (d) indoor air temperature difference ( $T_{a_{in}}$ ).

Figure 5.10 compares for the two modelling options  $S_{McZM}$  and  $S_{Tws}$  : the (a) air temperature difference  $\Delta T_{a_{ext}}$  of the outdoor air zones adjacent to the walls and roofs of the studied dwelling, the (b) surfaces temperature difference  $\Delta T_{s_{ext}}$  of the exterior walls and roofs of the studied dwelling and the (c) indoor air temperature difference in the studied dwelling  $\Delta T_{a_{in}}$ .

The temperature difference refers to the discrepancy between the  $S_{McZM}$  and  $S_{Tws}$  scenarios. The results of both figures pertain to August 12.

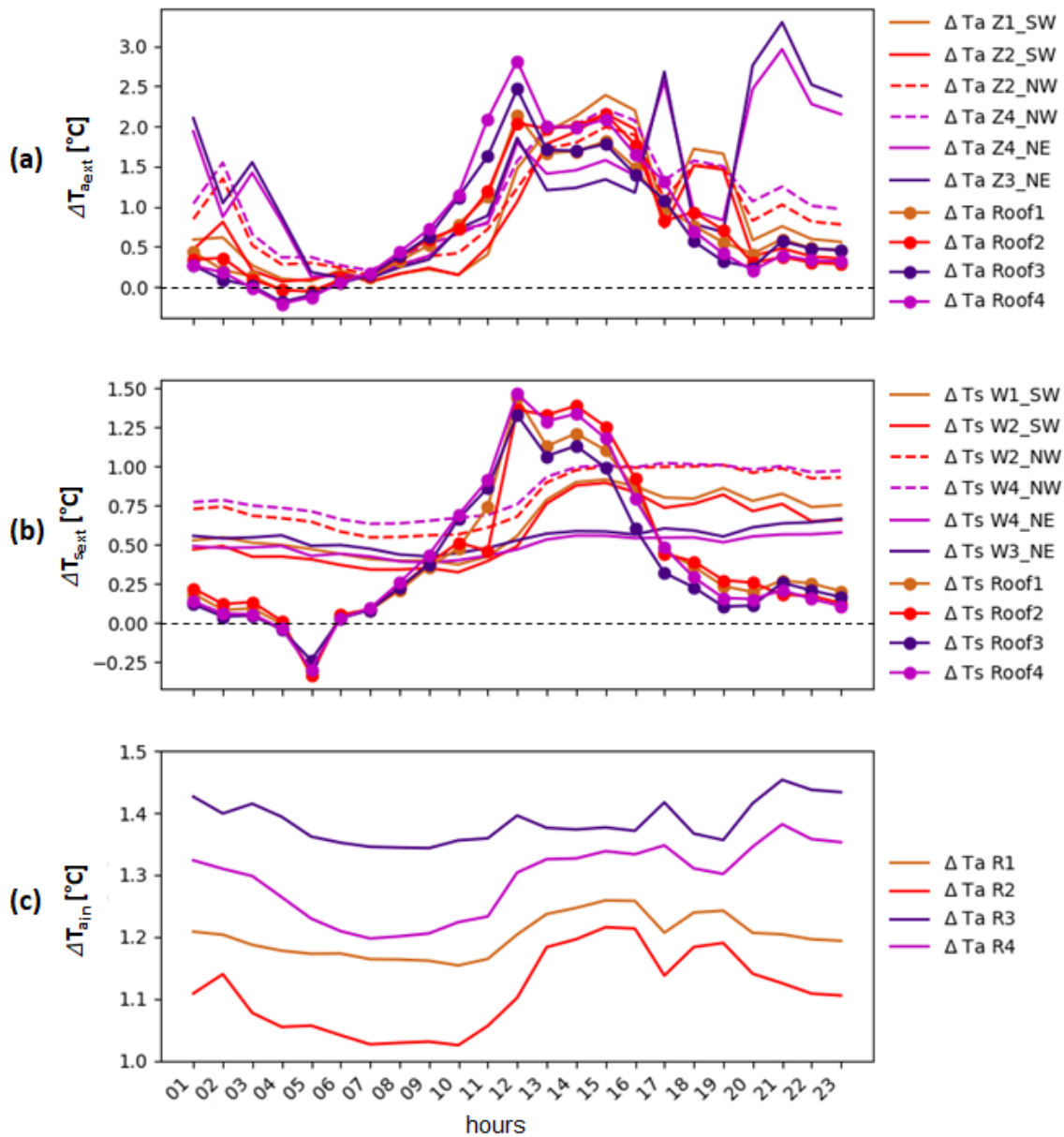


Figure 5.10:  $S_{McZM}$  and  $S_{T_{ws}}$  the 12th of August : (a) outdoor air temperatures difference of air zones adjacent to walls  $\Delta T_{a,ext}$ , (b) outdoor walls and roofs surfaces temperature difference  $\Delta T_{s,ext}$  (c) indoor air temperature difference  $\Delta T_{a,in}$ .

The assumption that uniform outdoor air temperature matches the temperature at the weather station ( $S_{T_{ws}}$ ) has repercussions on the final indoor air temperature.

While in the  $S_{T_{ws}}$  scenario, outdoor air temperature remains unaffected by heat exchange with the buildings. However, in the  $S_{McZM}$  scenario, outdoor air temperatures in the air zones are influenced by both advective heat exchanges between indoor and outdoor air zones and convective heat exchanges with the building envelope and soil. This results in varying outdoor air temperatures, as depicted in Figure 5.10 (a), with differences in air zones adjacent to the studied dwelling reaching up to  $3.3\text{ }^{\circ}\text{C}$  (recorded at 9 PM in the North-West

region), which correlates with a situation of low wind speed (Figure 5.9 (a)).

As shown in Figures 5.9 (b) and 5.10 (b), the surface temperatures in the  $S_{McZM}$  scenario are usually higher than those in the  $S_{T_{ws}}$  scenario. However, as indicated in Figure 5.10 (b), the surface temperature difference varies only between  $0.5^{\circ}\text{C}$  to  $1^{\circ}\text{C}$  on the walls and from  $-0.25^{\circ}\text{C}$  to  $1.5^{\circ}\text{C}$  on the roofs.

The difference in indoor air temperatures is not as noticeable as it is for outdoor temperatures. The variation between the two scenarios ranges from  $1^{\circ}\text{C}$  to  $1.48^{\circ}\text{C}$ , contingent on the specific room. Inside a single room, temperature fluctuations are very subtle: approximately  $0.2^{\circ}\text{C}$  for R2 and R4 and around  $0.1^{\circ}\text{C}$  for R1 and R3. This discrepancy results from the combined effects of the air temperature differences in each scenario, along with a double sun exposure effect in rooms R2 and R4.

### 5.3.3 Conclusion on the modelling comparison

The comparison of the McZM's modelling approach and the two simplified modelling scenarios,  $S_{h_{c}const}$  and  $S_{T_{ws}}$ , showcases discrepancies in indoor temperatures reaching  $1.1^{\circ}\text{C}$  and  $1.5^{\circ}\text{C}$ , respectively, in a well-insulated dwelling. These findings underscore the importance of precise boundary condition estimation for building modelling and the advantages of local microclimate modelling.

## 5.4 Results: base scenario

This section presents the simulation results for the base configuration scenario ( $S_{Base}$ ). Two exposure durations (seasonal and daily) and two exposure locations (indoor and outdoor) are studied under the two Eulerian and Lagrangian exposure perspectives. For the indoor analysis, both the top floor and the studied dwelling are considered. A 3D and 2D vision of the studied dwelling is provided in Figure 5.11 and Figure 5.12. For the outdoor analysis, the pedestrian level (corresponding to the first level of the zoning from  $z \in [0\text{ m to }3\text{ m}]$ ) is considered.

### 5.4.1 Daily exposure analysis

The daily exposure analysis encompasses both the Eulerian and Lagrangian exposure methods. The Eulerian method aligns daily heat stress with a fixed location, while the Lagrangian approach links daily heat stress and heat strain to a person's movements between various locations throughout the day. The next section presents a preceding analysis of climatic variables to clarify the correlated PET values.

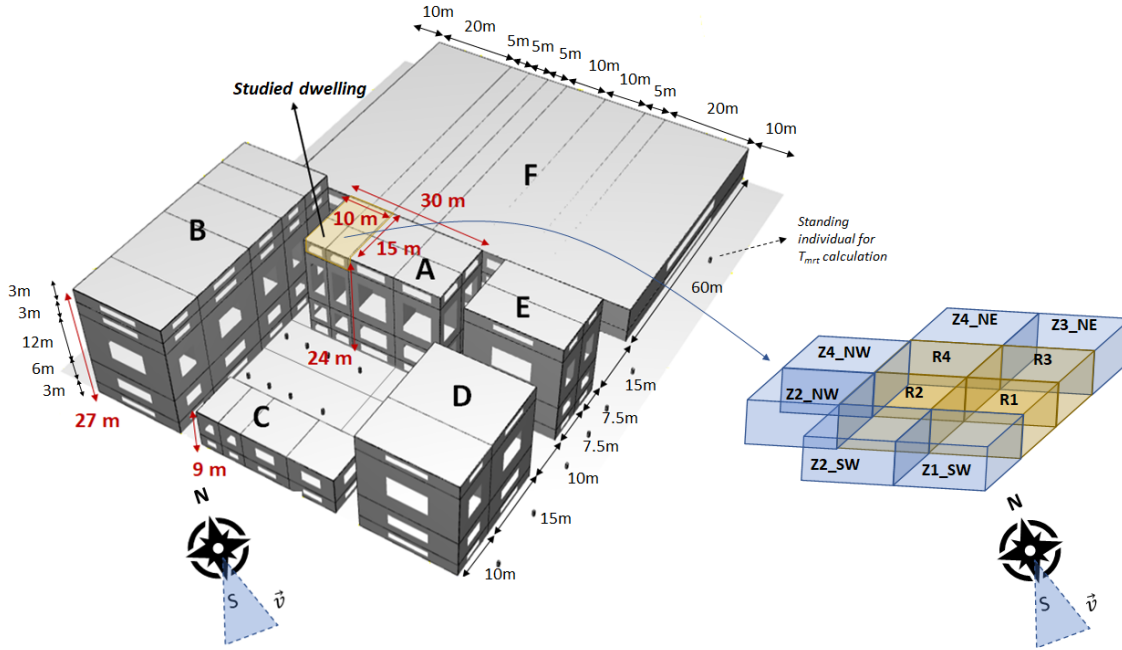


Figure 5.11: 3D view of the modelled scene and the target dwelling.

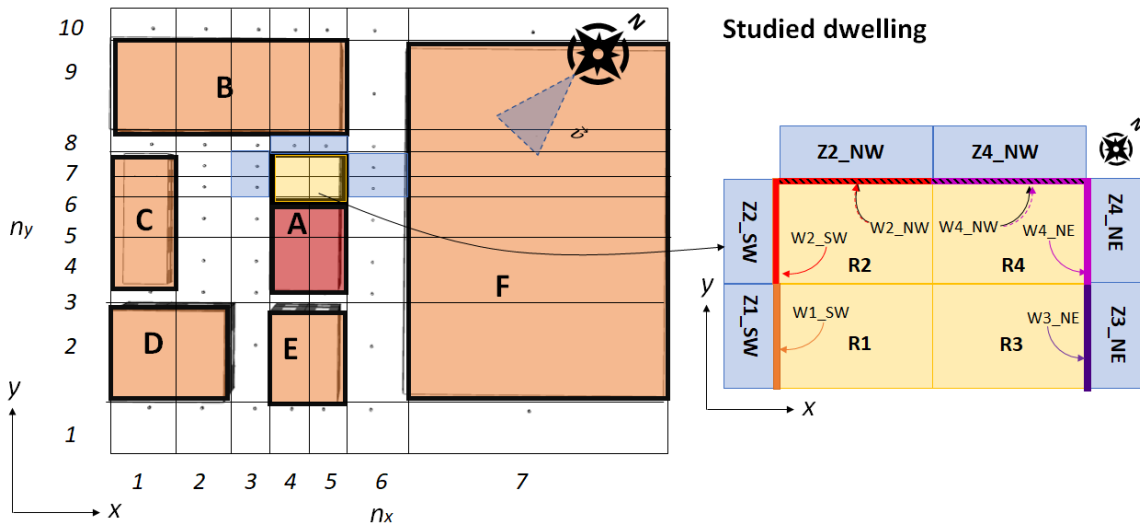


Figure 5.12: 2D view of the  $(x,y)$  horizontal plan at the top level corresponding to  $z \in [21 - 24m]$  and 2D plan of the studied dwelling.

#### 5.4.1.1 Climatic variables analysis

Section 1.5 reveals that PET is primarily influenced by  $T_a$ .  $T_{mrt}$  is another critical parameter, particularly outdoors, due to its substantial variations throughout the day. While PET is not greatly affected by  $v_a$ , the latter indirectly impacts air temperature, thus influencing PET. Lastly, a 1% increase in RH induces a minor PET increment, typically less than  $0.1^\circ\text{C}$ . The effects of wind speed and solar radiation on climatic variables and their subsequent influence on PET are examined.

Figure 5.13 illustrates the wind flow at the pedestrian level, stemming from a CFD simulation that corresponds to a 10m-high inlet wind speed of  $2 \text{ m s}^{-1}$ , accounting for two distinct wind directions. They represent the main wind directions considered in the current application case. Zones with higher wind speeds can be discerned from the figure. Using the pre-computed wind speed from the CFD, an average wind speed for each pedestrian-level region in the McZM is extrapolated. This average wind speed is further used to calculate the outdoor PET.

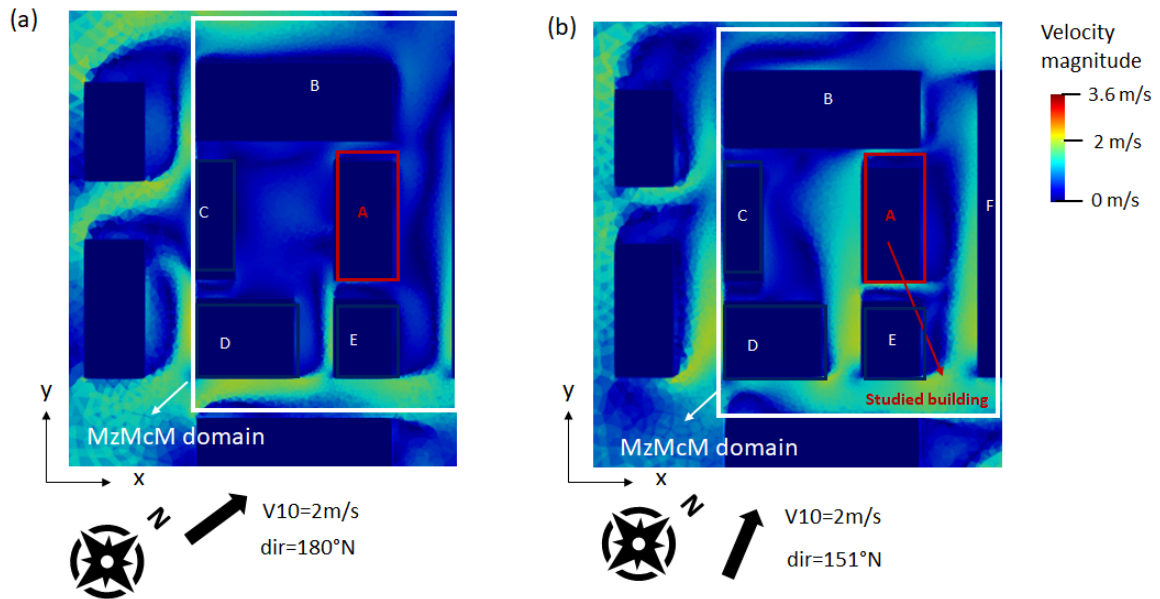


Figure 5.13: Wind speed magnitude for an inlet velocity of  $2 \text{ m s}^{-1}$  and a wind direction of (a)  $180^\circ\text{N}$  and (b)  $151^\circ\text{N}$ .

Figure 5.14 displays the spatial distribution of climatic variables -  $T_a$ ,  $T_{mrt}$ ,  $v_a$  and  $HR$  - at the pedestrian level for two distinct periods (9 AM and 5 PM) on August 12th, a notably hot day. The corresponding PET is provided in Figure 5.15. One key observation from these figures is the impact of solar radiation on  $T_a$  and  $T_{mrt}$ .

Areas exposed to sunlight exhibit higher  $T_a$  values as solar radiation heats adjacent surfaces such as the ground and walls, thus indirectly increasing the surrounding air temperature. This is evident in the air zones between buildings A and F at 9 AM, which receive the most sunlight at that hour, as the distribution of mean radiant temperature ( $T_{mrt}$ ) also demonstrates. By 5 PM, while the southern side of building A absorbs the most sunlight, its  $T_a$  is lower than the ones recorded in three air zones: those situated between buildings A and F and between buildings A and B. This can be attributed to the fact that air zones with higher  $T_a$  are in direct contact with walls that generate additional heat via convection. Furthermore, the presence of low wind speeds restricts advective heat exchanges between warmer and cooler air zones. The effect of the advection is also evident in the airzone on the northeast side of building F. A singularity, where the  $T_a$  is unusually high ( $26.7^\circ\text{C}$ ) compared to the surrounding air zones and the air temperature boundary condition, emerges

due to the low wind speed inhibiting airflow exchanges with other air zones. This illustrates a flaw in the current model. It only acknowledges advection and fails to explicitly account for turbulence and buoyancy effects on air movement.

The impact of wind speed on heat transfers, particularly advection, becomes noticeable at 9 AM. High wind speeds tend to equalize  $T_a$  in various zones. In contrast, areas with low wind speeds primarily experience  $T_a$  changes due to convective heat transfers with surfaces. This phenomenon is particularly noticeable at 5 PM in areas close to buildings A and B. During this time, though these zones are shaded, they maintain a higher air temperature than other areas because of minimal heat exchange through advection.

Under a constant specific humidity, an increase in  $T_a$  results in a decrease in  $RH$ . However,  $T_a$  has a more significant impact on the PET than  $RH$  does, making its effect more dominant. Additionally, with rising temperatures, the reduction in  $RH$  becomes less noticeable for every 1 °C increase, as evident on a psychrometric chart.

In conclusion, solar radiation impacts PET both directly through  $T_{mrt}$  and indirectly by increasing  $T_a$  by heating surrounding surfaces outdoors or penetrating windows indoors. Wind speed impacts PET indirectly by affecting advection within air zones. Moreover, while the spatial distribution of PET mirrors that of  $T_{mrt}$ , its intensity is primarily influenced by  $T_a$ . This is evident as PET values are more aligned with  $T_a$  rather than  $T_{mrt}$ .

#### 5.4.1.2 Outdoor and indoor daily heat stress related to a place

The PET serves as a daily indicator of heat stress. As analyzed in the earlier section, Figure 5.17 displays the progression of PET on August 12th, from 8 AM to 7 PM, both outdoors at pedestrian level and indoors on the top floor of the examined dwelling. Three key periods of the day have been chosen for this: sunrise, midday - when the sun is at its peak -, and sunset. Two intervals within these periods have been chosen to emphasize the hourly changes in the PET. The figure's zoning clearly shows outdoor heat shelters situated between buildings A and B, as well as A and E.

Indoors, the correlation between PET and  $T_a$  becomes very clear due to the uniform  $T_{mrt}$ . Indoor  $T_a$  often remains high because there's no easy way to dissipate the heat stored in the air and the heat given off by the walls. This happens especially in rooms facing East due to solar radiation absorption in the morning (9 AM to 12 PM) and the difficulty in dissipating this absorbed heat throughout the day because of high insulation, as shown in Figure 5.16. As illustrated in Figure 5.16, the  $T_a$  inside the dwelling remains elevated throughout the day.

Additionally, in this particular case, where no adaptive cooling action is taken by the occupant, the temperatures of the exposed zones in the East are consistently higher than those in the exposed ones in the West. It must be noted that building B is taller than the studied building; North-West exposed rooms are therefore partially shaded in the evening.

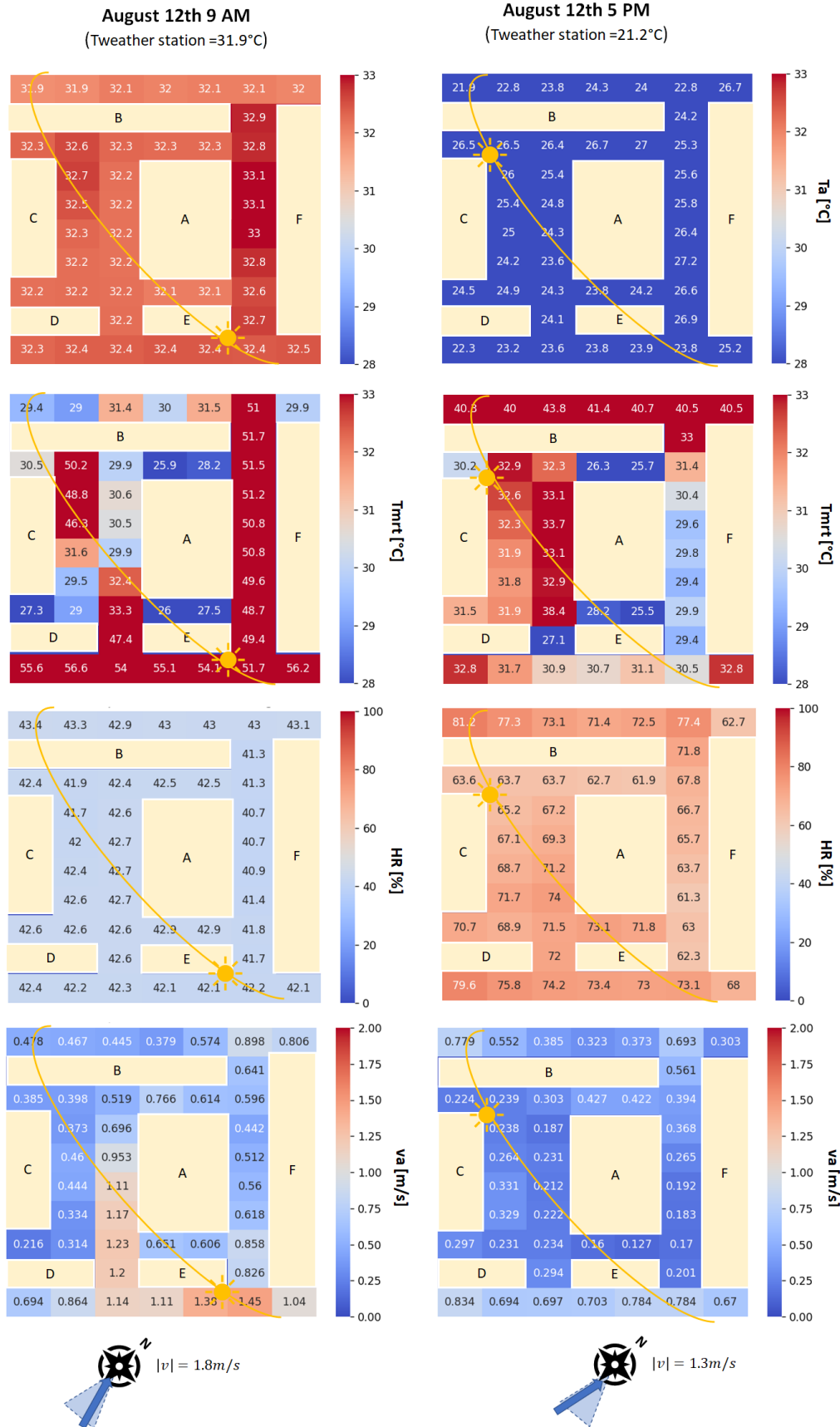


Figure 5.14: Pedestrian level spatial distribution of climatic variables on August the 12th at 9 AM and 5 PM. Note: Sun position is purely indicative.

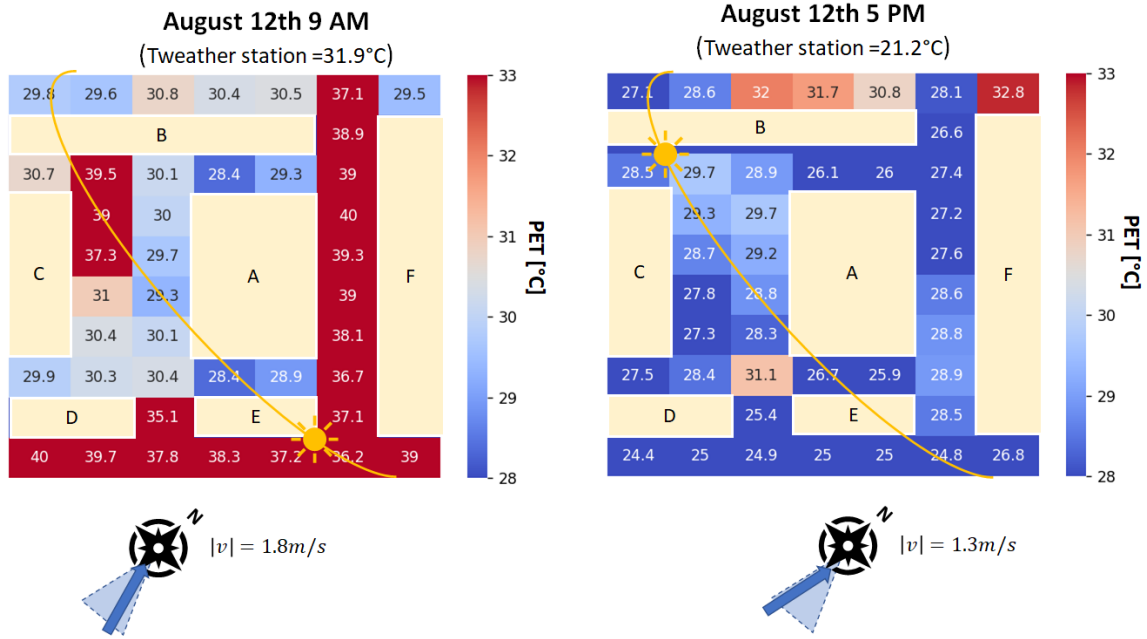


Figure 5.15: Pedestrian level PET spatial distribution on August the 12th at 9 AM and 5 PM. Note: Sun position is purely indicative.

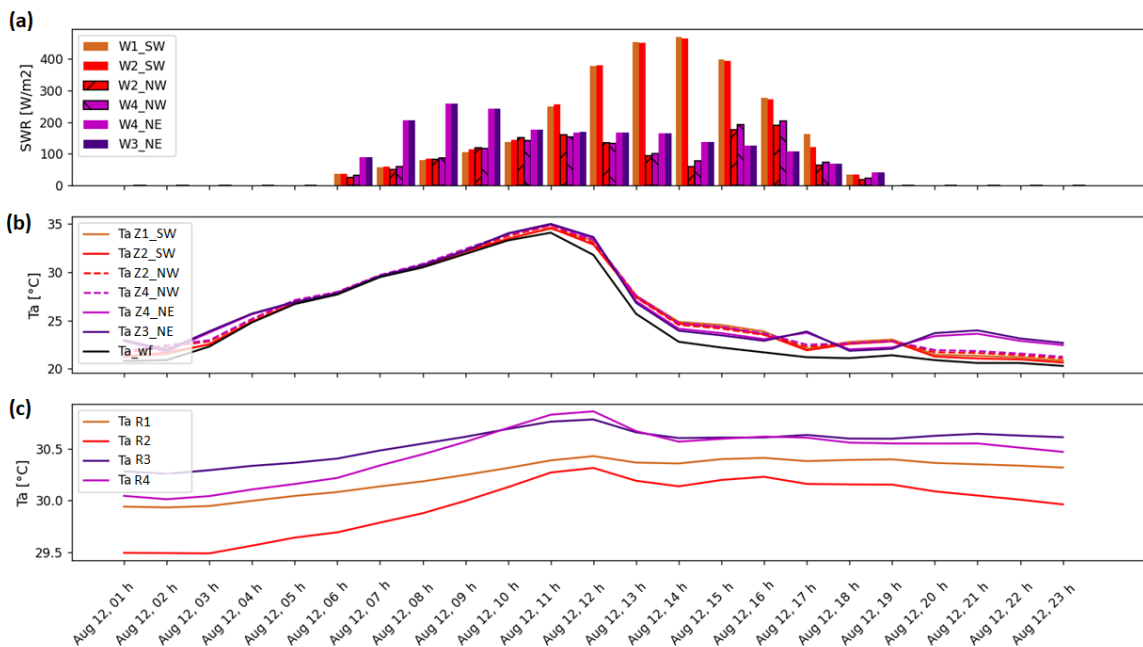


Figure 5.16: August the 12<sup>th</sup>, studied dwelling: (a) Walls incident solar radiation (b) Air temperature of the air-zones adjacent to the walls (c) Indoor air temperature.



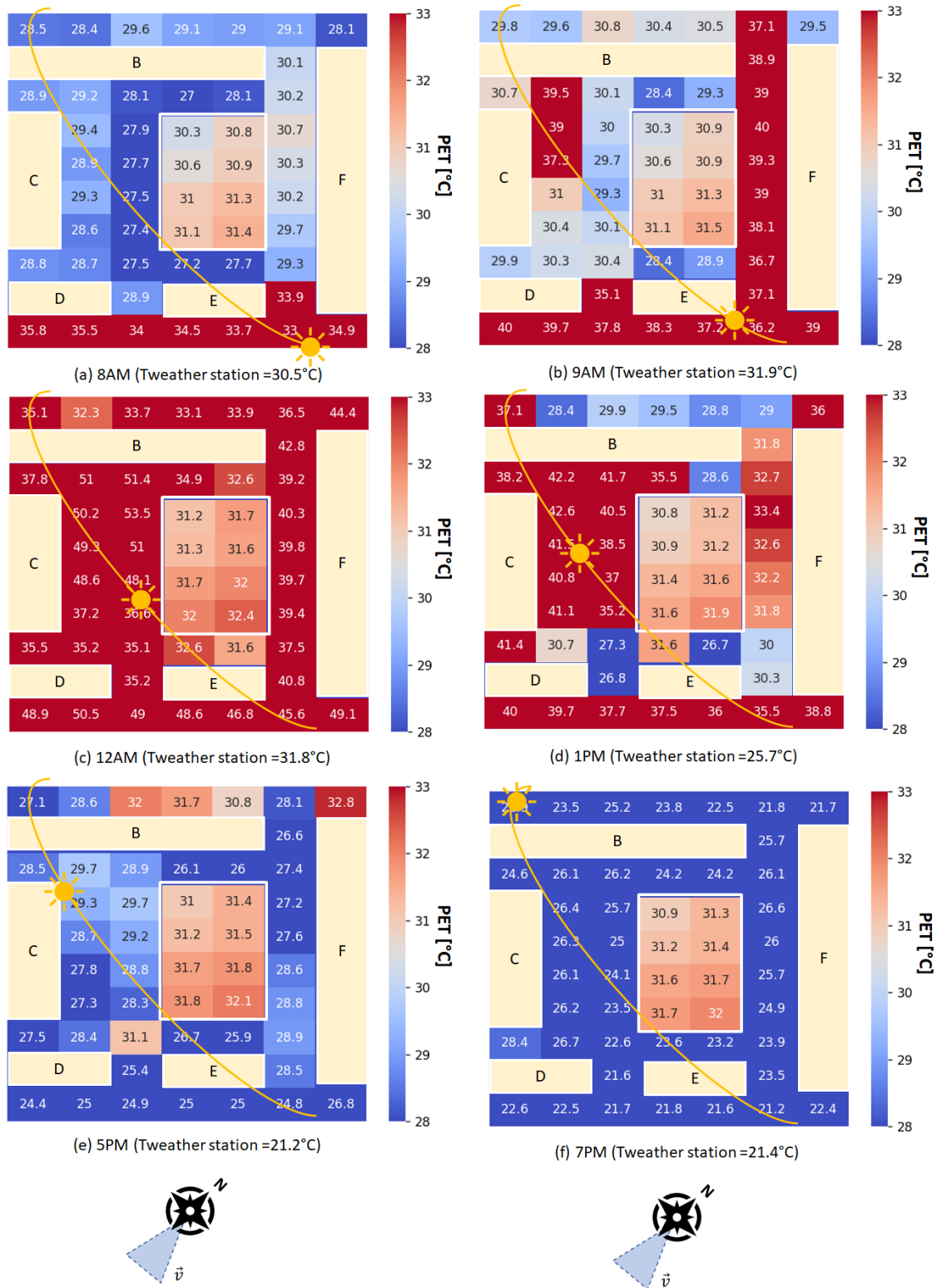


Figure 5.17: Pedestrian level and top floor PET spatial distribution on August 12th from 9 AM to 7 PM. Note: Sun position is purely indicative.

### 5.4.1.3 Daily heat stress and heat strain related to the individual displacement

The following analysis illustrates the evolution of PET in relation to an ever-changing exposure environment, as depicted in Figure 5.18. This path might represent the typical daily routine of a person who spends their day in and around their home. The term ‘dwelling’ refers to the area of focus, and ‘immediate surrounding’ pertains to the studied outdoor perimeter. The location of the individual during each time interval is indicated in the figure.

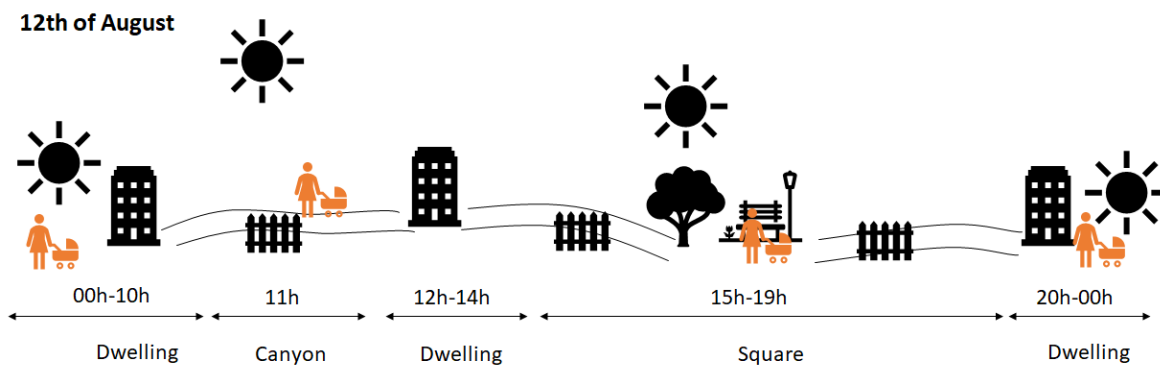


Figure 5.18: An example of the daily path of a person spending the day in his dwelling and its surroundings.

Figure 5.20 shows in dotted line the PET evolution for the individual’s path, as well as the PET associated with three different zones in which the individual moves (Figure 5.19).

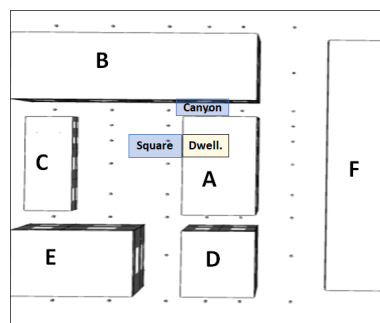


Figure 5.19: Illustration of the three displacement zones.

This path underscores the individual’s peak exposure times, exposure duration, and resting phases throughout the day. The coloured bars on the graph align with the PET evaluation scale’s colour codes, as defined by Matzarakis and Mayer (1996). The person’s journey primarily falls within the intervals of slight to moderate heat stress, with a short stint of intense heat stress between 2 and 3 PM.

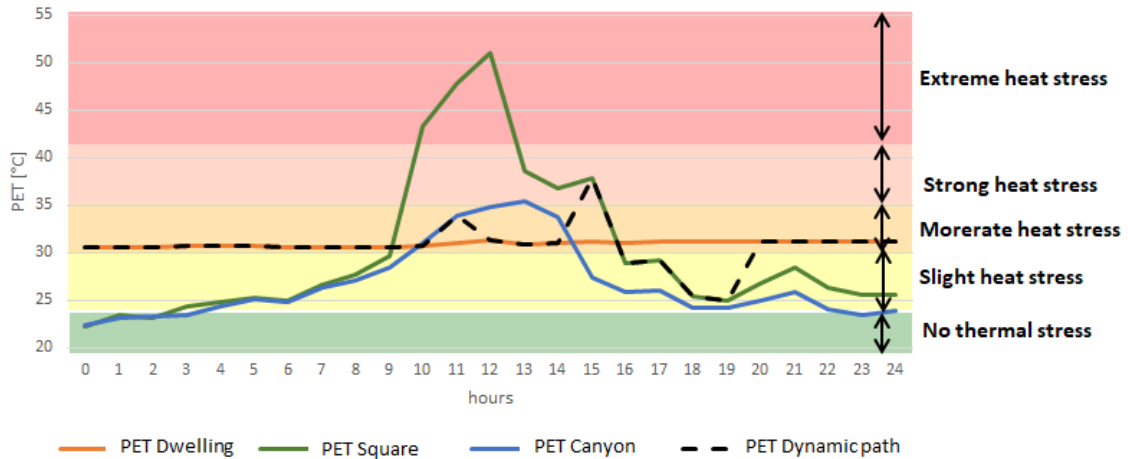


Figure 5.20: August the 12<sup>th</sup>. PET evolution related to the dynamic path (PET Dynamic) and PET evolution in the dwelling, in the square and in the canyon air zone.

At the individual level, heat strain indices described in Section 1.6 can also be used. This portrays a person's physiological response to heat stress. Figure 5.21 depicts the progression of five heat strain indices proposed in Chapter 1, as demonstrated by the JOS-3 model. Pelvic core temperature ( $T_{core}$ ) and skin temperature ( $T_{sk}$ ) represent thermal strain, while the sweat rate - weight loss through evaporation and respiration ( $sw_R$ )- and skin wettedness ( $SkinWet$ ) denote hydration strain.  $SkinWet$  indicates the necessary hydration level based on the body's water evaporation. Lastly, cardiac output ( $CO$ ) signifies cardiac strain. Figure 5.21 indicates that thermal strain poses the most significant stress on the body, evidenced by skin temperatures surpassing the recommended thresholds (marked by the orange band in the graph). Meanwhile, the other heat strain indices never breach the critical thresholds.

The initial results underline the drawbacks of exclusively examining heat strain through the absolute values of physiological variables offered by the JOS-3 model. A more effective approach would involve a comparative analysis of these indices. This will be explored further in our comparative study of cooling scenarios.

## 5.4.2 Seasonal exposure analysis

This analysis covers the summer period from June 20 to September 20, 2020, and aims to provide a stable, spatial perspective of heat stress in a fixed zone. By assessing heat stress, it highlights the most impacted areas along with potential heat shelters. The indices used for this analysis are detailed in Section 1.6 of Chapter 5.8.

### 5.4.2.1 Global analysis

For global seasonal heat stress analysis, the indicator used is the Heat Stress Distribution ( $HSD[\%]$ ). The  $HSD$  represents the occurrences of PET within a range of temperatures to

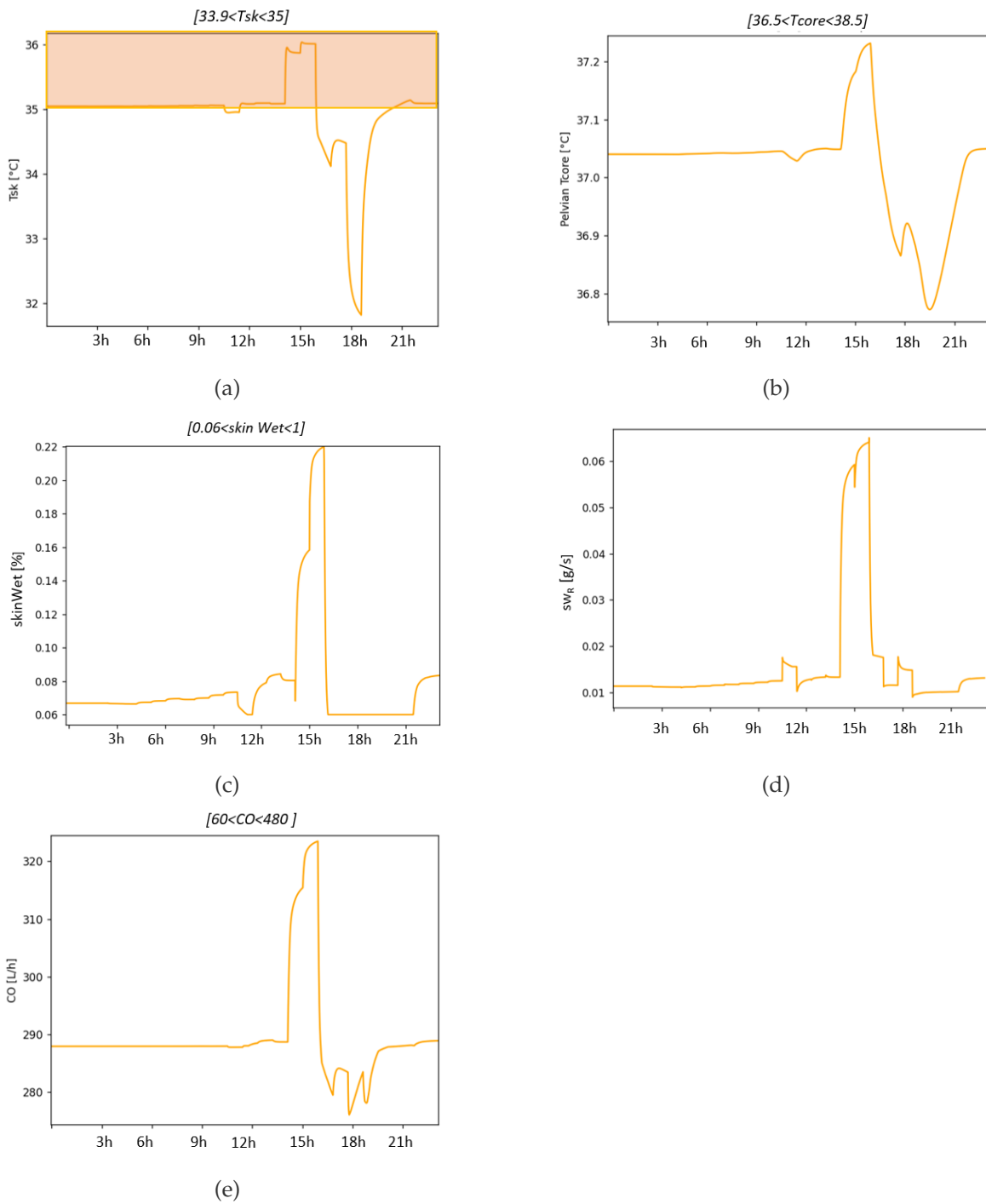


Figure 5.21: Heat strain response corresponding to the exposure path of Figure 5.20: (a)  $T_{sk}$ , (b)  $T_{core}$ , (c)  $SkinWet$  (d)  $sw_R$ , (e)  $CO$ .

which correspond an heat stress assessment (Figure 5.22).

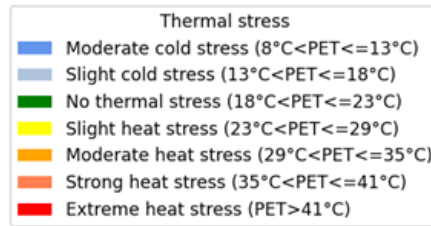


Figure 5.22: PET assessment scale (Matzarakis and Mayer, 1996).

Maximum and minimum  $HSD$  is calculated for three areas : outdoor at pedestrian level, indoor at the top floor and indoor considering only the studied dwelling. Each area includes different air zones with different values of PET. The minimum  $HSD$  ( $HSD_{Min}$ ) and maximum  $HSD$  ( $HSD_{Max}$ ) given in Figures 5.23, 5.24 and 5.25 correspond respectively to the distribution of the minimum and maximum PET over the given area for the global seasonal period, the month of June, July, August and September.

The maximum and minimum  $HSD$  are calculated for three distinct areas: outdoors at pedestrian level, indoors at the top floor, and indoors in the area under study. Each area incorporates various airzones featuring different PET values. Figures 5.23, 5.24 and 5.25 illustrate the distribution of minimum ( $HSD_{Min}$ ) and maximum ( $HSD_{Max}$ ) PET across the given areas for the overall seasonal period and the months of June, July, August, and September, respectively.

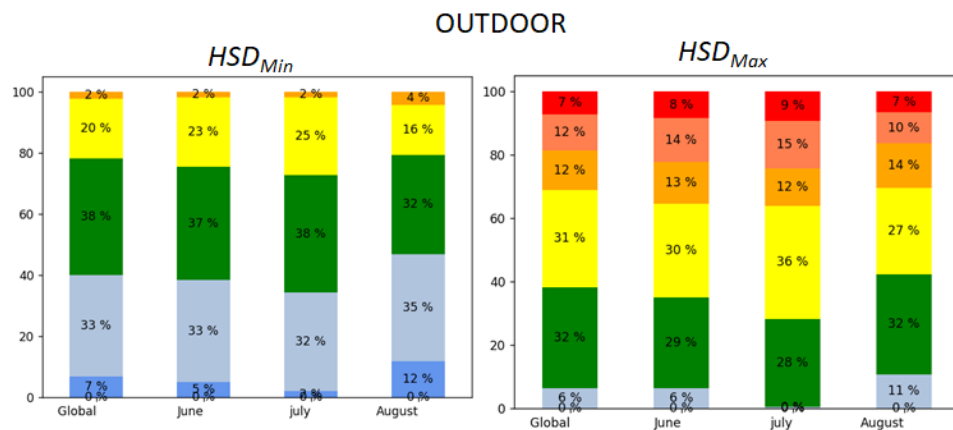


Figure 5.23: Outdoor minimal and maximal HSD for the global season and for June, July, August and September.

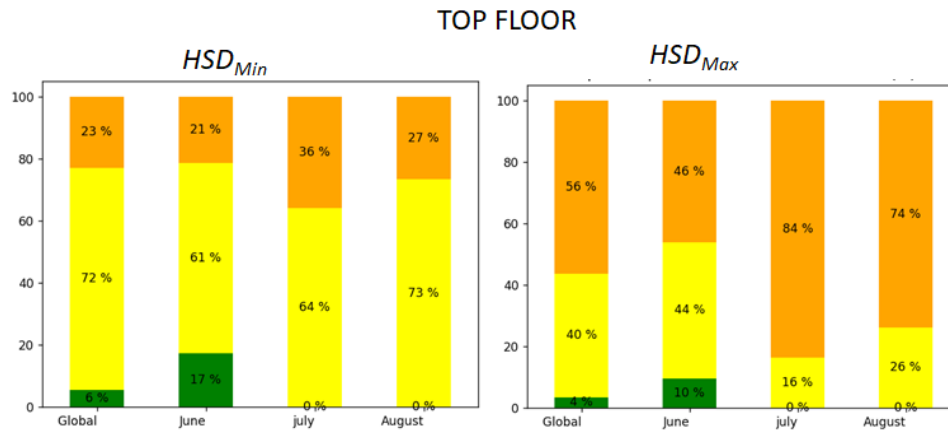


Figure 5.24: Top floor minimal and maximal HSD for the global season and for June, July, August and September.

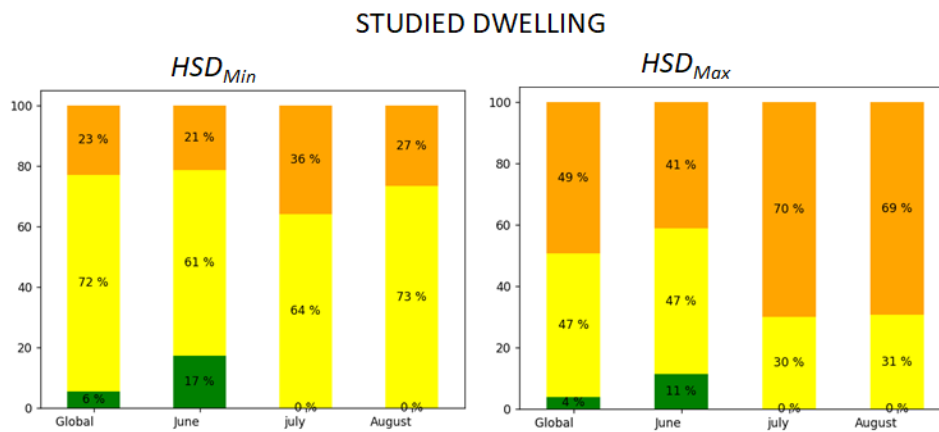


Figure 5.25: Studied dwelling minimal and maximal HSD for the global season and for June, July, August and September.

Figure 5.23 shows a range of variation in outdoor heat stress, corresponding to significant variations in air temperature and solar radiation. Figures 5.24 and 5.25 show indoor heat stress characterized by dominant slight to moderate PET values, with maximum values peaking in July and August. When compared to the entire top floor, the dwelling under study experiences less heat stress. This can be attributed to its orientation and the solar shading provided by Building B. The subsequent section presents a detailed spatial analysis that further explores the behaviour of each zone.

#### 5.4.2.2 Spatial analysis

In the spatial analysis, each region is identified by its location in the orthogonal XYZ coordinate system. The identifier used is  $Z_{n_x n_y n_z}$ , where  $Z$  represents the zone, and  $n_x$ ,  $n_y$  and  $n_z$  refer to the zone numbers along the  $x$ ,  $y$ , and  $z$ -axis, respectively. For instance, the identifier  $Z_{1_1_1}$  denotes the first cell in the bottom left of the division. In order to eliminate any effects from boundary conditions, the perimeter areas are excluded from the analysis. Only

zones with  $n_x$  values ranging from 2 to 6 and  $n_y$  values from 3 to 8 are analysed.

The indices analyzed (Section 1.6) include maximal overheating duration ( $OhD_{max}[h]$ ), cumulative overheating intensity equivalent to the day degrees hours ( $OhI_{max}[^{\circ}Ch]$ ), maximal overheating ( $Oh_{max}[^{\circ}C]$ ) and average overheating ( $Oh_{mean}[^{\circ}C]$ ). These indices are depicted for outdoor at the pedestrian level and for indoor at the top floor in Figures 5.26, 5.27, 5.28 and 5.29.

Outdoors, the zones that experience the most intense heat are those near the leeward side of the building (Z\_6\_4\_1 to Z\_6\_7\_1), as well as those most exposed to sunlight (Z\_2\_8\_1, Z\_2\_7\_1). This is especially noticeable in building C, which has two floors. Zones experiencing less frequent and severe overheating are those situated between two buildings. On the top floor, the zones exposed to the east are the most stressed. As explained in Section 5.4.1.2, these zones receive the highest amount of solar radiation in the morning, and they struggle to cool down by evening. Their leeward location further reduces convective and advective exchanges.

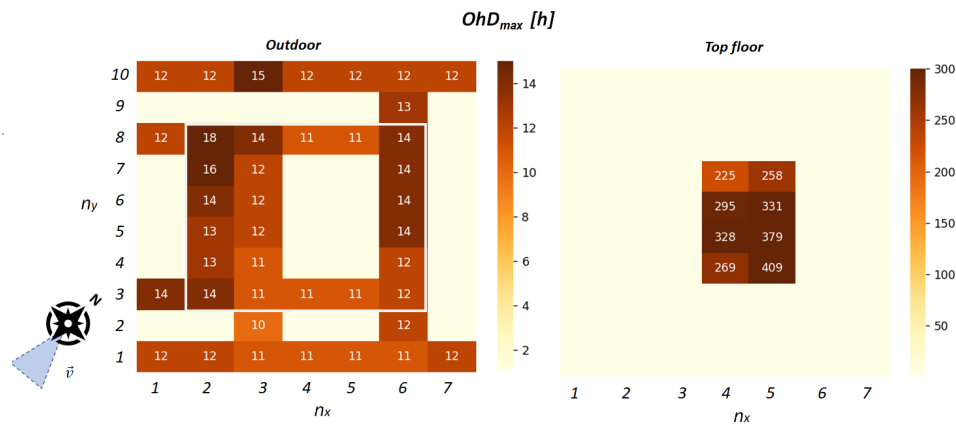


Figure 5.26: Outdoor and top floor Maximal overheating duration ( $OhD_{max}[h]$ ).

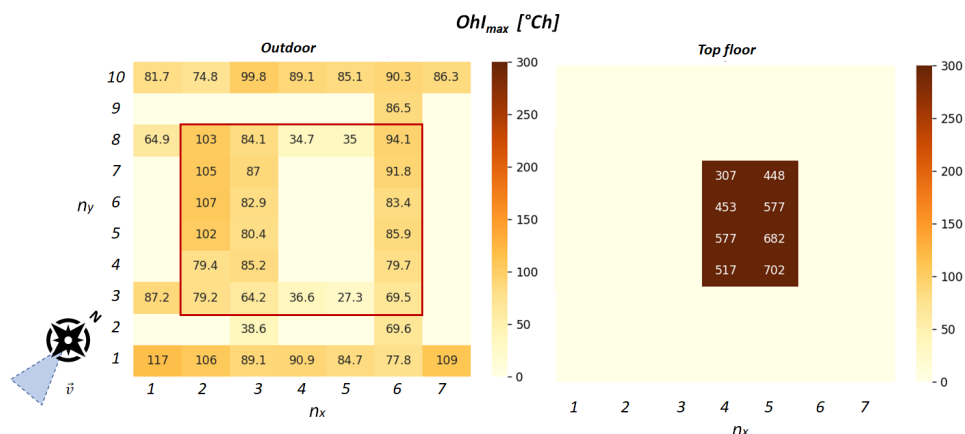


Figure 5.27: Outdoor and top floor Cumulative overheating intensity ( $OhI_{max}[^{\circ}Ch]$ ).

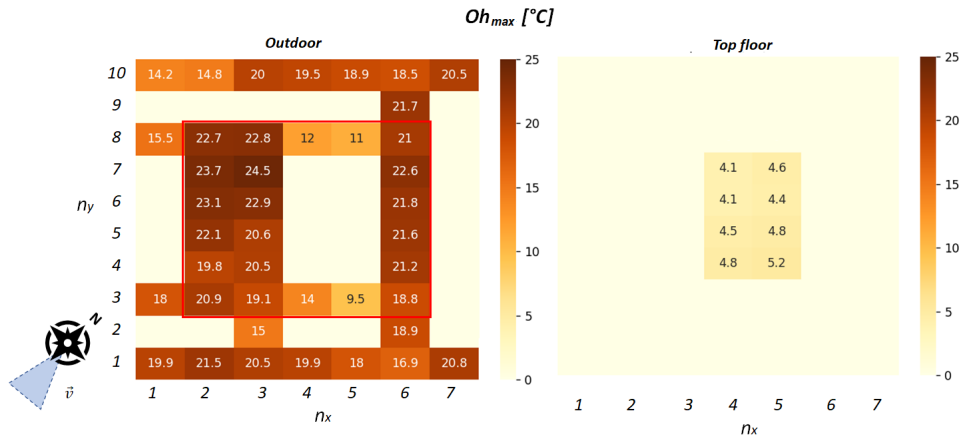


Figure 5.28: Outdoor and top floor Maximal overheating ( $Oh_{max}$  [°C]).

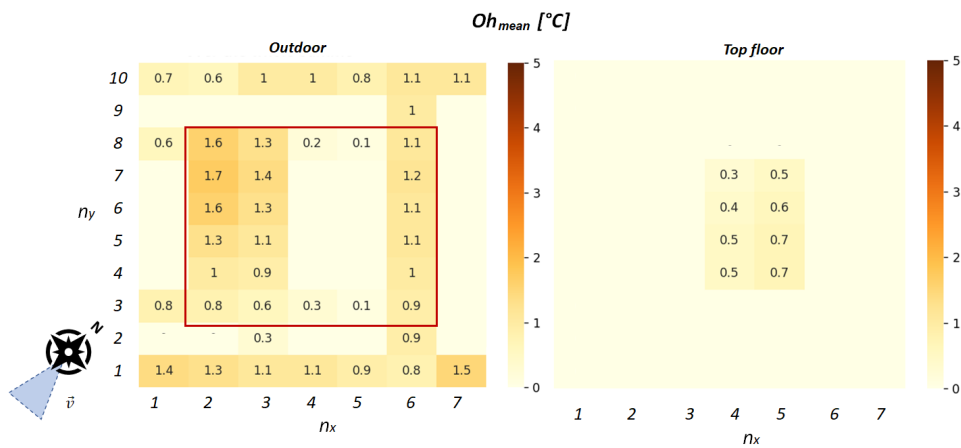


Figure 5.29: Outdoor and top floor Average overheating ( $Oh_{mean}$  [°C]).

The optimal zone is the one that faces the North-West and South-West, as it enjoys the shading effect from Building B.

$OhD_{max}$  and  $OhI_{max}$  are notably more extended and intense indoors compared to outdoors, as shown in Figures 5.26 and 5.27.

Figure 5.30 focuses on the top floor and reports the period corresponding to the  $OhD_{max}$ . The size and colour of the bubble represent the  $OhD_{max}$  value. Besides the bubble, the black number indicates the average degrees of exceedance ( $^{\circ}C h^{-1}$ ), and the red number shows the maximum temperatures ( $^{\circ}C$ ), both during the most severe overheating episode.

The chart reveals two distinct periods of maximum overheating: one from August 9th to 10th, which affects rooms exposed to the South-West, and another from July 19th to 22nd, focusing on North-East-facing rooms. These patterns primarily arise due to the shifting position of the sun from July to August.

With the exception of Zone Z\_4\_7\_4, maximum temperatures are fairly consistent across different zones, averaging at around  $33^{\circ}C$ . The average degree of exceedance stays below  $2^{\circ}C$  across all zones. In line with the trend observed for the maximum overheating duration,



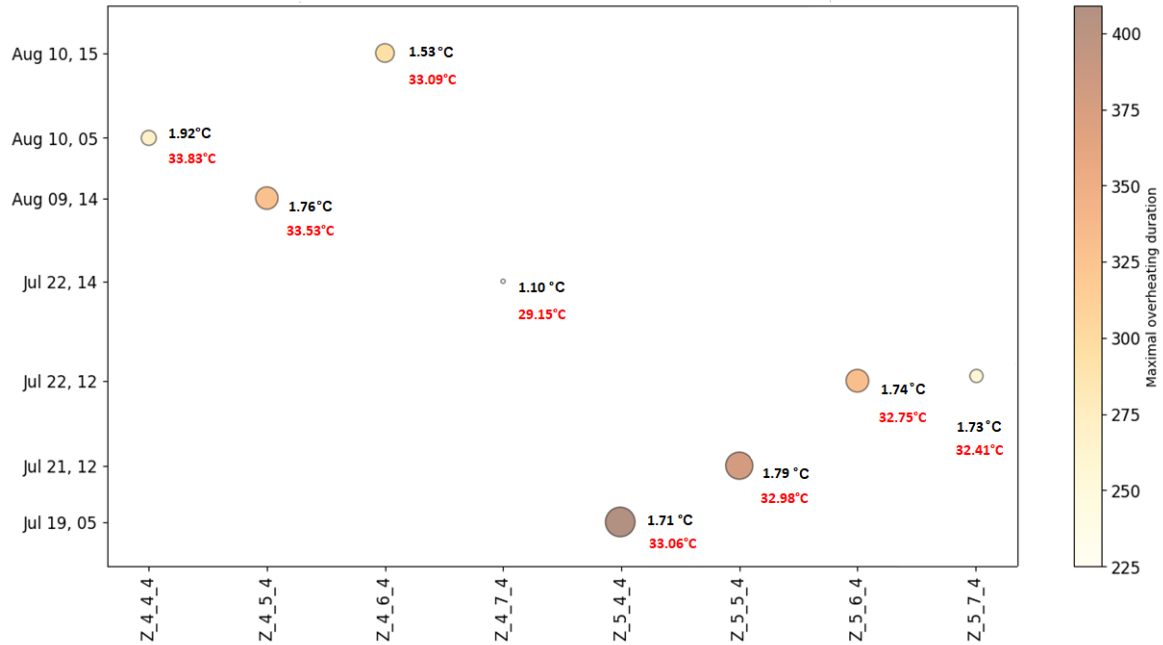


Figure 5.30: From June to September 2020: periods corresponding to the maximal overheating duration ( $OhD_{max}$ ) represented by the bubble size and color, the average degrees of exceedance ( $^{\circ}\text{C}$ ) during the  $OhD_{max}$  episode represented by the black number, the maximum temperatures ( $^{\circ}\text{C}$ ) during the  $OhD_{max}$  episode represented by the red number.

the average overheating follows a similar pattern, but the maximum overheating values are more consistent across various dwelling zones.

### 5.4.3 Conclusions on the base scenario results

Examining heat stress using an Eulerian approach highlights the importance of spatial thermal zones, as indicated by PET gradients at the pedestrian level. This shows the significant impact that building geometry and layout can have on the resulting thermal conditions. Additionally, the proposed zoning method allows us to differentiate the various thermal conditions in different rooms within a dwelling.

Outdoors, the distribution of climatic variables depends on sunlight exposure, along with the intensity and direction of the wind. Variations in air temperature ( $T_a$ ), mean radiant temperature ( $T_{mrt}$ ), and air velocity ( $v_a$ ) are noticeable. In the given scenario, the differences can exceed  $5^{\circ}\text{C}$  for  $T_a$  and up to  $25^{\circ}\text{C}$  for  $T_{mrt}$  between different areas. Depending on the wind exposure, air velocity ( $v_a$ ) can also differ by a multiple of three. Indoors, these differences are less stark, but they do exist, primarily owing to the sun's exposure to the dwelling. This spatial variation is reflected in the PET values.

The significance of a spatial approach becomes clear when considering heat stress from a Lagrangian exposure perspective. Indeed, PET along a dynamic path is influenced by variations at different exposure locations. This methodology is also used to calculate the

fluctuating heat strain indices. While skin temperature ( $T_{sk}$ ) presents critical values, other indices do not. However, the assessment of heat strain should not be restricted to these indices alone. It is essential to consider other individual factors that affect bodily strain.

The global view analysis estimates heat stress levels in different zones, differentiating between indoor and outdoor areas. It assigns a percentage occurrence to varying levels of heat stress, from moderate cold to extreme heat. This method determines the amount of time an area experiences overheating. However, it fails to identify the exact locations of the most overheated zones. This data is supplied by the seasonal spatial analysis.

The seasonal spatial analysis also reveals the effect of solar exposure, as observed in the daily analysis, both outdoors and indoors. This exposure influences the duration indices ( $OhD_{max}$ ), cumulative indices ( $OhI_{max}$ ), peak indices ( $Oh_{max}$ ), and average overheating indices ( $Oh_{aver}$ ).

Outdoor variations in these indices are slightly more prominent than indoor ones, where differences from room to room are minimal. Despite the subtle changes between zones in this case study, this method allows us to pinpoint zones under greater heat stress. Consequently, we can implement specific cooling measures in these areas.

## 5.5 Results : cooling strategy comparison

This section compares the results obtained with  $S_{Base}$  with those obtained by applying  $S_{NV}$  and  $S_{Veg}$ .

### 5.5.1 Daily exposure analysis

#### 5.5.1.1 Outdoor and indoor daily heat stress related to a place

Figure 5.31 presents the PET for  $S_{Base}$  and  $S_{NV}$  and  $S_{Veg}$  at different times of day on August 12th.

The figure highlights the heat stress mitigation benefits of natural ventilation as compared to other scenarios. The benefits are particularly noticeable in rooms where natural ventilation is in use, with the most effective heat stress reduction occurring at 5 PM when the outdoor air temperature is lower than indoors. Indeed, in this scenario, natural ventilation is activated continuously.

While  $S_{NV}$  shows more effectiveness in naturally ventilated rooms - particularly in windward rooms -,  $S_{Veg}$  offers global benefits both indoors on the upper floor and outdoors at the pedestrian level. The temperature reduction at this particular moment of the day, however, remains low even in the  $S_{NV}$  scenario, on the order of 1 °C.

Lower PET values observed on the top floor within the  $S_{Veg}$  scenario compared to the

$S_{Base}$  can be attributed to the  $S_{Base}$ 's higher air temperatures near the ground when the sun is at its peak. This results in higher ground floor temperatures indoors, which in turn impacts the temperatures of the upper floors.

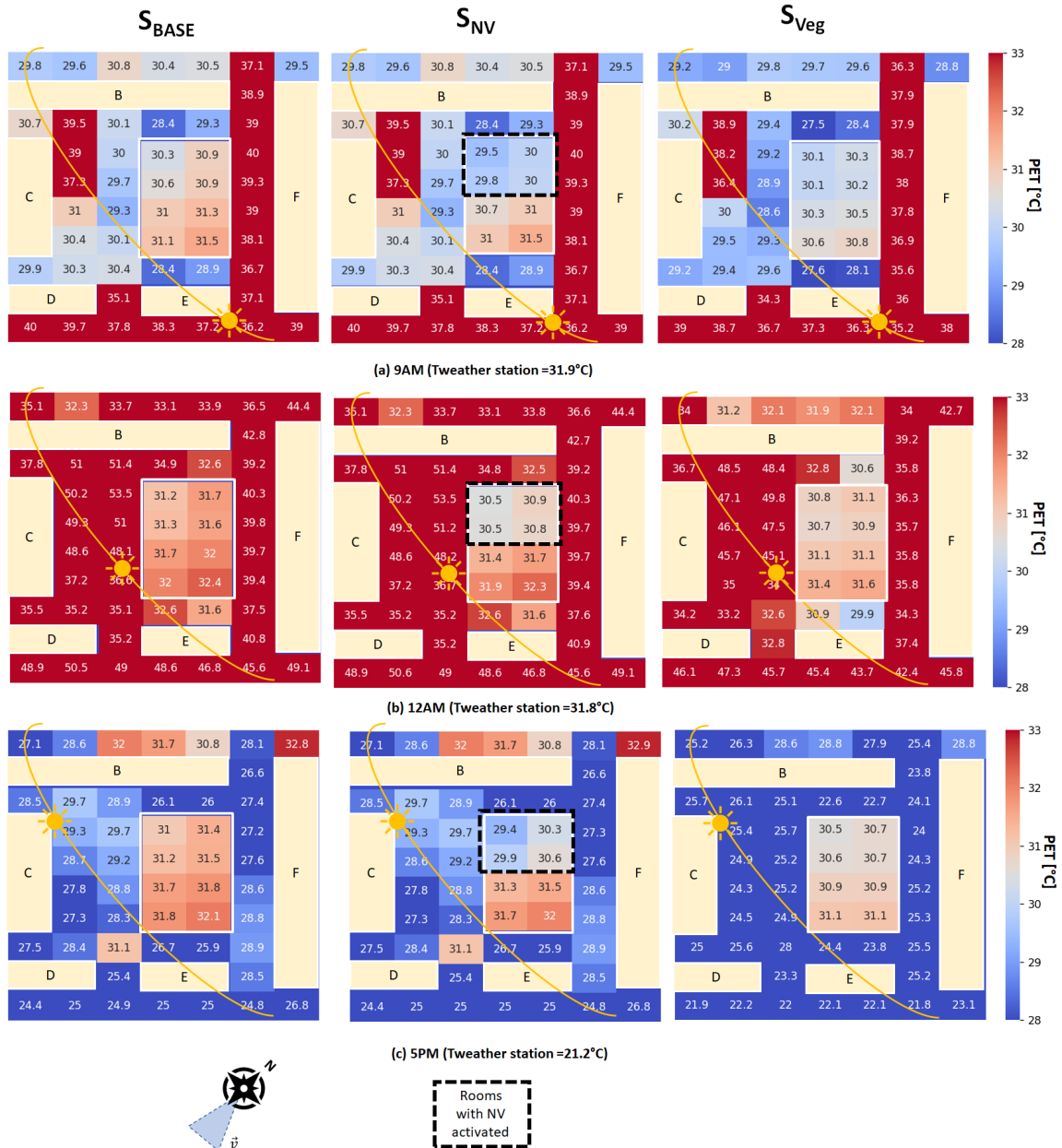


Figure 5.31: Pedestrian level and top floor PET spatial distribution for  $S_{Base}$  and  $S_{NV}$  and  $S_{Veg}$  at 9AM, 12AP and 5PM the 12th of August. Note: Sun position is purely indicative.

Figure 5.32 illustrates the evolution in indoor air temperature in Room R1 of the studied dwelling for the three different scenarios, spanning three consecutive days from August 12th to 15th. The figure highlights pronounced variations in indoor temperatures within the  $S_{NV}$  compared to the other two scenarios. These fluctuations align with changes in outdoor temperatures and could potentially lead to discomfort.

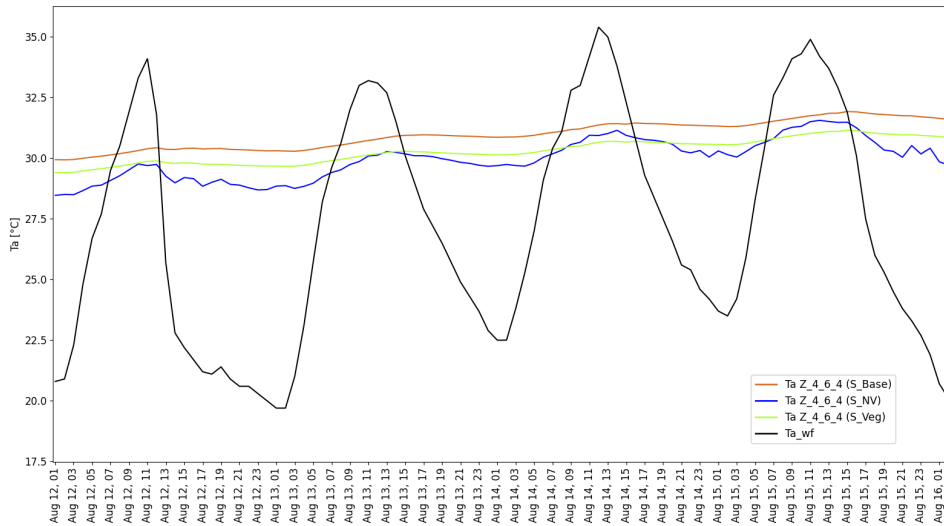


Figure 5.32: Weather station ( $T_{wf}$ ) air temperature and the air temperature in the R1 air-zone (Z\_4\_6\_4) from the 12th to the 15th of August 12 AM.

### 5.5.1.2 Daily heat stress and heat strain related to the individual displacement

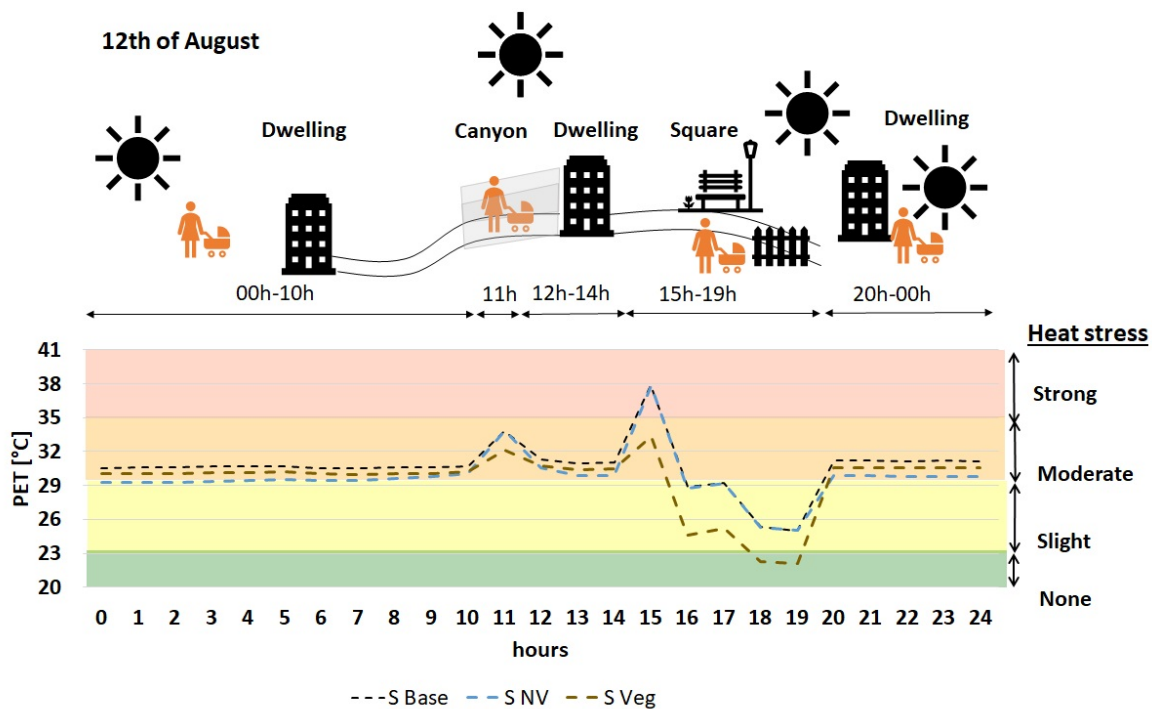


Figure 5.33: August the 12<sup>th</sup>. Comparison of the  $S_{Base}$ ,  $S_{NV}$  and  $S_{Veg}$  : PET evolution related to the dynamic path.

The displacement shown in Figure 5.18 is applied to both  $S_{NV}$  and  $S_{Veg}$ . Figure 5.33 shows that applying the  $S_{NV}$  scenario reduces indoor heat stress by about 1°C. Despite this reduction, the individual still experiences slight to moderate heat stress in the dwelling. However, implementing the  $S_{Veg}$  scenario decreases both outside and inside heat stress,

with a reduction reaching 4 °C during the period of strongest sunlight and with an average decrease of 2.1 °C. This adjustment places the individual in the slight to non heat at stress category from 6 PM to 7 PM.

Comparative analysis using heat strain indices can evaluate physiological stress progression from the  $S_{Base}$  scenario to the  $S_{Veg}$  scenario (Figure 5.34). Both scenarios trigger physiological reactions within recommended boundaries (Section 1.3.1). However, the  $S_{Veg}$  scenario elicits a more modest response with reduced impact on all physiological parameters. It should be noted that the implementation of  $S_{Veg}$  can also cause a skin temperature ( $T_{sk}$ ) increase beyond discomfort thresholds.

## 5.5.2 Seasonal analysis

As for the previous section, the seasonal analysis covers the period starting from June to September.

### 5.5.2.1 Global analysis

The global analysis looks at the  $HSD_{min}$  and  $HSD_{max}$  indices for all three scenarios, both at the pedestrian level and within the studied residence.

Figure 5.35 demonstrates that implementing natural ventilation ( $S_{NV}$ ) has no significant impact on outdoor PET distribution. However, it significantly reduces heat stress in the dwelling where it is in use (Figure 5.36). Replacing impervious soil with permeable soil ( $S_{Veg}$ ) effectively mitigates heat stress outdoors and to a lesser degree indoors due to the global reduction of air temperature and on the repercussion on the different floors of the building. In outdoor areas, the number of cases with at least one pedestrian-level zone with a PET exceeding  $> 29^{\circ}\text{C}$  reduces from 31% (in the  $S_{Base}$  scenario) to 26% when  $S_{Veg}$  is used throughout the summer. At the top floor of the studied dwelling, instances of zones with a PET over  $29^{\circ}\text{C}$  decrease from 49% to 36% with  $S_{Veg}$ , and further drop to 31% with  $S_{NV}$ .

### 5.5.2.2 Spatial analysis

The spatial analysis emphasizes the advantages of both the  $S_{NV}$  and  $S_{Veg}$  scenarios according to chosen indices  $OhD_{max}$ ,  $OhI_{max}$ ,  $Oh_{max}$  and  $Oh_{mean}$ .

When comparing outdoor analysis at the pedestrian level, we only consider  $S_{Veg}$  and  $S_{Base}$  (Figure 5.37) since  $S_{NV}$  does not significantly affect outdoor heat stress.

The  $S_{Veg}$  reduces the  $OhD_{max}$  by 1 to 6 hours, depending on the area. This benefit is most noticeable in less shaded regions where evaporation potential is higher due to the bare soil model used. This is also seen in the  $OhI_{max}$  reduction, which reaches  $34.6^{\circ}\text{C h}$ , and in the  $Oh_{mean}$  reduction, which reaches  $0.6^{\circ}\text{C}$  in zone Z\_2\_6\_1. The  $S_{Veg}$  scenario similarly results

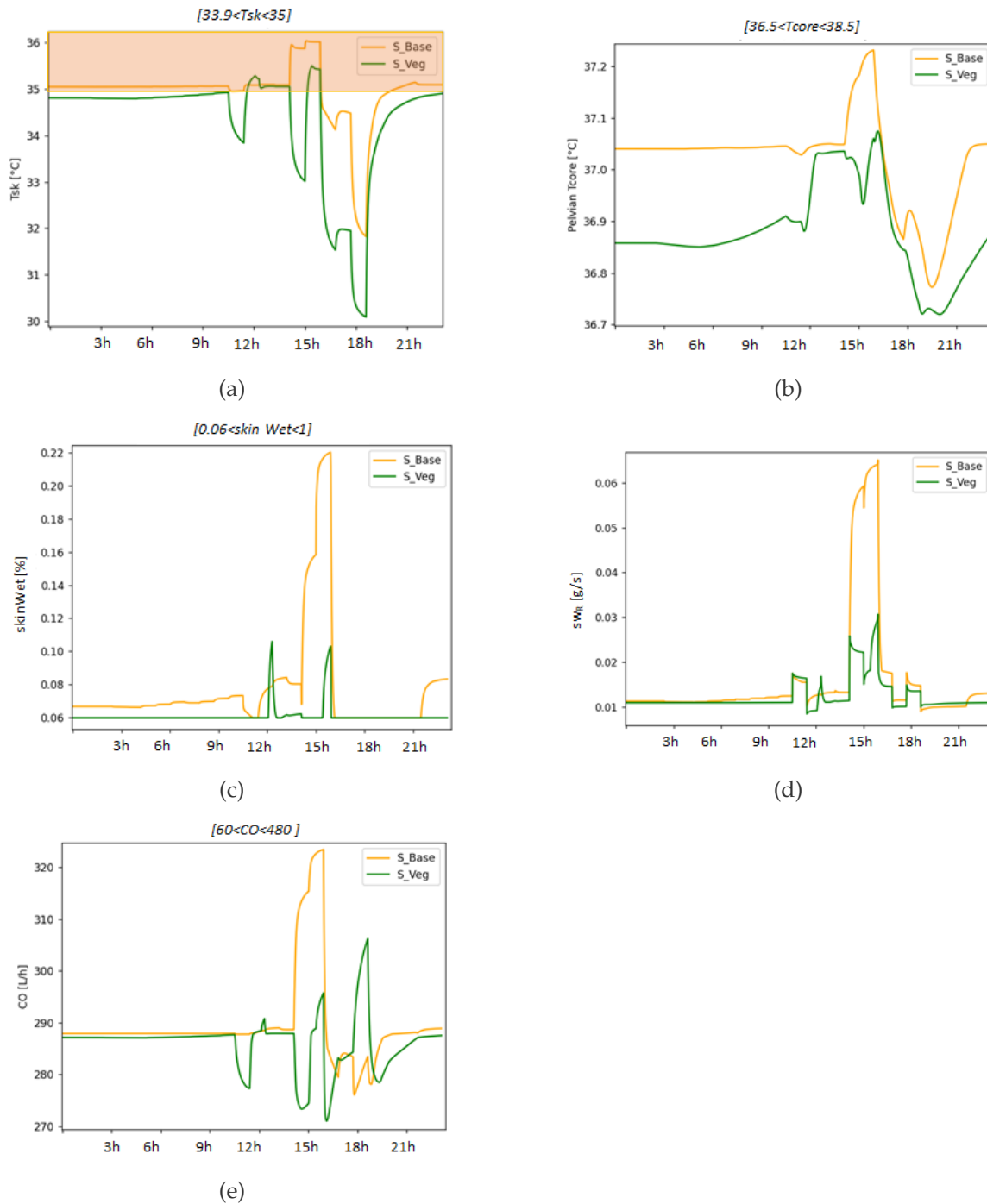


Figure 5.34: Comparison of heat strain response corresponding to the exposure path of Figure 5.20 for  $S_{Base}$  and  $S_{Veg}$ : (a)  $T_{sk}$ , (b)  $T_{core}$ , (c)  $SkinWet$  (d)  $sw_R$ , (e)  $CO$ .

in a reduction of  $Oh_{max}$  by up to 5 °C in areas exposed to more wind (Z\_3\_3\_1 to Z\_3\_7\_1) due to the positive effect of wind on potential evaporation.

Natural ventilation on the top floor, as depicted in Figure 5.38, reduces heat stress in all rooms of the dwelling. The average overheating degrees proportionately decrease by a factor of two to four, although the differences in the maximum overheating degrees are

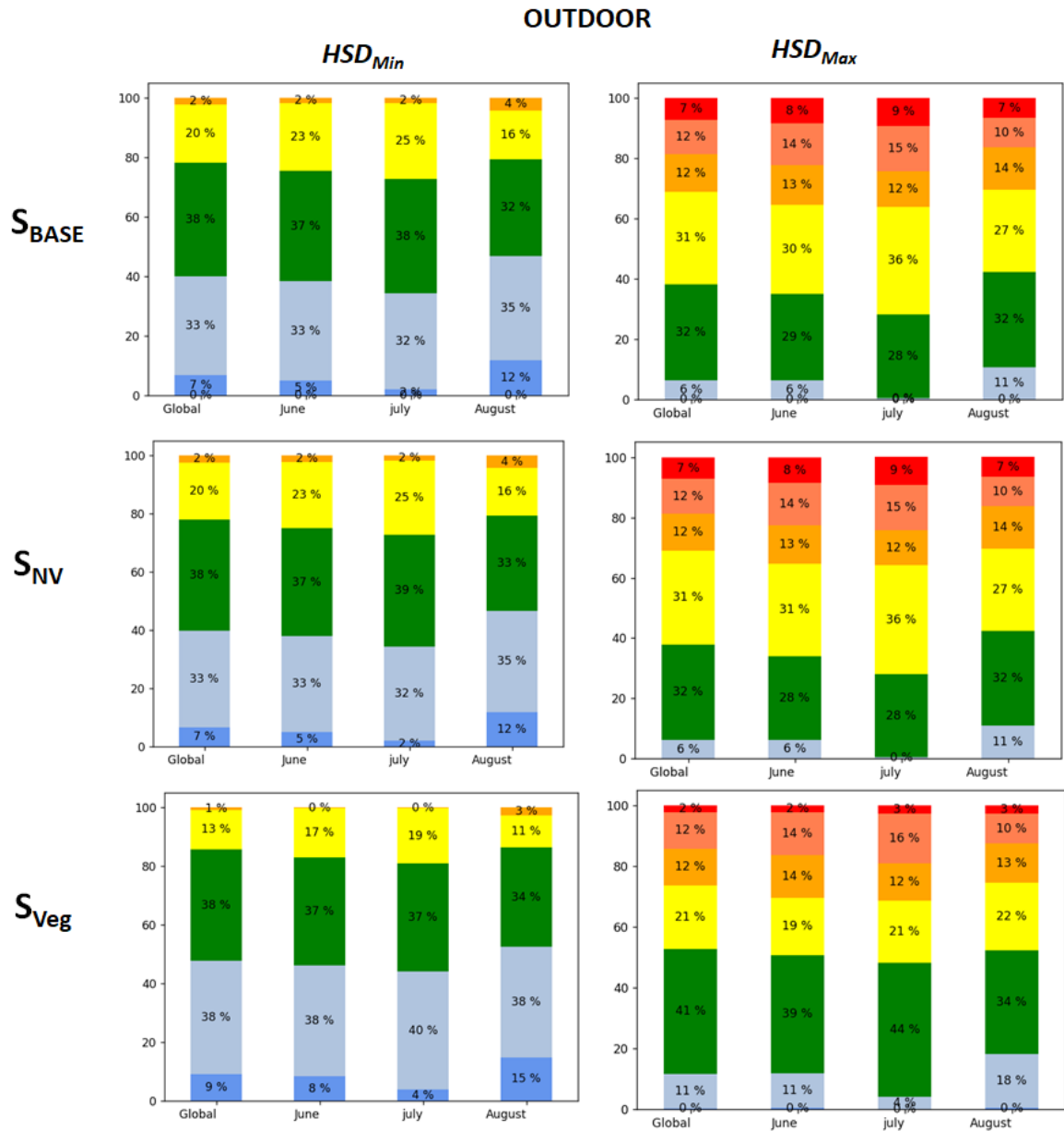


Figure 5.35: Outdoor  $HSD_{min}$  and  $HSD_{max}$  for the  $S_{Base}$  and  $S_{NV}$  and  $S_{Veg}$ .

less significant. This is because the natural ventilation in the  $S_{NV}$  operates uninterrupted, even when the outside temperature is higher than indoors, which can unintentionally cause temperature increases in the dwelling. This effect is exemplified in Figure 5.32 on the 14th of August. This figure highlights the larger temperature fluctuations within the  $S_{NV}$ .

The assumption of continuous natural ventilation can often apply to real-life scenarios, where real-time management of aperture opening and closing based on outside temperatures can be challenging. Figure 5.32 illustrates that the advantages of natural ventilation predominantly benefit the areas directly exposed to it. The daily analysis reveals that the presence of bare soil ( $S_{Veg}$ ), albeit to a lesser extent, mitigates heat stress on the top floor's entirety. The reduction is distributed uniformly.

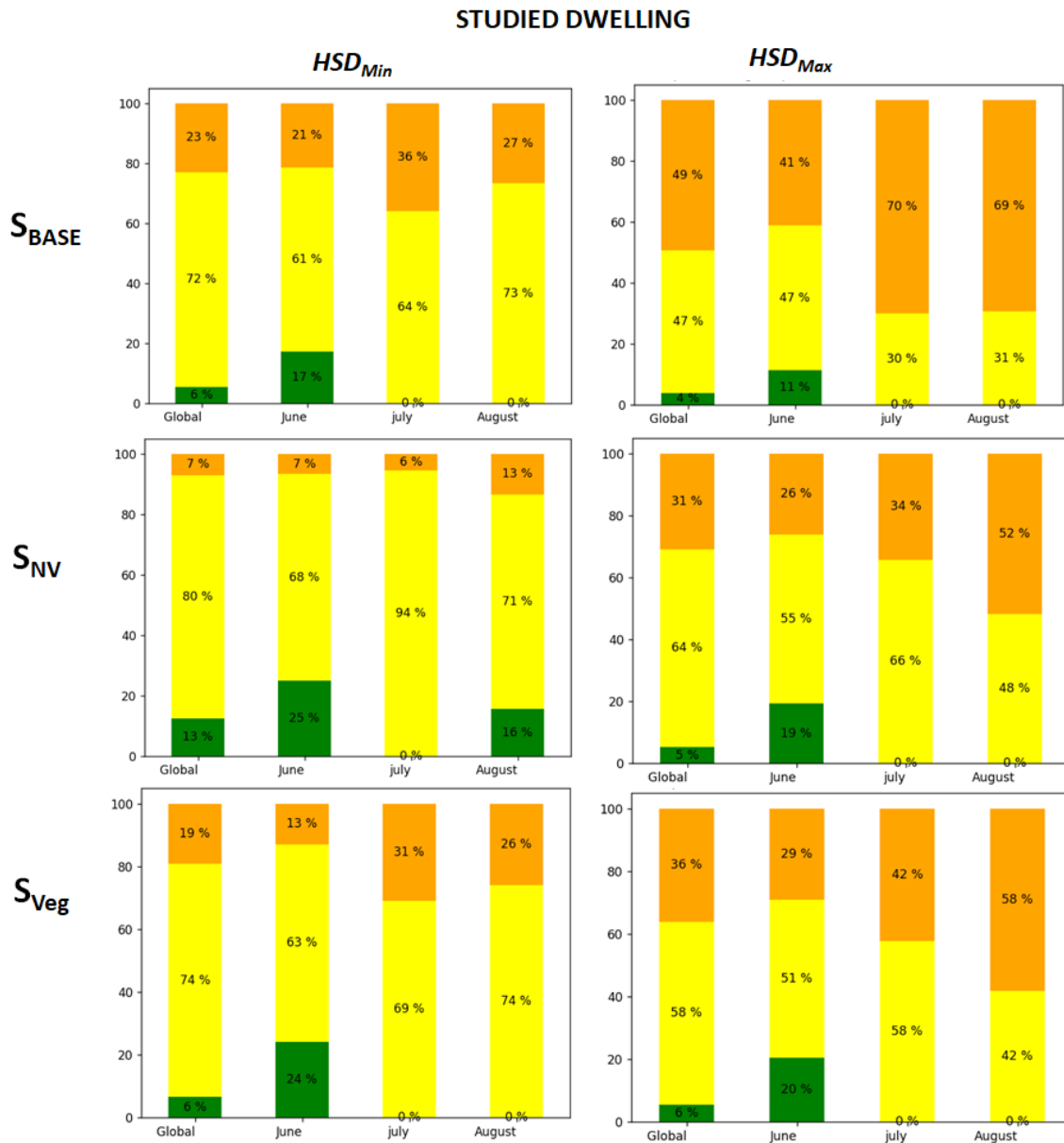


Figure 5.36: Studied dwelling  $HSD_{min}$  and  $HSD_{max}$  for the  $S_{Base}$ ,  $S_{NV}$  and  $S_{Veg}$ .

### 5.5.3 Conclusions on cooling strategy effects

The comparison between cooling strategies underscores the overall advantages of substituting a non-permeable floor with a permeable one and the localized benefits of natural ventilation. The effect of permeable soil is most noticeable at the pedestrian level, while a small decrease in indoor air temperatures is evident across all air zones. Heat peaks are also considerably diminished. These outcomes rely on the premise that the existing soil model continually offers an evaporation potential and that the soil is never completely parched. If the soil becomes excessively dry, the evaporation potential will decrease significantly. This specific situation needs experimental evaluation to be effectively taken into consideration in the current soil model. Another reason to exercise caution with these results concerns



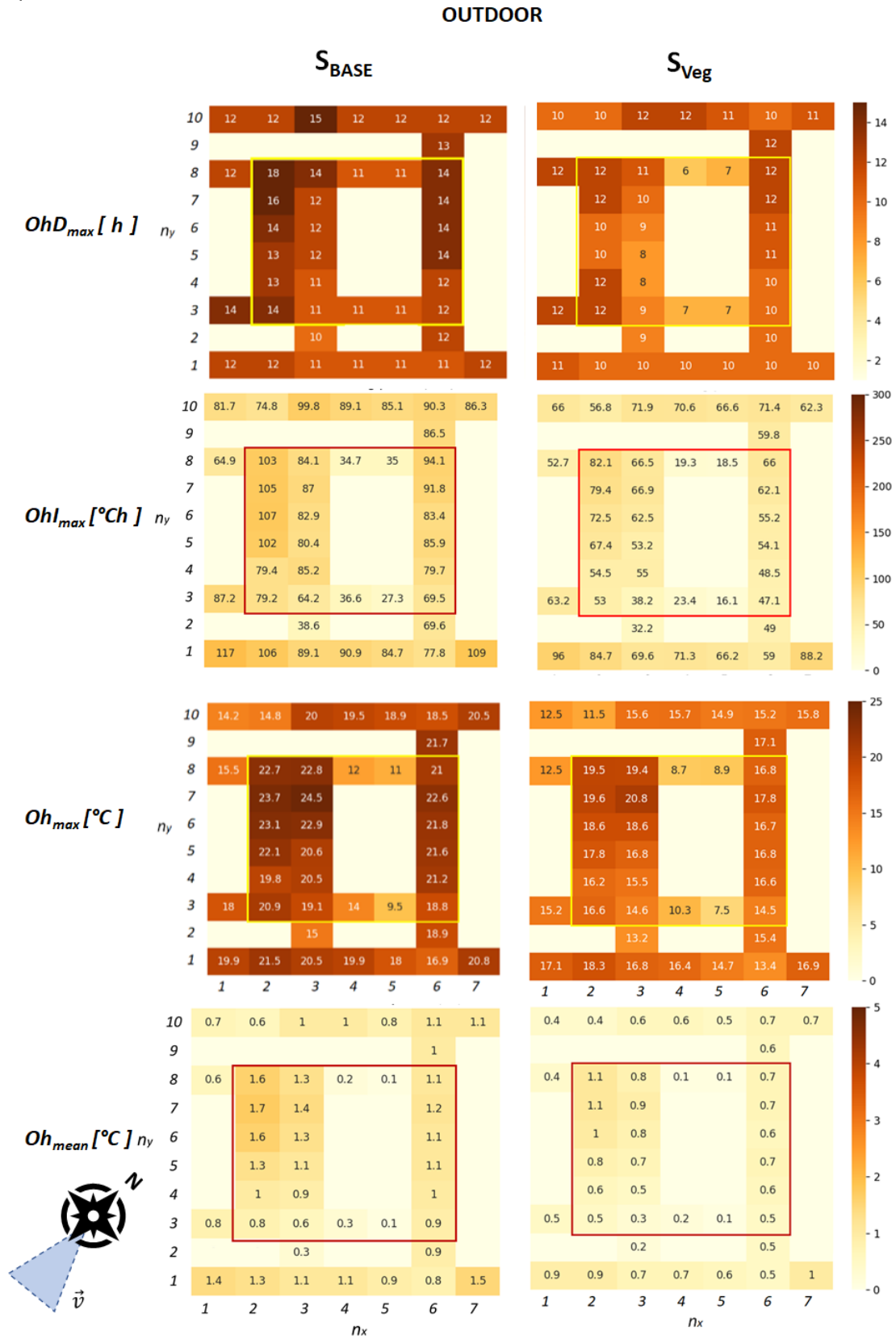


Figure 5.37:  $OhD_{max}$ ,  $OhI_{max}$ ,  $Oh_{max}$  and  $OhD_{mean}$  at pedestrian level for the  $S_{Base}$  and  $S_{Veg}$ .

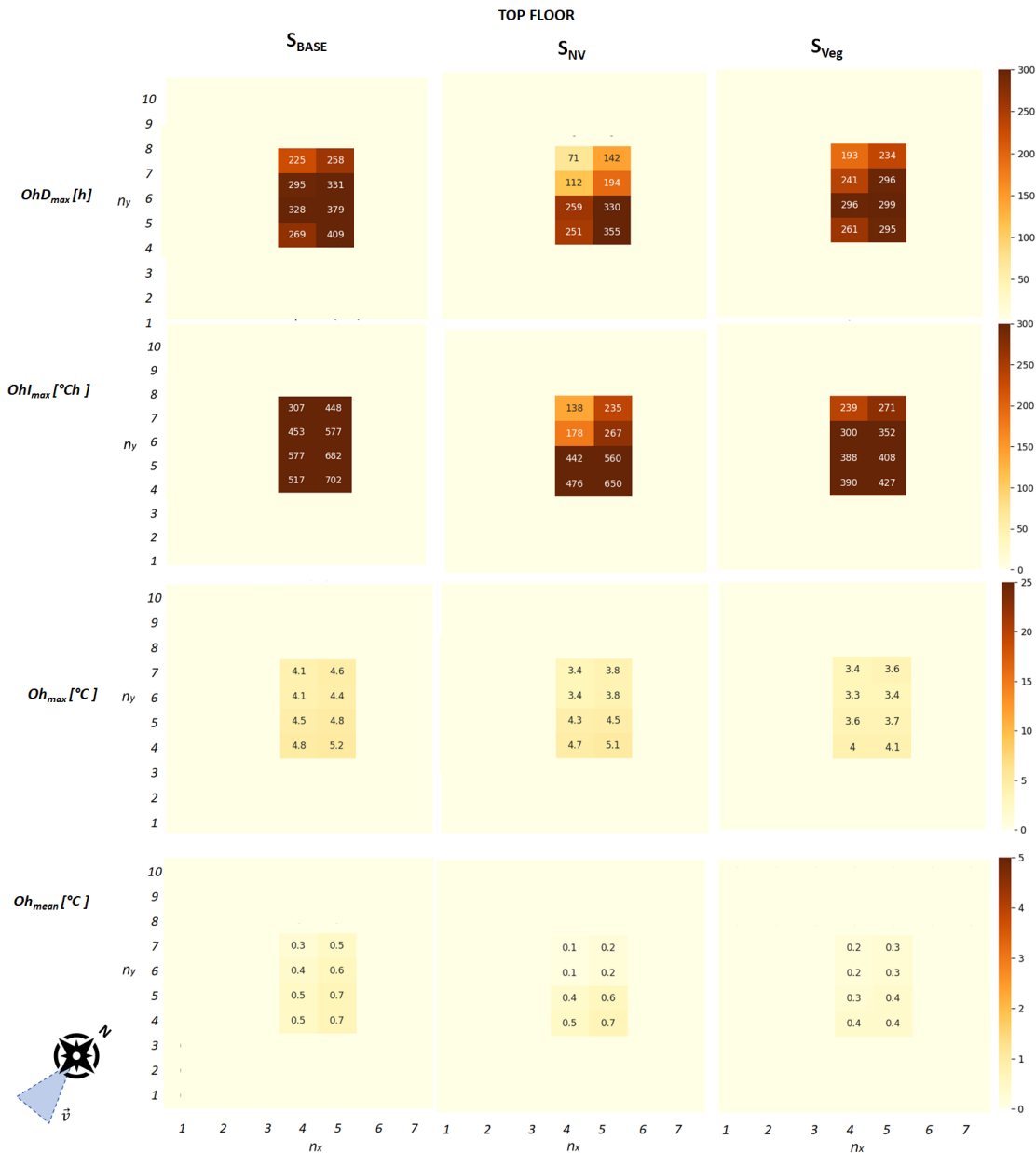


Figure 5.38:  $OhD_{max}$ ,  $OhI_{max}$ ,  $Oh_{max}$  and  $OhD_{mean}$  at the top floor for the  $S_{Base}$ ,  $S_{NV}$  and  $S_{Veg}$ .

the adopted natural ventilation scenario, which overlooks the actual user's behaviour in their dwelling, significantly impacting the indoor thermal environment. Despite these limitations, the analysis remains valuable as it facilitates a comparison of the efficacy of layout adjustments independent of user actions (e.g., floor permeabilization, tall vegetation) and provides an opportunity to test certain proof of concepts. Finally, the indices used are sensitive to the temperature threshold defined for overheating. An analysis of temperature distributions would also be interesting to conduct in certain critical areas.

## 5.6 Conclusions

The case study on Ydeal Square, evaluated in this chapter, underscores the relevance of the modelling approach, outlined in part II of the thesis, that couples a McZM model with a BEM.

An initial analysis contrasts indoor temperatures derived from the McZM model with those derived from simplified boundary condition assumptions on the  $h_c$  and the outdoor air temperature. The findings underscore the non-neglectable impact of boundary condition assumptions on indoor air temperatures in an insulated building and the importance of having an estimation of boundary conditions as close to reality as possible.

The primary focus of this chapter is the evaluation of heat stress and heat strain. Heat stress is examined through the Eulerian exposure approach on a daily and seasonal basis and also through the Lagrangian exposure approach, but only daily. On the other hand, the analysis of heat strain solely utilises the Lagrangian exposure approach on a daily basis.

The different levels of these analyses highlight the advantages of a spatial approach, both indoors and outdoors. The selected zoning shapes and resolutions highlight temperature gradients between zones. The spatial distribution of  $T_{mrt}$  further emphasizes the need for spatial discretization of areas exposed to heat in order to evaluate individual heat stress more effectively.

Analyzing the spatial representation of thermal environments daily allows us to model the impact of a person's movement on heat stress and heat strain using the Lagrangian approach. However, this analysis necessitates information about the person's movements and behaviour, such as their activity, clothing, and hydration level, which are typically unknown.

In addition, for heat strain assessment, it is difficult to draw conclusions solely on the basis of the selected physiological indices from the JOS-3 model. However, those indices can be used for comparative purpose when assessing the impacts of cooling measures.

These indices can be used to compare the effects of cooling measures. The daily analysis using the Eulerian exposure approach shows heat stress developments throughout the day in a specific location. It identifies areas with minimum or maximum heat stress every hour. This approach is particularly helpful in studying heat stress distribution during the hottest days and comparing the benefits of heat stress distribution while implementing cooling strategies.

The seasonal analysis emphasizes the varied levels of overheating in different areas, using specific indices that provide information on the longest, most intense, and average periods of overheating. It is observed that areas with the longest average duration of heat stress also experience the highest intensity and peaks. A cooling scenario may prove more interesting than another depending on the comparison index used. The index measuring the peak

favors the  $S_{Veg}$  over the  $S_{NV}$ .

The outdoor analysis at pedestrian level reveals significant solar influence on heat stress assessment in both daily and seasonal contexts. The effect of wind flow on heat stress is more evident in day-to-day analysis, where areas between buildings with lower wind speeds experience increased heat stress.

The indoor analysis currently focuses on rooms within the same floor, but it could also apply to other floors. It identifies areas that are consistently cooler due to less exposure to sunlight. The average overheating calculation demonstrates minimal variation between different zones on the same floor. However, differences between zones are more noticeable when at peak levels.

This chapter effectively illustrates the value of the McZM modelling approach in comparing the advantages of various cooling strategies in relation to heat stress. The outdoor cooling strategy, which involves replacing impervious soil with bare soil, offers dual benefits, both outdoors and indoors. Outdoors, the areas that demonstrate the most substantial decreases in overheating intensity and average values are those that receive the most sunlight. Indoor benefits are most pronounced in regions exposed to the east, which were initially the most stressed. These areas show the most considerable reduction in the maximum duration and intensity of overheating, as well as the highest and average values. As for the indoor cooling strategy, using natural ventilation in the targeted dwelling successfully reduces heat stress and overheating. However, this effect is largely confined to the specific dwelling, with limited impact on the top floor and no noticeable effect outdoors.

# General conclusion and enlarged perspectives

## General summary and conclusions of the work

Adapting to rising city temperatures is a significant challenge considering global warming and the growing frequency and intensity of heatwaves. Cities with dense buildings and extensive urbanization often experience the UHI effect, leading to higher temperatures than rural areas. This urban overheating, which includes the UHI effect and thermal discomfort, not only affects comfort but also public health, as higher outdoor temperatures are closely linked to increased morbidity and mortality rates.

The thesis focuses on modelling thermal environments at the dwelling and block scale to assess heat stress over daily and seasonal exposure periods and considering the mutual indoors and outdoors interactions. Key question includes understanding the influence of buildings and their surroundings on heat stress and identifying heat shelters or critical zones.

The specific problem consists on developing and coupling a microclimate zonal model (McZM) with a building energy model (BEM) in order to provide a spatial representation of the heat stress over both seasonal and daily period. The modelling approach being used should allow for both Eulerian (location-based) and Lagrangian (individual movement-based) exposure assessments for heat stress.

First, we introduce the concepts of heat stress, which refers to heat load, and heat strain, which describes the physiological and psychological responses to heat load (chapter 1). A biometeorological index analysis guides us to choose the PET index for heat stress assessment, yet also reveals its limitations. Chiefly, it fails to account for individual responses in heat stress assessments, and its applicability is limited to steady environments.

An analysis of the sensitivity of PET to climatic variables and its practicality in evolving environments is examined for definite thermal conditions. This aids in recognizing the climatic variables needed to create models and the spatio-temporal scales to be considered. Also, the usage of universal and localized PET-based indices is put forward. Indices for thermal, hydration, and cardiovascular physiological strain are included for immediate heat

strain analysis using the JOS-3 thermoregulation model.

In chapter 2, we examine key factors impacting urban climate, including urban and building cooling solutions and related physical phenomena. This analysis helps define the requirements for numerical modelling in heat stress assessment. The review of existing urban canopy models (UCMs), microclimate models (McMs), BEMs and radiative models reveals that there is no customised approach for providing a spatial assessment of heat stress seasonally, both indoors and outdoors. The specific problem of the thesis is then introduced and a modelling strategy is suggested.

To minimize computational time, we've separated the modelling strategy into two stages. The first is a pre-processing stage that handles calculations for airflow and radiative heat fluxes. The second, a dynamic simulation stage, deals with energy balance computations. We employ a simplified model for the solar calculation. It uses the ray tracing method and interpolates values of the sun's path. For the outdoor airflow model, a zonal model is developed. This model relies on a predictive mass flow rate model, which interpolates from a data set of mass flow rates. These mass flow rates are derived from steady CFD simulations conducted under varying wind speeds and directions. The CFD simulations utilise a RANS  $rk - \varepsilon$  turbulence model and a standard wall function. From these simulations, predictive models are developed to estimate average outdoor wind speed, external convective heat transfer coefficients, and pressure coefficients in each airzone. These estimates are averaged over the building and soil surfaces.

The dynamic simulation stage uses the Dymola environment to dynamically solve the energy balance in the combined McZM and BEM, employing the BuildSysPro library. At this stage, if natural ventilation is an option, an additional indoor airflow model can be integrated. Lastly, a post-processing stage is introduced to compute the outdoor mean radiant temperature ( $T_{mrt}$ ) along with the daily and seasonal heat stress and strain indices.

The global modelling approach is implemented using the MyBEM toolchain. MyBEM comes with a solar model, LWR model, BEM, and specific Python packages for automatic BEM generation. The thesis introduced two new models: the indoor airflow model and the McZM, which encompasses an energy balance model, zonal airflow model, soil model, and mean radiant temperature model.

Chapter 3 details the outdoor airflow modelling method and validates the CFD simulations. This method encompasses defining the experiment's design for the CFD simulation, executing said simulations, and generating an automatic outdoor zoning that aligns with the building's airflow zones. This is followed by implementing a mass balance approach and choosing the best predictive model for specific variables (namely  $mfr$ ,  $h_{c_{ext}}$  and  $cp$ ). The most successful predictive model, in this case, was linear interpolation. These coupling variables ( $mfr$ ,  $h_{c_{ext}}$  and  $cp$ ) are used during the dynamic simulation to calculate heat exchange through advection and convective methods. One of the main limits of this model is to not consider the buoyancy effects on airflow motion and the turbulence. In fact, only effect of

---

turbulence on the flow motion are considered.

The validity of the CFD simulations is suggested through the reproduction of a numerical simulation for heat transfer coefficient calculations and the replication of wind tunnel experiment results for airflow through isolated parallelepiped shapes and porous media. 3 introduces an indoor pressure-based airflow model. The model equations and the interconnection between indoor and outdoor airflow models are verified through a comparison with the CONTAM model.

The remaining model components, including the radiative models, BEM, soil model, and outdoor mean radiant temperature models, are outlined in chapter 4. The radiative models and outdoor  $T_{mrt}$  models are weighed against equivalent, validated models. We confirm the soil model's consistency by comparing it with experimental measurements and verifying it against other established models.

Chapter 5 outlines a case study that applies the modelling approach to the Ydeal Square block in Lyon Confluence. It primarily analyzes heat stress, assessing its impact under daily and seasonal exposure. The study is conducted from both Eulerian and Lagrangian perspectives, demonstrating the advantages of a zoning approach.

Analyzing heat stress daily with the Eulerian approach showcases how urban forms, such as fabric, cover, and structure, impact resulting thermal conditions. It underscores the necessity of spatially modelling thermal conditions in diverse urban environments and validates the selection of zonal form and resolution. It is evident that cool zones regularly appear between closely spaced buildings. An in-depth seasonal analysis of heat stress using the Eulerian approach allowed us to pinpoint areas with increased and prolonged overheating, assessed through various indices like duration, intensity, peak, and average overheating.

Indoor areas facing east are typically the most stressed, while outdoors, areas with the least shade experience the most stress. Therefore, solar exposure profoundly influences heat stress assessments. Wind flow also contributes to heat exchange, but its effect is less apparent over a season. Instead, its impact is more noticeable on a daily scale.

Cooling strategies such as natural ventilation are effective within the specific housing units where they're applied, but they do not impact the external environment. On the other hand, replacing non-permeable outdoor soil with permeable one benefits every housing unit despite the overall reduction in heat stress being less substantial.

For the analysis of heat stress associated with a location, it can be concluded that the modelling approach developed in this thesis allows for the modelling of the diversity of thermal environments highlighting the most stressed areas. It also allows the comparison of heat stress distribution when cooling strategies are implemented, enabling a qualitative evaluation of their efficacy.

The Lagrangian approach allows for daily evaluations of an individual's heat stress

across varying environments. This demonstrates the importance and need for progressive modelling, combining thermal conditions and personal movement.

In conclusion, this study highlights the importance of a modelling approach that combines McZM and BEM for seasonal and daily heat stress assessment.

It suggests a McZM that tackles the modelling challenges identified in deploying an outdoor airflow zonal model. This model has the ability to consider the effects of urban geometry, accommodate changes in wind speed and direction, offer proper zoning form and resolution, and provide thermal and airflow coupling between indoor and outdoor environments.

Furthermore, it has shown the added value of a spatial modelling approach in heat stress assessment and demonstrated the capability of the coupled McZM and BEM model to model commonly adopted cooling practices in the dwelling and certain observed practices outdoors (e.g. evaporative soil).

However, improvements are necessary. The perspectives of research are presented in the following section.

## **Enlarged perspectives of research**

This thesis is framed within the context of another research project in the social sciences field. The previous project sought to discern the challenges and enablers experienced by Lyon residents while implementing adaptive strategies during heatwaves, as determined through a field survey. Examining the results of this field survey alongside the cooling measures detailed in current BEMs has illuminated wider research perspectives on the modelling techniques employed for buildings and microclimate. A summary of the primary findings from the survey and comparative analysis can be found in I. The research outlook gleaned from the thesis and fieldwork is as follows:

### **From a static to a dynamic approach in modelling exposure environments**

Two research perspectives highlight the constraints of heat stress evaluation via frequently used steady indices in academic papers. The steady approach is apt for environments where dominant climatic parameters, including air temperature and mean radiant temperature, evolve slowly compared to physiological responses. However, this method proves ineffective for rapid fluctuations in exposure environments. Therefore, using dynamic indices is more effective for assessing heat stress related to a moving individual.

The first research approach involves evaluating an individual's heat stress by considering their movements over extended periods and larger spatial scales. This takes into account the interaction between the individual and their environment, prompting inquiries about



---

modelling a series of outdoor environments. It calls for the integration of agent-based models — which account for the interaction between the agent and its environment – alongside BEMs and McM.

The second research approach entails assessing heat stress through dynamic indices using transient thermoregulation models.

### **Long-term cumulative health effects on individuals and the contribution of thermal environment modelling in this assessment**

Existing thermoregulation models have demonstrated limitations, especially in terms of the duration of exposure covered, which is typically only a few days. A third research perspective is to study the cumulative effects of prolonged exposure to high temperatures over a season, focusing on resulting heat strain. This is important in understanding the impact of overexposure on the acclimatization process and thermoregulatory disorders. This field of study goes beyond traditional engineering sciences and could benefit from multidisciplinary research. This would connect long-term modelled climatic variables with health effects on different types of people and help establish more appropriate indices for extended exposures.

### **Improvement and development of new models to be integrated into the McZM**

To better understand the benefits of a multizone microclimate modelling approach, it would be insightful to compare its impact on heat stress with that of a monozone modelling approach, which uses a single temperature node for outdoor air. The same spatial breakdown of surfaces should be maintained for an accurate comparison of spatially resolved surface balances.

A fourth research perspective aims to enhance the models used in the McZM. Currently, the McZM only models impervious, bare, and low-vegetated soils. Moreover the latter has not been validated. Current soil models do not factor in the effects of high vegetation like trees on radiative heat exchanges, airflow, or other cooling strategies. These cooling strategies include methods adopted by cities, such as green roofing and water-based cooling solutions, revealing another research opportunity.

The fifth research perspective focuses on incorporating buoyancy into the McZM. Currently, the McZM is limited to scenarios where wind-driven forces supersede buoyancy-driven forces. Therefore, it is not appropriate to study flow in enclosed courtyards. This highlights the need to explore outdoor buoyancy modelling methods and how they can be integrated into zonal modelling approaches.

The sixth research perspective relates to the integration of the McZM with larger-scale models, such as mesoscale models, Urban Boundary Layer (UBL) models, or UCM. This integration aims to ensure consistency across data collected from meteorological stations

situated far from the research site. One typical limitation of the McZM, and microclimate models in general, is their capability to precisely predict boundary conditions at the edges of the domain. This thesis assumes that the climatic conditions at the domain's boundaries match the values from a nearby weather station.

### **Validating the entire McZM and BEM toolchain**

The seventh research perspective aims to validate the entire McZM using suitable experimental protocols and compare it against other validated models. Collaborative projects, like the ongoing DIAMS project, provide a platform for comparative evaluations of microclimate models in conjunction with building models.

### **Evolution of BEMs in regards of changing adaptive measures**

The local survey about measures individuals adopt during periods of overheating points out shortcomings in BEMs ability to capture the impact of individual behaviour while modelling thermal environments. These limitations stem from a poor understanding of personal behaviours in homes, such as opening windows, closing shutters, the presence of heat sources, and the use of air conditioning. Additionally, these behaviours are influenced by individual and social factors that affect how people perceive and respond to heat stress and strain. Other elements, such as economic, regulatory, and governance constraints, also impact the implementation of cooling strategies. A suggested area for further research is incorporating behavioural models into BEMs.

A limitation of current BEMs is their inability to accurately model the thermal effects associated with individuals' cooling strategies, such as evaporative cooling through wet laundry and indoor evaporative cooling via water evaporation on the ground or opening windows with mosquito nets. Consequently, a potential area of exploration could be the identification of these personal cooling strategies and the modelling of their impact on the thermal environment.

# Bibliography

- 3787, VDI (1998). "Environmental Meteorology, Methods for the human biometeorological evaluation of climate and air quality for the urban and regional planning at regional level. Part I: Climate". In.
- Abreu-Harbach, Loyde V., Lucila C. Labaki, and Andreas Matzarakis (June 2014). "Thermal bioclimate as a factor in urban and architectural planning in tropical climates—The case of Campinas, Brazil". en. In: *Urban Ecosystems* 17.2, pp. 489–500. issn: 1083-8155, 1573-1642. doi: [10.1007/s11252-013-0339-7](https://doi.org/10.1007/s11252-013-0339-7). url: <http://link.springer.com/10.1007/s11252-013-0339-7> (visited on 09/01/2023).
- ADEME (2017). *Diagnostic de la surchauffe urbaine - Méthodes et applications territoriales*. isbn: 979-10-297-0923-4.
- ADEME, CEREMA (Apr. 2021). "Rafraîchir les villes, des solutions variées". In.
- Allagnat, Malou (2020). "— « MÉTHODES ESTIVALES » : HABITER SAINT-PRIEST EN PÉRIODES DE FORTES CHALEURS". fr. In.
- Allen, R.G, L.S Pereira, and M Smith (1988). *Crop evapotranspiration —guidelines for computing crop water requirements*. Rome: Food and Agriculture Organization. url: <http://www.fao.org/docrep/x0490e/x0490e00.htm>.
- Allen, Richard G. et al. (1989). *Operational Estimates of Reference Evapotranspiration*.
- Amengual, A. et al. (Aug. 2014). "Projections of heat waves with high impact on human health in Europe". en. In: *Global and Planetary Change* 119, pp. 71–84. issn: 09218181. doi: [10.1016/j.gloplacha.2014.05.006](https://doi.org/10.1016/j.gloplacha.2014.05.006). url: <https://linkinghub.elsevier.com/retrieve/pii/S0921818114001015> (visited on 04/11/2023).
- Aubinet, M (1994). "Long wave sky radiation parametrization". en. In: *Solar Energy*.
- B., Givoni (1963). "Estimation of the effect of climate on man. Development of a new thermal index". en. In: *Building Research Station Report, Technion, Haifa, Israel*, 145 pp.
- Baxevanou, Catherine, Dimitris Fidaros, and Aris Tsangrassoulis (2017). "Management of Natural Ventilation in High-Rise Building – a CFD Study". en. In: *Procedia Environmental Sciences* 38, pp. 428–435. issn: 18780296. doi: [10.1016/j.proenv.2017.03.128](https://doi.org/10.1016/j.proenv.2017.03.128). url: <https://linkinghub.elsevier.com/retrieve/pii/S1878029617301329> (visited on 06/06/2023).
- Becker, Stefan, Oded Potchter, and Yaron Yaakov (Sept. 2003). "Calculated and observed human thermal sensation in an extremely hot and dry climate". en. In: *Energy and Buildings* 35.8, pp. 747–756. issn: 03787788. doi: [10.1016/S0378-7788\(02\)00228-1](https://doi.org/10.1016/S0378-7788(02)00228-1). url: <https://linkinghub.elsevier.com/retrieve/pii/S0378778802002281> (visited on 04/15/2023).

- Bergman, T. L., ed. (2011). *Introduction to heat transfer*. en. 6th ed. OCLC: ocn739732416. Hoboken, NJ: Wiley. isbn: 978-0-470-50196-2.
- Bittelli, Marco et al. (Dec. 2008). "Coupling of heat, water vapor, and liquid water fluxes to compute evaporation in bare soils". en. In: *Journal of Hydrology* 362.3-4, pp. 191–205. issn: 00221694. doi: [10.1016/j.jhydrol.2008.08.014](https://doi.org/10.1016/j.jhydrol.2008.08.014). url: <https://linkinghub.elsevier.com/retrieve/pii/S0022169408004290> (visited on 07/04/2022).
- Blazejczyk, Krzysztof et al. (May 2012). "Comparison of UTCI to selected thermal indices". en. In: *International Journal of Biometeorology* 56.3, pp. 515–535. issn: 0020-7128, 1432-1254. doi: [10.1007/s00484-011-0453-2](https://doi.org/10.1007/s00484-011-0453-2). url: <http://link.springer.com/10.1007/s00484-011-0453-2> (visited on 10/26/2022).
- Blocken, B. et al. (Dec. 2009). "High-resolution CFD simulations for forced convective heat transfer coefficients at the facade of a low-rise building". en. In: *Building and Environment* 44.12, pp. 2396–2412. issn: 03601323. doi: [10.1016/j.buildenv.2009.04.004](https://doi.org/10.1016/j.buildenv.2009.04.004). url: <https://linkinghub.elsevier.com/retrieve/pii/S0360132309001000> (visited on 06/20/2022).
- Blocken, Bert (Sept. 2015). "Computational Fluid Dynamics for urban physics: Importance, scales, possibilities, limitations and ten tips and tricks towards accurate and reliable simulations". en. In: *Building and Environment* 91, pp. 219–245. issn: 03601323. doi: [10.1016/j.buildenv.2015.02.015](https://doi.org/10.1016/j.buildenv.2015.02.015). url: <https://linkinghub.elsevier.com/retrieve/pii/S0360132315000724> (visited on 04/05/2022).
- Blocken, Bert, Ted Stathopoulos, and Jan Carmeliet (Jan. 2007). "CFD simulation of the atmospheric boundary layer: wall function problems". en. In: *Atmospheric Environment* 41.2, pp. 238–252. issn: 13522310. doi: [10.1016/j.atmosenv.2006.08.019](https://doi.org/10.1016/j.atmosenv.2006.08.019). url: <https://linkinghub.elsevier.com/retrieve/pii/S135223100600834X> (visited on 07/02/2021).
- Bouquerel, Mathias et al. (2019). "Building Energy Modeling at District Scale Through BIM Based Automatic Model Generation – Towards Building Envelope Optimization". en. In: Rome, Italy, pp. 3676–3683. doi: [10.26868/25222708.2019.211008](https://doi.org/10.26868/25222708.2019.211008). url: [http://www.ibpsa.org/proceedings/BS2019/BS2019\\_211008.pdf](http://www.ibpsa.org/proceedings/BS2019/BS2019_211008.pdf) (visited on 05/15/2023).
- Bouquerel, Mathias et al. (Sept. 2021). "Application of MyBEM, a BIM to BEM platform, to a building renovation concept with solar harvesting technologies". en. In: doi: [10.26868/25222708.2021.30153](https://doi.org/10.26868/25222708.2021.30153). url: [https://publications.ibpsa.org/conference/paper/?id=bs2021\\_30153](https://publications.ibpsa.org/conference/paper/?id=bs2021_30153) (visited on 12/20/2022).
- Bouyer, Julien et al. (2009). "Mitigating Urban Heat Island Effect by Urban Design: Forms and Materials". en. In:
- Bozonnet, Emmanuel (2005). "Impact des microclimats urbains sur la demande énergétique des bâtiments - Cas de la rue canyon". fr. In:
- Brager, Gail S. and Richard J. de Dear (Feb. 1998). "Thermal adaptation in the built environment: a literature review". en. In: *Energy and Buildings* 27.1, pp. 83–96. issn: 03787788. doi: [10.1016/S0378-7788\(97\)00053-4](https://doi.org/10.1016/S0378-7788(97)00053-4). url: <https://linkinghub.elsevier.com/retrieve/pii/S0378778897000534> (visited on 03/30/2023).
- Brake, Derrick John (2002). "The Deep Body Core Temperatures, Physical Fatigue and Fluid Status of Thermally Stressed Workers and the Development of Thermal Work Limit as an Index of Heat Stress". PhD thesis. Curtin University of Technology.

- Bruse, Michael and Heribert Fler (Oct. 1998). "Simulating surface-plant-air interactions inside urban environments with a three dimensional numerical model". en. In: *Environmental Modelling & Software* 13.3-4, pp. 373–384. issn: 13648152. doi: [10.1016/S1364-8152\(98\)00042-5](https://doi.org/10.1016/S1364-8152(98)00042-5). url: <https://linkinghub.elsevier.com/retrieve/pii/S1364815298000425> (visited on 12/20/2022).
- Cabanac, Michel (Sept. 1971). "Physiological Role of Pleasure: A stimulus can feel pleasant or unpleasant depending upon its usefulness as determined by internal signals." en. In: *Science* 173.4002, pp. 1103–1107. issn: 0036-8075, 1095-9203. doi: [10.1126/science.173.4002.1103](https://doi.org/10.1126/science.173.4002.1103). url: <https://www.science.org/doi/10.1126/science.173.4002.1103> (visited on 04/15/2023).
- Campbell-Lendrum, Diarmid et al. (2022). "Health, Wellbeing and the Changing Structure of Communities". en. In.
- Carlucci, S. et al. (June 2018). "Review of adaptive thermal comfort models in built environmental regulatory documents". en. In: *Building and Environment* 137, pp. 73–89. issn: 03601323. doi: [10.1016/j.buildenv.2018.03.053](https://doi.org/10.1016/j.buildenv.2018.03.053). url: <https://linkinghub.elsevier.com/retrieve/pii/S0360132318301884> (visited on 04/15/2023).
- Chalhoub, Maha and Mikael Philippe (2015). "A Field Experiment to Assess the Influence of Heat and Mass Transfer at the Soil Surface on Shallow Ground Heat Exchanger Performances". en. In: p. 7.
- Chalhoub, Maha et al. (Apr. 2017). "A simple heat and moisture transfer model to predict ground temperature for shallow ground heat exchangers". en. In: *Renewable Energy* 103, pp. 295–307. issn: 09601481. doi: [10.1016/j.renene.2016.11.027](https://doi.org/10.1016/j.renene.2016.11.027). url: <https://linkinghub.elsevier.com/retrieve/pii/S0960148116309909> (visited on 06/23/2022).
- Charalampopoulos, Ioannis et al. (June 2013). "Analysis of thermal bioclimate in various urban configurations in Athens, Greece". en. In: *Urban Ecosystems* 16.2, pp. 217–233. issn: 1083-8155, 1573-1642. doi: [10.1007/s11252-012-0252-5](https://doi.org/10.1007/s11252-012-0252-5). url: <http://link.springer.com/10.1007/s11252-012-0252-5> (visited on 09/01/2023).
- Cheshire, W. P. (Apr. 2016). "Thermoregulatory disorders and illness related to heat and cold stress". en. In: *Autonomic Neuroscience* 196, pp. 91–104. issn: 15660702. doi: [10.1016/j.autneu.2016.01.001](https://doi.org/10.1016/j.autneu.2016.01.001). url: <https://linkinghub.elsevier.com/retrieve/pii/S1566070216300017> (visited on 07/22/2021).
- Choudhury, A. K. Roy, P. K. Majumdar, and C. Datta (2011). "1 - Factors affecting comfort: human physiology and the role of clothing". In: *Improving Comfort in Clothing*. Ed. by Guowen Song. Woodhead Publishing Series in Textiles. Woodhead Publishing, pp. 3–60. isbn: 978-1-84569-539-2. doi: <https://doi.org/10.1533/9780857090645.1.3>. url: <https://www.sciencedirect.com/science/article/pii/B9781845695392500016>.
- Clusiault, David et al. (May 2022). "Scoping review on the state of the integration of human physiological responses to evaluating heat-stress". en. In: *Applied Ergonomics* 101, p. 103704. issn: 00036870. doi: [10.1016/j.apergo.2022.103704](https://doi.org/10.1016/j.apergo.2022.103704). url: <https://linkinghub.elsevier.com/retrieve/pii/S0003687022000278> (visited on 09/15/2022).
- Cramer, M. and O. Jay (Apr. 2016). "Biophysical aspects of human thermoregulation during heat stress". en. In: *Autonomic Neuroscience* 196, pp. 3–13. issn: 15660702. doi: [10.1016/j.autneu.2016.01.001](https://doi.org/10.1016/j.autneu.2016.01.001).

- 1016 / j. autneu. 2016. 03. 001. url: <https://linkinghub.elsevier.com/retrieve/pii/S1566070216300303> (visited on 04/11/2021).
- Crawley, Drury B et al. (2000). "EnergyPlus: Energy Simulation Program". en. In: *ASHRAE Journal*.
- Dear, Richard de (2011). "Revisiting an old hypothesis of human thermal perception: allies-thesis". In: *Building Research & Information* 39.2. Publisher: Routledge\_eprint: <https://doi.org/10.1080/09613218.2011.552269>. url: <https://doi.org/10.1080/09613218.2011.552269>.
- Dear, Richard J de and Gail Schiller Brager (n.d.). "Developing an Adaptive Model of Thermal Comfort and Preference". en. In: ().
- Defraeye, Thijs, Bert Blocken, and Jan Carmeliet (Jan. 2010). "CFD analysis of convective heat transfer at the surfaces of a cube immersed in a turbulent boundary layer". en. In: *International Journal of Heat and Mass Transfer* 53.1-3, pp. 297–308. issn: 00179310. doi: [10.1016/j.ijheatmasstransfer.2009.09.029](https://doi.org/10.1016/j.ijheatmasstransfer.2009.09.029). url: <https://linkinghub.elsevier.com/retrieve/pii/S0017931009005109> (visited on 07/06/2022).
- Deng, Q. et al. (June 2018). "Heatstroke at home: Prediction by thermoregulation modeling". en. In: *Building and Environment* 137, pp. 147–156. issn: 03601323. doi: [10.1016/j.buildenv.2018.04.017](https://doi.org/10.1016/j.buildenv.2018.04.017). url: <https://linkinghub.elsevier.com/retrieve/pii/S036013231830221X> (visited on 12/02/2021).
- Dickinson, Robert E. (1988). "The Force–Restore Model for Surface Temperatures and Its Generalizations". In: *Journal of Climate* 1.11. Place: Boston MA, USA Publisher: American Meteorological Society, pp. 1086–1097. doi: [https://doi.org/10.1175/1520-0442\(1988\)001<1086:TFMFST>2.0.CO;2](https://doi.org/10.1175/1520-0442(1988)001<1086:TFMFST>2.0.CO;2). url: [https://journals.ametsoc.org/view/journals/clim/1/11/1520-0442\\_1988\\_001\\_1086\\_tfmfst\\_2\\_0\\_co\\_2.xml](https://journals.ametsoc.org/view/journals/clim/1/11/1520-0442_1988_001_1086_tfmfst_2_0_co_2.xml).
- Dissegna, Maria Angela et al. (Apr. 2021). "Modeling Mean Radiant Temperature Distribution in Urban Landscapes Using DART". en. In: *Remote Sensing* 13.8, p. 1443. issn: 2072-4292. doi: [10.3390/rs13081443](https://doi.org/10.3390/rs13081443). url: <https://www.mdpi.com/2072-4292/13/8/1443> (visited on 03/07/2023).
- Dokken, David (2015). "Annex II - Glossary". en. In: p. 20.
- Dols, W Stuart, Steven J Emmerich, and Brian J Polidoro (Mar. 2016). "Using coupled energy, airflow and indoor air quality software (TRNSYS/CONTAM) to evaluate building ventilation strategies". en. In: *Building Services Engineering Research and Technology* 37.2, pp. 163–175. issn: 0143-6244, 1477-0849. doi: [10.1177/0143624415619464](https://doi.org/10.1177/0143624415619464). url: <http://journals.sagepub.com/doi/10.1177/0143624415619464> (visited on 06/06/2023).
- Dols, W. Stuart and Brian J. Polidoro (Aug. 2020). *CONTAM User Guide and Program Documentation Version 3.4*. en. Tech. rep. National Institute of Standards and Technology. doi: [10.6028/NIST.TN.1887r1](https://doi.org/10.6028/NIST.TN.1887r1). url: <https://nvlpubs.nist.gov/nistpubs/TechnicalNotes/NIST.TN.1887r1.pdf> (visited on 12/12/2022).
- Dorer, Viktor et al. (Aug. 2013). "Modelling The Urban Microclimate And Its Impact On The Energy Demand Of Buildings And Building Clusters". en. In: doi: [10.26868/25222708.2013.1176](https://doi.org/10.26868/25222708.2013.1176). url: [https://publications.ibpsa.org/conference/paper/?id=bs2013\\_1176](https://publications.ibpsa.org/conference/paper/?id=bs2013_1176) (visited on 02/07/2023).

- Ebi, Kristie L et al. (Aug. 2021). "Hot weather and heat extremes: health risks". en. In: *The Lancet* 398.10301, pp. 698–708. issn: 01406736. doi: [10.1016 / S0140 - 6736\(21\) 01208 - 3](https://doi.org/10.1016/S0140-6736(21)01208-3). url: <https://linkinghub.elsevier.com/retrieve/pii/S0140673621012083> (visited on 04/11/2023).
- Fanger, Poul O. (1970). *Thermal comfort: Analysis and applications in environmental engineering*. eng. Copenhagen: Danish Technical Pr. isbn: 978-87-571-0341-0.
- (1972). *Thermal comfort : analysis and applications in environmental engineering*. New York : McGraw-Hill. isbn: 0-07-019915-9.
- Feng, Guohui et al. (2022). "A review of heat stress evaluation indices in extremely hot environments". en. In: *E3S Web of Conferences* 356. Ed. by A. Li, T. Olofsson, and R. Kosonen, p. 03003. issn: 2267-1242. doi: [10.1051 / e3sconf / 202235603003](https://doi.org/10.1051/e3sconf/202235603003). url: <https://www.e3s-conferences.org/10.1051/e3sconf/202235603003> (visited on 09/05/2022).
- Fiala, Dusan (1998). "Dynamic Simulation of Human Heat Transfer and Thermal Comfort". en. In: p. 294.
- Frayssinet, Loïc (2018). "Adapting buildings heating and cooling power need models at the district scale". fr. PhD thesis. Lyon: Université de Lyon.
- Frich, P et al. (2002). "Observed coherent changes in climatic extremes during the second half of the twentieth century". en. In: *Climate Research* 19, pp. 193–212. issn: 0936-577X, 1616-1572. doi: [10.3354 / cr019193](https://doi.org/10.3354/cr019193). url: <http://www.int-res.com/abstracts/cr/v19/n3/p193-212/> (visited on 04/11/2023).
- Füssel, HansCEMartin (2005). "Vulnerability in Climate Change Research: A Comprehensive Conceptual Framework". en. In: 6.
- Gagge, A. P., J. A. J. Stolwijk, and Y. Nishi (1971). "An Effective Temperature Scale Based on a Simple Model of Human Physiological Regulatory Response". en. In: p. 17.
- Galtier, M. et al. (2022). "Assessment of narrow-band and full spectrum gas radiation methods in a real industrial glass furnace configuration". In: *Applied Thermal Engineering* 216, p. 119020. issn: 1359-4311. doi: <https://doi.org/10.1016/j.applthermaleng.2022.119020>. url: <https://www.sciencedirect.com/science/article/pii/S1359431122009541>.
- Ganio, Matthew S. et al. (Nov. 2011). "Mild dehydration impairs cognitive performance and mood of men". en. In: *British Journal of Nutrition* 106.10, pp. 1535–1543. issn: 0007-1145, 1475-2662. doi: [10.1017 / S0007114511002005](https://doi.org/10.1017/S0007114511002005). url: [https://www.cambridge.org/core/product/identifier/S0007114511002005/type/journal\\_article](https://www.cambridge.org/core/product/identifier/S0007114511002005/type/journal_article) (visited on 04/13/2023).
- Garbrecht, Oliver (Aug. 2017). "Large Eddy Simulation of Three-dimensional Mixed Convection on a Vertical Plate". PhD thesis. Faculty of Mechanical Engineering Rheinisch-Westfälische Technische Hochschule Aachen.
- Gonzalez, R. R., Y. Nishi, and A. P. Gagge (Mar. 1974). "Experimental evaluation of standard effective temperature a new biometeorological index of man's thermal discomfort". en. In: *International Journal of Biometeorology* 18.1, pp. 1–15. issn: 0020-7128, 1432-1254. doi: [10.1007 / BF01450660](https://doi.org/10.1007/BF01450660). url: <http://link.springer.com/10.1007/BF01450660> (visited on 11/21/2022).
- Gonzalez, R.R., C. Halford, and E.M. Keach (Dec. 2010). "Environmental and physiological simulation of heat stroke: A case study analysis and validation". en. In: *Journal of Thermal*

- Biology* 35.8, pp. 441–449. issn: 03064565. doi: [10.1016/j.jtherbio.2010.09.007](https://doi.org/10.1016/j.jtherbio.2010.09.007). url: <https://linkinghub.elsevier.com/retrieve/pii/S0306456510001063> (visited on 06/24/2022).
- Gresse, Teddy et al. (2023). *Microclimatic modeling and simulation tools : an academic benchmark*. Poster. AustrSydney, Australia.
- Gros, Adrien (2014). “Modélisation de la demande énergétique des bâtiments à l’échelle d’un quartier”. fr. In: p. 169.
- Hadianpour, Mohammad et al. (Mar. 2019). “Effects of windward and leeward wind directions on outdoor thermal and wind sensation in Tehran”. en. In: *Building and Environment* 150, pp. 164–180. issn: 03601323. doi: [10.1016/j.buildenv.2018.12.053](https://doi.org/10.1016/j.buildenv.2018.12.053). url: <https://linkinghub.elsevier.com/retrieve/pii/S0360132318308126> (visited on 04/17/2023).
- Haghighat, Fariborz and Ahmed Cherif Megri (Dec. 1996). “A Comprehensive Validation of Two Airflow Models - COMIS and CONTAM”. en. In: *Indoor Air* 6.4, pp. 278–288. issn: 0905-6947, 1600-0668. doi: [10.1111/j.1600-0668.1996.00007.x](https://doi.org/10.1111/j.1600-0668.1996.00007.x). url: <https://onlinelibrary.wiley.com/doi/10.1111/j.1600-0668.1996.00007.x> (visited on 06/06/2023).
- Hamdhan, Indra Noer and Barry G Clarke (2010). “Determination of Thermal Conductivity of Coarse and Fine Sand Soils”. en. In.
- Hanna, Elizabeth and Peter Tait (July 2015). “Limitations to Thermoregulation and Acclimatization Challenge Human Adaptation to Global Warming”. en. In: *International Journal of Environmental Research and Public Health* 12.7, pp. 8034–8074. issn: 1660-4601. doi: [10.3390/ijerph120708034](https://doi.org/10.3390/ijerph120708034). url: <http://www.mdpi.com/1660-4601/12/7/8034> (visited on 07/22/2021).
- Havenith, George and Dusan Fiala (Dec. 2015). “Thermal Indices and Thermophysiological Modeling for Heat Stress”. en. In: *Comprehensive Physiology*. Ed. by Ronald Terjung. Hoboken, NJ, USA: John Wiley & Sons, Inc., pp. 255–302. isbn: 978-0-470-65071-4. doi: [10.1002/cphy.c140051](https://doi.org/10.1002/cphy.c140051). url: <http://doi.wiley.com/10.1002/cphy.c140051> (visited on 04/22/2021).
- Herman, Jon and Will Usher (2023). “SALib Documentation”. en. In.
- Herrington, L. P., C. E. A. Winslow, and A. P. Gagge (Aug. 1937). “THE RELATIVE INFLUENCE OF RADIATION AND CONVECTION UPON VASOMOTOR TEMPERATURE REGULATION”. en. In: *American Journal of Physiology-Legacy Content* 120.1, pp. 133–143. issn: 0002-9513. doi: [10.1152/ajplegacy.1937.120.1.133](https://doi.org/10.1152/ajplegacy.1937.120.1.133). url: <https://www.physiology.org/doi/10.1152/ajplegacy.1937.120.1.133> (visited on 01/16/2023).
- Holmer, Björn et al. (2015). “How to transform the standing man from a box to a cylinder – a modified methodology to calculate mean radiant temperature in field studies and models”. en. In.
- Hooff, T. van et al. (Jan. 2015). “Reprint of: On the predicted effectiveness of climate adaptation measures for residential buildings”. en. In: *Building and Environment* 83, pp. 142–158. issn: 03601323. doi: [10.1016/j.buildenv.2014.10.006](https://doi.org/10.1016/j.buildenv.2014.10.006). url: <https://linkinghub.elsevier.com/retrieve/pii/S0360132314003278> (visited on 04/11/2023).
- Humphreys, Michael (Jan. 1978). “Outdoor temperatures and comfort indoors”. en. In: *Building International, Building Research and Practice* 6.2, pp. 92–92. issn: 0182-3329. doi:



- 10.1080/09613217808550656. url: <http://www.tandfonline.com/doi/abs/10.1080/09613217808550656> (visited on 04/15/2023).
- Hwang, Ruey-Lung, Tzu-Ping Lin, and Andreas Matzarakis (Apr. 2011). "Seasonal effects of urban street shading on long-term outdoor thermal comfort". en. In: *Building and Environment* 46.4, pp. 863–870. issn: 03601323. doi: 10.1016/j.buildenv.2010.10.017. url: <https://linkinghub.elsevier.com/retrieve/pii/S0360132310003094> (visited on 08/31/2023).
- Höppe, P (1992). "Ein neues Verfahren zur Bestimmung der mittleren Strahlungstemperatur in Freien." In: *Wetter und Leben*, 44, 147-151.
- Höppe, P. (1993). "Heat balance modelling". en. In: *Experientia*.
- Höppe, P. (Oct. 1999a). "The physiological equivalent temperature - a universal index for the biometeorological assessment of the thermal environment". en. In: *International Journal of Biometeorology* 43.2, pp. 71–75. issn: 0020-7128, 1432-1254. doi: 10.1007/s004840050118. url: <http://link.springer.com/10.1007/s004840050118> (visited on 04/11/2021).
- Höppe, P. (1999b). "The physiological equivalent temperature – a universal index for the biometeorological assessment of the thermal environment". en. In: *International Journal of Biometeorology*.
- Höppe, Peter (July 2002). "Different aspects of assessing indoor and outdoor thermal comfort". en. In: *Energy and Buildings* 34.6, pp. 661–665. issn: 03787788. doi: 10.1016/S0378-7788(02)00017-8. url: <https://linkinghub.elsevier.com/retrieve/pii/S0378778802000178> (visited on 04/07/2023).
- Ioannou, Leonidas G. et al. (July 2022). "Indicators to assess physiological heat strain – Part 1: Systematic review". en. In: *Temperature* 9.3, pp. 227–262. issn: 2332-8940, 2332-8959. doi: 10.1080/23328940.2022.2037376. url: <https://www.tandfonline.com/doi/full/10.1080/23328940.2022.2037376> (visited on 11/21/2022).
- Ipcc (June 2022). *Global Warming of 1.5°C: IPCC Special Report on Impacts of Global Warming of 1.5°C above Pre-industrial Levels in Context of Strengthening Response to Climate Change, Sustainable Development, and Efforts to Eradicate Poverty*. en. 1st ed. Cambridge University Press. isbn: 978-1-00-915794-0 978-1-00-915795-7. doi: 10.1017/9781009157940. url: <https://www.cambridge.org/core/product/identifiant/9781009157940/type/book> (visited on 07/20/2023).
- ISO7933 (2004). *Ergonomics of the thermal environment — Analytical determination and interpretation of heat stress using calculation of the predicted heat strain*. Tech. rep.
- Jendritzky, Gerd (1990). *Methodik zur raumlichen Bewertung der thermischen Komponente im Bioklima des Menschen : fortgeschriebenes*. fre. Ed. by Akademie für Raumforschung und Landesplanung. isbn: 9783888382079.
- Justo Alonso, M., W.S. Dols, and H.M. Mathisen (Mar. 2022). "Using Co-simulation between EnergyPlus and CONTAM to evaluate recirculation-based, demand-controlled ventilation strategies in an office building". en. In: *Building and Environment* 211, p. 108737. issn: 03601323. doi: 10.1016/j.buildenv.2021.108737. url: <https://linkinghub.elsevier.com/retrieve/pii/S0360132321011264> (visited on 06/06/2023).
- Katavoutas, George, Helena A. Flocas, and Andreas Matzarakis (Feb. 2015). "Dynamic modeling of human thermal comfort after the transition from an indoor to an outdoor hot

- environment". en. In: *International Journal of Biometeorology* 59.2, pp. 205–216. issn: 0020-7128, 1432-1254. doi: [10.1007/s00484-014-0836-2](https://doi.org/10.1007/s00484-014-0836-2). url: <http://link.springer.com/10.1007/s00484-014-0836-2> (visited on 12/19/2022).
- Katić, K., R. Li, and W. Zeiler (Sept. 2016). "Thermophysiological models and their applications: A review". In: *Building and Environment* 106, pp. 286–300. issn: 03601323. doi: [10.1016/j.buildenv.2016.06.031](https://doi.org/10.1016/j.buildenv.2016.06.031). url: <https://linkinghub.elsevier.com/retrieve/pii/S0360132316302384> (visited on 04/11/2021).
- Kobayashi, Yutaka and Shin-ichi Tanabe (Aug. 2013). "Development of JOS-2 human thermoregulation model with detailed vascular system". en. In: *Building and Environment* 66, pp. 1–10. issn: 03601323. doi: [10.1016/j.buildenv.2013.04.013](https://doi.org/10.1016/j.buildenv.2013.04.013). url: <https://linkinghub.elsevier.com/retrieve/pii/S0360132313001182> (visited on 01/09/2023).
- Kántor, Noémi, Tzu-Ping Lin, and Andreas Matzarakis (Sept. 2014). "Daytime relapse of the mean radiant temperature based on the six-directional method under unobstructed solar radiation". en. In: *International Journal of Biometeorology* 58.7, pp. 1615–1625. issn: 0020-7128, 1432-1254. doi: [10.1007/s00484-013-0765-5](https://doi.org/10.1007/s00484-013-0765-5). url: <http://link.springer.com/10.1007/s00484-013-0765-5> (visited on 03/07/2023).
- Lai, Dayi, Xiaojie Zhou, and Qingyan Chen (Sept. 2017). "Measurements and predictions of the skin temperature of human subjects on outdoor environment". en. In: *Energy and Buildings* 151, pp. 476–486. issn: 03787788. doi: [10.1016/j.enbuild.2017.07.009](https://doi.org/10.1016/j.enbuild.2017.07.009). url: <https://linkinghub.elsevier.com/retrieve/pii/S0378778817305601> (visited on 04/17/2023).
- Lai, Dayi et al. (July 2014). "Studies of outdoor thermal comfort in northern China". en. In: *Building and Environment* 77, pp. 110–118. issn: 03601323. doi: [10.1016/j.buildenv.2014.03.026](https://doi.org/10.1016/j.buildenv.2014.03.026). url: <https://linkinghub.elsevier.com/retrieve/pii/S0360132314000869> (visited on 04/15/2023).
- Lai, Dayi et al. (Nov. 2020). "A comprehensive review of thermal comfort studies in urban open spaces". en. In: *Science of The Total Environment* 742, p. 140092. issn: 00489697. doi: [10.1016/j.scitotenv.2020.140092](https://doi.org/10.1016/j.scitotenv.2020.140092). url: <https://linkinghub.elsevier.com/retrieve/pii/S0048969720336123> (visited on 03/24/2023).
- Lauzet, Nicolas (2019). "Prise en compte cumulée du réchauffement climatique et des surchauffes urbaines en phase amont de conception frugale des bâtiments centrée sur le confort des occupants: des propositions méthodologiques". fr. In.
- Lemonsu, A., V. Masson, and E. Berthier (July 2007). "Improvement of the hydrological component of an urban soil–vegetation–atmosphere–transfer model". en. In: *Hydrological Processes* 21.16, pp. 2100–2111. issn: 08856087, 10991085. doi: [10.1002/hyp.6373](https://doi.org/10.1002/hyp.6373). url: <https://onlinelibrary.wiley.com/doi/10.1002/hyp.6373> (visited on 06/22/2022).
- Lindsay, Amy et al. (2016). "ENHANCING BIFACIAL PV MODELLING WITH RAY-TRACING". en. In: Publisher: Unpublished. doi: [10.13140/RG.2.2.23758.00326](https://doi.org/10.13140/RG.2.2.23758.00326). url: <http://rgdoi.net/10.13140/RG.2.2.23758.00326> (visited on 08/23/2023).
- Loutan, L and F Chappuis (2002). "Coup de chaleur et survie dans le desert". fr. In: *Médecine Hygiène*.
- Mahfouf, J.-F. and J. Noilhan (1991). "Comparative Study of Various Formulations of Evaporations from Bare Soil Using In Situ Data." en. In: *Applied Meteorology*. (Visited on 08/15/2023).

- Masson, Valéry (Mar. 2000). "A Physically-Based Scheme For The Urban Energy Budget In Atmospheric Models". en. In: *Boundary-Layer Meteorology* 94.3, pp. 357–397. issn: 0006-8314, 1573-1472. doi: [10.1023/A:1002463829265](https://doi.org/10.1023/A:1002463829265). url: <http://link.springer.com/10.1023/A:1002463829265> (visited on 03/03/2022).
- Masson, Valéry et al. (2000). "Inclusion of a multi-layer drag approach in (TEB) urban surface scheme". en. In: p. 23.
- Masterton, J.M. and F.A. Richardson (1979). *Humidex: A Method of Quantifying Human Discomfort Due to Excessive Heat and Humidity*, by J.M. Masterton and F.A. Richardson. 28cm. cli,1. Service de l'environnement atmosphérique. url: <https://books.google.fr/books?id=DBIazQEACAAJ>.
- Matthies, Franziska (2008). *Heat-health action plans: guidance*. OCLC: 605537549. Copenhagen, Denmark: World Health Organization, Europe. isbn: 978-92-890-7191-8.
- Matzarakis, A. and H. Mayer (1996). "Another kind of environmental stress: thermal stress". In: *WHO Newsletter* 18:7–10.
- Matzarakis, Andreas, Frank Rutz, and Helmut Mayer (Feb. 2007). "Modelling radiation fluxes in simple and complex environments—application of the RayMan model". en. In: *International Journal of Biometeorology* 51.4, pp. 323–334. issn: 0020-7128, 1432-1254. doi: [10.1007/s00484-006-0061-8](https://doi.org/10.1007/s00484-006-0061-8). url: <http://link.springer.com/10.1007/s00484-006-0061-8> (visited on 07/22/2022).
- (Mar. 2009). "Modelling radiation fluxes in simple and complex environments: basics of the RayMan model". en. In: *International Journal of Biometeorology* 54.2, pp. 131–139. issn: 0020-7128, 1432-1254. doi: [10.1007/s00484-009-0261-0](https://doi.org/10.1007/s00484-009-0261-0). url: <http://link.springer.com/10.1007/s00484-009-0261-0> (visited on 12/28/2022).
- McGregor, Glenn R. (May 2012). "Special issue: Universal Thermal Comfort Index (UTCI)". en. In: *International Journal of Biometeorology* 56.3, pp. 419–419. issn: 0020-7128, 1432-1254. doi: [10.1007/s00484-012-0546-6](https://doi.org/10.1007/s00484-012-0546-6). url: <http://link.springer.com/10.1007/s00484-012-0546-6> (visited on 11/21/2022).
- Mei, Shuo-Jun and Chao Yuan (Feb. 2022). "Urban buoyancy-driven air flow and modelling method: A critical review". en. In: *Building and Environment* 210, p. 108708. issn: 03601323. doi: [10.1016/j.buildenv.2021.108708](https://doi.org/10.1016/j.buildenv.2021.108708). url: <https://linkinghub.elsevier.com/retrieve/pii/S0360132321010982> (visited on 10/03/2022).
- Meinders, E. R., K. Hanjalic, and R. J. Martinuzzi (Aug. 1999). "Experimental Study of the Local Convection Heat Transfer From a Wall-Mounted Cube in Turbulent Channel Flow". en. In: *Journal of Heat Transfer* 121.3, pp. 564–573. issn: 0022-1481, 1528-8943. doi: [10.1115/1.2826017](https://doi.org/10.1115/1.2826017). url: <https://asmedigitalcollection.asme.org/heattransfer/article/121/3/564/429996/Experimental-Study-of-the-Local-Convection-Heat> (visited on 10/26/2023).
- Meng, Yan and Kazuki Hibi (1998). "Turbulent measurements of the flow field around a high-rise building". In: *Wind Engineers, JAWE* 1998.76, pp. 55–64. doi: [10.5359/jawe.1998.76\\_55](https://doi.org/10.5359/jawe.1998.76_55).
- Merlier, Lucie (2015). "Pour obtenir: le grade de docteur". fr. In.

- Merlier, Lucie et al. (Apr. 2019). "On the impact of local microclimate on building performance simulation. Part I: Prediction of building external conditions". In: *Building Simulation* 12. doi: [10.1007/s12273-019-0507-7](https://doi.org/10.1007/s12273-019-0507-7).
- Mirsadeghi, M. et al. (July 2013). "Review of external convective heat transfer coefficient models in building energy simulation programs: Implementation and uncertainty". en. In: *Applied Thermal Engineering* 56.1-2, pp. 134–151. issn: 13594311. doi: [10.1016/j.applthermaleng.2013.03.003](https://doi.org/10.1016/j.applthermaleng.2013.03.003). url: <https://linkinghub.elsevier.com/retrieve/pii/S1359431113001543> (visited on 11/29/2021).
- Molina, Géraldine (Jan. 2022). "Modèle d'analyse des "espaces refuges" des habitants des villes lors des évènements météorologiques extrêmes". Dates de démarrage du travail : 2022-01-05 jusqu'au 2022-03-31. url: <https://hal.science/hal-03927677>.
- Montain, S. J. and E. F. Coyle (Oct. 1992). "Influence of graded dehydration on hyperthermia and cardiovascular drift during exercise". en. In: *Journal of Applied Physiology* 73.4, pp. 1340–1350. issn: 8750-7587, 1522-1601. doi: [10.1152/jappl.1992.73.4.1340](https://doi.org/10.1152/jappl.1992.73.4.1340). url: <https://www.physiology.org/doi/10.1152/jappl.1992.73.4.1340> (visited on 04/13/2023).
- Monteiro, Leonardo Marques (2005). "REVIEW OF NUMERICAL MODELLING OF OUTDOOR THERMAL COMFORT". en. In: p. 8.
- Musy, Marjorie (2012). "Modélisation des interactions ville-climat-énergie". fr. In.
- Naboni, Emanuele et al. (Sept. 2017). "An overview of simulation tools for predicting the mean radiant temperature in an outdoor space". en. In: *Energy Procedia* 122, pp. 1111–1116. issn: 18766102. doi: [10.1016/j.egypro.2017.07.471](https://doi.org/10.1016/j.egypro.2017.07.471). url: <https://linkinghub.elsevier.com/retrieve/pii/S1876610217334331> (visited on 12/28/2022).
- Nag, Pranab Kumar, Anjali Nag, and Shirish Pratap Ashtekar (2007). "Thermal Limits of Men in Moderate to Heavy Work in Tropical Farming". en. In: *Industrial Health* 45.1, pp. 107–117. issn: 0019-8366, 1880-8026. doi: [10.2486/indhealth.45.107](https://doi.org/10.2486/indhealth.45.107). url: [http://www.jstage.jst.go.jp/article/indhealth/45/1/45\\_1\\_107/\\_article](http://www.jstage.jst.go.jp/article/indhealth/45/1/45_1_107/_article) (visited on 06/16/2022).
- Ndetto, Emmanuel Lubango and Andreas Matzarakis (Apr. 2015). "Urban atmospheric environment and human biometeorological studies in Dar es Salaam, Tanzania". en. In: *Air Quality, Atmosphere & Health* 8.2, pp. 175–191. issn: 1873-9318, 1873-9326. doi: [10.1007/s11869-014-0261-z](https://doi.org/10.1007/s11869-014-0261-z). url: <http://link.springer.com/10.1007/s11869-014-0261-z> (visited on 09/01/2023).
- NIOSH (2016). "Occupational Exposure to heat and hot environments". en. In.
- Noilhan, J. and J.-F. Mahfouf (June 1996). "The ISBA land surface parameterisation scheme". en. In: *Global and Planetary Change* 13.1-4, pp. 145–159. issn: 09218181. doi: [10.1016/0921-8181\(95\)00043-7](https://doi.org/10.1016/0921-8181(95)00043-7). url: <https://linkinghub.elsevier.com/retrieve/pii/0921818195000437> (visited on 08/15/2023).
- Oke, T. R. (Dec. 1987). *Boundary Layer Climates*. 2nd ed. London: Routledge. isbn: 978-0-203-40721-9. doi: [10.4324/9780203407219](https://doi.org/10.4324/9780203407219).
- Oke, T. R. et al. (Sept. 2017). *Urban Climates*. en. 1st ed. Cambridge University Press. isbn: 978-1-139-01647-6 978-0-521-84950-0 978-1-107-42953-6. doi: [10.1017/9781139016476](https://doi.org/10.1017/9781139016476). url: <https://www.cambridge.org/core/product/identifier/9781139016476/type/book> (visited on 10/13/2022).

- Orme, Malcolm, Martin W Liddament, and Andrew Wilson (2010). "Numerical Data for Air Infiltration and Natural Ventilation Calculations". en. In: p. 108.
- P., Gagge A. (1937). "A new physiological variable associated with sensible and insensible perspiration". en. In: *J. Physiol.*
- Palme, M. et al. (June 2017). "From urban climate to energy consumption. Enhancing building performance simulation by including the urban heat island effect". en. In: *Energy and Buildings* 145, pp. 107–120. issn: 03787788. doi: [10.1016/j.enbuild.2017.03.069](https://doi.org/10.1016/j.enbuild.2017.03.069). url: <https://linkinghub.elsevier.com/retrieve/pii/S0378778817311027> (visited on 02/07/2023).
- Parkinson, Thomas (2016). "Thermal Pleasure and Alliesthesia in the Built Environment". en. In.
- Parsons, Ken (2002). *Human Thermal Environments: the Effect of Hot, Moderate and cold environments on human health, comfort and performance*. en. OCLC: 437083211. London: CRC Press. isbn: 978-0-203-30262-0. url: <http://public.eblib.com/choice/publicfullrecord.aspx?p=180466> (visited on 11/23/2021).
- Peeters, Leen et al. (May 2009). "Thermal comfort in residential buildings: Comfort values and scales for building energy simulation". en. In: *Applied Energy* 86.5, pp. 772–780. issn: 03062619. doi: [10.1016/j.apenergy.2008.07.011](https://doi.org/10.1016/j.apenergy.2008.07.011). url: <https://linkinghub.elsevier.com/retrieve/pii/S0306261908001785> (visited on 03/25/2023).
- Perkins-Kirkpatrick, S. E. and S. C. Lewis (July 2020). "Increasing trends in regional heatwaves". en. In: *Nature Communications* 11.1, p. 3357. issn: 2041-1723. doi: [10.1038/s41467-020-16970-7](https://doi.org/10.1038/s41467-020-16970-7). url: <https://www.nature.com/articles/s41467-020-16970-7> (visited on 07/03/2023).
- Peuportier, Bruno (2016). *Energétique des bâtiments & simulation thermique*. Eyrolles.
- Plessis, Gilles, Aurelie Kaemmerlen, and Amy Lindsay (Mar. 2014). "BuildSysPro: a Mod-elica library for modelling buildings and energy systems". en. In: pp. 1161–1169. doi: [10.3384/ecp140961161](https://doi.org/10.3384/ecp140961161). url: [https://ep.liu.se/en/conference-article.aspx?series=ecp&issue=96&Article\\_No=122](https://ep.liu.se/en/conference-article.aspx?series=ecp&issue=96&Article_No=122) (visited on 12/20/2022).
- Périard, J. D., S. Racinais, and M. N. Sawka (June 2015). "Adaptations and mechanisms of human heat acclimation: Applications for competitive athletes and sports: Adaptations and mechanisms of heat acclimation". en. In: *Scandinavian Journal of Medicine & Science in Sports* 25, pp. 20–38. issn: 09057188. doi: [10.1111/sms.12408](https://doi.org/10.1111/sms.12408). url: <http://doi.wiley.com/10.1111/sms.12408> (visited on 04/11/2021).
- Ramspeck, Claire B et al. (2003a). "ASHRAE STANDARDS COMMITTEE 2003-2004". en. In. — (2003b). "ASHRAE STANDARDS COMMITTEE 2003-2004". en. In: p. 30.
- Rawls, Walter J, Donald L Brakensiek, and KE Saxton (1982). "Estimation of soil water properties". In: *Transactions of the ASAE* 25.5, pp. 1316–1320.
- Reynolds, John S. (1982). "PASSIVE COOLING AND COURTYARDS IN COLIMA, MEXICO". en. In: *Passive and Low Energy Alternatives I*. Elsevier, pp. 13–15–13–21. isbn: 978-0-08-029405-6. doi: [10.1016/B978-0-08-029405-6.50050-7](https://doi.org/10.1016/B978-0-08-029405-6.50050-7). url: <https://linkinghub.elsevier.com/retrieve/pii/B9780080294056500507> (visited on 12/28/2022).
- Robinson, Darren et al. (2009). "CITYSIM: COMPREHENSIVE MICRO-SIMULATION OF RESOURCE FLOWS FOR SUSTAINABLE URBAN PLANNING". en. In: p. 9.

- Rodriguez, Fabrice, Hervé Andrieu, and Floriane Morena (Apr. 2008). "A distributed hydrological model for urbanized areas – Model development and application to case studies". en. In: *Journal of Hydrology* 351.3-4, pp. 268–287. issn: 00221694. doi: [10.1016/j.jhydrol.2007.12.007](https://doi.org/10.1016/j.jhydrol.2007.12.007). url: <https://linkinghub.elsevier.com/retrieve/pii/S0022169407007299> (visited on 08/15/2023).
- Rosenberg, Norman J., Blaine L. Blad, and Shashi B. Verma (Sept. 1983). *Microclimate: The Biological Environment*. en. Google-Books-ID: c6MI6VvTqTsC. John Wiley & Sons. isbn: 978-0-471-06066-6.
- Sadeghipour Roudsari, Mostapha, Michelle Pak, and Anthony Viola (Aug. 2013). "Ladybug: A Parametric Environmental Plugin For Grasshopper To Help Designers Create An Environmentally-conscious Design". en. In: doi: [10.26868/25222708.2013.2499](https://doi.org/10.26868/25222708.2013.2499). url: [https://publications.ibpsa.org/conference/paper/?id=bs2013\\_2499](https://publications.ibpsa.org/conference/paper/?id=bs2013_2499) (visited on 01/24/2023).
- Salagnac, Jean-Luc (2007). "Lessons from the 2003 heat wave : a French perspective". In: *Building research & information*.
- Salvati, Agnese, Helena Coch Roura, and Carlo Cecere (2015). "URBAN MORPHOLOGY AND ENERGY PERFORMANCE: THE DIRECT AND INDIRECT CONTRIBUTION IN MEDITERRANEAN CLIMATE". en. In.
- Santos Nouri, Andre et al. (Mar. 2018). "Approaches to Outdoor Thermal Comfort Thresholds through Public Space Design: A Review". en. In: *Atmosphere* 9.3, p. 108. issn: 2073-4433. doi: [10.3390/atmos9030108](https://doi.org/10.3390/atmos9030108). url: <http://www.mdpi.com/2073-4433/9/3/108> (visited on 01/19/2023).
- Santé, Organisation mondiale de la (2016). *Rapport mondial sur le vieillissement et la santé*. url: <https://www.who.int/fr/news-room/fact-sheets/detail/ageing-and-health> (visited on 12/21/2021).
- Sawka, M.N and K.B Pandolf (1990). *Effects of body water loss on physiological function and exercise performance*. In *Handbook of Physiology: Environmental Physiology*.
- Schmitt, Félix et al. (2023). "IMPACT OF THE SPECTRAL COUPLING BETWEEN NON-GRAY SKY BOUNDARY CONDITIONS AND A URBAN ATMOSPHERE IN THE CALCULATION OF NET FLUXES IN A STREET CANYON". English. In: Begel House Inc. doi: [10.1615/RAD-23.490](https://doi.org/10.1615/RAD-23.490). url: <https://www.dl.begellhouse.com/references/1bb331655c289a0a,6aab6e2d4fa83503,4a18eeb215ae53e4.html> (visited on 10/31/2023).
- Schwede, Dirk A (2007). "Interpreting Fanger's Comfort Equation within the Adaptive Paradigm". en. In.
- Schweiker, Marcel et al. (Apr. 2020). "A seasonal approach to alliesthesia. Is there a conflict with thermal adaptation?" en. In: *Energy and Buildings* 212, p. 109745. issn: 03787788. doi: [10.1016/j.enbuild.2019.109745](https://doi.org/10.1016/j.enbuild.2019.109745). url: <https://linkinghub.elsevier.com/retrieve/pii/S0378778819317086> (visited on 04/15/2023).
- Soulhac, Lionel (2018). "Modélisation de la dispersion atmosphérique à l'intérieur de la canopée urbaine". fr. In: p. 349.
- Steadman, Robert G. (Dec. 1984). "A Universal Scale of Apparent Temperature". In: *Journal of Climate and Applied Meteorology* 23 N.12.
- Stocker, Thomas F et al. (2013). "Résumé à l'intention des décideurs". fr. In.

- Stolwijk, J A J (1971). "A mathematical model of physiological temperature regulation in man". In: *NASA Contract. Rep.* NASA Contractor Report CR-1855 August, p. 77.
- Su, Mi Aye et al. (May 2021). "Empirical evidence on the impact of urban overheating on building cooling and heating energy consumption". en. In: *iScience* 24.5, p. 102495. issn: 25890042. doi: [10.1016/j.isci.2021.102495](https://doi.org/10.1016/j.isci.2021.102495). url: <https://linkinghub.elsevier.com/retrieve/pii/S2589004221004636> (visited on 07/03/2023).
- Takahashi, Yoshito et al. (Jan. 2021). "Thermoregulation model JOS-3 with new open source code". en. In: *Energy and Buildings* 231, p. 110575. issn: 03787788. doi: [10.1016/j.enbuild.2020.110575](https://doi.org/10.1016/j.enbuild.2020.110575). url: <https://linkinghub.elsevier.com/retrieve/pii/S0378778820333612> (visited on 05/12/2022).
- Tominaga, Yoshihide et al. (Oct. 2008). "AIJ guidelines for practical applications of CFD to pedestrian wind environment around buildings". en. In: *Journal of Wind Engineering and Industrial Aerodynamics* 96.10-11, pp. 1749–1761. issn: 01676105. doi: [10.1016/j.jweia.2008.02.058](https://doi.org/10.1016/j.jweia.2008.02.058). url: <https://linkinghub.elsevier.com/retrieve/pii/S0167610508000445> (visited on 07/27/2021).
- Truong, Phan Hue (2012). "Recommendations for the Analysis and Design of Naturally Ventilated Buildings in Urban Areas". en. In: p. 121.
- Tseliou, Areti et al. (2016). "Outdoor thermal sensation in a Mediterranean climate (Athens): The effect of selected microclimatic parameters". In: *Architectural Science Review* 59.3. Publisher: Taylor & Francis \_eprint: <https://doi.org/10.1080/00038628.2015.1028022>, pp. 190–202. doi: [10.1080/00038628.2015.1028022](https://doi.org/10.1080/00038628.2015.1028022). url: <https://doi.org/10.1080/00038628.2015.1028022>.
- Valko, P. (Mar. 1966). "Die Himmelsstrahlung in ihrer Beziehung zu verschiedenen Parametern". de. In: *Archiv für Meteorologie, Geophysik und Bioklimatologie, Serie B* 14.3, pp. 336–359. issn: 1434-4483. doi: [10.1007/BF02243366](https://doi.org/10.1007/BF02243366). url: <https://doi.org/10.1007/BF02243366> (visited on 11/06/2023).
- Vargas, Nicole T. et al. (Nov. 2018). "Skin wettedness is an important contributor to thermal behavior during exercise and recovery". en. In: *American Journal of Physiology-Regulatory, Integrative and Comparative Physiology* 315.5, R925–R933. issn: 0363-6119, 1522-1490. doi: [10.1152/ajpregu.00178.2018](https://doi.org/10.1152/ajpregu.00178.2018). url: <https://www.physiology.org/doi/10.1152/ajpregu.00178.2018> (visited on 06/01/2023).
- Vinet, Jérôme (2000). "Contribution à la modélisation thermo-aéraulique du microclimat urbain. Caractérisation de l'impact de l'eau et de la végétation sur les conditions de confort en espaces extérieurs". fr. In.
- Vogt, J.J. et al. (1981). "Chapter 6 Required Sweat Rate as an Index of Thermal Strain in Industry". en. In: *Studies in Environmental Science*. Vol. 10. Elsevier, pp. 99–110. isbn: 978-0-444-99761-6. doi: [10.1016/S0166-1116\(08\)71083-5](https://doi.org/10.1016/S0166-1116(08)71083-5). url: <https://linkinghub.elsevier.com/retrieve/pii/S0166111608710835> (visited on 11/28/2022).
- Walther, E. and Q. Goestchel (June 2018). "The P.E.T. comfort index: Questioning the model". en. In: *Building and Environment* 137, pp. 1–10. issn: 03601323. doi: [10.1016/j.buildenv.2018.03.054](https://doi.org/10.1016/j.buildenv.2018.03.054). url: <https://linkinghub.elsevier.com/retrieve/pii/S0360132318301896> (visited on 11/28/2022).

- Walton, G N (1989). "Airflow Network Models for Element-Based Building Airflow Modeling". en. In.
- Wetter, M (2006). "Multizone Airflow Model in Modelica". en. In.
- WHO (2015). *Vagues de chaleur et santé : guide pour l'élaboration du système d'alerte*. Tech. rep. World Health Organization (2018). *WHO housing and health guidelines*. en. Tech. rep. OCLC: 1089417323. Geneva. (Visited on 04/11/2021).
- Yaglou, C.P and D. Minard (1957). "Control of heat casualties at military training centers". In: *Archives of Industrial Health* 16, pp. 302–305.
- Yang, Shi-Qui and Andreas Matzarakis (2016). "Implementation of human thermal comfort information in Köppen-Geiger climate classification—the example of China". en. In: *International Journal of Biometeorology*.
- Yang, Xiaoshan et al. (Nov. 2012). "An integrated simulation method for building energy performance assessment in urban environments". en. In: *Energy and Buildings* 54, pp. 243–251. issn: 03787788. doi: [10.1016/j.enbuild.2012.07.042](https://doi.org/10.1016/j.enbuild.2012.07.042). url: <https://linkinghub.elsevier.com/retrieve/pii/S0378778812003970> (visited on 12/29/2022).
- Yang, Y. and Albert P.C. Chan (Feb. 2015). "Perceptual strain index for heat strain assessment in an experimental study: An application to construction workers". en. In: *Journal of Thermal Biology* 48, pp. 21–27. issn: 03064565. doi: [10.1016/j.jtherbio.2014.12.007](https://doi.org/10.1016/j.jtherbio.2014.12.007). url: <https://linkinghub.elsevier.com/retrieve/pii/S0306456514001910> (visited on 07/23/2021).
- Yao, Jiawei et al. (May 2018). "The effect of personal and microclimatic variables on outdoor thermal comfort: A field study in a cold season in Lujiazui CBD, Shanghai". en. In: *Sustainable Cities and Society* 39, pp. 181–188. issn: 22106707. doi: [10.1016/j.scs.2018.02.025](https://doi.org/10.1016/j.scs.2018.02.025). url: <https://linkinghub.elsevier.com/retrieve/pii/S2210670717310806> (visited on 04/15/2023).
- Zare, Sajad et al. (Mar. 2018). "Comparing Universal Thermal Climate Index (UTCI) with selected thermal indices/environmental parameters during 12 months of the year". en. In: *Weather and Climate Extremes* 19, pp. 49–57. issn: 22120947. doi: [10.1016/j.wace.2018.01.004](https://doi.org/10.1016/j.wace.2018.01.004). url: <https://linkinghub.elsevier.com/retrieve/pii/S221209471730110X> (visited on 03/03/2022).
- Zhao, Jinping et al. (Apr. 2020). "Heatstroke recovery at home as predicted by human thermoregulation modeling". en. In: *Building and Environment* 173, p. 106752. issn: 03601323. doi: [10.1016/j.buildenv.2020.106752](https://doi.org/10.1016/j.buildenv.2020.106752). url: <https://linkinghub.elsevier.com/retrieve/pii/S0360132320301104> (visited on 08/23/2021).
- Zhou, Yichen, Na An, and Jiawei Yao (June 2022). "Characteristics, Progress and Trends of Urban Microclimate Research: A Systematic Literature Review and Bibliometric Analysis". en. In: *Buildings* 12.7, p. 877. issn: 2075-5309. doi: [10.3390/buildings12070877](https://doi.org/10.3390/buildings12070877). url: <https://www.mdpi.com/2075-5309/12/7/877> (visited on 10/17/2023).
- Zuo, Jian et al. (Apr. 2015). "Impacts of heat waves and corresponding measures: a review". en. In: *Journal of Cleaner Production* 92, pp. 1–12. issn: 09596526. doi: [10.1016/j.jclepro.2014.12.078](https://doi.org/10.1016/j.jclepro.2014.12.078). url: <https://linkinghub.elsevier.com/retrieve/pii/S0959652614013754> (visited on 02/08/2023).



# Appendices



## A Heat stress index and thermophysiological models

### A.1 Rational index

The **operative temperature** ( $T_o$ ), is often used for indoor environments. The concept of  $T_o$  was introduced by Herrington and Gagge in 1937 (Herrington, Winslow, and Gagge, 1937). ASRHAE Standards (Ramspeck et al., 2003a) define it as the uniform temperature of an enclosure in which an occupant would exchange the same amount of heat by radiation plus convection as in the actual non-uniform environment. For indoor applications it is approximated as the average of indoor  $T_a$  and the  $T_{mrt}$ .

**Environmental applicability limits** : Not considering the effect of humidity.

### A.2 Empirical indices

- **Net Effective Temperature (NET)** (Choudhury, Majumdar, and Datta, 2011): is an adaptation of the Equivalent Temperature (ET) where the wind speed component is added to better quantify the thermal sensations. The ET is the effective temperature felt by the human organism for certain values of air temperature, relative humidity, and wind speed. It was introduced by Houghton and Yaglou (1923) to assess the impact of humidity and temperature on thermal comfort.

**Environmental applicability limits**: Only for outdoor applications.

- **Apparent Temperature (AT)** (Steadman, 1984): is an adjustment to the ambient temperature based on the level of humidity. Is the temperature at the reference dew point temperature ( $T_d$ ) level of 14°C,  $v_a = Q = 0$ , producing the same amount of discomfort as that experienced under the current ambient temperature, humidity, and solar radiation.

AT calculation is based on a body thermal balance calculating the thermal resistance required by a human body to maintain the  $T_{core}$  equilibrium (Steadman 1971). The index is valid for healthy adults at moderate activity levels with a  $T_{core}$  limited to 39.5°C.

**Environmental applicability limits**: Only for outdoor applications. Valid on the range of temperatures [-40°, 50°]. The effects of wind speed are under-estimated for low and high temperatures > 40°C.

- **Heat index (HI)**: is the hot version of the apparent temperature (AT). The HI equation (Rothfus 1990) is derived by multiple regression analysis in temperature and relative humidity derived from the Steadman's apparent temperature (AT).

**Environmental applicability limits**: Only for outdoor applications. HI is valid for  $T_a > 26C$  and  $RH > 40\%$  (WHO, 2015) and valid in shade locations.

- **Wet Bulb Globe Temperature (WBGT)** (Yaglou and Minard, 1957): was developed by the US Navy as part of a study on heat related injuries during military training (Yaglou and Minard, 1957). Is a weighted average of the dry-bulb temperature ( $T_a$ , the

natural wet-bulb temperature ( $T_{wb}$ ) and the black-globe temperature ( $T_g$ ). The two last are dependent on radiation and wind speed. WBGT is applicable in direct sunlight.

**Environmental applicability limits:** Outdoor in direct sunlight, underestimate the effect of heat stress for high humidity rates or low wind speed.

- **Humidex** (Masterton and Richardson, 1979): was elaborated by the Canadian meteorologist, *Humidex* was first used in 1965 and revised by Masterton and Richardson in 1979. It is used to describe the feel like temperature of an average person in an hot and humid weather (Krzysztof Blazejczyk). As it does not consider the effects of wind speed and radiant heat sources, it is only applicable when these components can be neglected.

**Environmental applicability limits:** Only for outdoor applications. Do not consider the effects of wind speed or radiant heat sources.

- **Indoor stress index (ISI)** (Deng et al., 2018): it uses a regression model from the Deng multi-segment multi-node human thermoregulation model considering the dehydration effect on sweating and vasodilatation. The *ISI* is also used to assess the risk of heat stroke occurrence, corresponding to a  $T_{core} > 40.6^\circ\text{C}$ .

**Environmental applicability limits:** Indoor application only.

- **Predicted Heat Strain (PHS)** index (ISO7933, 2004) which returns the  $T_{core}$ , the maximum allowable exposure time for water loss, the maximum allowable time for heat storage and the maximum water loss. This index is generally used to assess the risk related to hot working environments.

### A.2.1 Human thermal balance indices

- **Index of thermal stress (ITS)** (B., 1963): The ITS was proposed in 1969 by Givoni. This index allows the prediction of the *SWR* required for thermal equilibrium in subjects wearing summer clothing (Vogt et al., 1981). It considers the heat exchange, the metabolism and clothes. The radiative effect has been added in a further version by the author by replacing the globe temperature ( $T_g$ ) instead of  $T_a$ .

**Environmental applicability limits:** it depends on the regression model used for this index. There is no model adapted for both outdoor and indoor environments.

- **Predicted Mean Vote (PMV)** and the **Predicted percentage of dissatisfaction (PPD)** indices: these indices use the Fanger (Fanger, 1970) body thermal balance model adapted for uniform indoor environments and for young persons (as the experience was made in a conditioned thermal environment with college-aged students). **Environmental applicability limits:** only for indoor conditioned environments.

- **Perceived Temperature (PT)**(VDI, 1998): this index belongs to the Klima-Michel Model and is an adaptation of the Fanger model for outdoor application. This model is ap-

plicable to a standard individual (35 years, 1.75 m, 75 kg, walking at  $4 \text{ km h}^{-1}$ ,  $M=2.3$  met). **Environmental applicability limits:** only outdoor application.

Within equivalent temperature indices, it is possible to cite the following:

- **Standard Effective Temperature (SET):** this index is derived from the two nodes the Gagge steady model (P., 1937) introduced in 1967 by Gagge. The SET is the equivalent air temperature of an isothermal environment in which a subject, while wearing clothing standardized for the activity concerned, has the same heat stress (skin temperature  $T_{sk}$ ) and thermoregulatory strain (skin wetness *SkinWet*) as in the actual environment (ref. Definition of the ASHRAE Handbook 2017). The reference environment is defined as:  $T_a = T_{mrt} = 26.87^\circ\text{C}$ ,  $v_a = 0.1 \text{ m s}^{-1}$ ,  $HR = 50\%$ ,  $M = 1$  met and clothing insulation  $I_c = 0.6$  clo. In 1999, Pickup & Dear (Monteiro, 2005) proposed the Outdoor Standard Effective Temperature OUT SET, an adaptation of the SET which considers an outdoor radiative model to compute the  $T_{mrt}$ .  
**Environmental applicability limits:** Limited for sunny outdoor applications as  $10^\circ\text{C} < T_{mrt} < 40^\circ\text{C}$  and  $2.1 > v_a > 0 \text{ m s}^{-1}$  and  $10^\circ\text{C} < T_a < 40^\circ\text{C}$ .
- **Physiological Equivalent Temperature (PET):** this index is derived from the two node MEMI steady model (Höppe, 1993) introduced in 1984 by Höppe (Höppe, 1999b). The PET is the equivalent temperature of an isothermal reference environment at which the heat balance of a reference person is maintained with  $T_{core}$  and  $T_{sk}$  equal to those under the considered environment. The reference environment is defined as:  $T_{mrt} = T_a$ ,  $v_a = 0.1 \text{ m s}^{-1}$ ,  $p_v = 12 \text{ hPa}$ ,  $HR = 50\%$ ,  $M = 114\text{W}$  and clothes resistance  $I_{clo} = 0.9$  clo. PET is adapted to both indoor and outdoor environments.  
**Environmental applicability limits:** Not adapted for specific meteorological conditions with high values of  $T_a$  and  $RH$  (ex:  $T_a > 40^\circ\text{C}$ ,  $RH > 80\%$ ). In this case heat strain induced by an increasing  $v_a$  is not considered and the heat stress decreases instead of increasing.
- **Universal Thermal Index (UTCI):** this index was conceived by the International Society of Biometeorology (ISB) (Commission Blazejczyk et al., 2012; McGregor, 2012) in 2002. UTCI index results from the multi segment transient Fiala thermoregulation model (Fiala, 1998), and an adaptative clothing model, considering seasonal clothing adaptation habits of Europeans (clothes resistance ranges ( $I_{clo}$ ) from 0.5 to 2 clo). Equal physiological conditions are calculated based on the equivalence of the dynamic physiological response predicted by the model for the actual and reference environment: walking  $4 \text{ km/h}$  (2.3 met),  $T_{mrt} = T_a$ ,  $v_a(10\text{m}) = 0.5 \text{ m s}^{-1}$ ,  $RH = 50\%$ , levelled off at  $v_p = 20 \text{ hPa}$  ). As the response is multidimensional ( $T_{core}$ ,  $T_{sk}$ , sweat rate at different exposure times) the UTCI is calculated using principal component analysis.  
**Environmental applicability limits:** not used for indoor environment as the model has been established for  $v_a > 0.5 \text{ m s}^{-1}$ .

### A.2.2 Thermoregulation models

Thermoregulation models simulate body heat diffusion and thermoregulatory processes. They're typically divided into two systems: passive, which represents heat exchanges within the body and with the environment, and active, which models thermoregulation. This text discusses the models that established some of the previous heat stress indices:

- **Gagge two node model** (Gagge, Stolwijk, and Nishi, 1971): this model assumes that the human body can be represented as two separate compartments or nodes, each with its own temperature. The two nodes in the model are the skin surface (represented by the  $T_{sk}$ ) and the deep body core (represented by the  $T_{core}$ ). The model considers the heat transfer between the skin surface and the deep body core, as well as the heat transfer between the skin surface and the surrounding environment. Three energy balances are therefore performed: full-body balance, skin balance and core balance. The model can be used on a uniform environment for low or moderate levels of activity and for standard man (81.7 kg, 1.77 m). The SET index is derived from Gagge's model.
- **Munich Energy balance Model for Individuals (MEMI)** (Höppe, 1999a): This model is derived from Gagge's model with an additional balance equation between skin and clothes, a more complete model of heat exchanges with the environment and a different method to calculate the sweat rate. The PET has been created from MEMI. Later, Höppe extended MEMI into a dynamic model, the Instationary Munich Energy Balance Model (IMEM) Katavoutas, Flocas, and Matzarakis, 2015.
- **Fiala's model** (Fiala Fiala, 1998): is a thermoregulation model predicting thermal sensations in transient and non-uniform environments, applicable in wide ranges of temperature and activity. The model divides the body into 15 cylindrical or spherical segments and each segment is divided into three angular sectors (anterior, posterior and inferior) and several layers. The active model has been developed by comparing experiments and the model's results with only the passive system and by regression. The UTCI has been created from a large number of simulations with Fiala's model.

### A.3 Heat wave indices

A correlation exists between the intensity of a heat wave and corresponding heat stress and strain. Interestingly, heat wave indices cannot accurately represent the severity of heat waves and, therefore, the resulting heat stress and strain based on exposure conditions.

The concept of a heat wave is inherently tied to location, climate, and the heat wave's perception. Consequently, due to varying circumstances, there is no standardized definition of a heat wave, and different characterizations have emerged.

For example, the Heat Wave Duration Index (HWDI)(Frich et al., 2002) is used to iden-

tify the occurrence of a heat wave. According to Frich et al. (2002) a heat wave occurs the peak temperatures observed for five consecutive days exceed the highest temperatures recorded between 1961 and 1990 by  $5^{\circ}\text{C}$  yet are less than the maximum period. However, the HWDI has drawn criticism for not factoring in climate variability. WHO defines heat waves as "episodes of unusually hot and dry or hot and humid weather that begin and end imperceptibly, last at least two to three days, and most often produce a significant impact on human health and natural systems" (WHO, 2015). During such periods, both daytime and nighttime temperatures are high (exceeding the local 95th percentile for two or more days), and humidity levels may surpass long-term averages. Separate definitions note a heat wave as occurring when the three-day average of minimum and maximum temperatures exceeds the 99.5 percentile of the distribution of minimum and maximum temperatures, respectively (www.santepubliquefrance.fr).

Heat waves can be classified into two categories based on the perceived temperature ( $T_{th}$ ) and duration ( $dth$ ), as proposed by Amengual et al. (2014).  $T_{th}$  can be considered equivalent to any of the above-mentioned heat stress indices, such as PET, depicted in Figure a.1. The two categories are:

- **Strong Heat Wave (SHW)**: corresponding to a  $dth$  of at least 6 consecutive days where the maximum  $T_{th}$  is over  $35^{\circ}\text{C}$
- **Extreme Heat Wave (EHW)**: corresponding to a  $dth$  of at least 3 consecutive days where the maximum  $T_{th}$  is over  $41^{\circ}\text{C}$  and where the minimum  $T_{th}$  is over  $18^{\circ}\text{C}$

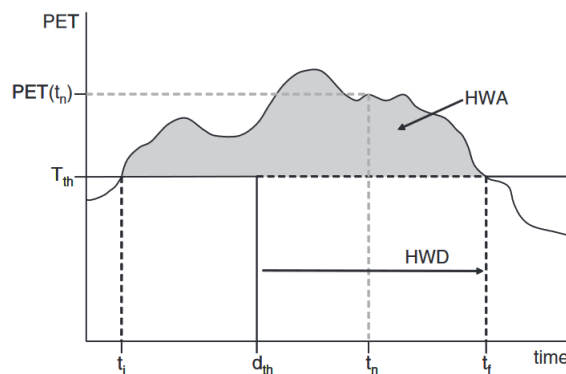


Figure a.1: Graphical sketch of heat wave duration (HWD) and amplitude (HWA, grey shading) exceedances.  $T_{th}$  and  $dth$  denote the thermal stress and duration thresholds, respectively (Amengual et al., 2014).

Accordingly to this last definition, the following indices have been introduced to demonstrate the existing correlation between heat waves and health:

- **Heat Wave Number (HWN)**: corresponding to the number of heat waves occurring in a given time interval (ex. several years, or summer period)
- **Heat Wave Day Frequency (HWDF)**: The number of days under heat wave conditions in a given time interval. **Heat Wave Duration Exceedence (HWD)**: The total number

of consecutive days exceeding the duration threshold for all the heat waves in a given time interval:

$$HWD = HWF - d_{th}HWN$$

- **Heat wave amplitude exceedance (HWA):** Expressed in degree-days, is the accumulation of thermal stress exceedance for all the days under heat wave conditions in a given time interval:

$$HWA = HWT - T_{th}HWF$$

Where HWT is the integral of the PET (Figure a.1) over the duration of each heat wave, and accumulated for all heat waves in a given time interval.

Other indices adapted to indoor heat stress assessment during a heat wave are suggested in the literature (Hooff et al., 2015):

- **Overheating hours:** Corresponds to the number of hours where the felt indoor temperature (ex.  $T_o$ , or PET) is over an upper limit temperature ( $T_{upper}$ ) fixed accordingly to the chosen threshold scale.
- **Degree hour (dhr):** Index used to assess the overheating amplitude. It is defined by the number of overheating hours ( $hr$ ) multiplied by the difference between the felt temperature (e.g.  $T_o$ , or PET) and the limit temperature  $T_{upper}$  when the latter is lower than the felt temperature:

$$dhr = hr(PET - T_{upper})$$



## B Dynamic response of $T_{core}$ in JOS-3 model

### B.1 Response of the $T_{core}$ over the long time step evolution of $T_a$

In order to observe the stabilization time of the  $T_{core}$  in the JOS-3 model, a  $3^\circ\text{C}$  positive and negative variation of the  $T_a$ , within three time steps of of 8h are studied: In the first time step the  $T_a = 30^\circ\text{C}$ , in the second  $T_a = 33^\circ\text{C}$  and in the last  $T_a = 30^\circ\text{C}$ . The variation of  $3^\circ\text{C}$  corresponds to the maximum outdoor air temperature variation observed in an interval of one hours during the summer using the local Confluence (Lyon) weather file.

To evaluate the stabilization time of the  $T_{core}$  in the JOS-3 model, we study a fluctuation of  $3^\circ\text{C}$  above and below the ambient temperature ( $T_a$ ) over three 8-hour intervals: initially,  $T_a$  equals  $30^\circ\text{C}$ , then it increases to  $33^\circ\text{C}$  and finally returns to  $30^\circ\text{C}$ . This  $3^\circ\text{C}$  fluctuation mirrors the peak changes in the outdoor air temperature recorded within an hour during summer, as per the local Confluence (Lyon) weather file

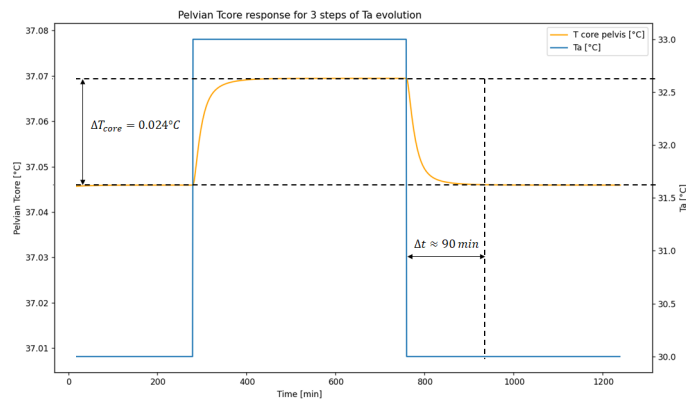


Figure a.2: Evolution of the  $T_{core}$  in the JOS-3 model under  $T_a$  variation from  $30^\circ\text{C}$  to  $33^\circ\text{C}$  and from  $33^\circ\text{C}$  to  $30^\circ\text{C}$ .

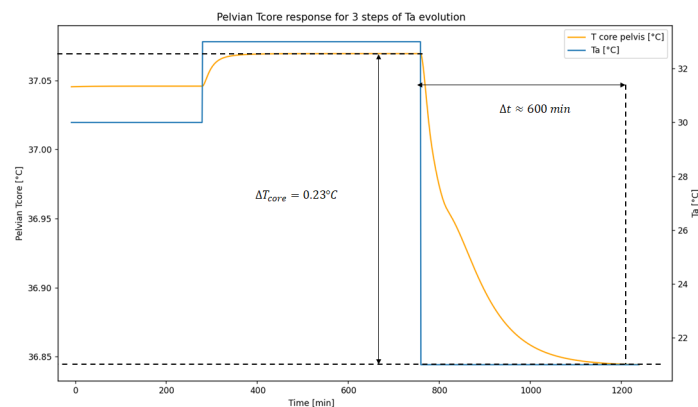


Figure a.3: Evolution of the  $T_{core}$  in the JOS-3 model under  $T_a$  variation from  $30^\circ\text{C}$  to  $33^\circ\text{C}$  and from  $33^\circ\text{C}$  to  $21^\circ\text{C}$ .

Figure a.2 illustrates the initial 120 min needed for the  $T_{core}$  to stabilize and discard the

impact of the starting condition. It then takes approximately 90 min for the  $T_{core}$  to stabilize following a positive or negative 3 °C temperature adjustment ( $T_a$ ). This challenges the appropriateness of steady thermoregulation models when climate exposure parameters fluctuate within a 90-min timeframe. However, if the  $T_a$  alterations in the exposure environments are no more than 3 °C, the related  $T_{core}$  variation is under 0.03 °C. In such cases, the use of steady thermoregulation models is acceptable.

Conversely, as depicted in Figure a.3, when the amplitude of the exposure environment's temperature variation exceeds 10 °C – for example, transitioning from a hot outdoor environment to a conditioned indoor environment – the stabilization time for  $T_{core}$  is prolonged, approximately 600 min, and its variation is more significant, around 0.23 °C. In contrast, a steady thermoregulation model directly provides the  $T_{core}$  value attained in a steady state. It is also important to note that, particularly in outdoor settings, an individual rarely remains stationary for extended periods and tends to be more mobile.

Therefore, it can be concluded that the greater the amplitude of environmental temperature variation, the more appropriate dynamic thermoregulation models become.

## C Richardson number in thermal convection problem

The Richardson number ( $Ri$ ) is used to determine the balance between buoyancy forces and wind-driven forces (Mei and Yuan, 2022). Typical values range from 0.1 to 10, with values below one suggesting considerable turbulence (Skybrary). When dealing with thermal convection issues, the  $Ri$  number signifies the importance of natural convection compared to forced convection. Here, the  $Ri$  number is denoted by the following ratio:

In this context the  $Ri$  number is expressed by the following ratio:

$$Ri = \frac{Gr}{Re^2} \quad (.2)$$

where  $Gr$  is the Grashof number and  $Re$  is the Reynolds number.

$$Gr = \frac{g\beta H^3(T_s - T_{ref})}{\nu^2} \quad (.3)$$

$$Re = \frac{vH}{\nu} \quad (.4)$$

Where  $g[\text{m s}^{-2}]$  is the gravitational constant,  $\beta = \frac{1}{\rho} \frac{\partial \rho}{\partial T_z} [\text{K}^{-1}]$ , is the expansion coefficient, where  $\rho[\text{kg/m}^3]$  is the air density and  $T_z[\text{K}]$  the potential temperature. The expansion coefficient is evaluated for a constant pressure at ambient or free-stream temperature,  $T_s[\text{K}]$  and  $T_{ref}[\text{K}]$  are respectively the surface temperature and the air temperature next to the surface,  $\nu[\text{m}^2 \text{s}^{-1}]$  is the air cinematic viscosity,  $H[\text{m}]$  is the characteristic length,  $v[\text{m s}^{-1}]$  is the wind speed.

Typically, natural convection is negligible for  $Ri < 0.1$ , forced convection is negligible when  $Ri > 10$ , and neither is negligible when  $0.1 < Ri < 10$ . The  $Ri$  calculated here is based in the following hypothesis:  $T_s$  and the  $T_{ref}$  corresponds to the average surface temperatures

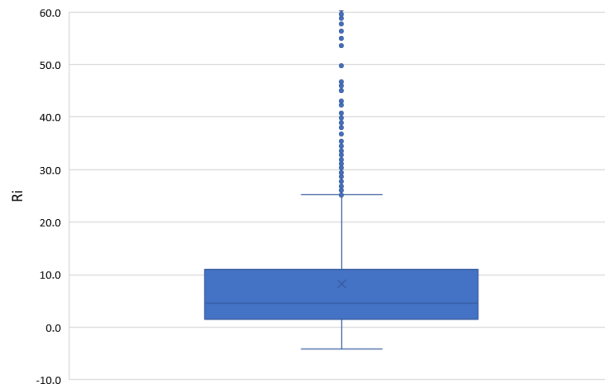


Figure a.4: Plot box of the Richardson number calculated based on the hypothesis described above from June to September 2020.

and the average adjacent air zones temperatures resulting from the dynamic simulation of

the microclimate model for the zonal model described in Chapter 3 and the base case study described in Chapter 5 and is assumed  $\beta = 1/T_{ref}$  (its average value is here of 0.0037). The characteristic length  $H$  is fixed to 27 m, corresponding to the highest building and the wind speed corresponds to the wind speed provided in the Lyon Confluence weather file.

Figure a.4 shows a plot box of the Richardson number calculated during the summer season from June to September 2020. The values are predominantly located between 1.55 and 11 where both natural and forced convection are present (Garbrecht, 2017).

## D Velocity profile at a specific point in the domain

We aim to investigate the correlation between wind speed and orientation at the domain inlet and the wind velocity at a specific location within this domain. Specifically, we will analyze changes in wind speed at point  $V_1$  in an  $(x, y)$  plane at varying heights ( $z$ ). Two scenarios will be considered: one where the inlet wind speed ( $V_{10}$ ) is varied while the wind direction remains constant, and another where the inlet wind direction is varied while the wind speed remains constant.

### D.1 Variation of inlet wind speed with constant inlet wind direction

The wind speed  $V_{10}$  at the inlet ranges from  $1 \text{ m s}^{-1}$  to  $7 \text{ m s}^{-1}$ , with a wind direction of  $\beta = 180^\circ N$  (Figure a.5 (a)).

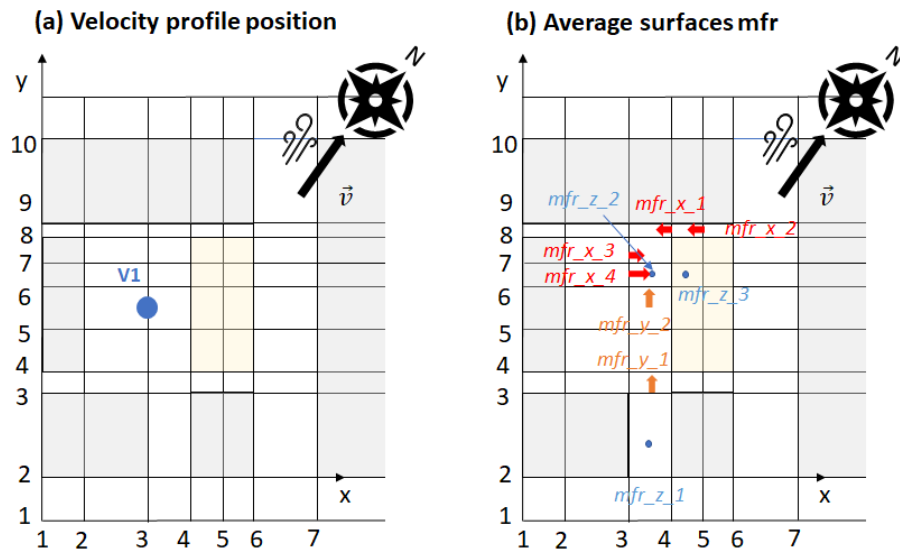


Figure a.5: Location of (a) the  $V_1$  wind profile and (b) average surface  $mfr$  in the  $(xy)$  plan for a wind coming from South to North.

Figure a.6 illustrates a nearly linear correlation between the velocity at a specific point within an area and the velocity at the inlet, given the wind direction. This correlation also applies to mass flow rate ( $mfr$ ). Figure a.7 emphasizes the linear relationship between the velocity at the inlet ( $V_{10}$ ) and the calculated average  $mfr$  from CFD simulations on different surfaces of the zone (Figure a.5(b)) with a cross-section at  $z = 3 \text{ m}$ . Given this direct correlation and that the line passes through the origin, it is feasible to choose a single velocity point to construct the DOE for a specific orientation.

## D. Velocity profile at a specific point in the domain

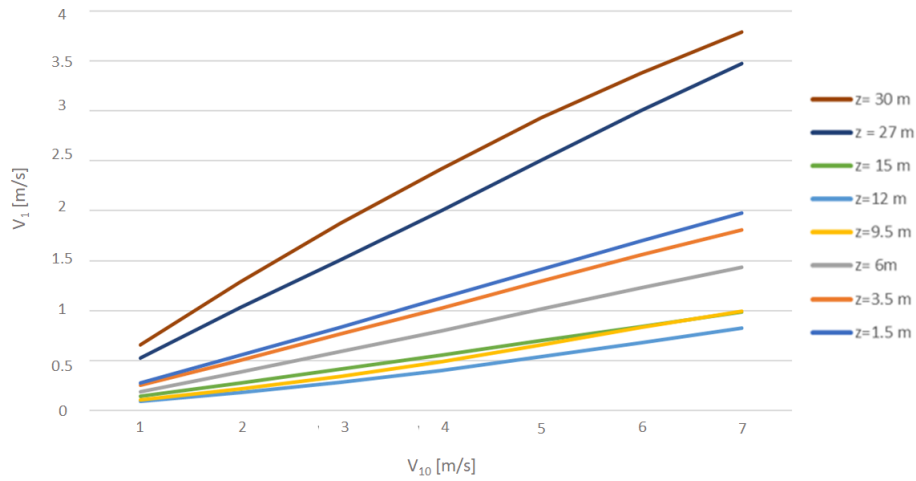


Figure a.6: Evolution of the wind speed at different heights in  $V_1$  as a function of the inlet wind speed  $V_{10}$  for a constant inlet wind direction ( $\beta = 180^\circ$  N).

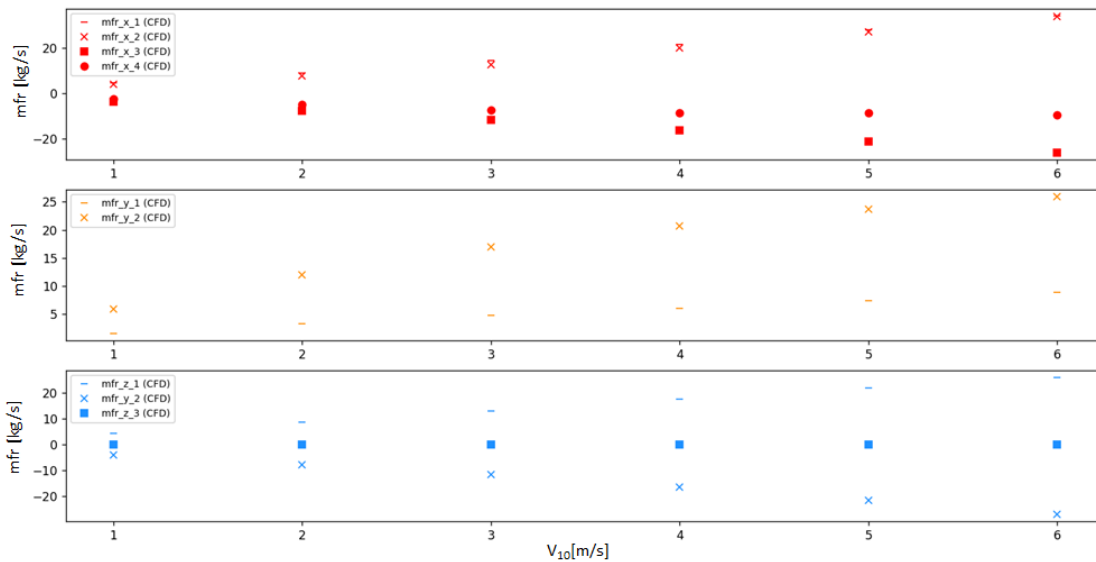


Figure a.7: Evolution of the average  $mfr$  across different air zone surfaces.

## D.2 Variation of inlet wind direction with constant inlet wind speed

The wind direction at the inlet fluctuates between  $150^\circ$ ,  $160^\circ$ ,  $170^\circ$ ,  $180^\circ$ ,  $190^\circ$ ,  $200^\circ$ ,  $210^\circ$  relative to the North, with an inlet wind speed  $V_{10} = 2 \text{ m s}^{-1}$ . As depicted in Figure a.8, discerning a definitive relationship between the wind direction at the domain inlet and the velocity at various points within the domain is challenging. This is largely due to the varying geometric configuration of the surrounding environment at specified points. Accordingly, it is advised to initially select narrower wind direction intervals for the DOE. These can then be further refined if necessary. For our study, we've chosen an interval of  $5^\circ$  N.

## D. Velocity profile at a specific point in the domain

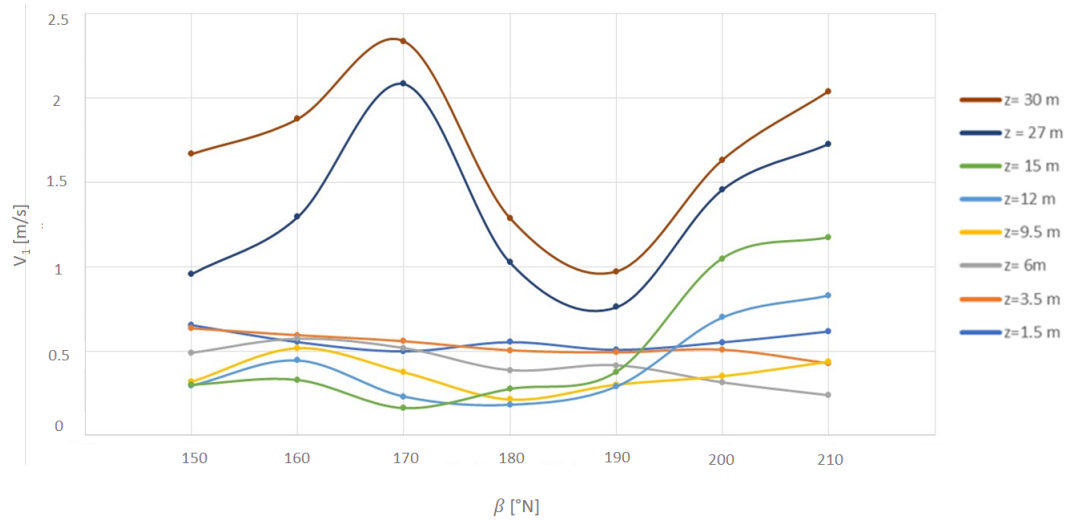


Figure a.8: Evolution of the wind speed at different heights in  $V_1$  as a function of the inlet wind direction  $\beta$  for a constant inlet wind speed ( $V_{10}$ )= $2 \text{ m s}^{-1}$ .

## E DOE segmentation

This appendix presents a segmentation of DOE obtained by applying the method described in Section 3.1.2

Plan	Nbr points	Wind speed ranges [m/s]	Wind direction ranges[°]	Train values [v10,β]	Test values [v10,β]
I a (SSO-O)	14	[0.2, 3]	[200, 270]		
I b (SE-SOS)	11	[0.2, 6]	[140,200]	[4.5,155] [1.3,159] [2.4,162] [3.5,166] [3.1,170] [0.9,177] [4.9,181] [1.6,185] [1.3,189] [5.3,193] [0.6,196]	[2,160] [1,180] [2,180] [3,180] [4,180] [5,180] [6,180] [2,150]
I c (E-SE)	12	[0.2,2]	[90,140]		
II a (O-ONO)	10	[0.2, 2.5]	[270,320]		
II b (ONO-N)	7	[0.2,3.8]	[320,360]	[1.7,323] [1.1,330] [1.4,335] [1.9,340] [1.5,343] [1.7,346] [2.6,353]	
II c (N-NE)	10	[0.2,5]	[0,50]		
II d (NE-E)	8	[0.2,2.5]	[50,90]		

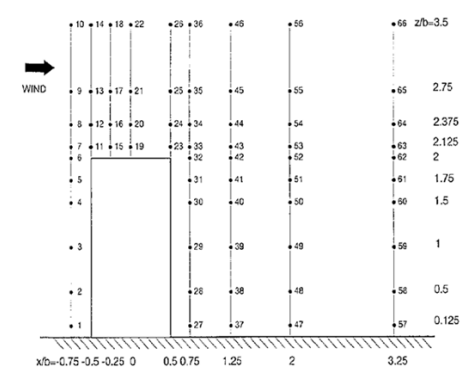
Figure a.9: DOE segmentation for different ranges of wind speed and direction.



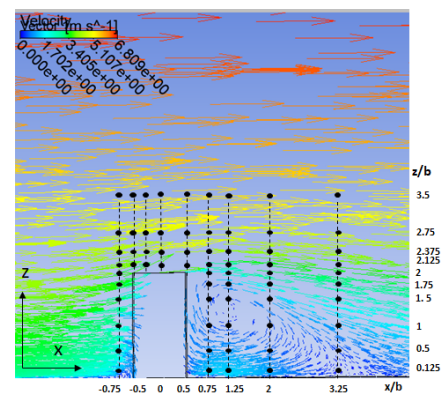
## F Comparison of CFD results with the isolated building experiment

In this appendix are reported the results referring to the experiment described in the Section 3.1.3.1.

### F.0.1 Wind profile for XZ vertical section



(a) Point of measure of the square prism experiment.



(b) Airflow simulated by CFD  $k - \epsilon$  in the reproduction of the square prism experiment.

Figure a.10: Measurement points - Vertical section (Meng and Hibi, 1998).

## F. Comparison of CFD results with the isolated building experiment



Figure a.11: Wind profile for XZ vertical section (Part I : from  $x=-0.75b$  to  $0.5b$ ). Average RNMSE on  $x = 0.89$ , on  $y = 7.08$  on  $z = 1.70$ . Average error relative to  $U_0$  on  $x = 9.6\%$ , on  $y = 0.9\%$  on  $z = 4.9\%$ .

## F. Comparison of CFD results with the isolated building experiment

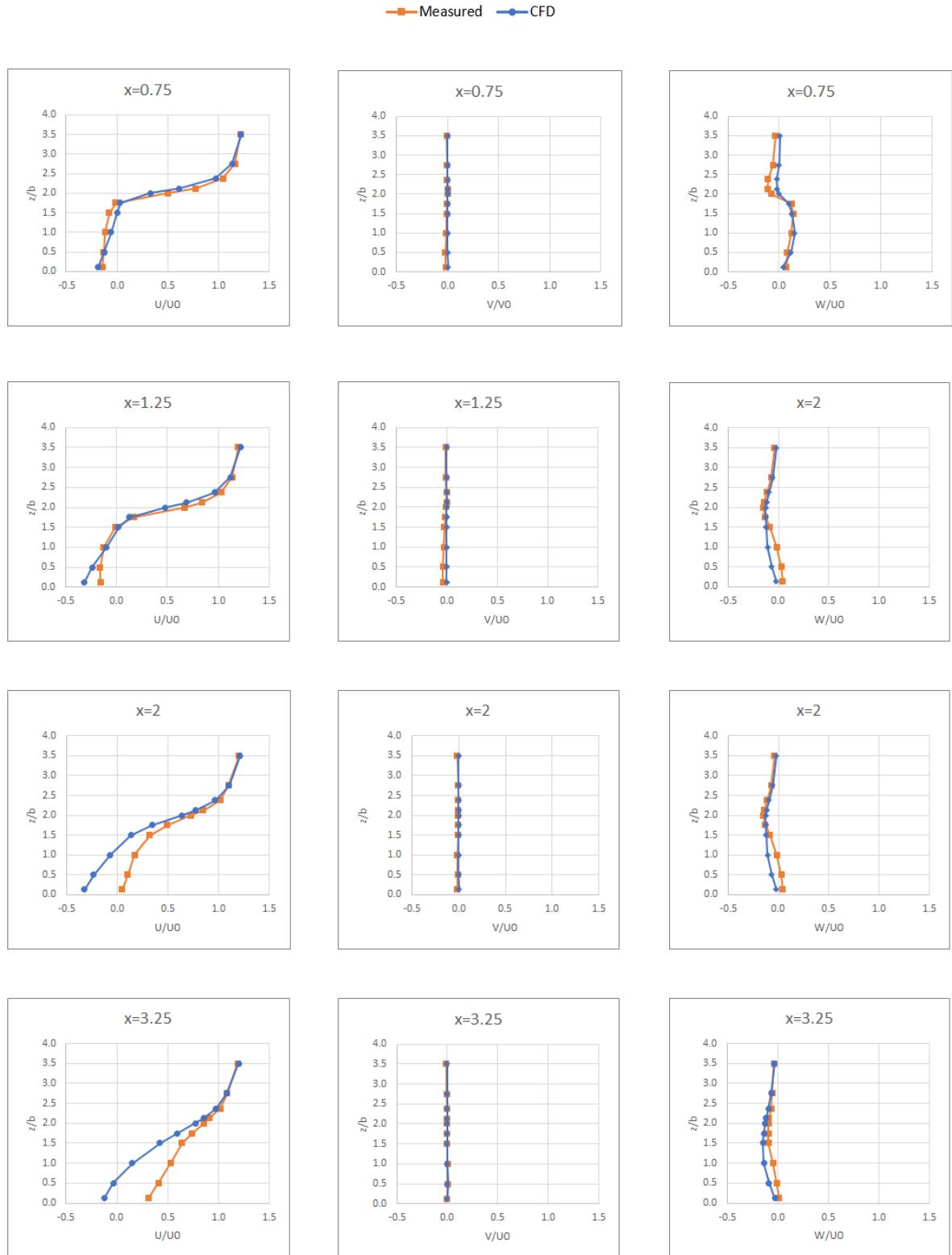
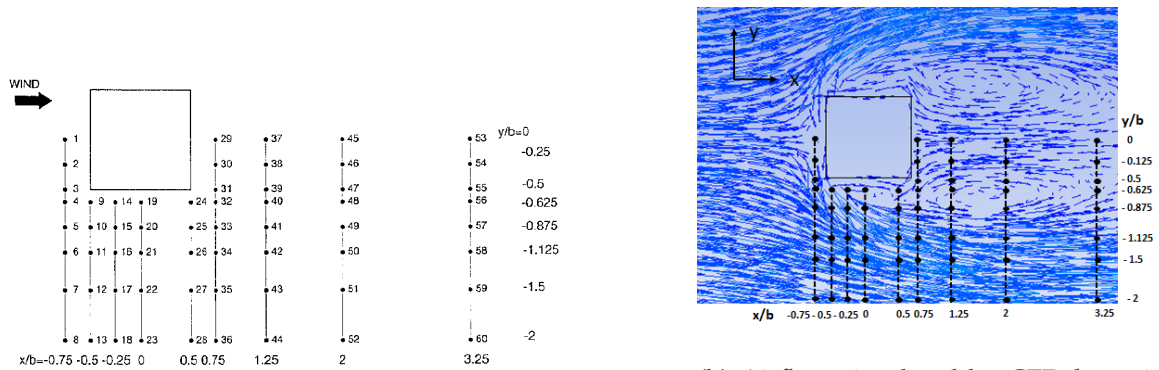


Figure a.12: Wind profile for XZ vertical section (Part II : from  $x=0.75b$  to  $3.25b$ ). Average RNMSE on  $x = 0.89$ , on  $y = 7.08$  on  $z = 1.70$ . Average error relative to  $U_0$  on  $x = 9.6\%$ , on  $y = 0.9\%$  on  $z = 4.9\%$ .

F.0.2 Wind profile for XY horizontal section in  $z=0.125b$



(a) Points of measure of the square prism experiment.

(b) Airflow simulated by CFD  $k - \epsilon$  in the reproduction of the square prism experiment.

Figure a.13: Measurements points - Horizontal section ( $z=0.125b$ ) (Meng and Hibi, 1998).

## F. Comparison of CFD results with the isolated building experiment

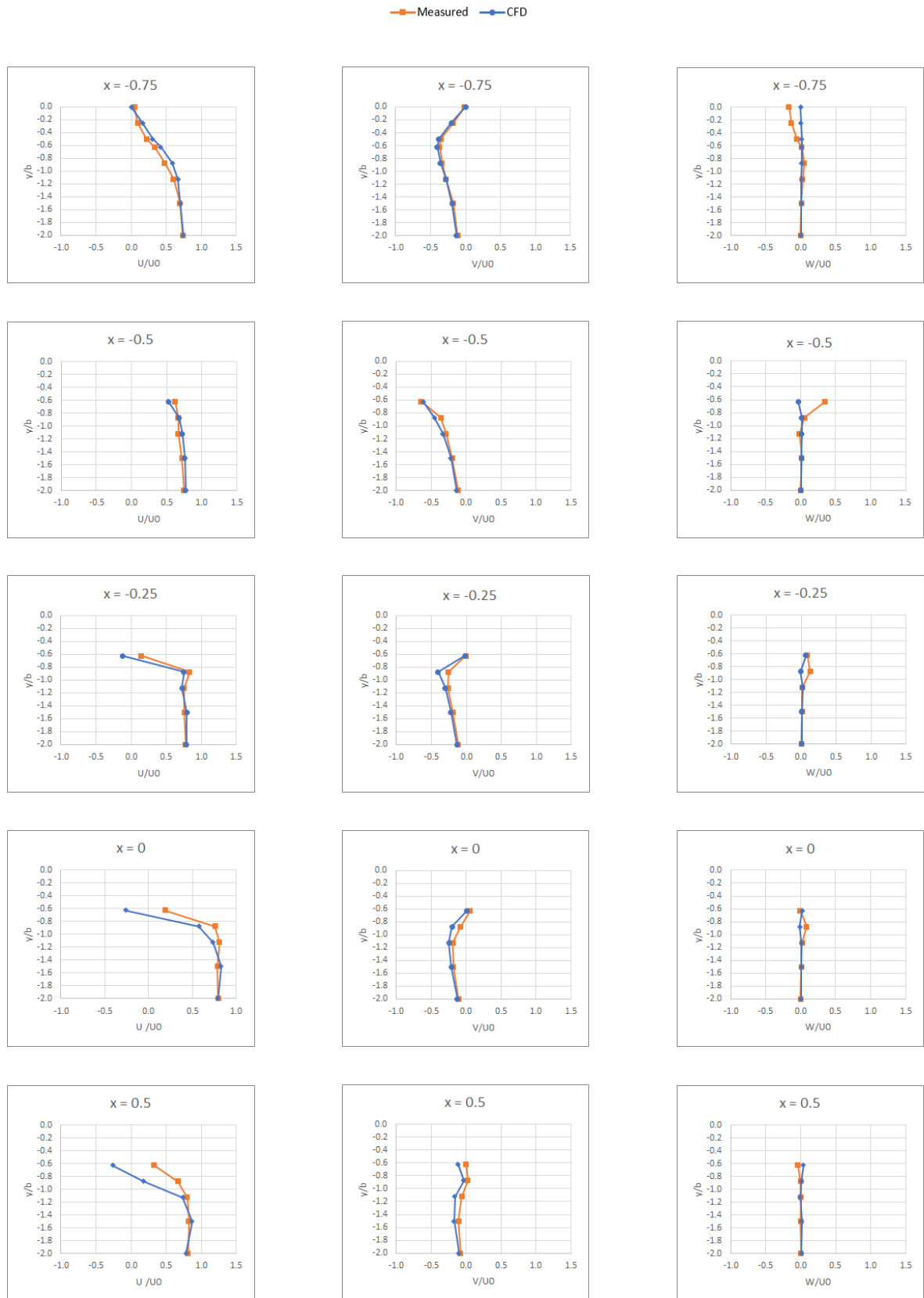


Figure a.14: Wind profile for xy section, (Part I: from  $x = -0.75b$  to  $0.5b$  and  $z = 0.125b$ ). Average RNMSE on  $x = 0.88$ , on  $y = 1.49$  on  $z = 2.9$ . Average error relative to  $U_0$  on  $x = 20.0\%$ , on  $y = 4.6\%$  on  $z = 3.6\%$ .

## F. Comparison of CFD results with the isolated building experiment

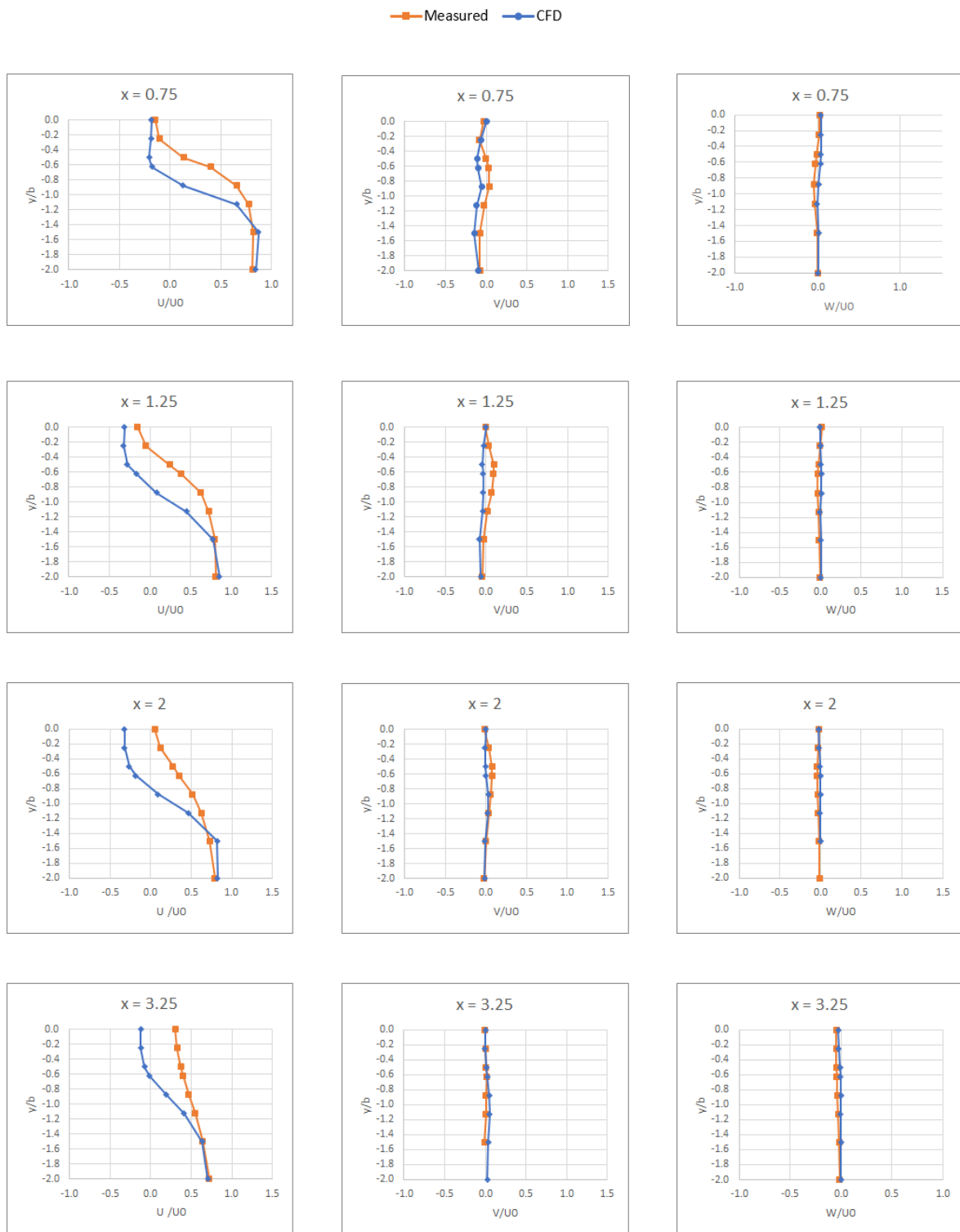
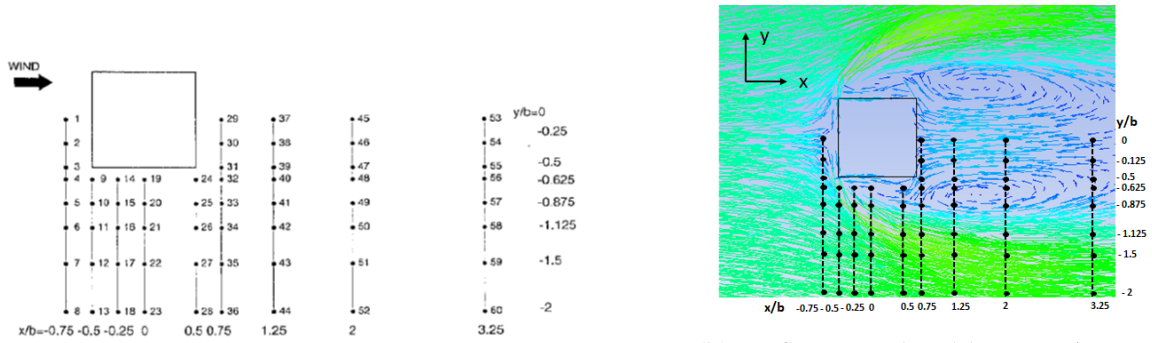


Figure a.15: Wind profile for xy section, (part II, from  $x=0.125b$  to  $3.25b$  and  $z=0.125b$ ). Average RNMSE on  $x = 0.88$ , on  $y = 1.49$  on  $z = 2.9$ . Average error relative to  $U_0$  on  $x = 20.0\%$ , on  $y = 4.6\%$  on  $z = 3.6\%$ .

F.0.3 Wind profile for XY horizontal section in  $z=1.25b$



(a) Point of measure of the square prism experiment.

(b) Airflow simulated by CFD  $k - \epsilon$  in the reproduction of the square prism experiment.

Figure a.16: Measurements points - Horizontal section ( $z=1.25b$ ) (Meng and Hibi, 1998).

## F. Comparison of CFD results with the isolated building experiment

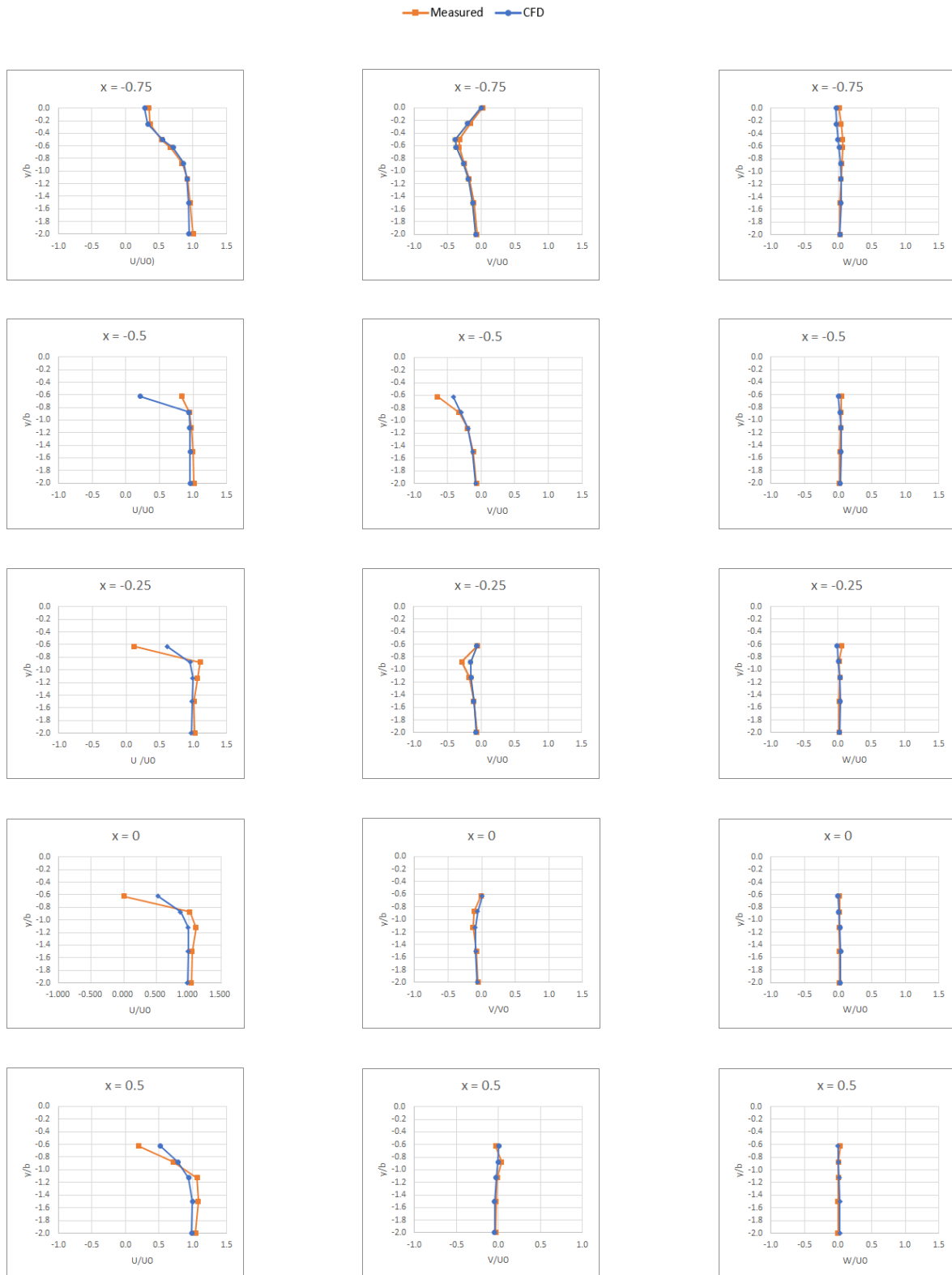


Figure a.17: Wind profile for xy section, (Part I: from  $x=-0.75b$  to  $0.5b$  and  $z=1.25b$ ). Average RNMSE on  $x = 0.78$ , on  $y = 1.7$  on  $z = 1.8$ . Average error relative to  $U_0$  on  $x = 10.6\%$ , on  $y = 3.4\%$  on  $z = 2.6\%$ .



## F. Comparison of CFD results with the isolated building experiment

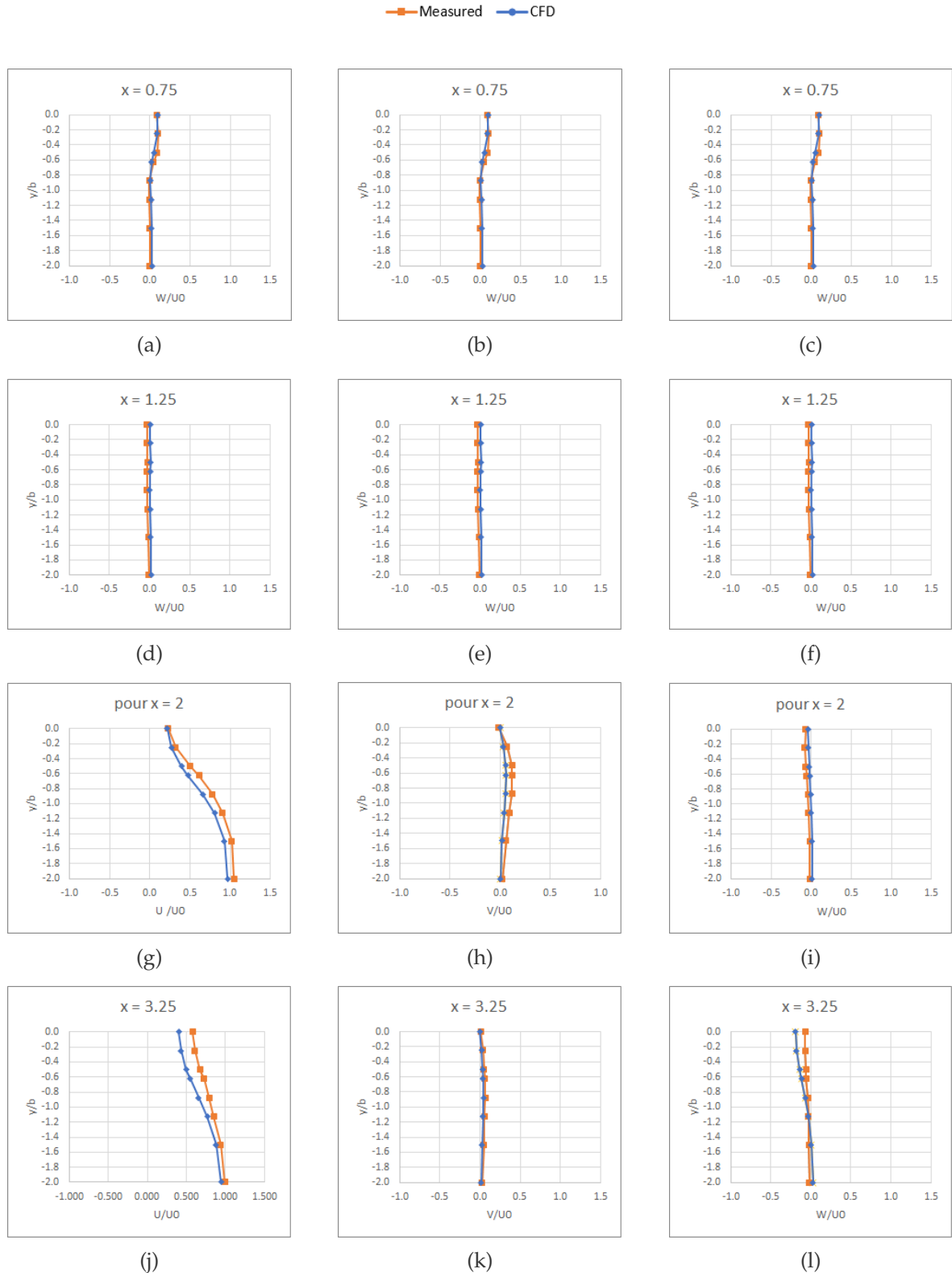


Figure a.18: Wind profile for xy section, (Part II: from  $x=0.75b$  to  $3.25b$  and  $z=0.125b$ ). Average RNMSE on  $x = 0.78$ , on  $y = 1.7$  on  $z = 1.8$ . Average error relative to  $U_0$  on  $x = 10.6\%$ , on  $y = 3.4\%$  on  $z = 2.6\%$ .

## G Building model - Conduction model comparison

In Figures a.19 and a.20, the irradiations of SWR and LWR on walls A and B, roof, and floor are depicted for both McZM and Monte Carlo models, referring to the case study presented in section 4.4.

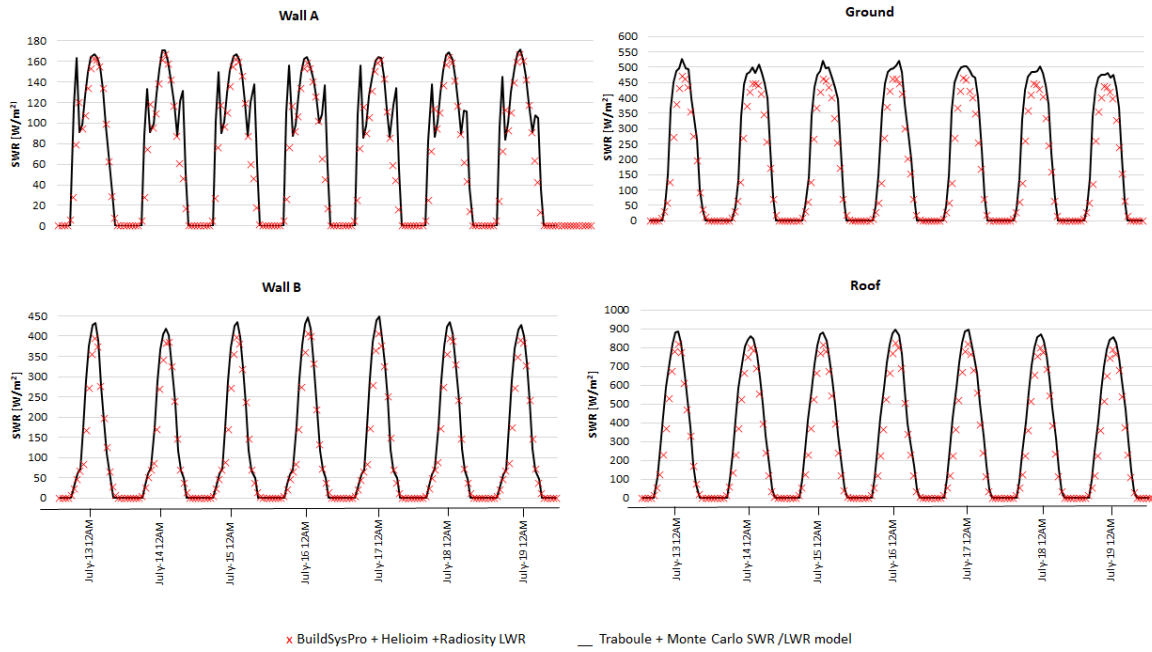


Figure a.19: SWR on Wall A, Wall B, Roof A and Ground.

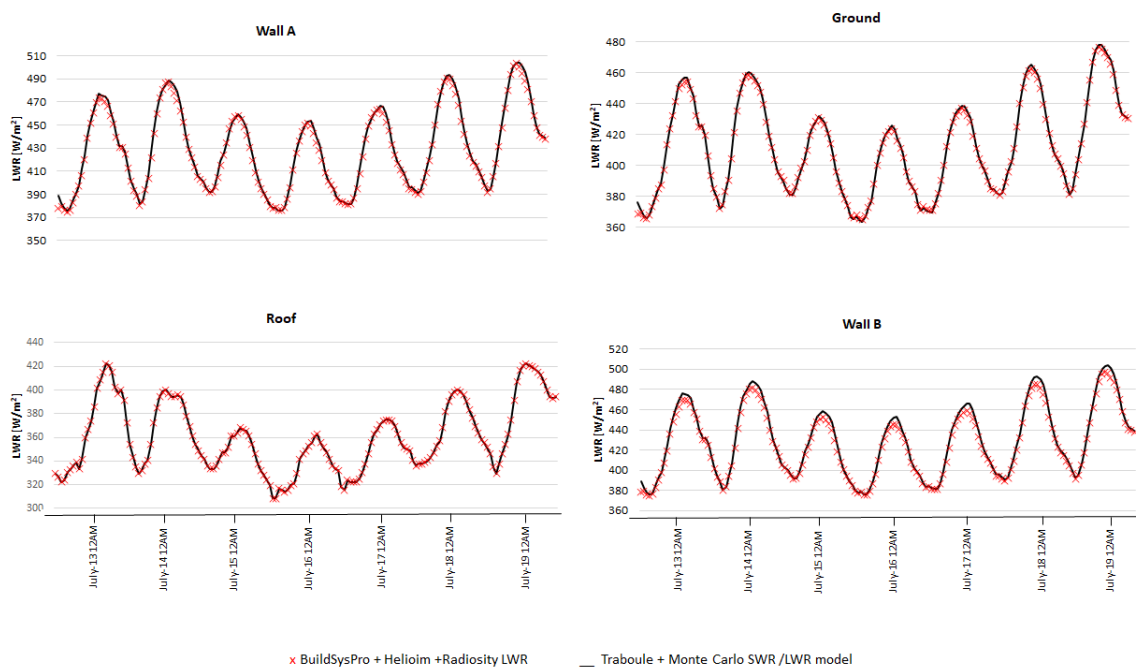


Figure a.20: LWR on Wall A, Wall B, Roof A and Ground.

## H Soil model - Penman-Monteith equation

In this section, the reasoning behind the derivation of the Penman-Monteith equation is explained in detail. The global surface balance of an evaporating soil can be expressed as follows:

$$R = H + G + LE \quad (.5)$$

Where  $R[\text{W m}^{-2}]$  is the net incoming or outgoing radiative flux,  $H[\text{W m}^{-2}]$  is the sensible heat flux,  $G$  is the conductive heat flux and  $LE[\text{W m}^{-2}]$  is the latent heat flux. From the existing proportionality relationship between the variation in sensible flux and the variation in latent flux, it is possible to introduce the Bowen ratio  $B$ , which represents the ratio of sensible flux to latent flux:

$$B = \frac{H}{LE} \quad (.6)$$

For an ideal gas, the variation in enthalpy (or sensible heat)  $dH$  is proportional to the variation in temperature  $dT$ :

$$dH = \gamma dT \quad (.7)$$

Moreover, the variation in latent heat flux is proportional to the variation in vapour pressure  $v_p$  [kPa].  $dv_p$  is the vapour pressure deficit at saturation (the difference between the saturated vapour pressure at the water surface and the vapour pressure of the air):

$$dLE \propto dv_p \quad (.8)$$

Equations .6, .7 and .8 yield the following relationship, where the  $T_{sw}$  K is the wet-bulb temperature,  $T_a$  K is the air temperature,  $v_{ps}^*$  [kPa] is the saturated vapour pressure at the surface temperature and  $v_{pa}$  [kPa] is the vapour pressure at air temperature:

$$B = \gamma \frac{T_{sw} - T_a}{v_{ps}^* - v_{pa}} \quad (.9)$$

Substituting .9 and .6 into .5 yield the following equation:

$$LE = \frac{R - G}{1 + \gamma \frac{T_{sw} - T_a}{v_{ps}^* - v_{pa}}} \quad (.10)$$

Evaporation  $E$  can be estimated by Dalton's equation, published in 1802, as a function of wind speed  $v$   $\text{m s}^{-1}$ :

$$E = f_D(v)(v_{ps}^* - v_{pa}) \quad (.11)$$

In 1948, Penman defined  $E_v$  as the value of evaporation  $E$  obtained by replacing  $v_{ps}^*$  with  $v_{pa}^*$ , the saturated vapour pressure at air temperature:

$$E_v = f_D(v)(v_{pa}^* - v_{pa}) \quad (.12)$$

By denoting  $E_0$  the evaporation obtained using the Dalton's equation .11, Penman established the following relationship:

$$\frac{E_v}{E_0} = \frac{f_D(v) (v_{p_a}^* - v_{p_a})}{f_D(v) (v_{p_s}^* - v_{p_a})} \quad (.13)$$

In simplified form, this yields to:

$$\frac{E_v}{E_0} = 1 - \frac{(v_{p_s}^* - v_{p_a}^*)}{(v_{p_s}^* - v_{p_a})} \quad (.14)$$

Penman assumes that the slope of the vapour pressure curve  $\Delta \text{kPa K}^{-1}$  is directly proportional to the difference between the saturation vapour pressure of water and the saturation vapour pressure of air, and inversely proportional to the difference in surface water temperature:

$$\Delta = \frac{(v_{p_s}^* - v_{p_a}^*)}{(T_{sw} - T_a)} \quad (.15)$$

Furthermore,  $\Delta$  is defined as follows:

$$\Delta = \frac{4098 v_{p_a}^*}{T_a^2} \quad (.16)$$

The Penman-Monteith equation is then obtained by replacing .15 in .10:

$$LE_0 = \frac{\Delta(R - G) + L\gamma E_v}{\Delta + \gamma} \quad (.17)$$

By replacing  $E_v$  with:

$$E_v = f(v)(v_{p_a}^* - v_{p_a}) \quad (.18)$$

with:

$$f_D(v) = \frac{1}{L} \frac{\rho_a C_a}{r_a} \frac{1}{\gamma} \quad (.19)$$

and:

$$\gamma = \frac{v_{p_a}^* - v_{p_a}}{T_a - T_{aw}} \quad (.20)$$

Equation .17 can be written as follows:

$$LE_0 = \frac{\Delta(R - G) + \frac{\rho_a C_a (v_{p_a}^* - v_{p_a})}{r_a}}{\Delta + \gamma} \quad (.21)$$

When foliage is present, the evaporation rate decreases. This is represented by a term in the equation's denominator that stands for the foliage resistance. This resistance is proportionate to the stomatal resistance and inversely related to the LAI:

$$LE_0 = \frac{\Delta(R - G) + \frac{\rho_a C_a (v_{p_a}^* - v_{p_a})}{r_a}}{\Delta + \gamma \left(1 + \frac{r_c}{r_a}\right)} \quad (.22)$$

When the surface temperature is known, the evaporation  $E_0$  can be directly estimated by replacing equation .20 (adding a stomatal resistance) with Dalton's equation .11 :

$$E_0 = \frac{\rho_a C_a}{L} \frac{(v_{p_s}^* - v_{p_a})}{\gamma(r_a + rc)} \quad (.23)$$

## I Individuals' cooling measures implementation in BEMs

This appendix evaluates how accurately current McM and BEM replicate the cooling techniques observed in a field survey by Marianna Fontaccia in Lyon during the summer of 2022. This survey is a component of a Master's internship project at ENS (Ecole Normale Supérieure) Lyon and Université Lumière Lyon 2. The main objectives were to identify the cooling strategies homeowners use during extreme heat, understand the various actors involved in implementation, and pinpoint the challenges and enabling factors associated with these practices.

The survey involved 29 residents from three distinct residential buildings in Lyon, along with private and institutional participants who take part in executing special adaptive measures during heatwaves. These participants also participate in energy renovation projects and funding of high-efficiency energy devices.

### Main survey findings

This survey highlighted social inequalities relevant to the use of cooling methods from a social sciences perspective. One inequality involves the affordability of air conditioning due to financial circumstances and tenancy restrictions. Another involves the challenges faced by isolated and economically disadvantaged individuals in accessing cool shelters. Cost also prevents these individuals from implementing thermal refurbishments.

These socio-economic factors impact thermal lifestyles and practices. Migration to outdoor "refuge spaces" like parks, air-conditioned areas, and secondary homes in the countryside offers a widespread solution, although economic disparity affects how it is implemented (Molina, 2022). Those facing financial challenges cannot afford to relocate to such cooler places outside the city. The most disadvantaged are often limited to finding cooler spots within their homes, while some remain in dark indoor spaces. Therefore, the responsibility falls on urban planners to minimize social inequalities by designing accessible, cool public spaces.

The survey also shed light on how nearby urban contexts, building layouts, and thermal properties can obstruct certain practices. It questions the adaptation of traditional construction methods intended for winter comfort to address summer comfort issues (discomfort caused by loggias, openings unsuitable for mosquito screens, and materials with very low albedo). The optimization of public spaces to reduce noise pollution is also under scrutiny.

In collective residential buildings, collective approval is needed for measures that affect the building's structure and common areas (facade renovation, facade greening, centralized heating or cooling systems, installation of solar shades), which is hard to achieve unanimously. Moreover, the process of obtaining subsidies involves complex administrative procedures, which can be off-putting. These factors serve as significant obstacles to

implementing collective practices.

In conclusion, individuals commonly adopt methods that are easy to implement, accessible, and provide immediate thermal effects, such as shading windows to reduce solar heat, opening windows or doors to invite airflow, using fans, moving to cooler locations, taking showers, and reducing physical activities.

The survey's measures only address residential areas, with no mention of common areas around the building. This could be due to the limited possibility of implementing outdoor cooling measures or because residents may not care about such spaces. That said, this issue was not investigated.

### **Implementation of cooling adaptive measures in BEMs**

Figures a.21 and a.22 illustrate the cooling practices as reported in Marianna Fontaccia's interviews. These practices align with the categories suggested in Section 2.2, differentiating between "exposure-oriented" (Figure a.21) and "individual-oriented" (Figure a.22) practices. Within these categories, various classifications, such as grey, blue, green, and orange solutions, are identifiable. The demand for modelling is detailed in the second column, with the third indicating the extent to which current BEMs or McMs encompass the reported practices. The fourth column highlights the restrictions of existing BEMs in portraying the practice and pinpoints any necessary progressions. The requirements include three aspects: input data, the development of new models, and novel modelling approaches. Lastly, the multidimensional nature of the measure is shown in the fifth column, specifying the potential models that could be employed.

The cross-analysis sheds light on some limitations associated with current BEMs. These constraints impact both the ability to quantify thermal environments and evaluate the heat stress and strain experienced by individuals. Apart from long-term solutions like insulation or air conditioning installation, modelling individual behaviour is essential for any temporary practice.

This modelling process entails integrating BEMs or McMs with behavioural models drawn from the social sciences. Moreover, when behaviour involves moving to cooler areas, agent-based models should be considered. These models allow for an examination of the interaction between the agents and their environment, suggesting a three-tier model coupling: BEMs, McMs, and agent-based models.

Thermo-physiological models are necessary for studying the effects of individual-based practices on heat stress. Some BEMs include thermal stress indices that are applicable in nearly stable environmental settings. However, when climate variables vary rapidly - as is the case when moving from a hot to a cool location - it is essential to use transient models of human thermoregulation to account for heat strain and stress. In these instances, integrating these models with BEMs or urban McMs should be considered.

## I. Individuals' cooling measures implementation in BEMs

---

Moreover, with the rising prevalence of personal cooling practices like evaporative cooling (such as using a wet sheet, creating a water layer on the ground, installing mosquito nets, localized fan usage, and so on), there's a justified need for creating new physical models within the BEMs themselves. This underscores the growing necessity for interdisciplinary modelling approaches.



EXPOSURE ORIENTED 	MODELLING NEEDS	AVAILABLE IN CURRENT BEM or Microclimate models	LIMITS / REQUIRED DEVELOPMENTS	MULTIDISCIPLINARITY
 Closing shutters	Indoor / outdoor radiative exchange + blinding schedules	Partial in BEM	<b>Input data:</b> need to know individual practices in relation to opening/closing schedules. A behavioral model is needed.	<b>Multidisciplinarity:</b>  BEM ↔ Social Model
 Parasols	Indoor / outdoor radiative exchange	Available in BEM and in Microclimate models		
 Windows / door opening and application of mosquito netting	Indoor / outdoor airflow (with or without mosquito netting) + opening schedules +	Partial in BEM and Microclimate models	<b>Input data:</b> need to know individual practices in relation to opening/closing schedules, opening form and fraction. A behavioral model is needed. <b>New development:</b> specific development to consider the impact of mosquito netting on airflow.	<b>Multidisciplinarity:</b>  BEM ↔ Social Model
 Hanging wet sheets	Evaporation from a wet sheet	Not available in BEM	<b>Input data:</b> need to quantify schedules and physicals model input data. A behavioral model is needed. <b>New development:</b> specific development for indoor	<b>Multidisciplinarity:</b>  BEM ↔ Social Model
 Wetting the soil	Evaporation of a layer of water on the soil	Not available in BEM		
 Air conditioning	Cooling and dehumidification	Available in BEM		
 Building envelope insulation	Surface and air heat balance	Available in BEM		
 Reduction/ displacement of heat-sources (plancha / oven ...)	Indoor / outdoor heat sources in the air energy balance + application schedules	Partial in BEM and microclimate models	<b>Input data:</b> need to quantify heat sources reductions and the schedules. A behavioral model is needed.	<b>Multidisciplinarity:</b>  BEM ↔ Social Model

Figure a.21: Identification of BEM needs corresponding to exposure-oriented cooling measures from the local survey.

I. Individuals' cooling measures implementation in BEMs


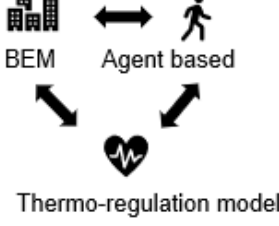

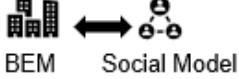

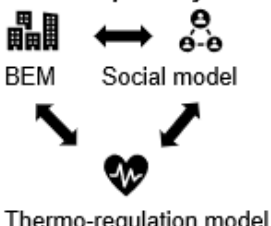

INDIVIDUAL ORIENTED	MODELLING NEEDS	AVAILABLE IN CURRENT BEM or Microclimate models	LIMITS / REQUIRED DEVELOPMENTS	MULTIDISCIPLINARITY
 Moving to cooler locations within the dwelling or indoor / outdoor displacements	Evolution of indoor exposure environments based on individual displacements + Impact on heat stress	Partial in BEM and microclimate models	<b>Input data:</b> need to know the displacement schedule. A behavioral model is needed. <b>Modelling approach</b> Need of coupling agent base model and with BEM. Current BEM only consider heat stress in the basis of steady index. When moving to rapid changing environments a coupling with transient thermo-regulation models is needed	Combining agent-based modelling approach with BEM and thermoregulation model  <b>Multidisciplinarity:</b> 
 Fan use	Local airflow generated by the fan + Impact on heat stress (steady approach)	Not available in BEM	<b>Input data:</b> need to know the schedules. A behavioral model is needed. <b>New development:</b> specific development for indoor	Provide data from social survey to BEMs  <b>Multidisciplinarity:</b> 
 Reduce physical activity	Impact of metabolism reduction on heat stress	Partial in BEM models	<b>Input data:</b> Need to know the schedules and quantify the metabolism. A behavioral model is needed.	<b>Multidisciplinarity:</b> 
 Hydration / diet adaptation / showering...	Impact of metabolism reduction on heat stress	Not available in BEM models	<b>Input data:</b> A behavioral model is needed. <b>Modelling approach:</b> Need of coupling BEM with thermoregulation models to assess the impact of hydration	

Figure a.22: Identification of BEM needs corresponding to body oriented cooling measures from the local survey.







## FOLIO ADMINISTRATIF

### THESE DE L'INSA LYON, MEMBRE DE L'UNIVERSITE DE LYON

NOM : BARONE MOURAND

DATE de SOUTENANCE : 15/02/2024

Prénoms : Flavia

**TITRE : Numerical assessment of heat stress in dwellings and immediate surroundings: development of a Microclimate Zonal Model coupled to Building Models**

NATURE : Doctorat

Numéro d'ordre : 2024ISAL0020

Ecole doctorale : MEGA (Mécanique, Énergétique, Génie Civil, Acoustique)

Spécialité : Énergétique, physique des bâtiments

#### RESUME :

La persistance des épisodes de surchauffe urbaine affecte directement l'exposition à la chaleur, augmentant ainsi les risques pour la santé tout particulièrement en milieu urbain. Le but de cette thèse est donc de développer une méthodologie pour évaluer le stress thermique sur une base quotidienne et saisonnière dans le logement et son environnement proche. Deux approches d'exposition sont suggérées : une approche eulérienne par rapport à un lieu fixe, et une approche lagrangienne par rapport au déplacement de l'individu. Une méthode d'évaluation numérique est choisie. Ainsi, la thèse introduit les concepts de stress thermique et de contrainte thermique, définit les indicateurs journaliers et saisonniers et identifie les variables climatiques influentes ainsi que leurs échelles spatiales et temporelles. Un aperçu des facteurs influençant l'exposition à la chaleur urbaine met en évidence les besoins en modélisation numérique pour l'évaluation du stress thermique, tandis que l'analyse des modèles existants de microclimat et de simulation thermique dynamique (STD) du bâtiment met en évidence l'absence d'une approche de modélisation appropriée. Par conséquent, le travail actuel consiste à développer et à coupler un modèle zonal de microclimat (McZM) avec un modèle de STD du bâtiment. Le McZM repose sur une interpolation linéaire des débits massiques obtenus avec un précalcul CFD (Computational Fluid Dynamics) réalisable k-epsilon RANS stationnaire. Les simulations CFD sont également utilisées pour prédire les vitesses du vent spatialisées, les coefficients de transfert convectifs extérieurs et les coefficients de pression. Le McZM inclut un modèle de sol et des modèles radiatifs pour les calculs du rayonnement solaires et de grandes longueurs d'ondes, ainsi que pour le calcul de la température radiante moyenne. Pour les écoulements dans le bâtiment, un modèle de pression couplé au McZM et au modèle de STD du bâtiment est développé. Les composants des modèles sont soumis à une validation à l'aide de données expérimentales ou de comparaisons de modèles. Une application du modèle couplé au cas d'étude de l'îlot Ydeal Square à Confluence, confirme les avantages de l'utilisation d'une approche spatialisée dans l'évaluation du stress thermique. Ce cas permet également d'évaluer les avantages relatifs de la mise en œuvre de différentes mesures de rafraîchissement sur le stress thermique. Enfin, cette thèse suggère des perspectives élargies sur l'évolution de la modélisation du microclimat et des bâtiments, basées en partie sur une enquête sociale sur les pratiques de rafraîchissement des résidents pendant l'été. D'autres perspectives se concentrent sur l'amélioration du McZM actuel et de son processus de validation.

**MOTS-CLÉS :** Surchauffe urbaine, stress thermique, Modélisation de microclimat, Modélisation énergétique du bâtiment, Modèle zonal.

Laboratoire (s) de recherche : Centre d'Énergétique et de Thermique de Lyon (CETHIL UMR 5008)

Directeur de thèse: Frédéric KUZNIK (CETHIL UMR 5008)

Président de jury : Monika WOLOSZYN

Composition du jury : Andreas MATZARAKIS, Emmanuel BOZONNET, Frédéric KUZNIK, Lucie MERLIER, Jean-Jaques ROUX, Monika WOLOSZYN.

